

TIME-DEPENDENT STRAIN ACCUMULATION AND RELEASE
AT ISLAND ARCS: IMPLICATIONS FOR THE
1946 NANKAIDO EARTHQUAKE

by

Albert Turner Smith, Jr.

B.A., University of California at San Diego (1969)

M.S., Massachusetts Institute of Technology (1971)

SUBMITTED IN
PARTIAL FULFILLMENT
OF THE REQUIREMENTS FOR THE
DEGREE OF DOCTOR OF PHILOSOPHY

at the

MASSACHUSETTS INSTITUTE OF TECHNOLOGY

November, 1974

Signature of Author *Albert Turner Smith, Jr.*
Department of Earth and Planetary Sciences, Nov. 1974

Certified by.....
Thesis Supervisor

Accepted by.....
Chairman, Departmental Committee on Graduate Students

**WITHDRAWN
FROM
MIT LIBRARIES**

TIME-DEPENDENT STRAIN ACCUMULATION AND RELEASE
AT ISLAND ARCS: IMPLICATIONS FOR THE
1946 NANKAIDO EARTHQUAKE

by

Albert Turner Smith, Jr.

Submitted to the Department of Earth and Planetary Sciences

8 November 1974

in Partial Fulfillment of the Requirements for the
Degree of Doctor of Philosophy

ABSTRACT

Underthrusting and the elastic-rebound theory are consistent with the gross static deformations after earthquakes for island-arc regions such as Japan, Alaska, and Chile. Yet anomalous, time-dependent post-earthquake adjustments suggest additional processes. Here the asthenosphere or mantle becomes the element that both determines the post-seismic deformation and controls the accumulation of strain. The lithosphere and asthenosphere represent a coupled system. A large earthquake strains the entire system; stress relaxation in the viscous asthenosphere follows and allows the post-seismic readjustments.

The convergence zone is first considered as a semi-infinite, elastic plate overlying a viscoelastic foundation.

Analytic solutions for short-period deformations place bounds on the behavior for the surface deformations, boundary conditions on the fault interface, and stress-propagation following an earthquake. Detailed models are then considered using a novel, time-dependent, finite element solution for the convergence zone. The solution avoids propagation of errors in time and readily accommodates inversion theory. The method clearly defines the behavior for realistic models. Thus, scaling with the fault depth and lithospheric thickness controls the shape for simple, planar fault models, while the time scale depends on the asthenospheric viscosity. Different boundary conditions imposed on the fault, whether a constant dislocation or a constant stress with time, strongly affect the resulting deformations and stresses. Finally, stresses introduced by thermal density anomalies within the descending lithosphere are compared to earlier models and focal mechanisms near Hokkaido.

Generalized-matrix inversion theory now places bounds on the effective viscosity and fault parameters using geodetic data, focal mechanisms, and tectonic setting for the 1946 Nankaido earthquake (M 8.2) in southwest Japan. Using the assumption of stress relaxation in the asthenosphere, the data constrains the fault geometry to a shallow 15° dip, followed by a 60° dip from 26 km depth to the base of the lithosphere at 60 km depth. Near the hypocenter the slip is 3 meters, while the maximum slip is less than

15 meters. Other models with constant dip or shallower dip beyond 25 km do not satisfy these constraints. The viscosity of the asthenosphere now becomes 10^{20} poise. The results suggest segmentation of the lithosphere and deformations that generate the embayed shoreline, sedimentary basins off southwest Japan, seismicity, and focal mechanisms.

Thesis Supervisor: M. Nafi Toksöz

Title: Professor of Geophysics

ACKNOWLEDGEMENTS

To my adviser, Professor M. Nafi Toksöz, goes my appreciation for his support and encouragement. During my discussions with Professor Keiiti Aki and Dr. Katsuyuki Abe I found many fruitful paths and notions. Professor T. Pian of the Department of Aeronautics and Astronautics gave useful feedback on the finite element method, while FEABL (Finite element analysis basic library) introduced a computational framework. Carl Johnson inspired exotic uses of the computer, and Sara Brydges has gone above and beyond the call of duty during the typing and organization. Frank Richter was always a challenging colleague and reassuring friend. Finally, I thank all my friends for their patience and love.

A Fannie and John Hertz Foundation Fellowship allowed extensive opportunities for research; I am grateful for their generous and continuing support. The research has been supported by the Advanced Research Projects Agency, monitored by the Air Force Office of Scientific Research under contract F44620-71-C-0049, by the Air Force Cambridge Research Laboratories, Air Force Systems Command under contract F19628-74-C-0072, and by the Earth Sciences Section, National Science Foundation, grant GA-36132X.

TABLE OF CONTENTS

	PAGE
ABSTRACT	2
ACKNOWLEDGEMENTS	5
LIST OF FIGURES	9
CHAPTER 1: INTRODUCTION	13
CHAPTER 2: VARIATIONAL FORMULATION AND THE FINITE ELEMENT METHOD	22
2.1 Introduction	22
2.2 Variational Problem for Linear Viscoelasticity	24
2.3 Finite Element Method for Operational Variational Principles	29
2.4 Modified Variational Principle for Hydrostatic Stress	39
2.5 Fault Zone in Finite Elements	40
2.6 Inversion to the Time Domain	45
2.7 Boundary Conditions	50
2.8 Inversion Theory Applied to Finite Elements	52
CHAPTER 3: FIRST ORDER ANALYSIS OF MANTLE INTERACTIONS	62
3.1 Introduction	62
3.2 Elastic Plate on a Viscoelastic Half-Space	63
3.3 Note on the Wavelength of Relaxation	80
3.4 Dislocation Within a Layered Medium	84
3.5 Stress Propagation	88

	PAGE
3.6 Predictions and Conclusions	97
CHAPTER 4: FINITE ELEMENT MODELS OF TIME-DEPENDENT STRAIN FIELDS	99
4.1 Introduction	99
4.2 Dip-Slip Fault in an Elastic Media	107
4.3 Models for Island Arcs	110
4.4 Geometrical Scaling	4.4
4.5 Descending Lithosphere as a Boundary Condition	132
4.6 Fault Interface: Stress Drop or Dislocation Boundary Conditions	135
4.7 Initial Stress State Within the Lithosphere	168
4.8 Predictions and Conclusions	178
CHAPTER 5: AN ISLAND-ARC MODEL: THE 1946 NANKAIDO EARTHQUAKE AND SOUTHWEST JAPAN	180
5.1 Introduction	180
5.2 Interpretation of Constraining Data	181
5.3 Discussion of Earthquake Selection	186
5.4 1946 Nankaido Earthquake	193
5.5 Models for the 1946 Nankaido Earthquake	206.
CHAPTER 6: CONCLUSIONS AND DIRECTIONS	246
6.1 Conclusions	246
6.2 Implications and Future Directions	254
REFERENCES	256

	PAGE
APPENDIX A: IMPLEMENTATION OF TIME-DEPENDENT, FINITE ELEMENT METHOD	267
APPENDIX B: TEST PROBLEM: PRESSURIZATION OF A VISCOELASTIC CYLINDER WITH AN ELASTIC CASE	274
APPENDIX C: RESULTS FOR MODELS A-1 AND A-5	284
APPENDIX D: GLOSSARY OF SYMBOLS	288
BIOGRAPHICAL NOTE	291

LIST OF FIGURES
AND TABLES

FIGURE	PAGE
2.1 Configuration for representative elements.	35
2.2 Representation for fault using finite elements.	43
3.1 Configuration for an elastic beam on a viscoelastic foundation.	65
3.2 Displacement profiles for two boundary conditions, stress and displacement.	71
3.3 Vertical displacements fitted to leveling data for the 1946 Nankaido earthquake.	74
3.4 Stress using beam model compared to after-shock energy.	78
3.5 Time versus wavenumber for elastic layer on viscous half-space.	83
3.6 Strike-slip fault in an elastic layer overlying a viscoelastic half-space.	87
3.7 Model for stress propagation.	90
3.8 Displacement and stress for propagating displacement impulse.	94
3.9 Propagation distance and velocity versus time.	96
4.1 Coarse finite element mesh.	104
4.2 Refined finite element mesh.	106
4.3 Two finite element solutions compared to analytic solution for 45° thrust fault in elastic half-space.	109
4.4 Vertical, post-seismic deformations for a 100 km lithosphere.	113
4.5 Perturbations introduced by gravity on vertical surface deformations.	116

FIGURE	PAGE
4.6 Vertical surface deformations for $D/H=1$. and .5.	119
4.7 Schematic of post-seismic deformations from Figure 4.6.	122
4.8 Four models with different fault depths for a 50 km lithosphere dipping at 35° .	126
4.9 Comparison of two descending lithospheres terminating at 150 km or 650 km depth.	134
4.10 Vertical displacements for constant dislocation or constant stress release with time when faulting extends through the lithosphere.	139
4.11 Horizontal displacements on the fault in Figure 4.10.	144
4.12 Maximum shear stress and direction of principle compressive stress for the fault in Figure 4.10.	147
4.13 Profiles of maximum shear stress for a 10 meter offset on the fault.	152
4.14 Stress propagation far from the fault.	155
4.15 Diffusive stress-front compared to first-order model of stress propagation.	157
4.16 Vertical displacements for constant disloca- tion or constant stress release when fault terminates in lithosphere.	159
4.17 Horizontal displacements for models in Figure 4.16.	163
4.18 Shear stress for models in Figure 4.16.	166
4.19 Initial shear stress introduced by thermal density anomalies.	173
4.20 Comparison of Figure 4.19 to focal mechanisms near Hokkaido.	177

FIGURE	PAGE
5.1 Fault model analogous to possible 1964 Alaskan deformations.	190
5.2 Tectonic structures of southwest Japan.	196
5.3 Historic earthquakes near southwest Japan.	200
5.4 Microseismicity for Kii peninsula and schematic of focal mechanisms for 1944 and 1946 earthquakes.	203
5.5 Schematic of five fault models plotted on the microseismicity in Figure 5.4.	208
5.6 Location of displacement profiles from Fitch and Scholz (1971).	212
5.7 Aftershock epicenters following 1946 Nankaido earthquake.	216
5.8 Displacement profile A from Fitch and Scholz (1971).	218
5.9 Reduced profile A.	221
5.10 Vertical displacements and data for model A-1 using a 35° dipping fault.	227
5.11 Fault parameters and resolution for model A-5.	231
5.12 Vertical displacements and data for model A-5.	233
5.13 Tilt data from Muroto promontory.	236
5.14 Tilts from model A-5.	238
5.15 Horizontal displacements from model A-5.	241
5.16 Maximum shear stress from model A-5.	244
6.1 Tectonic structure of southwest Japan based on model A-5	252

FIGURE		PAGE
A.1	System structure for finite element computations.	270
B.1	Finite element net for viscoelastic cylinder with elastic case.	278
B.2	Principle stresses plotted on the element array.	280
B.3	Normalized radial stress from the finite element solution compared to an analytic solution for pressurization of a viscoelastic cylinder with an elastic case.	282

TABLE		
5.1	Finite element models for 1946 Nankaido earthquake.	224
C.1	Model A-1 for 1946 Nankaido earthquake.	286
C.2	Model A-5 for 1946 Nankaido earthquake.	287

1. INTRODUCTION

Large shallow earthquakes at island arcs such as Japan and Alaska are attributed to convergence and subduction of lithospheric plates. The majority of mechanisms fit neatly into the framework provided by new global tectonics: the earthquakes occur as a megathrust between the continental and underthrusting oceanic lithosphere (McKenzie and Parker, 1967; Isacks, et al., 1968). The 1964 Alaska earthquake and the 1960 Chilean earthquake appear as notable examples (Plafker, 1972). The earthquakes indicate the accumulation and release of strain energy, but they do not reveal the processes controlling the accumulation. New global tectonics synthesizes the observations into an empirical description, and outlines possible driving mechanisms for the plates. These suggest a probable cause for earthquakes: they are the sudden release of elastic strain energy primarily at the edges of or within lithospheric plates. Yet global tectonics does not treat the physics controlling the time-dependent process of strain accumulation prior to an earthquake, nor the readjustments following a major earthquake. Theoretically only the static problem for a fault dislocation has been treated; the factors effecting the slow accumulation of strain and post-earthquake deformations have not been studied adequately.

Moreover, observations suggest the importance for a time-dependent analysis of strain fields associated with major

earthquakes. Geodetic data has long indicated a succession of crustal warping and rebounds for major earthquakes in Japan. In addition, anomalous crustal movements that are inconsistent with Reid's (1910) elastic rebound theory are prominent in these geodetic observations (e.g. Matuzawa, 1964). The anomalies are not isolated to any one earthquake; instead, post-seismic movements are observed after many earthquakes: 1906 San Francisco, 1923 Kanto, 1927 Tango, 1946 Nankaido, 1964 Niigata, and 1966 Parkfield earthquakes (Matuzawa, 1964; Fitch and Scholz, 1971; Scholz, 1972; Thatcher, 1974). Different explanations are possible to account for the behavior. Aftershock patterns also reflect the changing stress field caused by a major earthquake. Besides their location, aftershocks show continuing alterations after major earthquakes (Aver'yanova, 1973). Seismicity gaps indicate stress variations on a larger scale. Here the interaction of adjacent seismic zones requires further analysis (e.g. Kelleher, 1970; Mogi, 1973). All these separate observations offer constraints on the possible modes of strain accumulation at island arcs.

In this thesis I propose the mantle or asthenosphere as a key element controlling the strain accumulation and influencing the long-term strain release. Its influence potentially extends from aftershocks and seismicity gaps to post-glacial rebound and convection. Here we examine the effects

of the asthenosphere on processes of strain accumulation and release associated with major thrusting earthquakes. The interaction of an elastic lithosphere overlying a viscous asthenosphere represents the significant concept. Solving such a problem yields relaxation times for the diffusion of strains, the effective viscosity of the asthenosphere, and a deeper understanding of the interaction and its consequences at island arcs. In short, the lithosphere and mantle represent a coupled system which is important on time scales comparable to the strain accumulation of earthquakes.

The sequence of crustal deformations associated with a major thrust earthquake such as the 1946 Nankaido have particular significance in this proposal. These movements reduce to four stages: secular, pre-earthquake, earthquake or seismic, and post earthquake (Scholz, 1972). The first is slow (secular) strain accumulation occurring between major earthquakes. Here the driving forces responsible for plate tectonics manifest themselves by crustal warping. This stage and the third phase, the earthquake, combine to form the elastic rebound theory of Reid (1910): tectonic movements produce a slow and steadily increasing elastic strain until failure occurs and crustal rebound releases the potential energy. Thus, these two phases directly follow from elasticity theory. Yet even here stress relaxation may determine the rate.

The other phases introduce new phenomena. The second phase, pre-earthquake deformations, occurs as a rapid change in crustal deformation patterns. Many observations are available prior to major earthquakes (Matuzawa, 1964); unfortunately, they are often dubious and fragmentary. The anomalous movements preceeding the 1964 Niigata earthquake by a year at tidal stations are perhaps the best documented case for pre-earthquake tectonic movements (Tsubokawa, et al., 1964). Even here sources of error cast doubt on the results (Tsumura, 1970; section 5.2). Matuzawa (1964) and Scholz (1972) summarize observations preceding other major earthquakes including the 1923 Kanto, the 1966 Parkfield, and the 1966 Tashkent earthquakes. Simple mantle relaxation does not readily account for these observations since the hypothesis does not predict any pre-earthquake movements, only post-earthquake deformations. Other candidates include dilatancy or premonitory fault creep along the zone (Scholz, 1972, 1974; Kanamori, 1973). If dilatancy proves correct, it will also generate post-earthquake deformations.

Rapid crustal movements when compared to the slow, secular accumulation also characterize post-seismic or post-earthquake deformations. The movements have either the same or the reverse sense as the earthquake phase; the sense of movement and the overall pattern depend on the particular earthquake. The 1966 Parkfield earthquake appears as a

buried fault: the post-earthquake movements correspond to creep along the surface extension of the buried fault (Scholz, et al., 1969). Thus, the post-seismic movements have the same direction as the earthquake and approach its inferred offset. Scholz (1972) documents similar observations for other strike-slip faults. Thatcher (1974) suggests this behavior for the 1906 San Francisco earthquake except along deeper segments. All these appear directly attributable to fault creep on buried faults.

Another group of earthquakes do not readily lend themselves to this mechanism for post-earthquake adjustments; instead, asthenospheric stress relaxation gives a concise explanation. These earthquakes include the 1946 Nankaido, the 1923 Kanto, and perhaps the 1964 Niigata earthquakes. One might also include the 1964 Alaskan earthquake. All these earthquakes conform to a dip-slip mechanism, and the post-earthquake deformations have both reverse and similar sense to the seismic deformations. Fault creep or after-shocks may contribute to these deformations. Yet unlike the previous case, the geodetic data would indicate both forward creep extending the fault and reverse slip on the existing rupture (Fitch and Scholz, 1971). The rapid decay of after-shocks, however, suggests fault slip may not be the only mechanism since the geodetic data varies long after the 1946 Nankaido earthquake (Matuzawa, 1964; Fujita, 1969; Fitch and

Scholz, 1971; Tsumura, 1970).

Dilatancy may also contribute to the post-earthquake deformations (Scholz, 1974). If dilatancy is proven for a pre-earthquake phase similar to the 1964 Niigata earthquake, it introduces a strong case for post-earthquake dilatant recovery that at least contributes to the surface deformations. The effects of dilatancy on seismic waves, however, have proven elusive under controlled conditions (i.e. Allen and Helmberger, 1973), and an adequate model to simulate surface deformations is not available. Scholz (1974) uses a one-dimensional model based on fluid outflow using the theory of consolidation. Qualitative agreement results for the recovery time using the tilt data at Muroto promontory for the 1946 Nankaido earthquake or using the tidal data from the 1964 Niigata earthquake. The recovery time defines the ratio of the hydraulic diffusivity and dilatant thickness. This qualitatively agrees with the diffusivity-dimensional relation deduced from seismic velocities (Scholz, et al., 1973; Anderson and Whitcomb, 1973), but the short decay time disagrees with the geodetic observations occurring years after the 1946 Nankaido earthquake. Beyond this relationship, problems arise in the description. Dilatancy predicts post-seismic subsidence which may increase approaching the fault (Scholz, 1974). Yet the 1946 Nankaido earthquake involves post-seismic uplift over a broad area

(Fujita, 1969). This tends to contradict dilatancy, at least in a qualitative sense. If it exists, the assumption remains that it is a short term anomaly obscured in the geodetic measurements. Consequently, dilatancy effects are not included in the present analysis.

The analysis here will attempt to define just one effect of the asthenosphere on the strain field: the post-seismic geodetic deformations following the 1946 Nankaido earthquake. Other contributions such as fault creep are not directly treated in the analysis, but are discussed through idealized models. Inclusion of these factors, fault creep and mantle flow, presents a difficult problem for solution. A model or simulation must be developed which contains the essential physics and assumptions while ignoring unwarranted or unresolvable complications. The approach taken uses a linear viscoelastic continuum for the mantle and lithosphere. It contains the essential features, initial elasticity and time-dependent stress relaxation, and avoids further material and numerical complications inherent in nonlinear stress-strain relaxation. A novel approach in the Laplace plane using the finite element method results in a very tractable model for the time-dependent problem when inertial terms are ignored. Generalized matrix inversion theory can then be applied to yield the bounds upon the parameters such as fault creep and viscosity. The assumptions and methods are the topics of Chapter 2.

Prior to this analysis long-term, time-dependent deformations are primarily confined to dislocations in an elastic medium. Analytic solutions for strike-slip and dip-slip faults give fundamental insights (i.e. Maruyama, 1963, 1964; Burridge and Knopoff, 1964). Using these simple models at island arcs, Savage and Hastie (1966) were able to confirm major thrust faults at continental margins or island arcs. They appear as a megathrust between the subducting oceanic and continental lithospheres. Fitch and Scholz (1971) employ a simple analytic solution in their analysis of the 1946 Nankaido data. Each time-interval conforms to a separate dislocation model, thereby representing fault creep by successive fault displacements. Using the correspondence principle (Biot, 1954; Lee, 1955), solutions for a dip-slip fault in a viscoelastic half-space are available (Rosenman and Singh, 1973b); unfortunately, the elastic lithosphere makes this a very poor model for an island arc. To extend the solution to a layered medium generally requires an analytic solution in closed form for the dip-slip fault; however, none exists. On the other hand, Nur and Mavko (1974) use Rybicki's (1971) analytic solution for a strike-slip fault to generate a viscoelastic solution with an elastic lithosphere.

Numerical methods and hybrid techniques appear as the best alternative. Braslau and Lieber (1968) proposed a

solution method using Galerkin vectors for a Volterra dislocation, but never could implement the technique. Other possible methods include propagator matrices, yet the assumption limits the solution to a layered medium (Barker, 1974). Consequently, the finite element method becomes the most feasible method for an island arc. Chapter 2 extends this discussion to numerical methods and inversion theory.

In Chapter 3 idealized models define characteristic interactions between the asthenosphere and lithosphere. Simple, first-order analytic models suggest directions and approaches to the problem: Crustal deformations, boundary conditions along the fault, and viscosity of the asthenosphere are significant factors for the analysis. The results encourage an idealized two-dimensional analysis using the finite element method. This is the topic of Chapter 4. Finally, in Chapter 5 detailed models using geodetic data, inverse theory, and the finite element method define the fault geometry and slip for the 1946 Nankaido earthquake when stress relaxation in the asthenosphere occurs after the earthquake.

2. VARIATIONAL FORMULATION AND THE FINITE ELEMENT METHOD

2.1 Introduction

The earth exhibits a complex structure along island arcs: a dipping fault plane often separating continental and oceanic lithosphere. This real earth domain can include geometrical and material inhomogeneities, and irregular boundaries. And all this may also be imposed on the time-domain. A solution strategy for the time-dependence of strain must be capable of handling these problems. Analytic solutions are virtually limited to the half-space (Rosenman and Singh, 1973a,b). Hybrid analytic solutions with propagator matrices are possible for a linear viscoelastic model, but one is limited to a layered media. This may be suitable for a strike-slip fault, however, island arcs do not correspond to a layered media. Numerical solutions appear as the only real technique that holds any promise for even a simple dipping lithosphere.

Not every problem is suitable for numerical solution. Our intent is not brute force. A reasonably efficient and versatile solution strategy must be found that includes the essential feature of the problem: time-dependent relaxation of the stress within the mantle, inhomogeneities within the mantle (i.e. dipping slab), and fault dislocation. Two general strategies immediately suggest themselves, use of the finite element method and finite differences.

The finite element method solves the variational problem, that is, minimizing an energy functional or similar expression over subregions and then combining into a banded symmetric matrix. The engineering sciences have provided the impetus for its development, for it is ideally suited to elliptical boundary value problems as encountered in elasticity theory. For these the method is efficient and has flexible resolution. But time dependence introduces problems. One could discretize in time and solve; however, this normally requires a two-point boundary value problem, while time represents an initial value domain. It is at this point that finite differences is usually introduced together with all its difficulties.

The finite difference technique has been the usual solution strategy for time dependent problems (Richtmeyer and Morton, 1967). It is also notorious for its idiosyncrasies: unstable convergence, slowness, and difficulties at discontinuities. If we use an integral technique for generating the difference equations (Smith and Toksöz, 1972), and then step in time, one does better. Yet this is basically equivalent to a finite element solution in space and finite-differences in time. This is better than finite differences in time and space, but not by much considering the bookkeeping needed during the solution.

An alternate method uses an approximate Laplace transform inversion and applies the finite element method to the

Laplace domain of the variational-evolutionary principle. First developed by Schapery (1962) for the Rayleigh-Ritz method, the technique immediately limits one to linear viscoelasticity, actually a very desirable assumption. Adey and Brebbia (1973) suggested extending the finite element method to it since the strategy obviously overcomes the problems of stability and error propagation found in the finite difference technique. Indeed it is applicable to any problem formulated as a Stieltjes integral having a well behaved kernel. The next section will elaborate on this strategy.

2.2 Variational Problem for Linear Viscoelasticity

Essential to the finite element problem is a variational formulation of the problem: the solution technique is based on the minimization of an integral-differential operator. For boundary value problems as in the theory of elasticity, these variational principles are relatively straightforward and assert that a function u (displacement or stress) satisfies such a principle if and only if the given functional (i.e. potential or complementary energy) is stationary at u . However, viscoelasticity requires an "evolutionary" principle: a functional which is minimized along a trajectory in time.

Several derivations of variational theorems in quasi-static viscoelasticity are possible. Schapery (1962) has used Biot's thermodynamic theory to deduce one such principle.

This theorem imposes certain limitations on the class of problems. Instead, a simple generalization of the elastostatic variational principle due to Gurtin (1963) using Stieltjes convolutions will be proven. Later we will review Schapery's assumptions, for they bear upon the numerical technique.

For reference the differential equation defining the quasi-static viscoelastic boundary value problem are (Christensen, 1971)

$$\begin{aligned} \epsilon_{ij} &= 1/2(u_{i,j} + u_{j,i}) \text{ assuming infinitesimal strain} \\ &\quad \text{and } u_{i,j} = \frac{\partial u_i}{\partial x_j} \\ \sigma_{ij} &= \int_0^t G_{ijkl}(t-\tau) \frac{\partial \epsilon_{kl}(\tau)}{\partial \tau} d\tau \end{aligned} \quad (2.2.1)$$

or

$$\sigma_{ij} = G_{ijkl} * d\epsilon_{kl}$$

using the Stieltjes convolution form of the constituent relation. Note that σ_{ij} is the stress tensor and ϵ_{ij} is the strain tensor.

$$\sigma_{ij,j} + F_i = 0 \quad \text{for equilibrium relation,} \quad (2.2.2)$$

$$\text{and } \sigma_{ij} n_j = S_i \quad \text{on } B_\sigma \quad (2.2.3)$$

$$u_i = \Delta_i \quad \text{on } B_u \quad (2.2.4)$$

where S_i and Δ_i are the prescribed stresses and displacements on the boundaries B_σ and B_u , respectively, when n_j is the normal vector and F_i is the body force. The kernels $G_{ijkl}(t)$ are mechanical properties of the material and are termed relaxation functions.

The object is to derive a functional π whose variation $\delta\pi$ vanishes and yields equations (2.2.2) - (2.2.4). We now define the functional π according to Gurtin (1963):

$$\begin{aligned} \pi = & \int_V [1/2G_{ijkl} * d\varepsilon_{ij} * d\varepsilon_{kl} - \sigma_{ij} * d\varepsilon_{ij} - (\sigma_{ij,j} + F_i) * du_i] dv \\ & + \int_{B_u} [\sigma_i * d\Delta_i] da + \int_{B_\sigma} [(\sigma_i - S_i) * du_i] da \end{aligned} \quad (2.2.5)$$

where F_i , Δ_i , and S_i are given quantities and each variable is dependent upon the appropriate coordinates. We let $\sigma_i = \sigma_{ij} n_j$ on the boundary. π is the correct functional if the Euler equations give the proper field equations and boundary conditions. The first variational $\delta\pi$ of the functional π in equation (2.2.5) vanishes if and only if the field equations and boundary conditions given by equations (2.2.2) - (2.2.4) are satisfied. The variational principle is then a generalization to viscoelasticity of the Hu-Washizu theorem in elasticity (Hai-Chang, 1955; Washizu, 1955).

Suppose we take the variations in the histories $u_i(\tau)$, $\varepsilon_{ij}(\tau)$, and $\sigma_{ij}(\tau)$ to prove this statement; that is

$$\begin{aligned} u_i(\tau) + \delta u_i(\tau)\alpha \\ \varepsilon_{ij}(\tau) + \delta \varepsilon_{ij}(\tau)\alpha \\ \sigma_{ij}(\tau) + \delta \sigma_{ij}(\tau)\alpha \end{aligned} \quad (2.2.6)$$

where α is some small real number and $\delta u_i(\tau)$, $\delta \varepsilon_{ij}(\tau)$, and $\delta \sigma_{ij}(\tau)$ are sufficiently smooth, arbitrary functions. The

general variation of the function is desired (Gelfand and Fomin, 1963). The first variation of π becomes

$$\begin{aligned} \delta\pi = & \int_V [G_{ijkl} * d\epsilon_{kl} * d\delta\epsilon_{ij} - \sigma_{ij} * d\delta\epsilon_{ij} - \delta\sigma_{ij} * d\epsilon_{ij} - (\sigma_{ij,j} + \\ & F_i) * d\delta u_i - \delta\sigma_{ij,j} * du_i] dv \\ & + \int_{B_u} [\delta\sigma_i * d\Delta_i] da + \int_{B_\sigma} [(\sigma_i - S_i) * d\delta u_i + \delta\sigma_i * du_i] da \end{aligned} \quad (2.2.7)$$

Here the commutative property of Stieljes convolutions ($G_{ijkl} * d\delta\epsilon_{ij} * d\epsilon_{kl} = G_{ijkl} * d\epsilon_{kl} * d\delta\epsilon_{ij}$), and the symmetric relation ($G_{ijkl} = G_{klij}$) based on the existence of energy and Onsager's principle (Fung, 1965, pp. 373; Christensen, 1971). Following Gurtin's development the term $\int_{B_u} [\delta\sigma_i * du_i] da$ is subtracted from the integral over B_u and added to the last term of the B_σ integral. Using Green's theorem, the first variation results:

$$\begin{aligned} \delta\pi = & \int_V (G_{ijkl} * d\epsilon_{kl} - \sigma_{ij}) * d\delta\epsilon_{ij} - (\sigma_{ij,j} + F_i) * d\delta u_i \\ & - (\epsilon_{ij} - 1/2u_{i,j} - 1/2u_{j,i}) * d\delta\sigma_{ij} dv \\ & + \int_{B_\sigma} [(\sigma_i - S_i) * d\delta u_i] da + \int_{B_u} [(\Delta_i - u_i) * d\delta\sigma_i] da \end{aligned} \quad (2.2.8)$$

To satisfy $\delta\pi = 0$ for arbitrary $\delta\sigma_{ij}$, δu_i , and $\delta\epsilon_{ij}$ each integral must separately vanish. This requires that the integrand of each equal zero giving us the field equation and boundary conditions, equations (2.2.2) - (2.2.4).

Since a 'displacement' approximation will be used with the finite element method, a simplified variation principle is more useful:

$$\pi_d = \int_V [1/2 G_{ijkl} * d\epsilon_{ij} * d\epsilon_{kl} - F_i * du_i] dv - \int_{B_\sigma} (S_i * du_i) da \quad (2.2.9)$$

Only the displacements are varied subject to the constraint imposed by the displacement boundary conditions (2.2.4).

This variational principle is then analogous to stationary potential energy in elasticity and the proof proceeds as before (Christensen, 1971, sec. 5.4).

An operational form of the variational principle may now be obtained if the Laplace transform of π_d is taken (Schapery, 1962):

$$\bar{\pi}_d = \int_0^\infty e^{-pt} \pi_d(t) dt \quad (2.2.10)$$

obtaining

$$\bar{\pi}_d = \int_V [1/2 \bar{G}_{ijkl} * \bar{d}\epsilon_{ij} * \bar{d}\epsilon_{kl} - \bar{F}_i * \bar{d}u_i] dv - \int_{B_\sigma} (\bar{S}_i * \bar{d}u_i) da \quad (2.2.11)$$

where the bar denotes the Laplace transform of the function. The variation of $\bar{\pi}_d$ derives the Laplace transformed Euler equations. These are completely analogous to the Euler equations in the time domain. Using this operational variational principle we can easily compute the displacement

solution in the Laplace domain given the transformed relaxation function \bar{G}_{ijkl} for the material and the transformed boundary conditions. Only the solution must be inverted to the time domain. These are the topics of the next sections.

2.3 Finite Element Method for Operational Variational Principles

The finite element method is very similar to the Rayleigh-Ritz-Galerkin technique. Each begins with a functional or variational principle and minimizes it for an approximating function u . This in turn leads to the Euler equations for the system. While finite difference schemes approximate the derivatives after minimization in these Euler or field equations, both the finite element and Rayleigh-Ritz methods start with the actual variational principle, but with one significant difference: the Rayleigh-Ritz-Galerkin strategy chooses a finite number of trial functions $\phi_1 \dots \phi_N$ which span the whole domain and satisfy the boundary conditions for the variational principle. The finite element method, on the other hand, subdivides the domain into 'elements'. Within each element a simple, complete sequence of trial functions interpolates the function u . Compatibility with essential boundary conditions is easily achieved for the trial functions within each regular element, as opposed to the Rayleigh-Ritz method when irregular boundaries over the whole domain must be satisfied by the trial functions. Each subdivision

or element of the finite element domain can then be assembled with the others into discrete algebraic equations having banded properties, a significant advantage for efficient numerical solution. It is this simplicity of the trial or interpolation functions which gives the finite element method its power.

Courant (1943) first proposed the equivalent of the finite element method with a piecewise application of the Ritz method to the St. Venant torsion problem. Engineering problems, however, provided the real motivation for its development (Argyris, 1954; Turner, et al., 1956), while its relation to the Rayleigh-Ritz-Galerkin principles was only later recognized and used to advantage. It is not my intention here to outline the whole theory, for an excellent mathematical text is available (Strang and Fix, 1973). Instead the emphasis is placed upon the solution of the quasi-static viscoelastic problem using the operational formulation.

Common to all finite element problems is the variational formulation of the equations. These can be developed by using the principle of 'virtual work' for elasticity theory (Fung, 1965, sec. 10.7), by introducing the thermodynamics of the system (Biot, 1965, 1970), or by appealing to various mathematical operations as the Galerkin method (Strang and Fix, 1973, sec. 2.3). It is fundamental to remember, however, that the variational principle determines the boundary

conditions satisfied by the trial or interpolation functions for each element. The variational statement represents the primary physical principle, and the differential equation and boundary conditions are only a secondary consequence. Care must be taken then to preserve the proper boundary conditions within the variational principle. The results will be obvious as the finite element approximation emerges from the variational principle.

Let us begin with the simplified displacement variational principle developed in the previous section for viscoelasticity. Although the operational form in the Laplace domain is used for the derivation, the results are exactly analogous to the elasticity problem. The transformed operational variational principle is given by equation (2.2.11) if $\varepsilon_{ij} = 1/2(u_{i,j} + u_{j,i})$:

$$\bar{\pi} = \int_V [1/2 \bar{G}_{ijkl} * \bar{d}\varepsilon_{ij} * \bar{d}\varepsilon_{kl} - \bar{F}_i * \bar{d}u_i] dv - \int_{B_\sigma} (\bar{S}_i * \bar{d}u_i) da \quad (2.3.1)$$

when the integrations are carried over the volume V for the region and surface area B_σ for the applied tractions S_i . The bar denotes the Laplace transform of the function. Associated with this operational variational principle are the following Euler equations and boundary conditions in the Laplace domain:

$$\bar{\sigma}_{ij,j} + \bar{F}_i = 0 \quad (2.3.2)$$

$$\bar{\sigma}_{ij} n_j = \bar{S}_i \quad \text{on } B_\sigma \quad (2.3.3)$$

Now the approximation requires an interpolation function for u applied to each element, then summing the contributions of the elements.

The interpolation function for the subregion must satisfy certain conditions in displacement: first, rigid body motions must be possible. This is a consequence of the essential boundary conditions. Second, the admissible space of derivatives in the variational principle must be represented in the interpolation. Finally, the set of functions should be complete between the lowest and highest degree of approximation. With the variational principle (2.3.1) the interpolation of u must contain a constant displacement term u_0 and at least the linear term to represent the first derivative. Polynomial interpolation such as Hermite splines give the best and most complete representation. A discussion of this problem may be found in Strang and Fix (1973); here it will suffice to assume that a polynomial representation is optimum.

Let us represent the function (i.e. displacement) u as a sum of the basis or interpolation functions ϕ_j . If the problem is discretized, nodal parameters q_j can be associated with each element. Each of these q_j is the value at a given node z_j of either the function itself or one of its derivatives. Thus one has for trial function v^h

$$q_j = D_j v^h(z_j) \quad (2.3.4)$$

when D_j is the differential operator of order j . For each

element specific nodes are assigned for the approximation as illustrated in Figure 2.1. Now a trial function ϕ_j is assigned to each nodal parameter q_j having the following property: At node z_j , $D_j\phi_j$ equals 1, while at all other nodes the interpolation function is zero. One has

$$D_i\phi_j(z_i) = \delta_{ij} \quad (2.3.5)$$

Within the element the displacement trial function then becomes

$$u^h = \sum q_j \phi_j \quad (2.3.6)$$

This represents a local basis within one element.

If the variational principle is now considered as the sum of each element's contribution, one arrives at the following form after introducing matrix notation:

$$\bar{\pi} = \sum_n \left\{ \int_V [1/2 \bar{d}\epsilon^T \bar{G} \bar{d}\epsilon - \bar{d}u^T \bar{F}] dv - \int_{B_\sigma} (\bar{d}u^T \bar{S}) da \right\} \quad (2.3.7)$$

The interpolation basis function can be represented by

$$\bar{d}u = \phi \bar{q} \quad (2.3.8)$$

and

$$\bar{d}\epsilon = E \bar{d}u = E\phi \bar{q} \quad (2.3.9)$$

where E represents the strain operator, ϕ is the interpolation function, and \bar{q} represents the nodal values. The operator E depends upon the coordinate system and particular element.

Figure 2.1

Configuration for representative elements. Nodes Z_j define each element, where the values q_j approximate the trial function v at node Z_j .

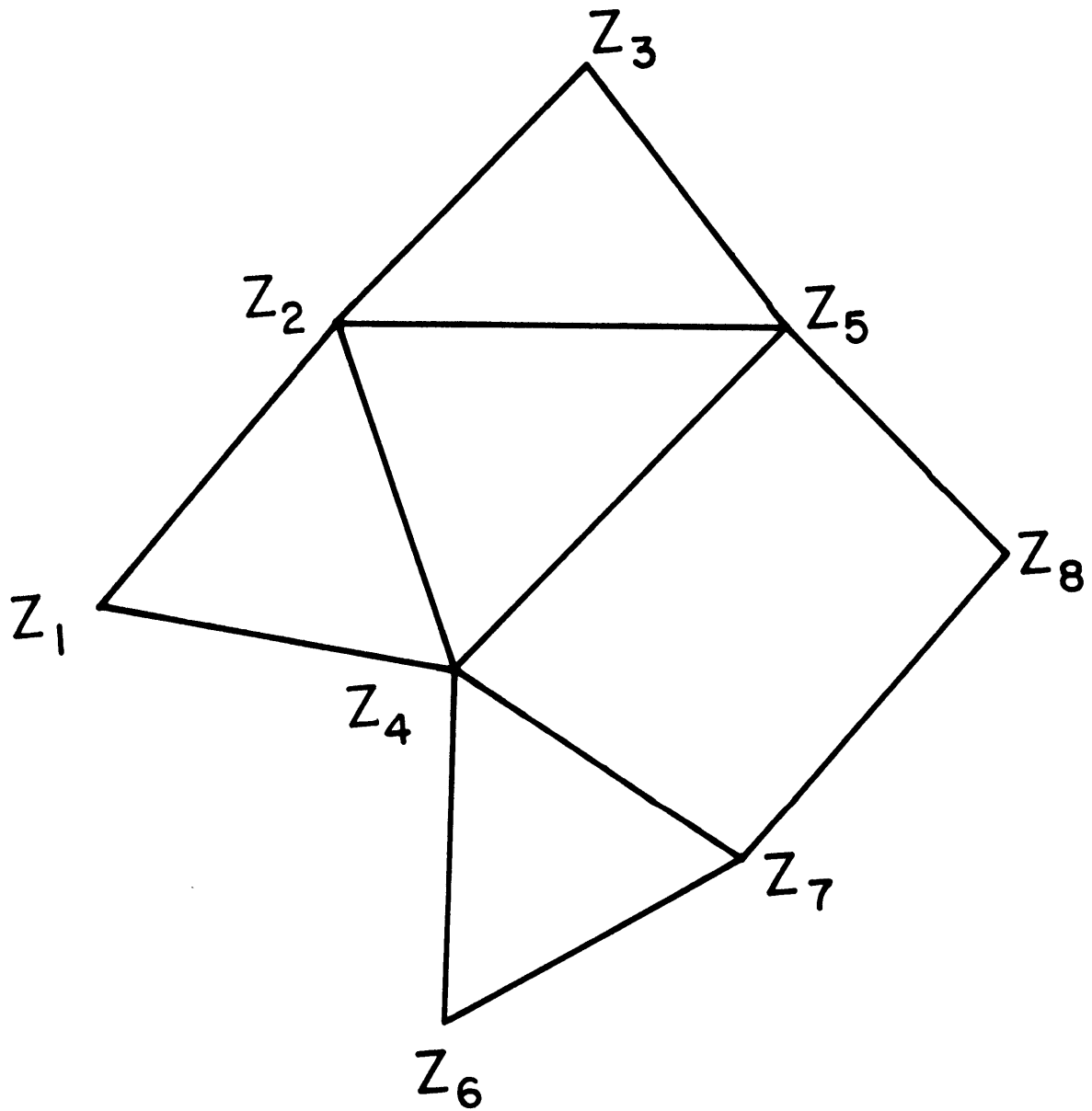


Fig. 2.1

Substituting these into the variational principle for each element yields

$$\bar{\pi} = \sum_n (\bar{q}^T \underset{\sim}{k} \bar{q} - \bar{q}^T \underset{\sim}{Q}^e) \quad (2.3.10)$$

where

$$\underset{\sim}{k} = 1/2 \int_V \phi^T \underset{\sim}{E} \underset{\sim}{G} \phi \, dv \quad (2.3.11)$$

$$\underset{\sim}{Q}^e = \int_V \phi^T \underset{\sim}{F} \, dv + \int_{B_\sigma} \phi^T \underset{\sim}{S} \, da \quad (2.3.12)$$

Here \bar{q} have been removed from the integrals since they represent the nodal values. All the elements may now be summed obtaining a matrix of the form

$$\bar{\pi} = \bar{q}^T \underset{\sim}{K} \bar{q} - \bar{q}^T \underset{\sim}{Q} \quad (2.3.13)$$

where

$$\underset{\sim}{K} = \sum_n \underset{\sim}{k} \quad (2.3.14)$$

$$\underset{\sim}{Q} = \sum_n \underset{\sim}{Q}^e \quad (2.3.15)$$

The quadratic form for $\bar{\pi}$ is minimized when

$$\underset{\sim}{K} \bar{q} = \underset{\sim}{Q} \quad (2.3.16)$$

Thus we need only solve this matrix equation.

The solution technique is improved if we observe certain properties of the matrix $\underset{\sim}{K}$: first, $\underset{\sim}{K}$ is banded if care is taken when numbering or ordering the displacements $\underset{\sim}{q}$. Each position in $\underset{\sim}{K}$ represents the coupling between two nodal

values; an entry will generally occur if the nodes are adjacent to one another. Thus adopting a uniform and sequential ordering scheme for q drastically reduces the bandwidth of \tilde{K} and its storage requirements. Second, \tilde{K} is symmetric and positive-definite since \bar{G}_{ijkl} are always positive. Under these circumstances Cholesky factorization and forward-backward substitution provides an efficient solution strategy for the problem (see Wilkinson and Reinsch, 1971, Part 1).

As one might have foreseen, the elements and their basis functions have a crucial position in the method. The degree of the approximation dictates the minimum possible bandwidth, but also the accuracy of the approximation. For example, if a linear approximation to the displacement u is used on a triangular element, stress will be constant throughout the element (hence the name Constant Strain Triangle), and six degrees of freedom are required for a two-dimensional element. The error for the displacement is proportional to h^2 where h is the characteristic dimension of the element (Strang and Fix, 1973, chapter 1). Introducing a quadratic approximation and six nodes or twelve degrees of freedom on the triangular element vastly improves the accuracy. One now has a linear approximation in stress and h^4 error in displacement; however, the bandwidth is increased with twelve degrees of freedom for one element giving a corresponding increase in solution time (Strang and Fix, 1973, sec. 1.9). A trade-off exists then

between the order of the approximation and the solution time. It may be more expedient to use more three node than six node triangular elements to achieve a desired accuracy for the displacements. The most desirable element for stress approximation is not obvious for most circumstances, since the twelve degree of freedom triangular element can make an immense difference (Desai and Abel, 1972, sec. 6.2). For the visco-elastic computations both six node triangular and four node isoparametric quadrilaterals also improve the stress approximation. Each problem, then, poses different conditions requiring careful thought for the grid structure.

The singularity introduced by the fault (i.e. crack tip) strongly effects the element configuration. The convergence error associated with the singularity depends on the dimension of the element and not the order of the approximation within the element (Strang and Fix, 1973, chapter 8). Unless a special element containing a singularity function is introduced, the grid must be more refined near the crack tip. For these computations I have opted for increasing the number of elements rather than using a singularity function. Arbitrary displacements are necessary along the fault which implies singularity functions for each element along the whole fault. This complication would significantly effect the bandwidth and computational speed, negating the effort required for development and incorporation of these singularity elements.

2.4 Modified Variational Principle for Hydrostatic Stress

Gravity introduces prestressing into the media which can be included in the variational principle. Biot (1965) has extensively treated this problem; his development will be cited in this section. The finite element method introduces special problems since the symmetry of the banded matrix must be maintained. The terms representing hydrostatic prestressing, however, retain a bilinear form allowing a simple transformation to a real symmetric quadratic matrix.

When the hydrostatic component of the initial stress is removed from the variational principle and only residual or deviatoric stress is expressed, two additional terms are introduced which represent the work of the buoyancy forces (Biot, 1965, sec. 3.6):

$$Y = \rho_f X_j u_j e + 1/2 X_j \frac{\partial \rho_f}{\partial x_i} u_i u_j \quad (2.4.1)$$

Here ρ_f denotes the fluid density of the media producing the hydrostatic stress; X_j is the j component of the body force; e is the dilatation; and u are the displacement components. The first term, $\rho_f X_j u_j e$, expresses a buoyancy effect arising from a change of volume, while the second, $1/2 X_j \frac{\partial \rho_f}{\partial x_i} u_i u_j$, represents a buoyancy generated from the displacement and the density gradient. The latter term appears as an elastic force proportional to the displacement directed normally to the equipotential surfaces. The modulus is proportional to

the product of the body force magnitude and the density gradient; hence, depending on the sign, it may be stabilizing or destabilizing.

To incorporate these terms within the finite element method, they must be represented in a symmetric quadratic form. We can represent the dilatation e using our nodal approximation in the finite element method (see section 2.3)

$$e = \underline{\underline{E}} \underline{\underline{\phi}} \underline{\underline{q}} \quad (2.4.2)$$

where $\underline{\underline{u}} = \underline{\underline{\phi}} \underline{\underline{q}}$ for the displacements and $\underline{\underline{E}}$ represents the strain-displacement operator. Thus a bilinear form also results for Y :

$$Y = \underline{\underline{q}}^T \underline{\underline{\alpha}}^T (\rho \underline{\underline{X}})^T \underline{\underline{E}} \underline{\underline{\alpha}} \underline{\underline{q}} + 1/2 \underline{\underline{q}}^T \underline{\underline{\alpha}}^T \frac{\partial \rho}{\partial \underline{\underline{x}}} \underline{\underline{X}} \underline{\underline{\alpha}} \underline{\underline{q}} \quad (2.4.3)$$

Any real bilinear matrix $\underline{\underline{A}}$ can be transformed to a real symmetric quadratic

$$\underline{\underline{x}}^T \underline{\underline{C}} \underline{\underline{x}} \quad (2.4.4)$$

if

$$\underline{\underline{C}} = 1/2 [\underline{\underline{A}} + \underline{\underline{A}}^T] \quad (2.4.5)$$

This formulation, then, readily accommodates initial hydrostatic prestressing within the media.

2.5 Fault Zone in Finite Elements

An earthquake fault zone is analogous to a crack or internal boundary condition within the media. Different boundary conditions are possible along each face of the

crack: a stress boundary implies a constant stress drop while a displacement boundary signifies a Somigliana dislocation (Bilby and Eshelby, 1968). In this section a method is indicated which incorporates either boundary condition along a fault so long as linearity assumptions are maintained for the deformation.

For simplicity let us consider a displacement dislocation along a crack or fault represented by $\Delta u = u^+ - u^-$. This internal boundary can be represented by two adjacent nodes with a prescribed displacement between the nodes. Each node is then free to deform within the media; yet their location relative to one another defines the dislocation. Figure 2.2 illustrates this configuration. To implement this strategy using the finite element method requires little additional effort if the coordinate system of the variational principle is transformed along the fault. We must express the absolute coordinates along one fault interface in terms of the opposing face. Assuming the elements have been assembled into a stiffness matrix, we have the following variational principle (see section 2.3):

$$\pi = \underline{\underline{q}}^T \underline{\underline{K}} \underline{\underline{q}} - \underline{\underline{q}}^T \underline{\underline{Q}} \quad (2.5.1)$$

where $\underline{\underline{q}}$ are the nodal parameters or generalized coordinates, $\underline{\underline{K}}$ is the stiffness matrix, and $\underline{\underline{Q}}$ represents the nodal forces. If the matrix is partitioned into sections

Figure 2.2

Representation for fault (or crack) within finite element region. Considering a pair of nodes, we define the u_2 coordinate in terms of u_1 ($u_2 = u_1 + \Delta u$) along the internal boundary.

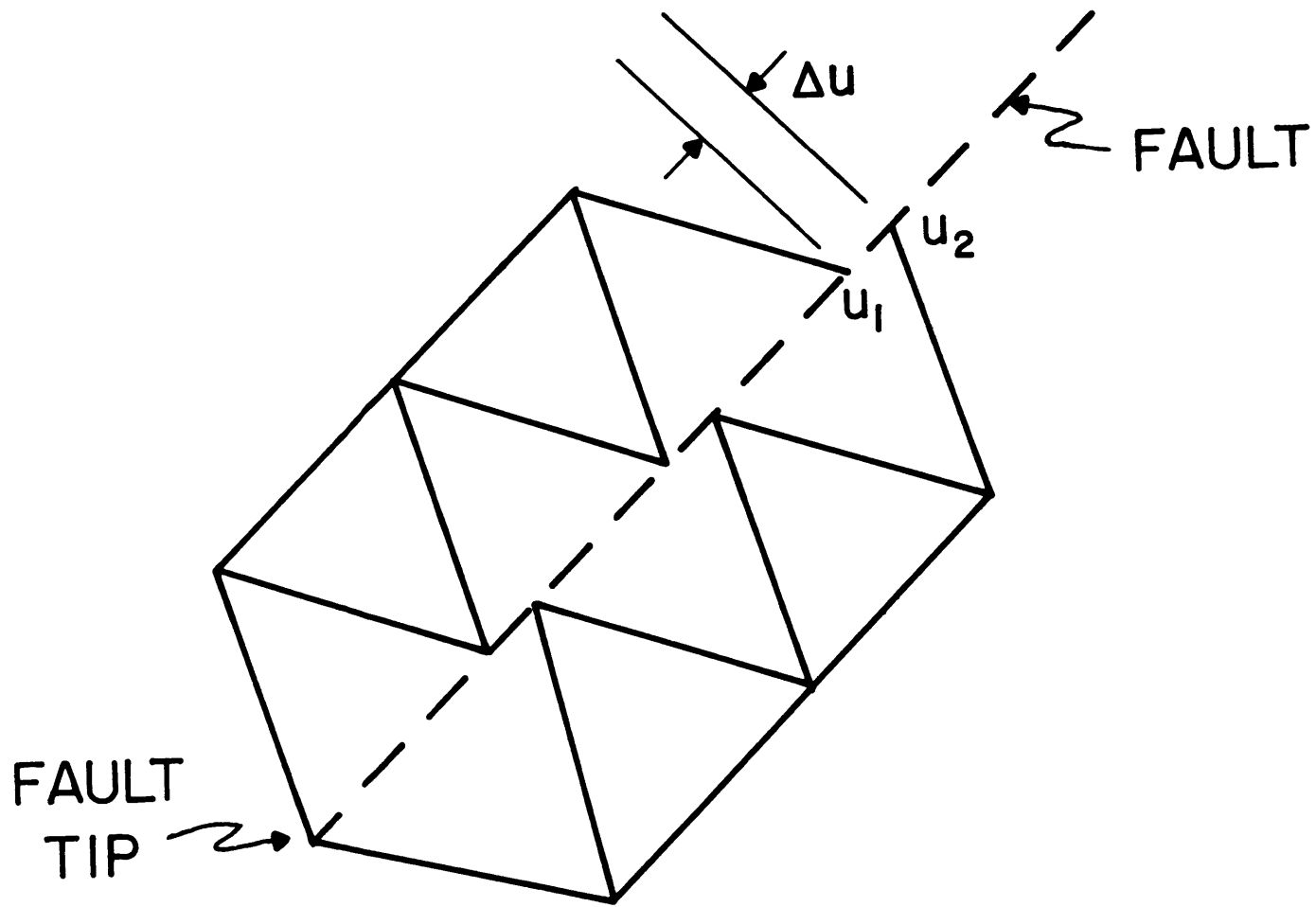


Fig. 2.2

$$\pi = \begin{bmatrix} q_\alpha & q_\beta & q_\gamma \end{bmatrix} \begin{bmatrix} K_{\alpha\alpha} & K_{\beta\alpha} & K_{\gamma\alpha} \\ K_{\beta\alpha} & K_{\beta\beta} & K_{\gamma\beta} \\ K_{\gamma\alpha} & K_{\gamma\beta} & K_{\gamma\gamma} \end{bmatrix} \begin{bmatrix} q_\alpha \\ q_\beta \\ q_\gamma \end{bmatrix} - \begin{bmatrix} q_\alpha & q_\beta & q_\gamma \end{bmatrix} \begin{bmatrix} Q_\alpha \\ Q_\beta \\ Q_\gamma \end{bmatrix} \quad (2.5.2)$$

where α are coordinates in the continuum, β are coordinates along one fault interface, and γ are the coordinates along the opposing fault interface. Introducing a new coordinate where

$$q_\gamma = q_\beta + \Delta, \quad (2.5.3)$$

we obtain

$$\pi = \begin{bmatrix} q_\alpha & q_\beta & \Delta \end{bmatrix} \begin{bmatrix} K_{\alpha\alpha} & K_{\beta\alpha} + K_{\gamma\alpha} & K_{\gamma\alpha} \\ K_{\beta\alpha} + K_{\gamma\alpha} & K_{\beta\beta} + K_{\gamma\gamma} & K_{\gamma\beta} + K_{\gamma\gamma} \\ K_{\gamma\alpha} & K_{\gamma\beta} + K_{\gamma\gamma} & K_{\gamma\gamma} \end{bmatrix} \begin{bmatrix} q_\alpha \\ q_\beta \\ \Delta \end{bmatrix} - \begin{bmatrix} q_\alpha & q_\beta & \Delta \end{bmatrix} \begin{bmatrix} Q_\alpha \\ Q_\beta + Q_\gamma \\ Q_\gamma \end{bmatrix} \quad (2.5.4)$$

Δ now represents the dislocation along the internal boundary independent of the coordinates; it can be either a free parameter or prescribed along the interface.

Introducing this coordinate change simplifies the computations and properly simulates the dislocation. Jungels and Frazier (1973) express the fault dislocation in the force or inhomogeneous vector \underline{Q} . This representation complicates the bookkeeping associated with assembling the elements. Each element location and submatrix adjacent to the fault must be retained in addition to any rows and

columns of the K matrix for successive application of the fault displacements. If instead the fault is prescribed in the absolute coordinate frame (i.e. left in q), the problem is completely wrong. Deformations of the crack or fault are then impossible. McCowan, Glover, and Alexander (1974) and Shimazaki (1974) are among those that have committed this error. The coordinate change appears then as the most efficient strategy to incorporate the fault.

2.6 Inversion to the Time Domain

Essential to the use of operational variational methods for transient problems is the final inversion to the time domain. A strategy is needed giving accuracy comparable to solutions in the Laplace domain, but unwarranted accuracy would be inefficient. Thus using Fast Fourier transforms are very inefficient for they require too many solutions and exact evaluation. Schapery (1962) developed, instead, a technique based upon the thermodynamic properties of linear viscoelasticity: apart from steady flow, the time dependence of all coordinates is given by a series of decaying exponentials (Biot, 1958). Schapery went on to prove uniform convergence for a finite sum of decaying exponentials and to demonstrate its power with the Rayleigh-Ritz method. But recognition of its potential usefulness to the finite element method is due to Adey and Brebbia (1973).

To prove this property of time dependence for the coordinates, we must first indicate certain properties of the kernel G_{ijkl} in the Stieltjes convolution or 'hereditary integral' (equation (2.2.1)). Using thermodynamics we can prove the following assertions (Christensen, 1971):

$$\text{I} \quad G_{ijkl}(t) \geq 0 \quad (2.6.1)$$

from the requirement of non-negative work.

$$\text{II} \quad \frac{\partial}{\partial t} G_{ijkl}(t) \leq 0 \quad (2.6.2)$$

from the requirement of non-negative dissipation or increasing entropy.

$$\text{III} \quad \frac{\partial^2}{\partial t^2} G_{ijkl}(t) \geq 0 \quad (2.6.3)$$

if we require a fading memory behavior.

These conditions are fulfilled if we assume a Prony series representation:

$$G_{\alpha}(t) = \sum_{n=1}^N G_{\alpha}^n e^{-t/\tau_{\alpha n}} + G_{\alpha}^{\circ} \quad (2.6.4)$$

Steady flow introduces a differential operator into the kernel. Biot (1958) has proven equation (2.6.4) represents the solution of the normal coordinates for a hereditary material. A concise treatment of this proof may be found in Fung (1965, sec. 13.5).

Once the form of the kernel G_{ijkl} has been established, the Laplace transform gives the operational moduli (Biot, 1958; Schapery, 1962):

$$\bar{G}_{ijkl} = \sum_n \frac{pG_{ijkl}^n}{p+1/\tau_n} + G_{ijkl}^o + pG_{ijkl}^s \quad (2.6.5)$$

where τ_n are the relaxation times and p is the Laplace transform variable. Each matrix is symmetric, real, and positive semi-definite; i.e.

$$G_{ijkl}^o, G_{ijkl}^s, G_{ijkl}^n \geq 0 \quad (2.6.6)$$

but the matrix made up of the sum is positive definite:

$$[\sum_n G_{ijkl}^n + G_{ijkl}^o + G_{ijkl}^s] e_{ij} e_{kl} > 0 \quad (2.6.7)$$

If the operational moduli G_{ijkl} is now substituted into the operational variational principle, one can now prove the following conjecture (Schapery, 1962, 1964):

$$q = \sum_n s^n (1 - e^{-t/\gamma_n}) + s^o + s^s t \quad (2.6.8)$$

where γ_n are the relaxation times for the series. We have assumed the relaxation times are independent of position within any one element and a finite number of degrees of freedom are used for q . These assumptions are completely consistent with the finite element method.

This relationship suggests a very simple procedure to calculate the time-dependent displacements (or stress) from our operational-variational principle. Provided that the undisturbed linear viscoelastic body is subject to prescribed loads and displacements which are step functions of time

applied at time zero, we can denote the stress or displacement response by

$$\psi(t) = \psi^{\circ} + \psi^S t + \Delta\psi(t) \quad (2.6.9)$$

where ψ° and ψ^S are constant with respect to time and $\Delta\psi(t)$ is the transient response:

$$\Delta\psi(t) = \int_0^{\infty} \phi(\tau) e^{-t/\tau} d\tau \quad (2.6.10)$$

$\phi(\tau)$ represents the temporal spectral distribution function of the variable τ . The function may consist of discrete frequencies represented by Dirac delta functions, ie.

$$\phi(\tau) = \sum_{i=1}^n \phi_i \delta(\tau - \tau_i) \quad (2.6.11)$$

One obtains then the series representation as in equation (2.6.4):

$$\Delta\psi(t) = \sum_{i=1}^n \phi_i e^{-t/\tau_i} \quad (2.6.12)$$

Representing the displacements or stress response by equation (2.6.9) for $\psi(t)$ and using $\Delta\psi(t)$ implies that the Laplace transform $\bar{\psi}(p)$ has singularities only on the non-positive real p axis, and that all poles are simple, except at the origin where a double pole is possible (Schapery, 1962, 1964).

The simplicity of the Laplace transform of $\psi(t)$ suggests that a reasonable approximation to the displacement solution is possible using collocation or least-squares (Schapery, 1961, 1962). If the transient response is given by the

Prony series

$$\Delta\psi_D = \sum_{i=1}^n s_i (1 - e^{-t/\gamma_i}) \quad (2.6.13)$$

where γ_i are prescribed relaxation times, the unspecified coefficients s_i are readily calculated by minimizing the total squared error between the actual displacements $\Delta\psi$ and the calculated displacement $\Delta\psi_D$. This total squared error is

$$E^2 = \int_0^{\infty} [\Delta\psi - \Delta\psi_D]^2 dt \quad (2.6.14)$$

with the minimization yielding

$$-1/2 \frac{\partial E^2}{\partial s_i} = 0 = \int_0^{\infty} [\Delta\psi - \Delta\psi_D] e^{-t/\gamma_i} dt \quad i=1, \dots, n \quad (2.6.15)$$

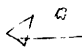
Collocation results in n relations between the Laplace transform of $\Delta\psi$ and $\Delta\psi_D$ evaluated at $1/\gamma_i$:

$$\Delta\bar{\psi}_D(p)_{p=1/\gamma_i} = \Delta\bar{\psi}(p)_{p=1/\gamma_i} \quad i=1, \dots, n \quad (2.6.16)$$

Substituting the Laplace transform for $\Delta\psi_D$ and multiplying by p , we obtain a convenient form for the variational solutions:

$$[p\Delta\bar{\psi}(p)]_{p=1/\gamma_j} = \sum_{i=1}^n \frac{s_i}{1 + \gamma_i p} \quad j=1, \dots, n \quad (2.6.17)$$

Additional p for evaluation allows calculating ψ^o and ψ^s ← ? in the series (2.6.9), or using a least-squares solution

to (2.6.17). $p\Delta\psi(p)$ is just the finite element solution  using the operational-variational principle for linear viscoelasticity. Thus the coefficients S_i when substituted into the series (2.6.13) and (2.6.9) immediately yield the time-dependent solution.

The total squared error involves both the accuracy of fitting the series to the calculated displacements and the numerical error introduced when the transformed displacements are calculated with the finite element method. Consequently, if an approximate inversion has been obtained with n terms and it is desirable to reduce the squared error by using additional terms, it will often be necessary to evaluate the transform $\Delta\bar{\psi}(p)$ and $\Delta\bar{\psi}_D(p)$ with increased accuracy. When the transforms are calculated with enough numerical accuracy, the total squared error (2.6.14) indicates that, if they are evaluated sufficiently close for $0 < p < \infty$, the error of the time-dependent approximation is arbitrarily small.

2.7 Boundary Conditions

Application of the finite element method to a problem normally occurring in a half-space entails artificial boundaries within the media. A slice of the media is taken rather than the half-space. Two approaches to simulate the boundary of a half-space suggest themselves. The first follows from the

flexibility afforded by the elements: we grade the element dimensions for the desired resolution. Near the fault the elements are fine, while along the boundary far from the fault, the elements increase in size. This maximizes the distance between the boundary and fault for a given number of unknowns. But this is nothing new.

An alternate strategy simulates the half-space on the boundary. This is analogous to Boussinesq and Cerruti's problem in elasticity: we desire the relation between displacement and force for the surface of an elastic or viscoelastic half-space. Since the two dimensional analogue of Boussinesq's solution does not tend to zero at infinity (Love, 1944 art. 150), we examine the behavior using an empirical relation. Boussinesq and Cerruti's problems indicate a linear relation between surface displacements u and load P for a half-space (Fung, 1965, sec. 8.8).

$$P = \alpha u \quad (2.7.1)$$

We can postulate a similar relation for the boundary of the region to simulate the infinite continuum. Along the diagonal of the stiffness matrix an additional constant α for the elastic support relates the displacement and reaction. This is equivalent to altering the variational problem for the new boundary condition. A term $1/2\alpha_{ij}u_iu_j$ enters the variational principle along the surface specified by these boundaries.

To estimate the best value for α , we compare an analytic solution for a fault within a half-space to the finite element method. Another comparison uses a second finite element model constructed by reducing the size of the original model. Varying the boundary conditions then allows a best fit for the reduced model to the original. Using this analogy to a half-space, a noticeable improvement occurs for the reduced model.

2.8 Inversion Theory Applied to Finite Elements

General inverse theory encompasses more than determining a particular solution that fits the data; knowing the uniqueness and resolution of the solution often gives more insight into the problem. A particular solution has only limited value if we cannot specify bounds upon it. The data,

in particular their errors, impose constraints on the model's uniqueness. The solution can be varied within these bounds while still satisfying the data. Essential to any inversion theory, then, are the data and their errors, and the assumed model.

The time-dependent deformations of the earth's surface introduce a special set of data and model parameters. The deformations consist of geodetic observations relative to some datum. This datum may be another bench mark or an absolute such as a tidal station. The former is also deforming with the surface, while the latter has uncertain errors. The model parameters, on the other hand, pose the problem. Time-dependent surface deformations may result from a series of fault movements, relaxation of the asthenosphere, or both. The gradual spreading of the oceanic lithosphere and accumulation of strain impose an additional freedom. Simplifying the problem and conditions yields a more tractable solution; we can then isolate individual contributions and test their significance.

In this thesis I confine the problem to stress relaxation within the asthenosphere. After the earthquake, the fault remains locked within the lithosphere, only segments within the asthenosphere relax with time. The effects of strain accumulation are removed from the data prior to any inversion. Given these assumptions, the free parameters are the fault

displacements during the earthquake, the viscosity of the asthenosphere, and the problem's geometry. The latter is constrained for any particular inversion. Only the first two, initial fault displacement and viscosity, are actually inverted with the data. Section 5.2 discusses these assumptions in greater detail.

In our case the finite element method generates the model. Given a set of m observations O_j where $j=1, \dots, m$ and a set of n parameters P_i where $i=1, \dots, n$, the finite element method provides the relationship between the two within a specific geometry. Any model must provide a functional (computational) relationship between the model parameters and the calculated value C_i corresponding to the observations:

$$C_j = F_i(P_i) \quad (2.8.1)$$

The inversion theory minimizes a norm expressing the distance between the observations and calculated values until the optimum parameters are found. Now the finite element method introduces simplifying assumptions.

First, the formulation of the variational principle and its minimization gives a linear functional. Although it may be linearized around an initial model for nonlinear problems, the functional is strictly linear for displacement with our problem, time-dependent linear viscoelasticity. The quadratic variational principle, (2.3.1), reduces to a set of linear

matrix equations in the Laplace domain:

$$\tilde{K} \tilde{q} = \tilde{Q} \quad (2.8.2)$$

relating nodal displacements \tilde{q} to the nodal forces \tilde{Q} . Given a set of boundary conditions, the surface displacements are a linear function of the fault displacements in the Laplace domain. This relation is preserved during the inversion to the time domain. Consequently, imposing a unit displacement for each fault parameter gives the variational parameters for the surface displacements after inversion to the time domain. Since the viscosity scales from dimensional and non-dimensional time, the variational parameters for the gross viscosity of the problem follow from the scaling. This, however, is a non-linear functional of time; thus, an initial model is necessary for viscosity. This procedure guarantees a linearized problem for the functional relationship.

Various approaches are possible for the inversion theory (Backus and Gilbert, 1967; Jordan and Franklin, 1971; Barcilon, 1974); however, here the problem will be treated as a generalized matrix inverse weighted according to the errors and parameters. The other methods which depend on variational parameters are analogous. Wiggins (1972) gives an adequate summary of the generalized inverse, its interpretation, and its relation to other inverses. Except for minor variations, we will follow his notation.

The finite element method has reduced the functional relating fault displacements \underline{q} and calculated surface displacements \underline{C} to a linear problem

$$\underline{C} = \underline{M}\underline{q} \quad (2.8.3)$$

where \underline{M} is the coupling matrix derived from the time inversion for each surface and fault displacement. We evaluate the matrix at specific times and an initial viscosity corresponding to the geodetic time intervals. A direct relationship results for the fault displacements rather than a matrix of variational parameters since the problem is linear. Inclusion of viscosity introduces one nonlinear parameter requiring a variational parameter evaluated around an initial model.

Using Wiggins's notation, we let

$$\Delta \underline{c}' = \begin{bmatrix} 0_1 \\ 0_2 \\ \vdots \\ 0_m \end{bmatrix} \quad \Delta \underline{p}' = \begin{bmatrix} q_1 \\ \vdots \\ q_{n-1} \\ \Delta \eta \end{bmatrix} \quad \text{var}\{\Delta \underline{p}'\} = \begin{bmatrix} \text{var}\{q_1\} \\ \vdots \\ \text{var}\{q_{n-1}\} \\ \text{var}\{\Delta \eta\} \end{bmatrix}$$

$$\underline{A}' = \begin{bmatrix} M_{11} & M_{12} & \cdot & \cdot & \cdot & M_{1 \ n-1} & \partial C_1 / \partial \eta \\ \cdot & & & & & \cdot & \cdot \\ \cdot & & & & & \cdot & \cdot \\ \cdot & & & & & \cdot & \cdot \\ M_{m1} & \cdot & \cdot & \cdot & \cdot & M_{m \ n-1} & \partial C_m / \partial \eta \end{bmatrix} \quad (2.8.4)$$

where $\text{var}\{\Delta \underline{p}'\}$ denotes the variance of the parameter $\Delta \underline{p}'$, and $\partial C / \partial \eta$ are evaluated using an initial model for both

fault displacements q° and viscosity η° . The inversion now has the form

$$O_j = \sum_{i=1}^{n-1} M_{ij} q_i + (\partial C_j / \partial \eta) \Delta \eta \quad (2.8.5)$$

or in matrix form

$$\tilde{A}' \tilde{\Delta p}' = \tilde{\Delta c} \quad (2.8.6)$$

In general there are only k independent equations where $k \ll n, m$. Thus \tilde{A}' is singular giving an unstable inverse. Additional constraints contained in the generalized inverse, however, allow a well-posed problem: Both $|\epsilon'|^2 = |\tilde{A}' \tilde{\Delta p}' - \tilde{\Delta c}'|^2$ and $|\tilde{\Delta p}'|^2$ are minimized simultaneously. The inverse selects the smallest change in $\tilde{\Delta p}'$ that satisfies the simultaneous equations (e.g. Lanczos, 1961, or Wiggins, 1972).

Weighting the parameters and observations are first necessary to remove the dimensionality of the vectors $\tilde{\Delta p}'$ and $\tilde{\Delta c}'$ (Searle, 1971; Wiggins, 1972). Defining a diagonal matrix W_{ii} proportional to the dimensions of the parameters, we now minimize $\tilde{\Delta p}'^T \tilde{W}^{-2} \tilde{\Delta p}'$ instead of $|\tilde{\Delta p}'|^2$. The lengths of the rows for $\tilde{A}' \tilde{W}$ are now invariant to the parameter interval. A covariance matrix \tilde{S} proportional to the dimensions of the observations or the errors

$$S_{ij}^2 = \text{Cov}\{O_i, O_j\} \quad (2.8.7)$$

weights the observations. The minimization becomes

$$\varepsilon'^T S^{-2} \varepsilon' \quad (2.8.8)$$

to bias the corrections towards the more accurate observations. This gives a maximum likelihood estimate. The new parameters are now introduced into the equation:

$$\begin{aligned} \tilde{A} &= \tilde{S}^{-1} \tilde{A}' \tilde{W} \\ \tilde{\Delta p} &= \tilde{W}^{-1} \tilde{\Delta p}' \\ \tilde{\Delta c} &= \tilde{S}^{-1} \tilde{\Delta c}' \end{aligned} \quad (2.8.9)$$

where we minimize

$$|\tilde{\varepsilon}|^2 = |\tilde{A} \tilde{\Delta p} - \tilde{\Delta c}|^2 \quad (2.8.10)$$

and

$$|\tilde{\Delta p}|^2 \quad (2.8.11)$$

The finite element method already forms a weighted matrix for the displacement parameters; we need only the covariance and viscosity weighting.

The generalized inverse gives a solution satisfying these constraints. The matrix \tilde{A} can be expressed as

$$\tilde{A} = \begin{array}{ccc} \tilde{U} & \tilde{\Lambda} & \tilde{V}^T \\ \text{mxn} & \text{mxk} & \text{kxk} \quad \text{kxn} \end{array} \quad (2.8.12)$$

where \tilde{A} contains k independent equations, \tilde{U} and \tilde{V} are k eigenvectors for the m columns (observations) and n rows (parameters) respectively with eigenvalues given by the

diagonal matrix Λ (Lancsoz, 1961; Wiggins, 1972). The generalized inverse picks p nonsingular eigenvalues in descending value to express A :

$$\underset{\sim}{A}_p = \underset{\sim}{U}_p \underset{\sim}{\Lambda}_{p \sim p} \underset{\sim}{V}_p^T \quad (2.8.13)$$

The inverse immediately follows:

$$\underset{\sim}{A}_p^{-1} = \underset{\sim}{V}_p \underset{\sim}{\Lambda}_{p \sim p}^{-1} \underset{\sim}{U}_p^T \quad (2.8.14)$$

where the solution to

$$\underset{\sim}{A} \underset{\sim}{\Delta p} = \underset{\sim}{\Delta c} \quad (2.8.15)$$

now becomes

$$\underset{\sim}{\Delta p}_g = \underset{\sim}{V}_p \underset{\sim}{\Lambda}_{p \sim p}^{-1} \underset{\sim}{U}_p^T \underset{\sim}{\Delta c} \quad (2.8.16)$$

Substituting $\underset{\sim}{\Delta p}_g$ into the norm for the error, we have

$$\begin{aligned} \underset{\sim}{\varepsilon} &= \underset{\sim}{\Delta c} - \underset{\sim}{A} \underset{\sim}{\Delta p}_g = \underset{\sim}{\Delta c} - \underset{\sim}{U}_p \underset{\sim}{\Lambda}_{p \sim p} \underset{\sim}{V}_p^T \underset{\sim}{V}_p \underset{\sim}{\Lambda}_{p \sim p}^{-1} \underset{\sim}{U}_p^T \underset{\sim}{\Delta c} \\ &= \underset{\sim}{\Delta c} - \underset{\sim}{U}_p \underset{\sim}{U}_p^T \underset{\sim}{\Delta c} \end{aligned} \quad (2.8.17)$$

using the orthogonality of the eigenvectors, $\underset{\sim}{V}_p^T \underset{\sim}{V}_p = \underset{\sim}{I}$. The components of the error $\underset{\sim}{\varepsilon}$ lie outside the solution space p , since

$$\begin{aligned} (\underset{\sim}{A} \underset{\sim}{\Delta p})^T \cdot \underset{\sim}{\varepsilon} &= \underset{\sim}{\Delta p}_g^T \underset{\sim}{V}_p \underset{\sim}{\Lambda}_{p \sim p} \underset{\sim}{U}_p^T (\underset{\sim}{\Delta c} - \underset{\sim}{U}_p \underset{\sim}{U}_p^T \underset{\sim}{\Delta c}) \\ &= \underset{\sim}{\Delta p}_g^T \underset{\sim}{V}_p \underset{\sim}{\Lambda}_{p \sim p} (\underset{\sim}{U}_p^T \underset{\sim}{\Delta c} - \underset{\sim}{U}_p^T \underset{\sim}{U}_p \underset{\sim}{U}_p^T \underset{\sim}{\Delta c}) \\ &= \underset{\sim}{\Delta p}_g^T \underset{\sim}{V}_p \underset{\sim}{\Lambda}_{p \sim p} (\underset{\sim}{U}_p^T \underset{\sim}{\Delta c} - \underset{\sim}{U}_p^T \underset{\sim}{\Delta c}) = 0 \end{aligned} \quad (2.8.18)$$

The solution represents a minimum in the p space.

The addition of the unconstrained eigenvectors $V_{\tilde{i}}$ in the singular space to the Δ_{p_g} solution gives the general solution

$$\Delta_{\tilde{p}} = \Delta_{p_g} + \sum_{i=p+1}^n a_i V_{\tilde{i}} \quad (2.8.19)$$

Using orthogonality, we obtain

$$|\Delta_{\tilde{p}}|^2 = |\Delta_{p_g}|^2 + \sum a_i^2 \quad (2.8.20)$$

which implies

$$|\Delta_{\tilde{p}}|^2 \geq |\Delta_{p_g}|^2 \quad (2.8.21)$$

Thus the generalized inverse gives the minimum solution in the domain of p eigenvectors.

The variance $\sigma_{p_i}^2$ for the new parameters space using p eigenvectors becomes

$$\sigma_{p_i}^2 = \sum_{j=1}^p V_{ij}^2 / \lambda_j^2 \quad (2.8.22)$$

where V_{ij} are the elements of the eigenvector matrix \tilde{V} .

The n parameters are not independently resolvable since there are only p independent vectors. Associated with these errors, then, is a resolution matrix \tilde{R} characterizing the parameter's closeness to a delta function:

$$\tilde{R} = \tilde{V}\tilde{V}^T \quad (2.8.23)$$

The j th column of the $n \times n$ matrix is the least-squares solution for maximizing the j th parameter. An analogous matrix determines the information resolution contained in the data space (Wiggins, 1972).

The generalized matrix inverse allows both direct inversion of the fault displacements and iterative refinement for the viscosity. Other formulations such as Backus and Gilbert's (1967) yield similar results. It is essential to remember, however, that the inversion minimizes both the perturbation $|p|$ from the initial model and the error $|\epsilon|$ simultaneously. Thus if we start from an initial model of zero, the inversion determines the closest model. In this sense the initial model is important even for a completely linear problem. This effect is also implicitly contained in Alewine and Jungels' (1974) model for the Alaskan earthquake, although they do not divulge whether their initial model is zero or if iterations are used from the initial model. In Chapter 5 the geodetic and tilt data for the 1946 Nankaido earthquake provides the format for the inversion of the fault displacements in the context of a viscoelastic model. Here the inversion applied to the real earth will be investigated given the initial model and its assumptions.

3. FIRST ORDER ANALYSIS OF MANTLE INTERACTIONS

3.1 Introduction

To gain insight into the importance of the mantle on strain release, simple analytic models are very useful. These have the advantages of simplicity and flexibility, while numerical models involve greater expense and extensive development. It is appropriate then to review various models that may clarify our intuition and understanding of processes associated with strain accumulation and release. In this chapter we consider analytic solutions for three separate problems involving an elastic layer and a viscoelastic half-space. Numerical solutions to such problems will be given in Chapter 4.

The earthquake may first be approached as a boundary condition on a semi-infinite plate or beam overlying a viscoelastic foundation. The beam represents the lithosphere and the foundation corresponds to the asthenosphere. The relaxation of the foundation to a load or displacement boundary condition applied to the free end of the beam suggests possible modes of deformation after an earthquake. These relaxation modes are analogous to those from post-glacial rebound. A second method proposed by Nur and Mavko (1974) uses a dislocation in an elastic layer overlying a viscoelastic half-space. An accurate solution, however, is still unavailable for a thrust fault. Finally,

stress propagation or diffusion in the lithosphere is modelled using an elastic beam overlying a viscous medium.

All these problems assume linear viscoelasticity for the media. It contains both the essential behavior of relaxation and reasonable analytic techniques. A more complex media such as power-law creep would retain the same characteristic behavior, but would introduce complex mathematics. Considering the other unknowns contained in the problem, this additional complexity is not justified until we understand the basic phenomena.

3.2 Elastic Plate on a Viscoelastic Half-Space

Surface deformations of the earth before and after an earthquake are analogous to the glacial loading problem. The accumulating strain from the descending oceanic lithosphere represents the loading; the earthquake and post-earthquake adjustments are the rebound phase. A simple model can be adopted to represent the accumulation and release of strain along the fault interface: a semi-infinite, thin, elastic beam or plate overlying a viscoelastic foundation that simulates the mantle. Along the edge of the beam a displacement or stress boundary condition with time replaces the fault. This model is simple and illustrates important phenomena.

Consider first the elements of the model as given in Figure 3.1. If we assume a Winkler foundation which

Figure 3.1

Configuration for a semi-infinite, thin, elastic beam with flexure rigidity D overlying a viscoelastic Winkler foundation with modulus k . Constant axial load N and saw-tooth end load P or displacement y_0 are boundary conditions. The restoring force for a Winkler foundation is proportional to the displacement y ; thus, it corresponds to a buoyant fluid.

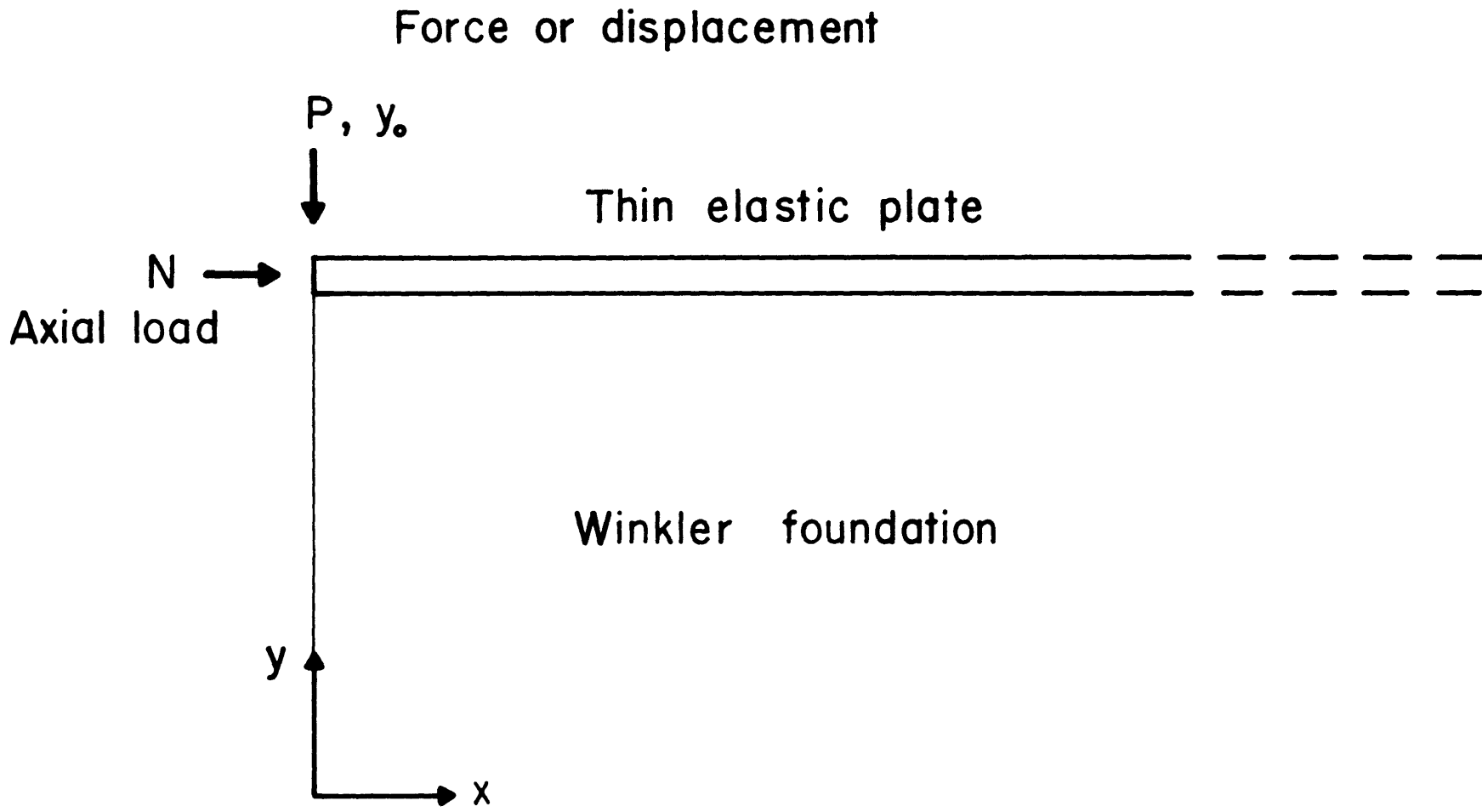


Fig. 3.1

implies a vertical restoring force proportional to the displacement, one obtains a fourth-order differential equation (Hetenyi, 1946):

$$D \frac{d^4 y}{dx^4} - N \frac{d^2 y}{dx^2} + ky = 0 \quad (3.2.1)$$

$$D = Eh^3/12(1 - \nu^2)$$

where N is the axial load on the beam (positive under tension), and k denotes the foundation modulus. The flexure rigidity D depends on the elastic moduli, Young's modulus E and Poisson's ratio ν , and the thickness of the beam h . Free boundary conditions at $x = 0$ are taken as:

$$D \frac{d^2 y}{dx^2} = 0 \quad , \text{ moment vanishes} \quad (3.2.2)$$

$$D \frac{d^3 y}{dx^3} + N \frac{dy}{dx} = 0 \quad , \text{ vertical shear stress vanishes.} \quad (3.2.3)$$

At infinity the solution must decay. For a concentrated normal end force P , these yield the displacement solution:

$$Y = \frac{P}{\beta k} \frac{2\lambda^2}{3\alpha^2 - \beta^2} e^{-\alpha x} [2\alpha\beta \cos\beta x + (\alpha^2 - \beta^2) \sin\beta x] \quad (3.2.4)$$

and the shear stress

$$Q_v = \frac{-P}{\beta} \frac{e^{-\alpha x}}{3\alpha^2 - \beta^2} [(3\alpha^2 - \beta^2)\beta \cos\beta x - (3\beta^2 - \alpha^2)\alpha \sin\beta x] \quad (3.2.5)$$

where

$$\begin{aligned}
\lambda &= (k/4D)^{\frac{1}{4}} \\
\alpha &= (\lambda^2 + N/4D)^{\frac{1}{2}} \\
\beta &= (\lambda^2 - N/4D)^{\frac{1}{2}}
\end{aligned} \tag{3.2.6}$$

If we prescribe a displacement y_0 at $x = 0$, the results are

$$y = y_0 e^{-\alpha x} \left[\cos \beta x + \frac{(\alpha^2 - \beta^2)}{2\alpha\beta} \sin \beta x \right] \tag{3.2.7}$$

and

$$Q_v = \frac{-y_0 k e^{-\alpha x}}{4\lambda^2 \alpha \beta} \left[(3\alpha^2 - \beta^2) \beta \cos \beta x - (3\beta^2 - \alpha^2) \alpha \sin \beta x \right] \tag{3.2.8}$$

These can be arranged into a nondimensional format for plotting. For a concentrated normal end force P , one now has

$$y/y_0 = e^{-a\zeta} \left[\cos \zeta + \frac{a^2 - 1}{2a} \sin \zeta \right] \tag{3.2.9}$$

$$\frac{Q_v}{P} = e^{-a\zeta} \left[\cos \zeta + \frac{(a^2 - 3)a}{3a^2 - 1} \sin \zeta \right] \tag{3.2.10}$$

where $a = \alpha/\beta$, $\zeta = \beta x$, and initial displacement $y_0 = \frac{4P\lambda^2 a}{k\beta(3a^2 - 1)}$.

When expressing the viscoelastic solutions, k is taken as the final buoyant support which will be discussed later.

There are significant assumptions involved in these solutions. The foundation transmits only normal forces to the plate or beam; shear tractions between the plate and underlying foundation are ignored in the model. This is not as severe as one might imagine. The overlying stiffness of the plate or beam acts to diffuse the stress along the

foundation. For example, the exact solution for a harmonic loading $\sin(mx)$ on a thin elastic plate overlying an elastic continuum is (Hoskin and Lee, 1959)

$$y(x) = \frac{1}{Dm^4 + \frac{\mu m}{1-\nu}} \sin(mx) \quad (3.2.11)$$

while the solution for a fluid foundation which transmits no shear stresses reduces to

$$y(x) = \frac{1}{Dm^4 + k} \sin(mx) \quad (3.2.12)$$

when μ is the shear modulus (Hoskin and Lee, 1959). If a spacial wavenumber m is examined, say $m \sim \beta$, the solutions (3.2.11) and (3.2.12) suggest that k can be approximated using

$$k \sim \frac{\mu \beta}{1-\nu} \quad (3.2.13)$$

if the two solutions (3.2.11) and (3.2.12) are the same. The wavenumber significantly effects the foundation modulus when the two terms Dm^4 and $\frac{\mu m}{1-\nu}$ are similar; thus, our solution can only provide a guide to the behavior.

Applying the correspondence principle to the elastic solutions (3.2.4) and (3.2.7) now gives the viscoelastic solutions (Christensen, 1971). The foundation modulus k becomes the transformed viscoelastic modulus. Since the mantle has an initial elastic behavior while approaching a dense fluid under gravity for large times, a standard solid is adopted as the response of k : an initial elastic

behavior, then decaying until the restoring force corresponds to a dense fluid in gravity. The Stieltjes convolution for $k * y$ becomes:

$$k * y = \int_0^t [k_e e^{-t/\tau} + k_f(1 - e^{-t/\tau})] \frac{dy}{d\tau} d\tau \quad (3.2.14)$$

where k_e is the elastic modulus for the foundation, τ corresponds to the relaxation time, and k_f is the modulus representing the buoyant restoring force. A modified Fast Fourier transform algorithm then inverts the operational form of equations (3.2.4) and (3.2.7) to the time domain (Dubner and Abate, 1968).

Figure 3.2 shows two models that are identical except for the boundary conditions. In one case a saw-tooth displacement profile is specified; for the second we prescribe a saw-tooth stress profile. The profile starts with a linear accumulation phase, jumps back to the initial state, then starts accumulating again, and repeats the cycle. The repetition rate is 33.3 when nondimensionalized by the relaxation time of the foundation. We reference the vertical deformations to the displacement either just prior to the step discontinuity or just after the jump. Again the relaxation time nondimensionalizes all time intervals.

The boundary conditions imposed upon the beam, whether stress or displacement, significantly effect the resulting deformations. If the relaxation time for the foundation or asthenosphere is much less than the accumulation time,

Figure 3.2

Dimensionless vertical displacement profile versus dimensionless distance βx from the fault for two boundary conditions, stress or displacement. The 'fault' or boundary condition is applied at $\beta x = 0$. Displacements are relative to the instant just prior to the step discontinuity and normalized by the step displacement. Time is non-dimensionalized by the relaxation time for the foundation. In these units the period equals 33.3. Solid and dashed curves represent $t/\tau = 0$ and $t/\tau = 6$, respectively.

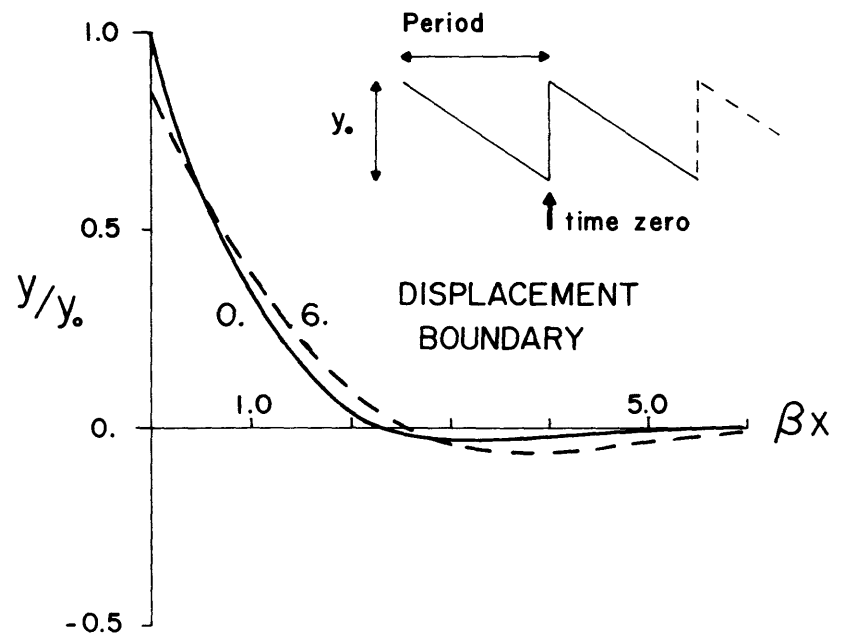
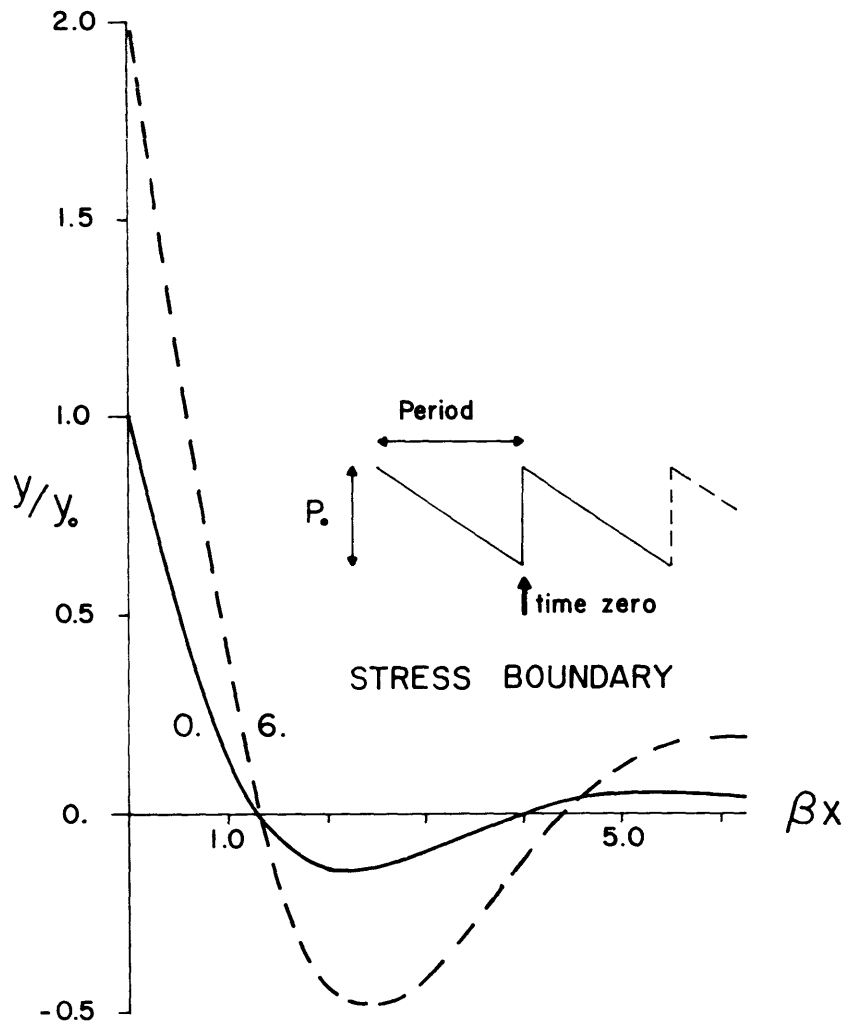


Fig. 3.2

a stress condition applies a relatively constant stress state to the foundation allowing deformations that increase with time. Thus the profiles have similar shape to one another. The displacement boundary condition, on the other hand, strains the foundation and then allows its relaxation. As the restoring force relaxes on the plate, the wavelength for the deformation increases thereby establishing a new equilibrium. The boundary conditions at the "fault" define then the stress state imposed on the foundation and, thus, determine the deformation behavior. We can now compare these deformations to geodetic observations after a major earthquake.

Figure 3.3 illustrates a model fitting the vertical surface deformations before and after the Nankaido earthquake of 1946. The model assumes that axial loading is insignificant, i.e., $\alpha/\beta \approx 1$, or N is less than a kilobar. The fluid buoyancy k_f corresponds to a density contrast of 3.4 gm/cm^3 between the surface and the mantle. The dominant wavelength β defines k_e in equation (3.2.14). To simulate the accumulation of strain and its release by the earthquake, a saw-tooth displacement profile is applied at the free boundary. The strain accumulation lasts 100 years, the earthquake occurs, and then the process repeats itself. This period approximates the periodicity of earthquakes in the Nankaido region. A best fit to the Nankaido data (Fitch and Scholz, 1971) then constrains the

Figure 3.3

Vertical deformations using a thin elastic plate overlying a viscoelastic foundation fitted to the leveling data for the 1946 Nankaido earthquake. This geodetic data is taken from Fitch and Scholz (1971), profile A. For the model parameters, the flexure rigidity D equals 2.78×10^{31} , giving a lithospheric thickness h of 65 km if Young's modulus E is taken as 10^{12} dyne/cm². The axial load N compressing the beam is 1.4×10^{10} bar-cm², or for a 65 km lithosphere 2.1 k bar. The elastic foundation modulus k_e is 3.12×10^5 dyne/cm² while the fluid foundation modulus k_f becomes 3.3×10^3 dyne/cm² for a density contrast of 3.4 gm/cm³. The relaxation time giving the best fit is 3 years, suggesting a viscosity of 7×10^{19} poise. The vertical slip y_0 becomes 3.1 m. The time intervals represent the two dates for the geodetic measurements where the changes in elevation between these dates are plotted as vertical bars. All deformations are tied to tidal stations as an absolute datum. The top figure (a) corresponds to the downwarping of the continental lithosphere on Shikoku island between 1895 and 1929 prior to the earthquake. This is the accumulation phase. Following the earthquake in 1946, the elastic-rebound phase recovers most of the accumulation as (b) illustrates between 1929 and 1947. Relaxation in the asthenosphere, however, gives post-seismic adjustments in (c) and (d).

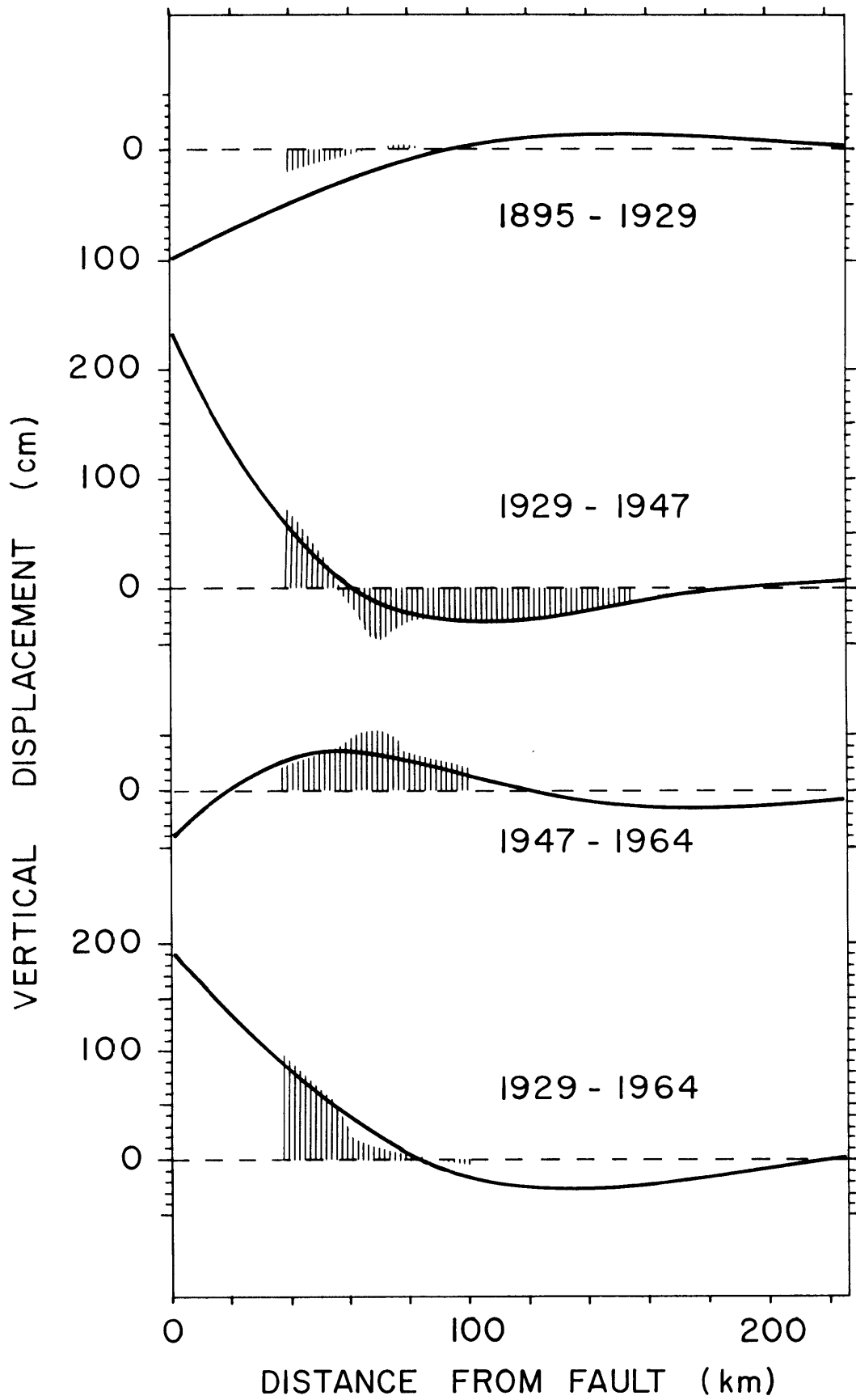


Fig. 3.3

lithosphere to 65 km thickness. These parameters yield a model surprisingly similar to the Nankaido deformations.

Both the model and data represent the difference between vertical deformations for two specific times. For the geodetic data, tidal stations tie the vertical displacements to an absolute datum. This allows comparison of the model to the data. Chapter 5 discusses the assumptions and implications involved in this comparison.

The data for the Nankaido earthquake contains three phases of deformation (Scholz, 1972), with corresponding behavior in the model. Prior to the 1946 earthquake, the descending oceanic lithosphere warps and strains the continental lithosphere as in Figure 3.3a. The strain energy within the asthenosphere relaxes during the slow warping, since the relaxation time for the asthenosphere is short compared to the repetition rate of large earthquakes. The 1946 earthquake signals the second phase of acute deformation. Here the large and destructive deformations commonly associated with an earthquake occur along the fault, while less obvious subsidence and uplift are found far from the fault. Reid (1910) recognized these two phases and related them in his elastic-rebound theory. The slow downwarping represents the accumulation of strain energy; the earthquake signals the fault rupture and rebound of the elastic media. But for a medium allowing stress relaxation, another phase of adjustment is possible after the earthquake.

During this third phase the asthenosphere relaxes after the strain step introduced by the earthquake. Noting that the mantle has little accumulated strain energy from the first phase, the earthquake acts as a step function in strain. The subsequent relaxation in the asthenosphere after the earthquake results in the surface deformations of Figure 3.3d. The wavelength of deformation increases and the hinge point for zero deformation moves away from the fault. This is analogous to glacial rebound (Haskell, 1935; McConnell, 1965). Yet this rebound differs in one significant aspect: the relaxation time and spacial harmonics are much shorter than any glacial rebound observations. In addition, no observations of glacial rebound are available at island arcs. If the effect of the boundary conditions and the finite thickness to the lithosphere can be resolved in our models, a new and independent viscosity for the asthenosphere is possible.

The stress relaxation within the asthenosphere strongly effects the state of stress along the free boundary or fault. Figure 3.4 shows a plot of stress versus time for the previous model, again related to the Nankaido earthquake of 1946. While we have no direct data for the absolute stress level, the aftershock frequency may be a reflection of the stress state (i.e., Rybicki, 1973). Thus the energy released by the aftershocks is also plotted on the diagram.

During the first year the energy released by the

Figure 3.4

Plot of stress on a linear scale along the fault for the model in Figure 3.2 overlain on the energy released by the aftershocks and a swarm on Shikoku. The fault length is taken as 100 km. Using the Catalogue of major earthquakes which occurred in or near Japan (1958) and the energy-magnitude relation according to Gutenberg and Richter, the rate of energy release for the swarm and all aftershocks is computed for the intervals shown by the open or closed circles. Notice that the exponential decay time for the aftershocks immediately preceding the earthquake is much shorter than the stress decay. The large peak in the aftershocks occurring more than a year following the main shock originates from a magnitude 6.8 and 7.0 aftershock on the Kii peninsula.

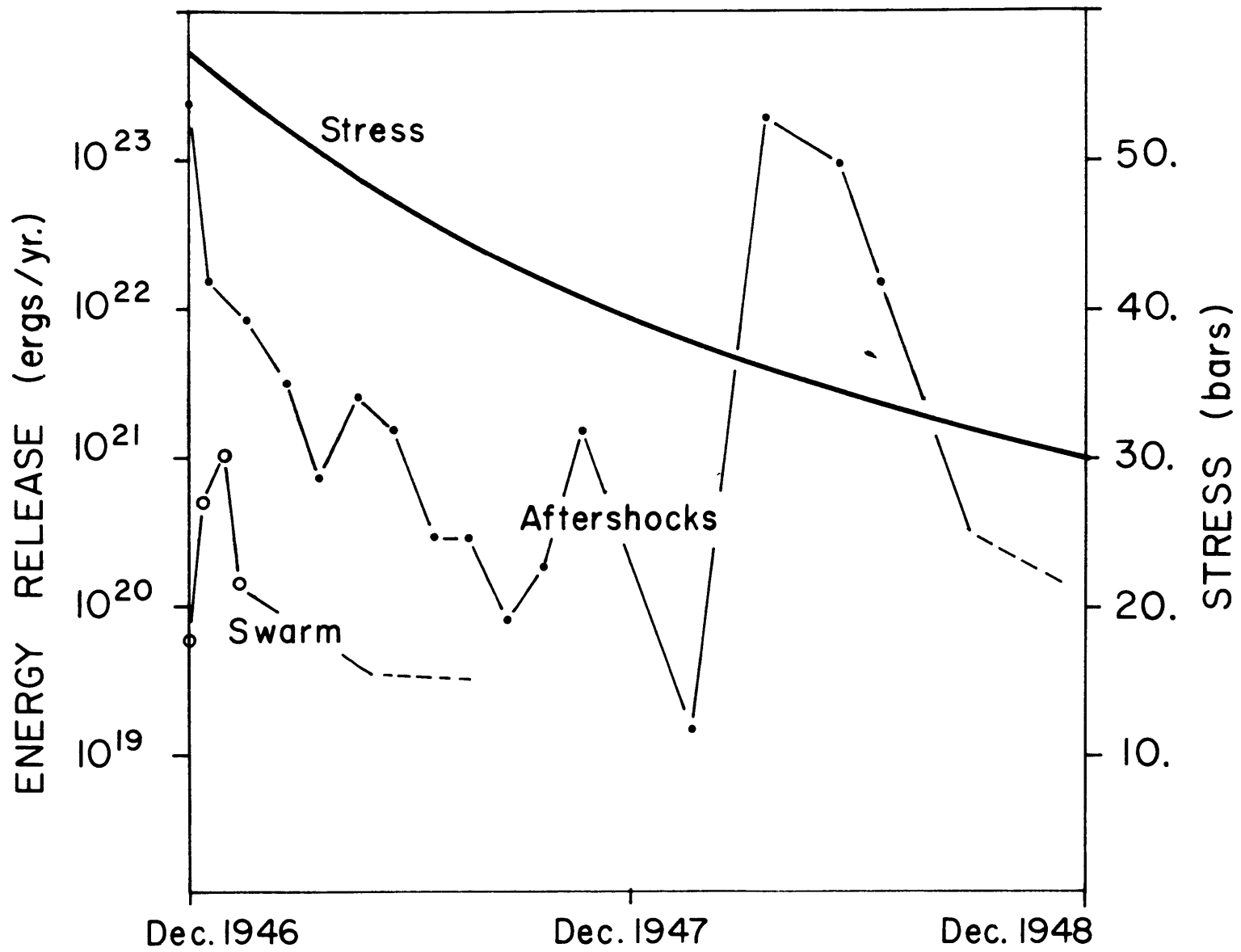


Fig. 3.4

aftershocks rapidly decreases giving a relaxation time for exponential decay of approximately one month. The stress along the fault for our model returns exponentially to the initial state, but with a relaxation time of approximately three years. This suggests independent processes unless the aftershock frequency is exceptionally sensitive to the stress level: a small change in the stress level during the first month produces a large change in aftershocks. In that case we would be appealing to a process similar to Benioff's (1951) or Lieber and Braslau's (1965) viscoelastic rebound mechanism for aftershocks.

As the stress returns to its initial state, however, the aftershock frequency would be expected to increase, not decrease as observed. A more plausible argument suggests that the aftershocks are a response to stress concentration and inhomogeneities near the fault tip (i.e., Mogi, 1963; Rybicki, 1973). These local concentrations are far larger than the stress variations envisioned by viscoelastic rebound in the asthenosphere. These local concentrations could produce the short decay time. Yet this does not rule out long term effects. Increasing stress along the fault could trigger the abnormally large aftershocks (M 7.0) occurring a year after the main earthquake. In addition, a swarm of earthquakes on Shikoku may be related to the main shock, but delayed by approximately three weeks. These large aftershocks and the swarm contaminate

the geodetic data. In Chapter 5 we further discuss the limitations imposed by the data.

With this model the three phases observed in the geodetic data translate into accumulation within the lithospheric plate, sudden rebound and straining of the asthenosphere, and post-earthquake relaxation within the asthenosphere. An alternate mechanism for the third phase, fault creep, cannot be excluded with the analytic simulations. The model can only broadly outline the probable phases.

3.3 Note on the Wavelength of Relaxation

The analog to the glacial loading problem may be further pursued using the analysis of McConnell (1965) for surface loading. Prior to his solution, a uniform Newtonian viscosity had been assumed for the earth models (Haskell, 1935), rather than an elastic lithosphere overlying a viscous asthenosphere. McConnell pointedly argued that the elastic lithosphere significantly alters the characteristic deformations for short wavelengths, just as we found for the thin plate or beam on a viscous foundation. We first must review his results.

The simplest model for glacial rebound is a homogeneous viscous half-space. Here the relaxation time τ for wavenumber u reduces to

$$\tau = 2\eta u / \rho g \quad (3.3.1)$$

where

$$u = 2\pi/\lambda \quad (3.3.2)$$

when λ is the wavelength of the deformation and η is the viscosity (Haskell, 1935). Introducing a characteristic length h , the time τ is nondimensionalized

$$\tilde{\tau} = \frac{\rho g h \tau}{2\eta} \quad (3.3.3)$$

and the dimensionless wavenumber becomes uh . Our relation for the relaxation time reduces to

$$\tilde{\tau} = uh \quad (3.3.4)$$

The relaxation time is then inversely proportional to the wavelength; thus long wavelength components decay faster than shorter ones.

Introducing an elastic layer on the surface diffuses the stress and allows rapid relaxation. In his analysis, McConnell (1965) solves the problem of an elastic layer overlying a viscous half-space. Figure 3.5 gives a plot of the solution in non-dimensional form where $\tilde{\mu}$ is the dimensionless shear modulus if

$$\tilde{\mu} = \mu/\rho g h \quad (3.3.5)$$

Upon inspection, one notices immediately that for short wavelengths the relaxation time $\tilde{\tau}$ asymptotically approaches $1/\tilde{\mu}$. Moving along constant $\tilde{\mu}$, the relaxation time first increases, then conforms to a viscous half-space for long wavelength deformations allowing the relaxation time to again decrease. The elastic layer controls, then, the

Figure 3.5

Dimensionless relaxation time $\tilde{\tau}$ as a function of dimensionless wave number uh for a single elastic layer of thickness h with Poisson's ratio 0.25 overlying a viscous half-space. Short wave-length deformations occupy the upper portion of the diagram where the transition is denoted by the dotted line. Here the relaxation time τ approaches $2\eta/\mu$ when $\lambda < 2h$. The values near the top, 100, 50, 20, 10, and 5, correspond to values of $\tilde{\mu}$. (Figure reproduced from McConnell, 1965).

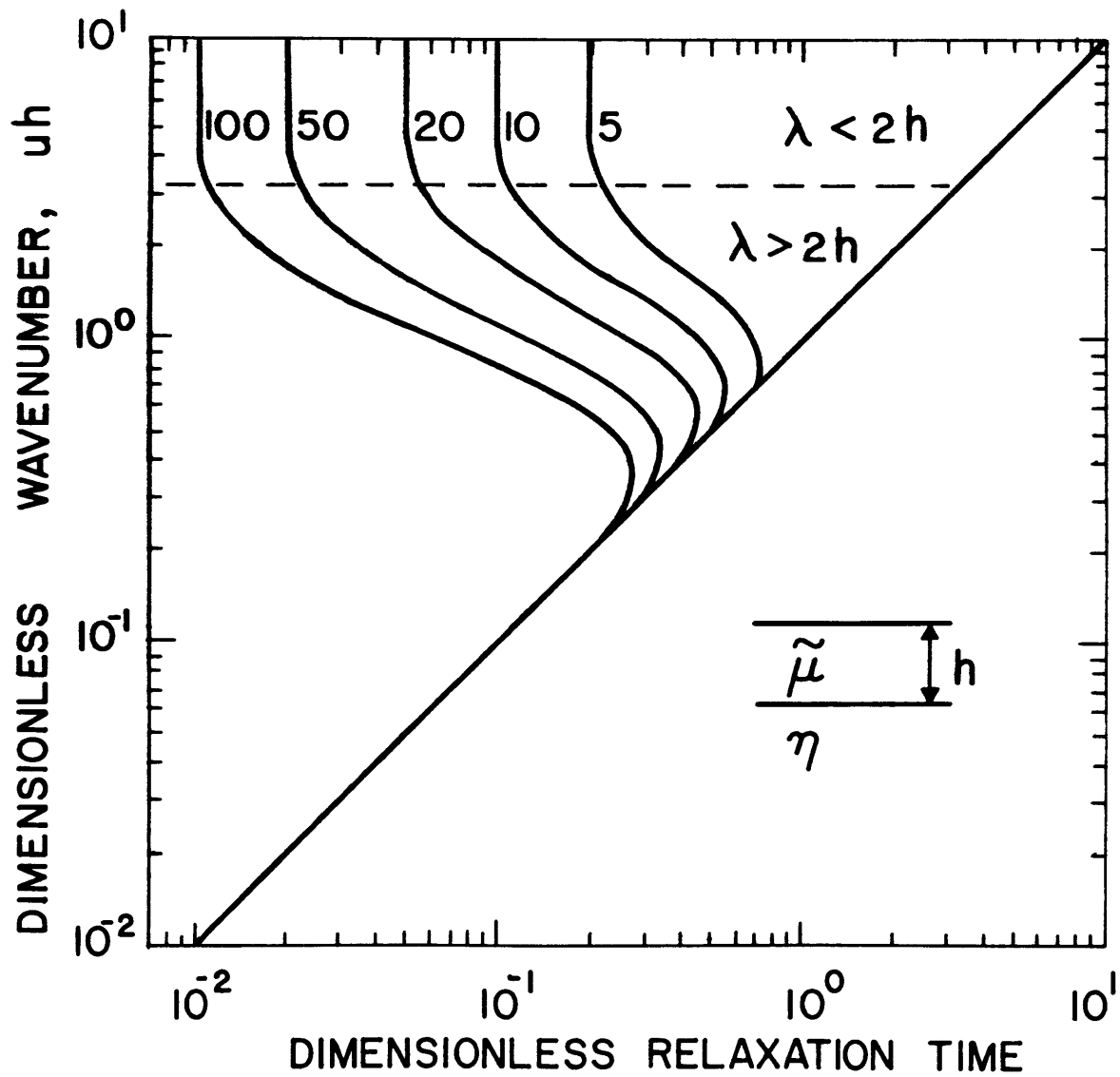


Fig. 3.5

short wavelength deformation.

A fault introduces short wavelength deformations; thus, one would expect rapid relaxation for short wavelengths and slower relaxation for greater wavelengths. The transition occurs near $uh = \pi$ or dimensionalized, $\lambda = 2h$. We expect then the following behavior for stress relaxation following a large earthquake:

1. The dominant wavelength for the post-seismic deformation conforms to $\lambda \lesssim 2h$ for the initial relaxation.
2. The wavelength increases during later post-seismic deformations.
3. Linear dependence roughly holds between the dominant relaxation wavelength and the lithospheric thickness.

In detailed models these relationships should be approached when we approximate initial conditions that are similar to a normal surface load.

3.4 Dislocation Within a Layered Medium

An alternate method which accurately models the fault dislocation uses the elastic solution for a screw or edge dislocation in an elastic layer over a half-space. Nur and Mavko (1974) have used these with the correspondence principle to calculate the rebound for a thrust or strike-slip fault. But again the solutions involve major

approximations for a dip-slip fault.

The viscoelastic solution depends on an elastic solution for a strike-slip or dip-slip fault within a layered media. Rybicki (1971) solved the problem of a strike-slip fault in a layered media using images, an extension of Maruyama's (1966) method. The resulting elastic solution is exact for the problem given by Figure 3.6:

$$u_2 = \frac{\Delta u}{\pi} \left\{ \tan^{-1} \frac{D}{Y_1} + \sum_{m=1}^{\infty} \left(\frac{1-\gamma}{1+\gamma} \right)^M \left[\tan^{-1} \frac{D-2m+1}{Y_1} + \tan^{-1} \frac{D+2mH}{Y_1} \right] \right\} \quad (3.4.1)$$

where $\gamma = \gamma_2/\mu_1$. Using the correspondence principle the solution immediately yields the viscoelastic solution. Figure 3.6 also illustrates a solution for the $u_2(t)$ component for a standard viscoelastic solid.

Unfortunately, Nur and Mavko (1974) do not fully define the parameters for the viscoelastic media. Stress asymptotically relaxes in a standard viscoelastic solid to a non-zero minimum. This minimum is not given. The figure, however, is still similar to complete relaxation of shear stress within the asthenosphere and sufficiently illustrates the point: relaxation of the asthenosphere allows further displacements far from the fault.

Nur and Mavko (1974) also give an incomplete solution for a dip-slip fault totally within the lithosphere. The solution is useless in its present form for it lacks the necessary geometric factors. A critical problem, however,

Figure 3.6

Viscoelastic model for a strike-slip fault according to Nur and Mavko (1974) using Rybicki's (1971) elastic solution. The dislocation occurs at $t = 0$, then relaxation of the asthenosphere produces the new profile at $t = \infty$. A standard viscoelastic solid is used for the asthenosphere allowing initial elastic behavior and relaxation to a non-zero stress level. Unfortunately, the parameters are not given. Figure reproduced from Nur and Mavko (1974).

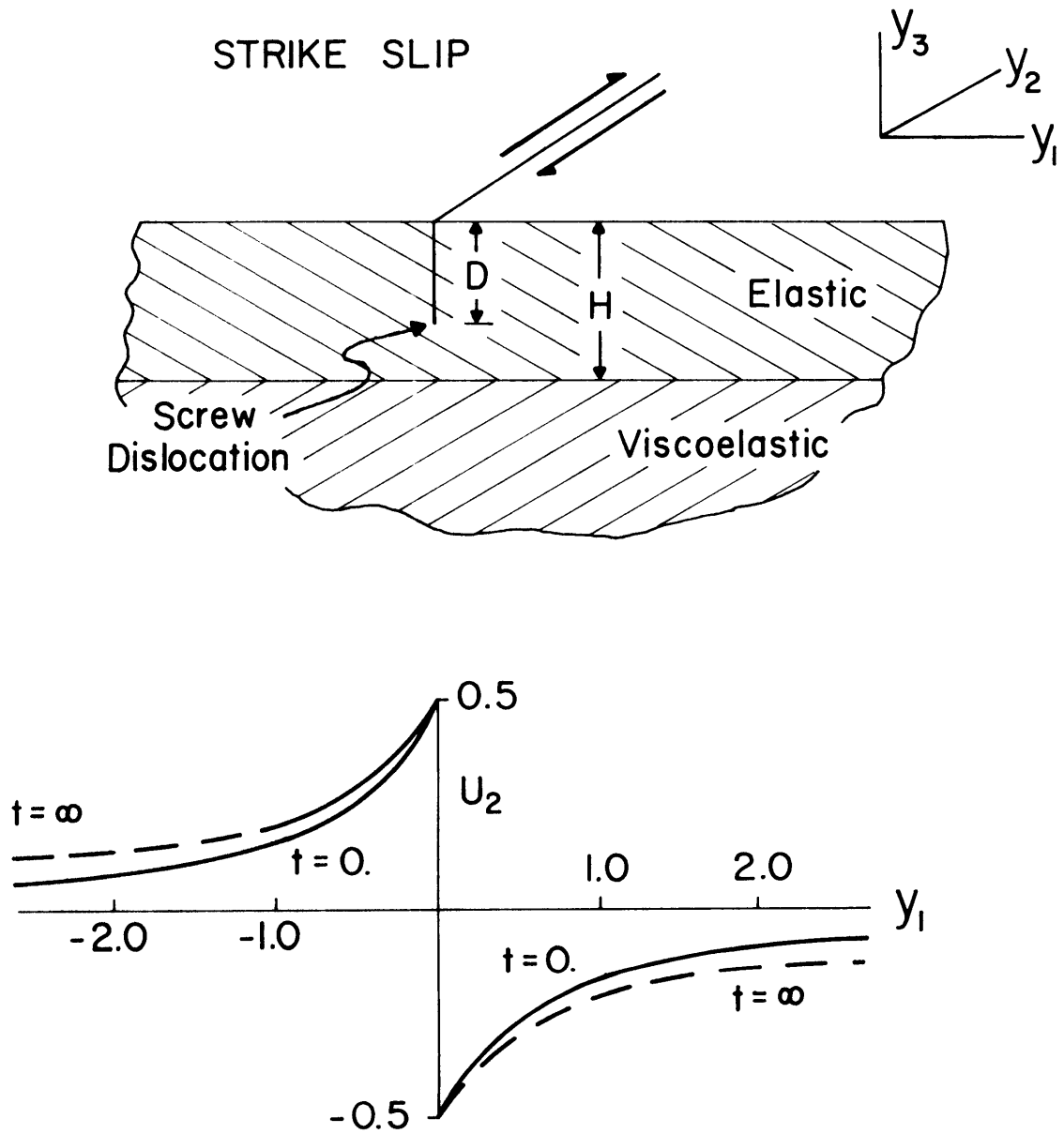


Fig. 3.6

lies with the solution technique. The solution for a layered half-space uses Head's (1953, or see Mura, 1968) solution for an edge dislocation within an elastic half-space when bonded to a second and different half-space. An image of the dislocation sharing a common slip plane with the original dislocation approximates the free surface midway between the two. This gives an incorrect boundary condition along the free surface, and neither does it satisfy the symmetry of the problem. In addition, Head used images for the solution of the original problem, and these images are not represented in Nur and Mavko's solution. Thus, their viscoelastic solution also represents a gross approximation for a fault within a layered media.

3.5 Stress Propagation

Among his many contributions, Elsasser (1969) realized the possibility of stress propagation within the lithosphere when overlying the viscous asthenosphere. A simple, one-dimensional model given in Figure 3.7 was suggested for the problem: a thin, elastic plate or beam of thickness h_1 and elastic modulus E represents the lithosphere. The asthenosphere conforms to a fluid layer of depth h_2 and viscosity η . Now consider a lateral transient load on the plate which locally deforms it. The load also stresses the asthenosphere which locally relaxes, and diffuses or propagates the stress down the plate. Thus the problem is

Figure 3.7

One dimensional model after Elsasser (1969) for an elastic lithosphere overlying a viscous asthenosphere. A step displacement is applied at the boundary on the left.

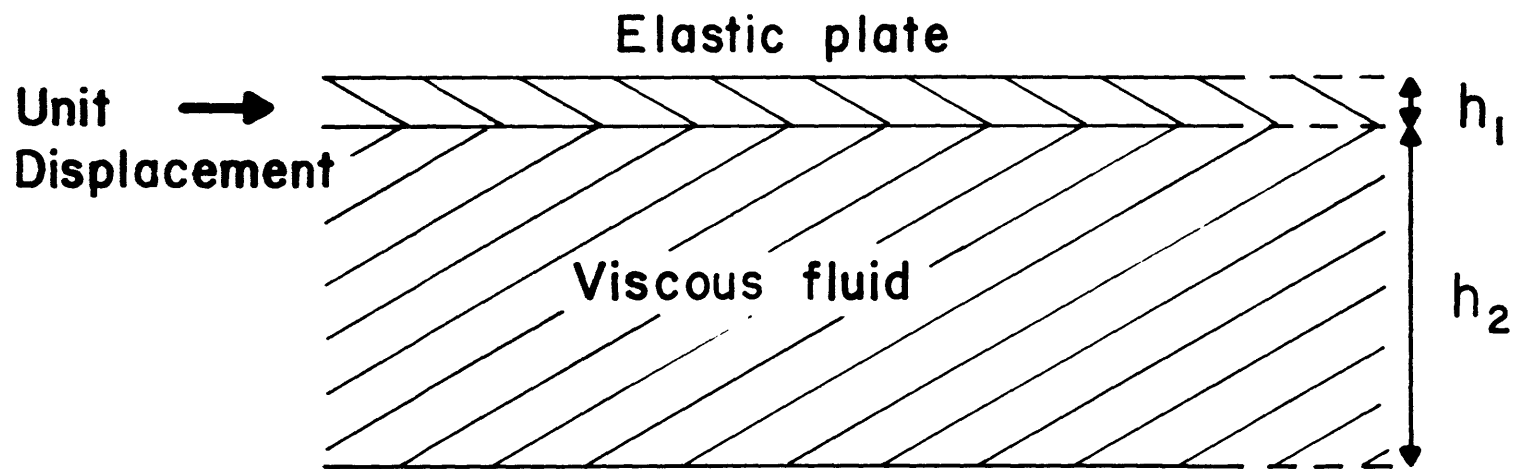


Fig. 3.7

analogous to heat conduction.

Let us consider the simple model. If the transient load results in pure elastic deformation within the plate, the horizontal displacement u within the plate depends on the local horizontal stress σ_x :

$$\sigma_x = E \frac{\partial u}{\partial x} \quad (3.5.1)$$

A traction T applied at the base of the plate introduces a horizontal gradient to the total load on the plate:

$$T = h_1 \frac{\partial \sigma_x}{\partial x} \quad (3.5.2)$$

If the motion is slow ($\frac{d}{dt} = \frac{\partial}{\partial t}$), the plate moving upon the viscous asthenosphere causes a traction at the base

$$T = \eta \frac{d\epsilon}{dt} = \frac{\eta}{h_2} \frac{\partial u}{\partial t} \quad (3.5.3)$$

Balancing the horizontal forces within the plate with the shear forces at its base gives the following parabolic equation:

$$\frac{\partial u}{\partial t} = \kappa \frac{\partial^2 u}{\partial x^2} \quad (3.5.4)$$

$$\kappa = \frac{h_1 h_2 E}{\eta}$$

Standard solutions are available for this diffusion equation. A unit displacement at the boundary of a semi-infinite solid yields a horizontal displacement

$$u = \operatorname{erfc} \left\{ \frac{x}{2\sqrt{\kappa t}} \right\} \quad (3.5.5)$$

or if

$$\zeta = x/2\sqrt{\kappa t} \quad , \quad u = \operatorname{erfc} \{\zeta\} \quad (3.5.6)$$

(Carslaw and Jaeger, 1959). The stress σ_x using equation (3.5.1) is then

$$\sigma_x = \frac{-E}{\sqrt{\pi\kappa t}} e^{-x^2/4\kappa t} \quad (3.5.7)$$

or

$$\sigma_x \frac{x\sqrt{\pi}}{2E} = -\zeta e^{-\zeta^2} \quad (3.5.8)$$

These are plotted in Figure 3.8.

The normalized stress propagates as a diffusion wave or front with velocity

$$v = \left(\frac{\kappa}{2t}\right)^{\frac{1}{2}} \quad \text{when} \quad x = \left(\frac{\kappa t}{2}\right)^{\frac{1}{2}} \quad (3.5.9)$$

Alternately, when σ_x is e^{-1} of its maximum at time t ; the velocity becomes

$$v = \sqrt{\kappa/t} \quad \text{when} \quad x = 2\sqrt{\kappa t} \quad (3.5.10)$$

These only differ by a constant. The solutions give a realistic approximation for times greater than zero. Substituting the values used for the surface deformation in section 3.2:

$$E = 10^{12} \text{ dyne cm}^{-2}$$

$$h_1 = 65 \text{ km}$$

$$h_2 = 200 \text{ km}$$

$$\eta = 5.10^{19} \text{ poise}$$

gives

$$\kappa = 2.6 \cdot 10^6 \text{ cm}^2 \text{sec}^{-1}$$

Figure 3.8

Normalized horizontal displacements and stress for the propagating displacement impulse. The displacement is normalized by the initial pulse, while the stress is normalized by two alternate models. Each shape is invariant in time, but the magnitude depends either on the time since the impulse or the distance from its application point.

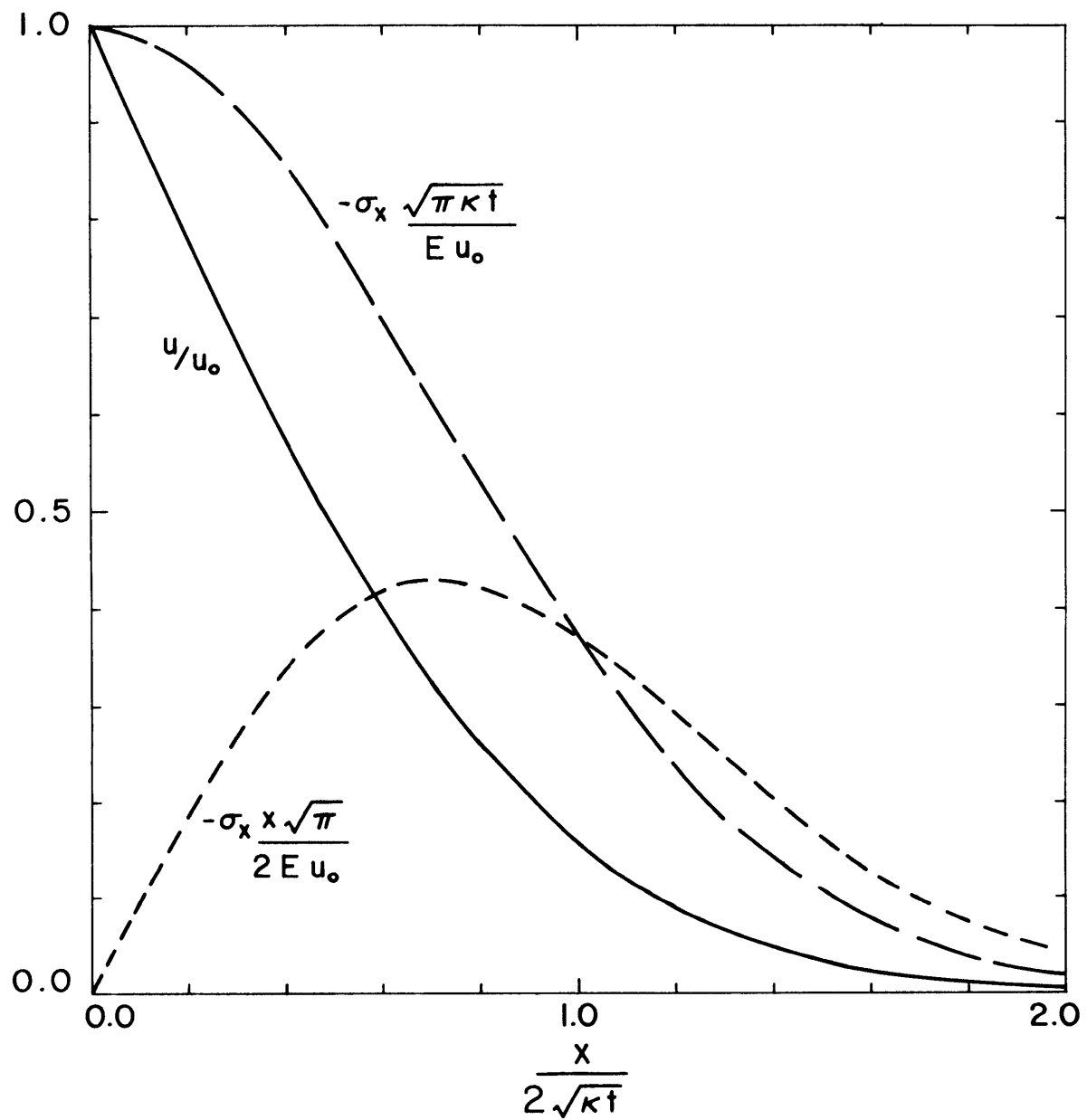


Fig. 3.8

Figure 3.9

Velocity and distance for diffusion propagation.

The two derivations in the text represent upper and lower bounds for each. Thus, 10 years after the strain step the diffusive front has propagated approximately 500 km and is now continuing at 30 km/yr.

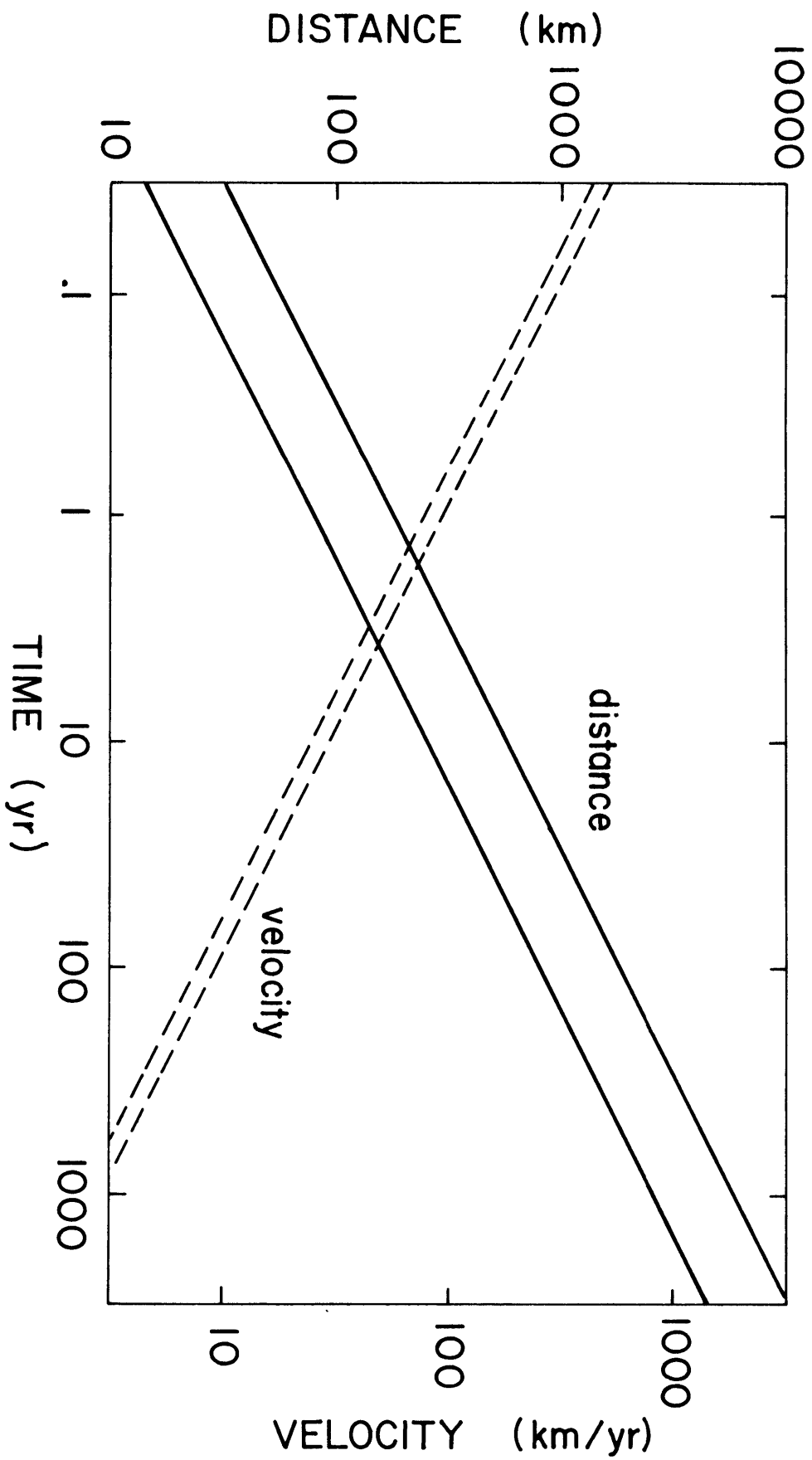


Fig. 3.9

Figure 3.9 plots the velocity and distance for the diffusion propagation of stress, where the two derivations represent upper and lower bounds. For distances between 10 and 1000 km the 'propagation time' is from .1 to 50 years, well within the accumulation interval between large earthquakes.

These models predict propagation of stress after large earthquakes. The perturbations in the stress pattern are not large, yet it may influence the probability of an earthquake in an adjacent region.

3.6 Predictions and Conclusions

The first-order analysis contained in this chapter suggests diverse effects introduced by mantle relaxation prior to and following major earthquakes. The most significant consequence is the post-seismic deformations since geodetic measurements can provide reasonable constraints on the model. In addition, the state of stress simultaneously varies during mantle relaxation. While aftershocks probably do not reflect this variation, stress relaxation and propagation following a major earthquake could influence the state of stress within adjacent regions during later times. This characteristic time would depend on the relaxation time of the asthenosphere. These variations could in turn trigger earthquakes in adjacent 'seismic gaps'. This suggests that a two-dimensional analysis containing the fault and descending lithosphere would further define the problem and the important factors.

The geodetic data for the 1946 Nankaido earthquake indicates that a detailed regional analysis would also be profitable. The following conditions in the problem may be further resolved using two-dimensional models:

1. Effective viscosity of the asthenosphere near the island arc during the deformations.
2. Thickness of the lithosphere at these time scales.
3. Geometry of the fault.
4. Boundary conditions on the fault.

In the next chapter idealized models for island arc systems attempt to resolve the various aspects of the problem. Later in the last chapter the geodetic data for the 1946 Nankaido earthquake will introduce constraints on the model for Southwest Japan and Shikoku.

4. FINITE ELEMENT MODELS OF TIME-DEPENDENT STRAIN FIELDS

4.1 Introduction

Analytic solutions give only a limited description of mantle relaxation. The solutions are first an approximation to the fault within a layered media. Even if exact, the descending lithosphere imposes important boundary conditions on the fault; that is, the slab penetrating into the mantle acts as a stress guide. Within this chapter we consider idealized models for an island arc using the finite element method to model the media.

Linear viscoelasticity characterizes the simplest medium which contains the desired behavior: stress relaxation and elastic response. But even with this simplification, previous numerical solutions have been inefficient. Our solution method using finite elements gives a simple and efficient technique yielding accurate results (see sections 2.1-2.6). Just as significant is its ability to include gravity and to generate the inverse model. Precedence also exists for the application of viscoelasticity to earth models. Almost all models for the earth's response to glacial loading assume linear viscoelasticity (i.e., Haskell, 1935; McConnell, 1965). Post and Griggs (1973) only recently advanced to material nonlinearities and suggested a relationship between the glacial rebound data and nonlinear creep. Generally the geodetic data, whether post-glacial rebound or post-seismic

adjustments, do not warrant a nonlinear analysis. Such an approach to our problem would entail vastly more complex mathematics and computational time. In view of the other inherent complications, a nonlinear analysis does not make sense when a simpler linear model gives the desired physics for the problem.

A second major assumption reduces the problem to two-dimensional plane strain for a flat-earth. Along the trend of an island arc the geometry does essentially conform to two-dimensions, depth and distance perpendicular to the arc. An earthquake, however, is finite along the arc rather than an infinite crack as two-dimensional models implicitly assume. Immediately, all edge effects introduced by the finite length are ignored in our models. So long as the model avoids the fault ends and remains within roughly a fault length of the rupture, the two dimensional approximation is reasonable and still retains the physics (Jungels and Frazier, 1973). Three dimensional models using the finite element method only require more computer time. This additional expense, however, does not seem justified at this moment.

The finite element method represents an ideal compromise to solve problems having dip-slip faulting. For the simplest problem, a fault within a half-space, analytic solutions exist and are far more efficient than the

numerical schemes. A layered media probably represents an even trade-off if a semi-analytic solution were available. Any greater complexity favors the finite element model for elastic solutions. Jungels and Frazier (1973) present a strong case for the finite element method when the media is inhomogeneous. As section 2.3 poignantly illustrates, the accuracy for the approximation depends on the degree of approximation within any one element, the number of elements within the region, and the presence of singularities. Under normal conditions increasing the elements or approximation degree insures any desired accuracy. The singularity introduced by the fault, however, slows the convergence rate for more elements, and eliminates the advantage of higher degree approximations within the element (Strang and Fix, 1973, chapt. 8). Yet convergence still does occur for displacement or stress; it only requires greater effort. This caution has not been sufficiently stressed in the literature. Given the appropriate problem, the finite element method gives an efficient solution technique.

The deformations of a dip-slip fault in a complex viscoelastic media is such a problem. At the present no other solution strategy exists that incorporates the complex geometry of the descending lithosphere and fault. We must still proceed with caution for the fault does intro-

duce a singularity. The trade-off between accuracy and computational speed must retain the physical behavior.

To satisfy these criteria, two models are adopted in the computations. A coarse array of elements demonstrates the phenomena. Figure 4.1 portrays the structure and properties for both a long 650 km and short 200 km depth slab. The grid contains 206 elements and 324 degrees of freedom graded toward the fault. Nine segments comprise the fault. The second array in Figure 4.2 improves the accuracy. The structure contains 467 elements and 956 degrees of freedom, while the fault contains 15 independent segments. This model allows detailed comparisons and inversions.

The next section begins with a linear viscoelastic media and approaches various simple problems. Once the effect of the boundary conditions has been resolved, we solve for a 45° dip-slip fault with and without gravity for an elastic media. The solutions without gravity have an analytic counterpart. Stress relaxation is then introduced into the asthenosphere. Later comparison of models indicates the effect of various geometric changes such as fault depth and lithospheric thickness, slab length, and dip. The boundary conditions imposed upon the fault are also discussed. Within these models the effects of stress propagation and gravity are evident. The behavior is then summarized in a set of predictions.

Figure 4.1

Coarse finite element grid for an idealized island arc. The grid contains 206 elements and 324 degrees of freedom. The fine shading denotes the continental and oceanic lithospheres where the boundary for the short descending slab corresponds to the heavy line between 100 and 200 km depth. The alternate model with the long descending lithosphere extends to 600 km depth. The lithosphere extends from 0 to 100 km depth; the asthenosphere lies between 100 and 350 km; and the mesosphere occupies depths greater than 350 km to the bottom artificial boundary. The side and bottom boundaries simulate a viscoelastic half-space (see section 2.7). Nine fault segments separate the continental and oceanic lithospheres. If the relative viscosity or relaxation time of the asthenosphere is taken as 1., the mesosphere becomes 20., and the slab and lithosphere are 2×10^5 . These are the relative viscosity ratios. Both finite element grids assume that the bulk modulus equals 1×10^{12} dynes/cm², and that the elastic shear modulus is $.7 \times 10^{12}$ dynes/cm².

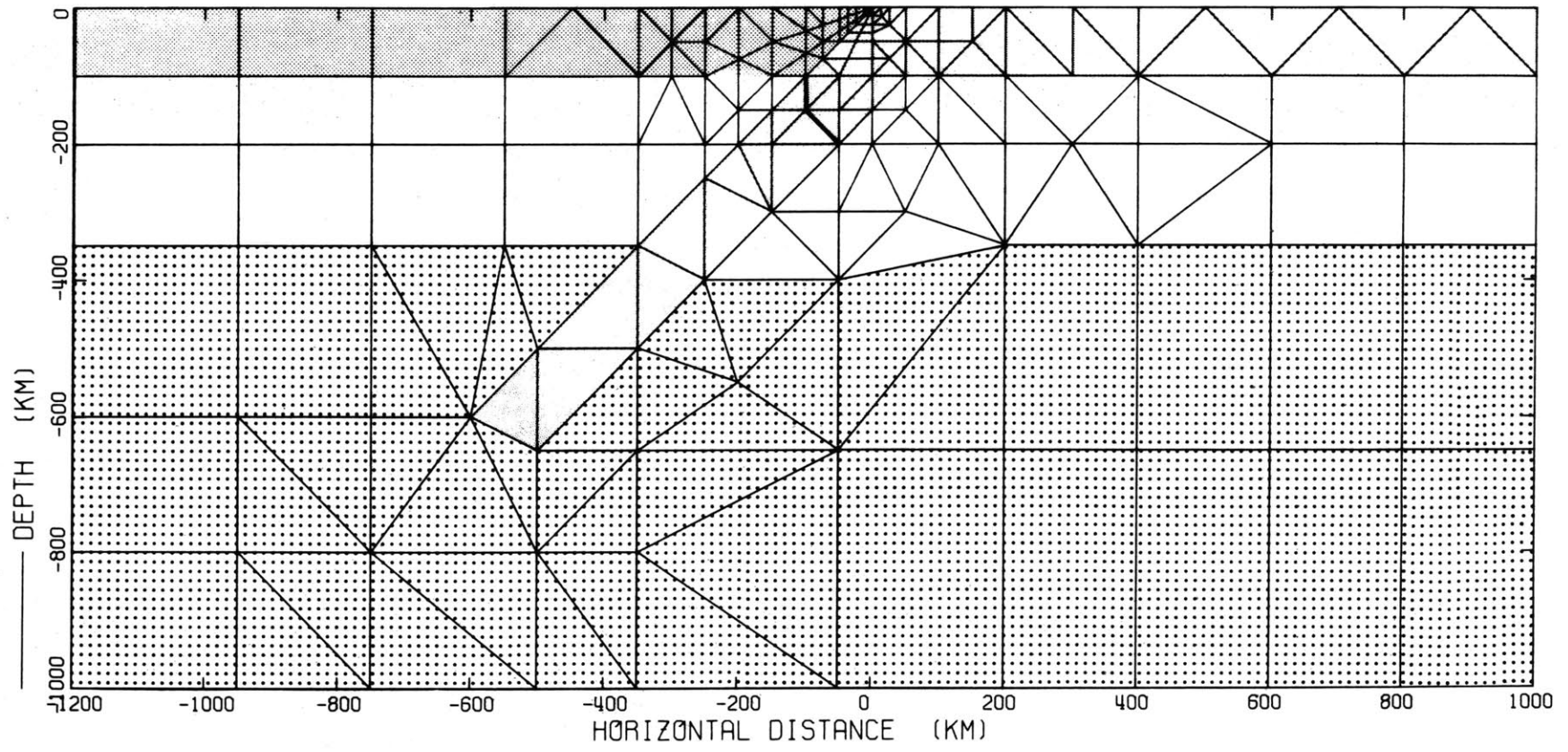


Fig. 4.1

Figure 4.2

Refined element grid for inversion problems and detailed models. Now 467 elements and 956 degrees of freedom define the net. In this configuration the fault dips at 35° between the continental lithosphere and a short descending lithosphere extending to 75 km depth. Again the continental and oceanic lithospheres conform to the light shading. Fifteen segments define the thrust fault between the two lithospheres. Again the outer boundaries simulate a viscoelastic half-space. Viscosity ratios to the asthenosphere (50-100 km) become: lithosphere and slab (0-50 km), 10^6 ; lower asthenosphere (100-350 km), 10.; mesosphere (350-500 km), 100. Rescaling this basic model generates new configurations with bends and different dips in the fault.

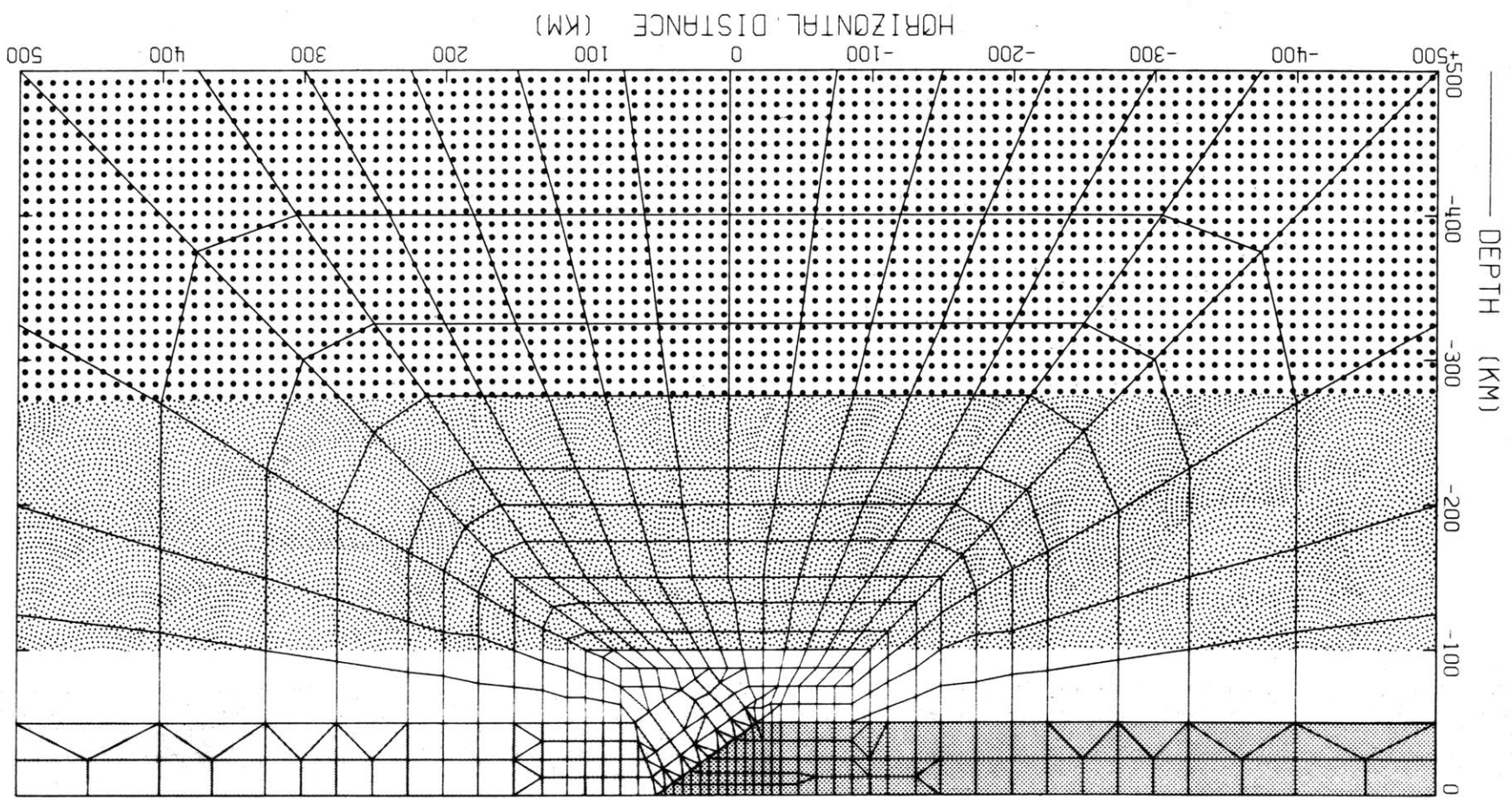


Fig. 4.2

4.2 Dip Slip Fault in an Elastic Media

A simple model having an analytic solution is a 45 degree dipping fault in a homogeneous elastic half-space. Using the elements in Figures 4.1 and 4.2, the finite element method yields an elastic solution for a Poisson solid without gravity. Figure 4.3 shows the non-dimensionalized vertical displacements for two models. The dimensions are normalized by the fault depth and the vertical offset on the fault. The first using the coarse grid imposes a dislocation extending to 100 km depth, but linearly decaying along the last 25 km. The diagram also depicts an analytic solution for the same model, except the dislocation remains constant along the full depth (Jungels and Frazier, 1973). The deviations between the fault conditions used for analytic calculations and finite element models are unavoidable; it results from the linear approximation used in the finite elements. The difference between the solutions amounts to 3 percent of the maximum displacement. A similar model with the detailed grid in Figure 4.3 gives similar deviations, while it closely follows the previous finite element model. Recalling the slightly different initial conditions for the analytic and finite element models, these results are adequate and conform to linear decay at the fault tip. Jungels and Frazier (1973) consider other elastic models which con-

Figure 4.3

Vertical displacements versus horizontal distance for two finite element models compared to an analytic solution for a 45° thrust fault in an elastic, Poisson half-space. The vertical offset is normalized to 1. The model denoted by the filled circles uses the coarse grid in Figure 4.1. Similarly, the crosses represent the surface displacements for the finer grid in Figure 4.2. The fault conforms to the line extending from $\bar{x}=0$, where the slip linearly decays to zero along the dashed portion for the finite elements models. The analytic solution has constant slip along its full length (Jungels and Frazier, 1973). The deviation between the numerical solutions and the analytic solution reflects this difference.

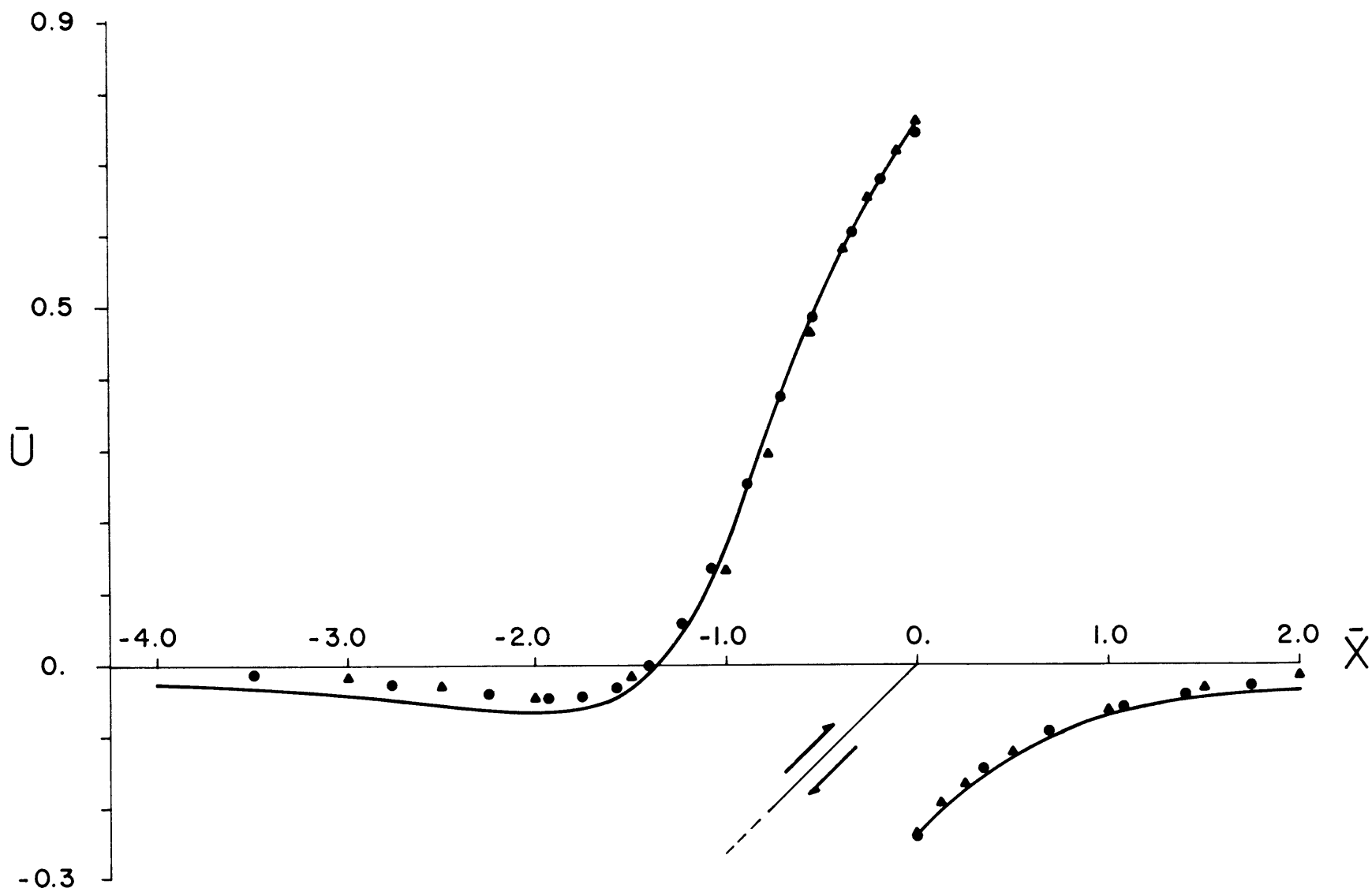


Fig. 4.3

tain variations along the fault and breaks in the dip. There is no inherent limitation to the accuracy, only the previously discussed trade-off between computational time and accuracy.

4.3 Models for Island Arcs

Certain structural features are essential to characterize an idealized island-arc structure, beginning with a descending oceanic lithosphere adjacent to the island arc or continental plate. A thrust fault separates the two domains and their independent motions. A distinct low velocity and low Q zone underlies both the oceanic and particularly the island arc (Utsu, 1967). These are also the essential features that dominate the model.

In section 4.1, the finite element grids are illustrated together with these essential regions. We now examine the behavior of these models to time-dependent deformations. The dominant interaction is one between the asthenosphere and the lithosphere; however, other factors are important. Gravity strongly perturbs the time-dependent deformations. The length of the descending lithosphere influences the possible modes of relaxation. Even more significant are the thickness of the lithosphere and the relative dimensions of the fault. The time-dependent deformations and their relation to these

factors are the topics of this section.

The simplest model and the one most closely approaching the analytic solutions uses a short descending slab illustrated in Figure 4.2. A 50 km lithosphere overlies an asthenosphere with viscosity of 7×10^{18} poise for the shear modulus or a relaxation time of .32 years. Starting at 100 km depth, the viscosity increases to 7×10^{19} poise. The viscosity of the lithosphere is 7×10^{24} poise. We can rescale these values, only their ratios remain constant. Thus the diagrams express the time in dimensionless units scaled by the relaxation time τ_0 for the asthenosphere where

$$\tau_0 = \eta/\mu$$

if η is the viscosity and μ the shear modulus. The dimensionless relaxation times become 10^5 for the lithosphere and 10-100 for the mesosphere. For all the models the shear modulus μ equals 7×10^{11} dyne/cm² and the bulk modulus is elastic at 1×10^{12} dyne/cm². All models include the gravitational potential unless otherwise noted.

Starting with a fault not quite extending through the lithosphere, we observe in Figure 4.4 significant post-earthquake deformations analogous to the analytic models in section 3.2. Just as before the hinge point of zero deformation expands from the fault along the "continental lithosphere" with increasing time. Yet now the finite fault contained within the lithosphere further perturbs

Figure 4.4

Post-seismic vertical deformations using a 100 km descending lithosphere in Figure 4.2. The fault dips at 35° , slips 7. m, and intersects the surface at 50 km. The geometry is shown in the upper left corner for all the forthcoming models where the lithosphere is outlined. The arrows indicate the direction of slip along the fault interface. Between the two filled circles the slip linearly decays to zero. Five nondimensional times are plotted where the increasing frequency for dashing denotes increasing time. When nondimensionalized by the relaxation time for the asthenosphere, the times for the plot are 0. (elastic), 3.16, 15.8, 31.6, 63.1. For a viscosity of 7×10^{18} poise for the asthenosphere, these correspond to 0., 1., 5., 10., and 20. years. The short lithosphere allows prominent post-seismic deformations on the continental lithosphere. The reaction to the fault tip causes the developing bulge at -75 km.

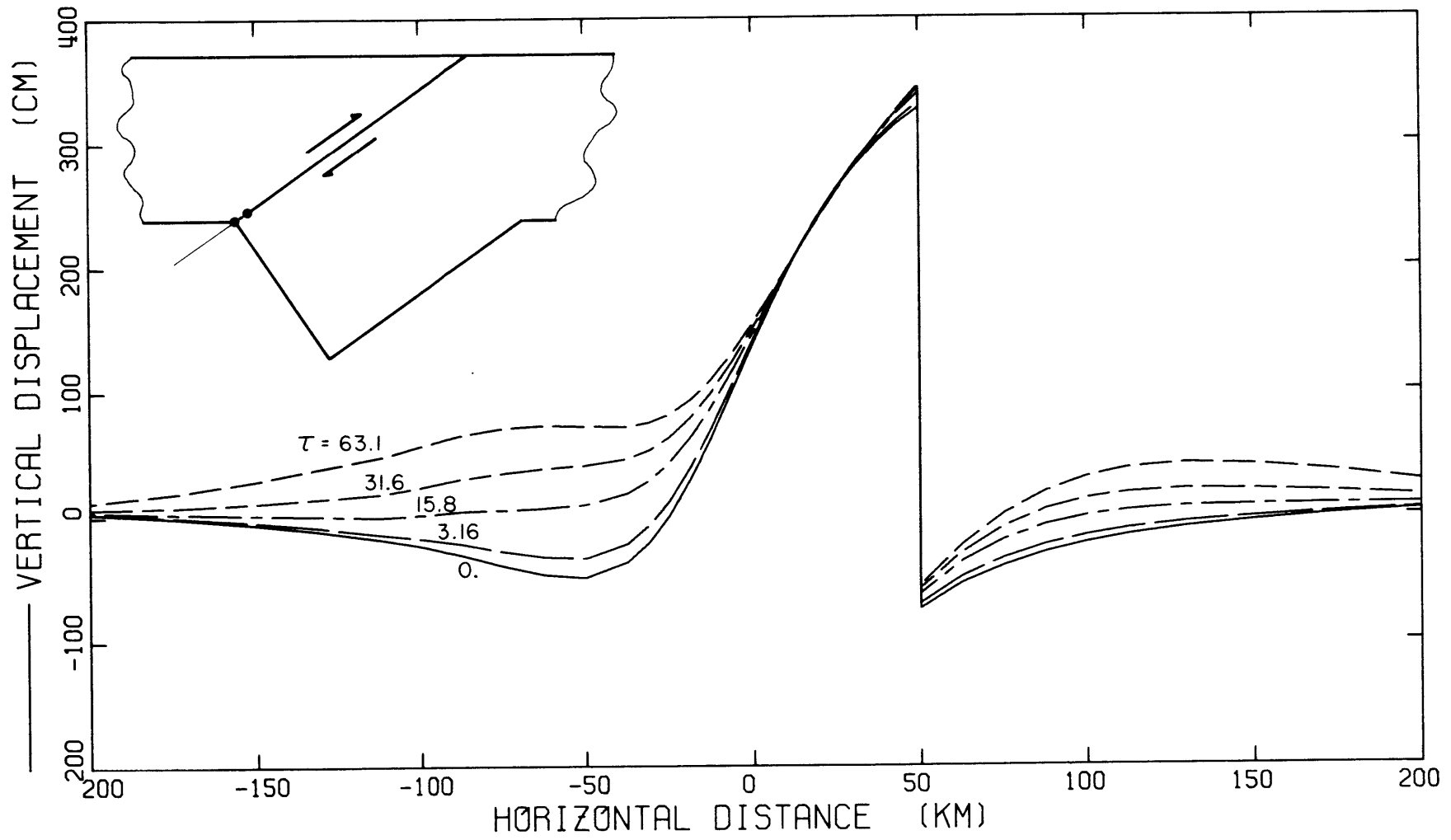


Fig. 4.4

the deformations; it determines the initial deformation field. It is this field that relaxes within the asthenosphere. Furthermore, the fault plane deforms with the lithosphere during this process. As we will see later, a long descending lithosphere restricts the possible relaxation modes for the lithosphere.

Gravity significantly perturbs the surface deformation caused by the fault. Figure 4.5 compares two finite element models, one without gravity and one with the gravitational potential introduced into the variational principle according to section 2.4. The deformations are for two times, zero or elastic and 12.6 after the dislocation. We observe its effect by the slight increase in the spacial wavelength for the vertical deformations and an overall perturbation. This represents a significant effect for times after the deformation. When the asthenosphere relaxes, the gravitational restoring force becomes relatively more important; the asthenosphere approaches a buoyant fluid. Even for the elastic solution, the gravitational potential introduces a significant perturbation when we invert the geodetic data.

4.4 Geometrical Scaling

The analytic solutions for a strike-slip fault suggest certain geometrical scalings within the problem. The

Figure 4.5

Perturbation introduced by gravity on the vertical surface deformations. The geometry is again shown in the upper left inset using the bottom distance scale. The fault slip is now 10 m with linear decay between the filled circles. The descending lithosphere penetrates to 600 km using the coarse finite element net in Figure 4.1.

The comparison is for two nondimensional times, 0. and 12.6. The solid line represents the solution with gravity; the dashed line is the solution without gravity. Thus gravity introduces an additional restoring force, thereby reducing the post-seismic deformations.

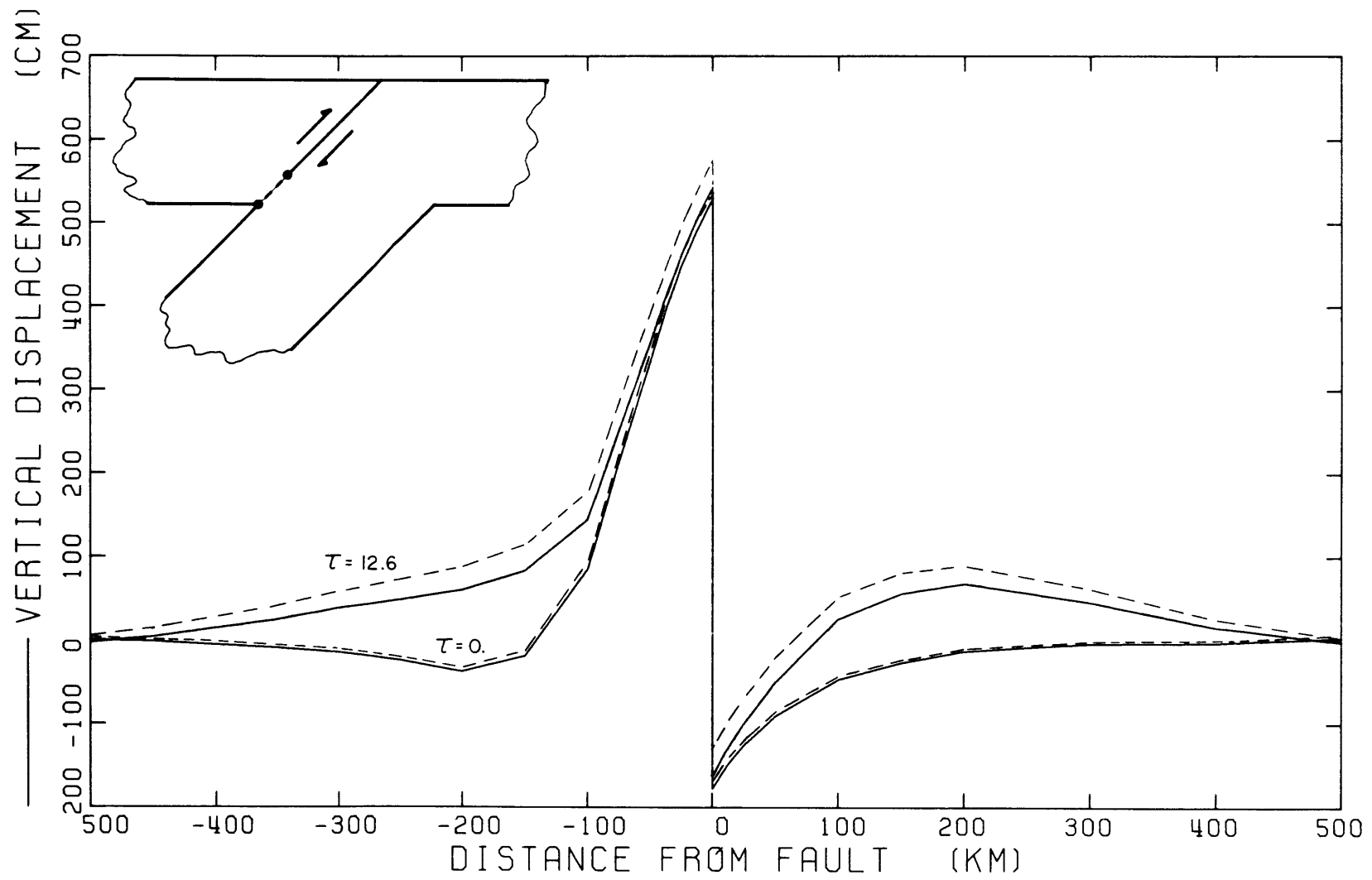


Fig. 4.5

most significant is the fault depth to lithospheric thickness. Let the fault dip at angle θ and extend to depth D , where the lithosphere has thickness H . The analytic solution suggests that D/H represents the nondimensional parameter (Nur and Mavko, 1974). Similarly, $(D/H)\cos\theta$ influences the horizontal scaling for a given θ . These scalings are evident in the numerical solutions.

First let us consider a change in the lithospheric thickness when the fault depth and dip remain constant. Figures 4.6a, b compare two models: a 50 km thick lithosphere and 50 km fault depth, to a 100 km lithosphere with the same 50 km fault. Both these models use the fine element grid in Figure 4.2 but with the fault dipping at 50 degrees. D/H now becomes 1. and .5 respectively. The results are distinctly different deformations. To decipher these changes, Figures 4.7 a,b, are schematics showing the slab and the net deformations introduced by relaxation.

Two processes are controlling the relaxation. For the first model the fault tip extends to the asthenosphere. The lithosphere is thinner, and relaxation occurs without any intervening lithosphere to diffuse the stress. Thus, the relaxation wavelength must be shorter due to the thinner lithosphere, and the stress concentration at the fault tip relaxes within the asthenosphere giving locally large changes. On the other hand, when the fault terminates

Figure 4.6a,b

The vertical surface deformations for $D/H=1.$ and $D/H=.5.$ The models use the elements in Figure 4.2 for a 50° dipping fault with 7 m slip. For each model, five non-dimensional times are denoted as before: 0., 3.16, 15.8, 31.6, and 63.1.

(a) The fault extends to 50 km depth corresponding to the thickness of the lithosphere. Thus, $D/H=1.$ The deformations are similar to Figure 4.4.

(b) The thickness of the lithosphere is now 100 km, while retaining a fault that extends to approximately 50 km depth. Here $D/H=.5.$ The relaxation wavelength now doubles with the lithosphere. Thus subsidence occurs in regions of uplift.

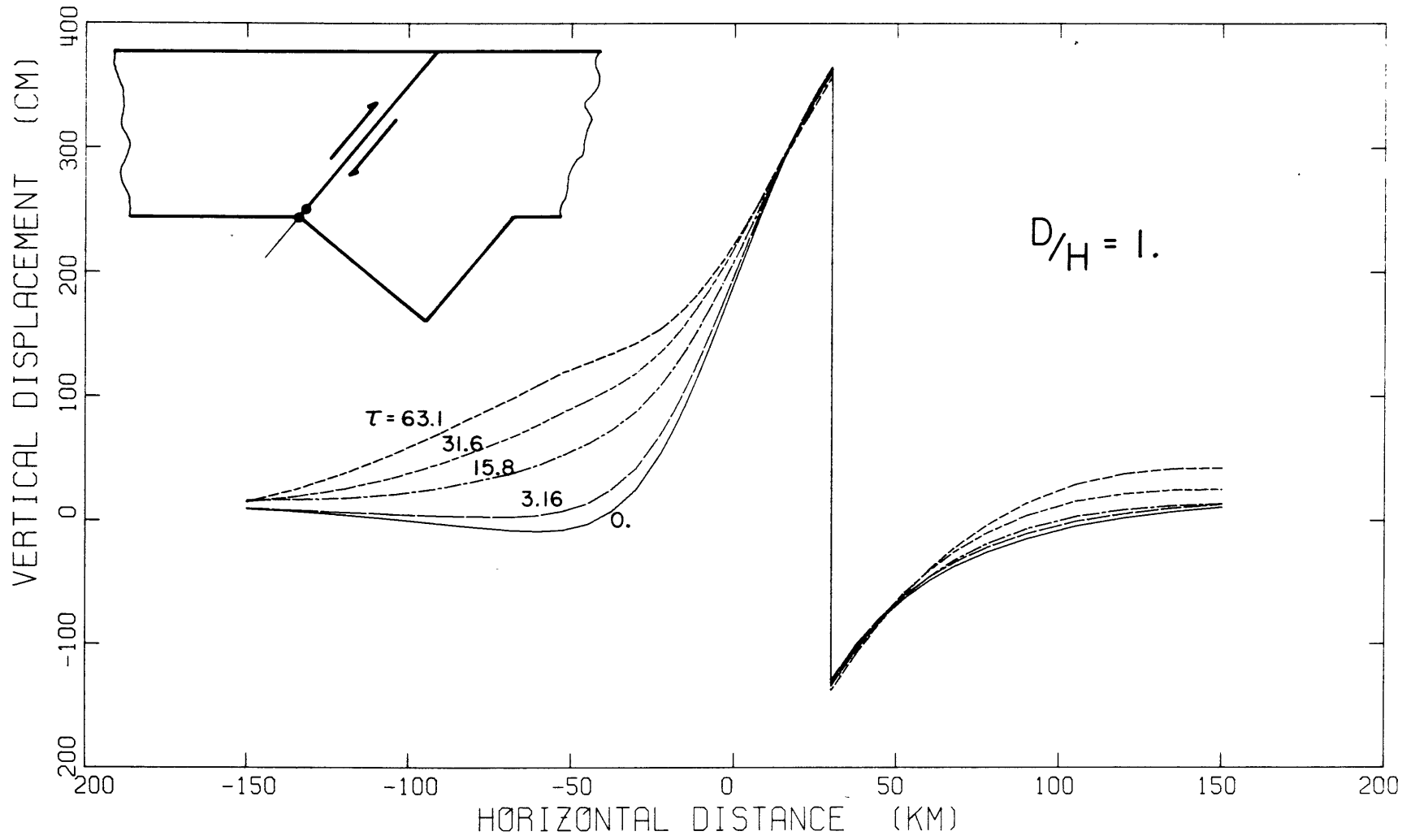


Fig. 4.6a

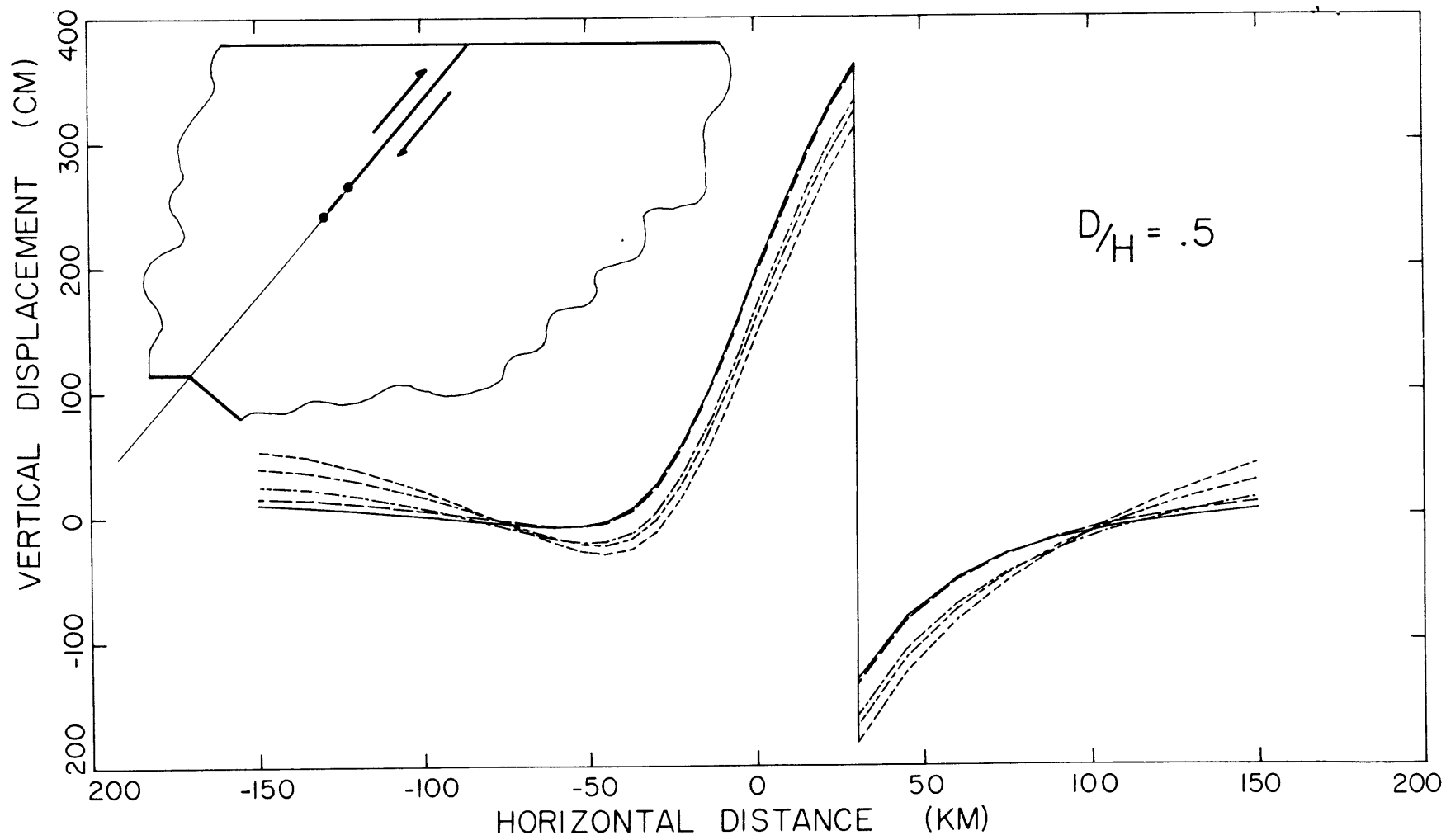


Fig. 4.6b

Figure 4.7a,b

Schematic of only the post-seismic, vertical displacements from Figure 4.6. Here the deformations are referenced to the initial elastic response at time 0. The four dashed lines then correspond to times 3.16, 15.8, 31.6, and 63.1 since the dislocation.

(a) When $D/H=1.$, strong asymmetric relaxation occurs for a short descending lithosphere. Uplift predominates over the whole region.

(b) When $D/H=.5$, the deformations are now more symmetric about the fault. Subsidence occurs near the fault and uplift at greater distances. Keeping the fault depth constant and doubling the lithospheric thickness implies that the relaxation wavelength doubles. Thus D/H is the essential scaling.

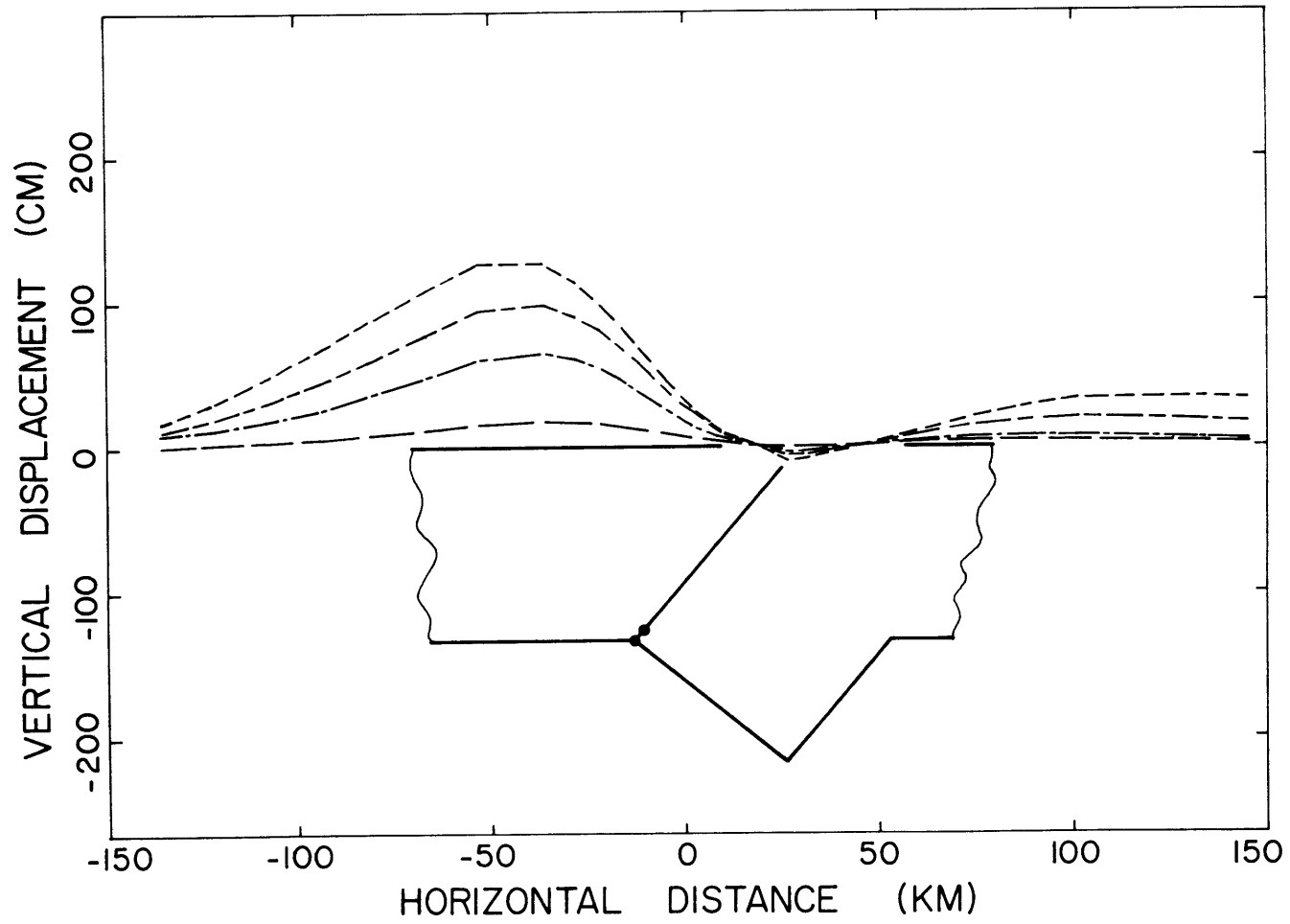


Fig. 4.7a

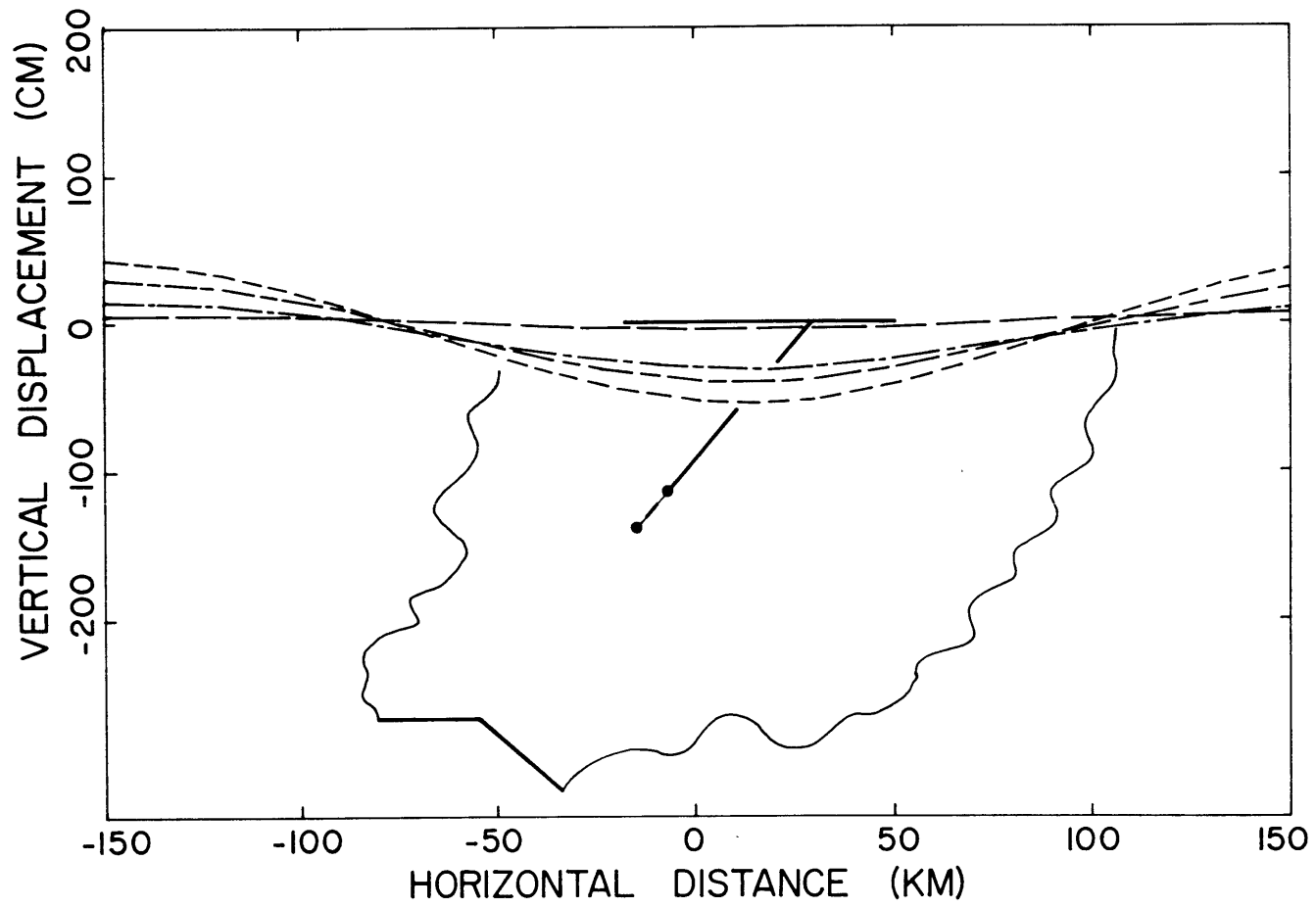


Fig. 4.7b

well within the lithosphere, the stress concentration at the fault tip lies further within the lithosphere, thereby filtering the high frequency spacial harmonics. Yet it is the increased thickness of the lithosphere that dominates the wavelength. Recalling McConnell's (1965) analysis in section 3.3 for relaxation of a viscous half-space with an elastic layer after removal of a surface load, the dominant wavelength should be proportional to the lithospheric thickness. This is indeed paramount for the present situation. For the 100 km lithosphere in Figure 4.6b or 4.7b the spacial wavelength is approximately 400 km, while it is 100 km for the 50 km lithosphere. As relaxation proceeds, Figure 4.7a suggests that the wavelength increases from time 3.16 to time 63.1, again agreeing in principle with the simplistic analog found in glacial rebound.

To validate the importance of the parameter D/H , a set of models having different fault depths while retaining the same lithospheric thickness is appropriate. Figures 4.8a,b consider such a comparison for fault depths from 25 km to 50 km. Again these new models are similar to the previous Figures 4.6a,b, when the lithospheric thickness is scaled by the fault depth, thus keeping the parameter D/H constant. The nondimensional parameter, D/H , then, primarily controls the shape of the profile. It is the lithospheric thickness that scales the primary

Figure 4.8a,b,c,d

Vertical displacements for different fault configurations with a 35° dipping fault and a 50 km lithosphere. The elements conform to Figure 4.2. The fault geometry for each model is pictured in the upper left corner, where the dashed line between the filled circles indicates linear decay of the slip. The arrows denote the 7 m fault slip. The dashed lines again correspond to times 0. (solid), 3.16, 15.8, 31.6, and 63.1.

(a) Fault extending through the lithosphere to the asthenosphere. This model duplicates Figure 4.4 where $D/H=1$.

(b) Fault extends only 25 km through the lithosphere. The scaling factor $D/H=.5$; thus, the model has similar characteristics to Figure 4.6b: a broad zone of subsidence near the fault.

(c) A buried fault segment within the lithosphere. A broad zone of uplift occurs above the fault.

(d) A buried fault segment within the asthenosphere.

Initial uplift is followed by complete relaxation of the displacements as the surrounding mantle relaxes around the fault.

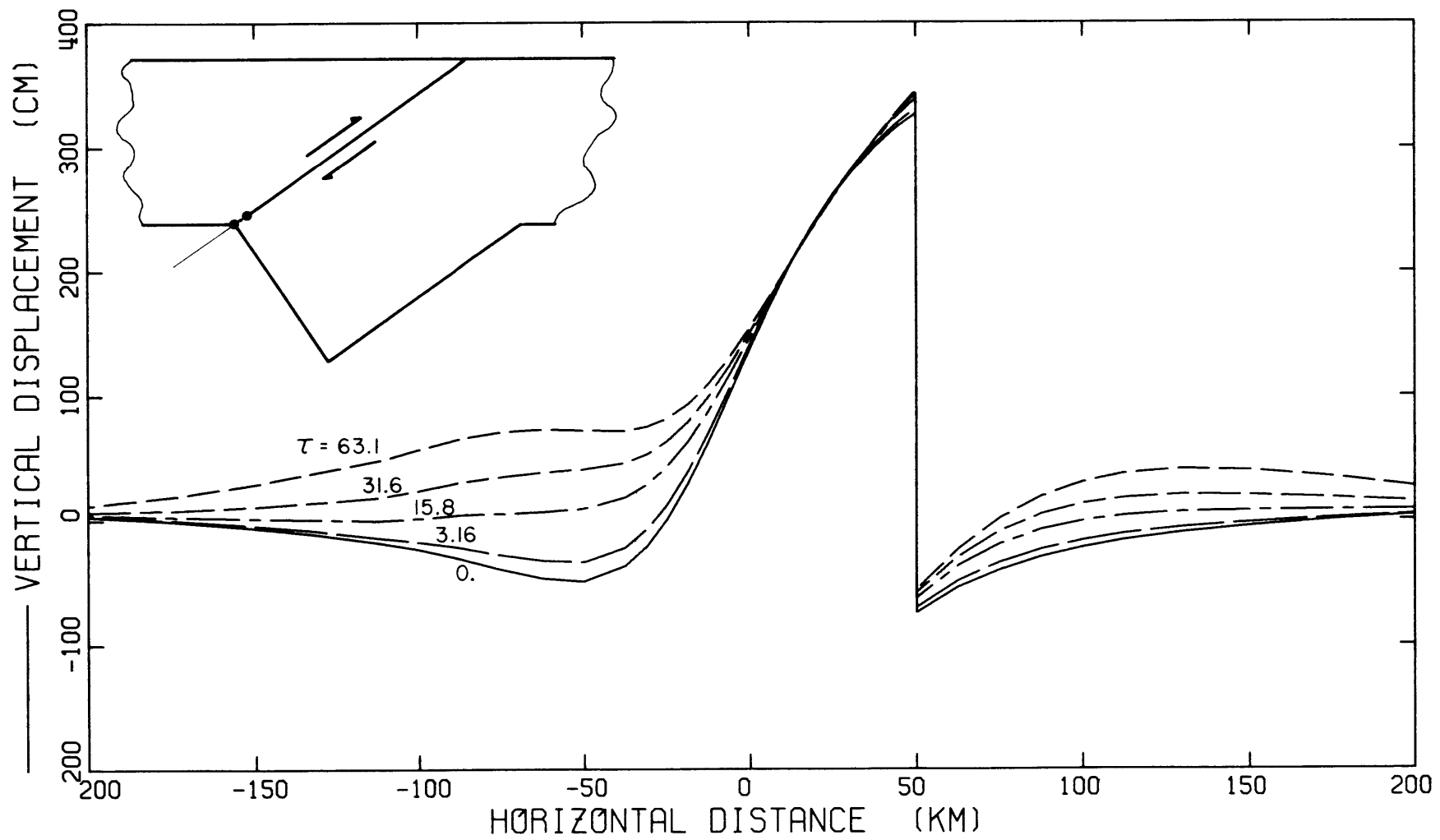


Fig. 4.8a

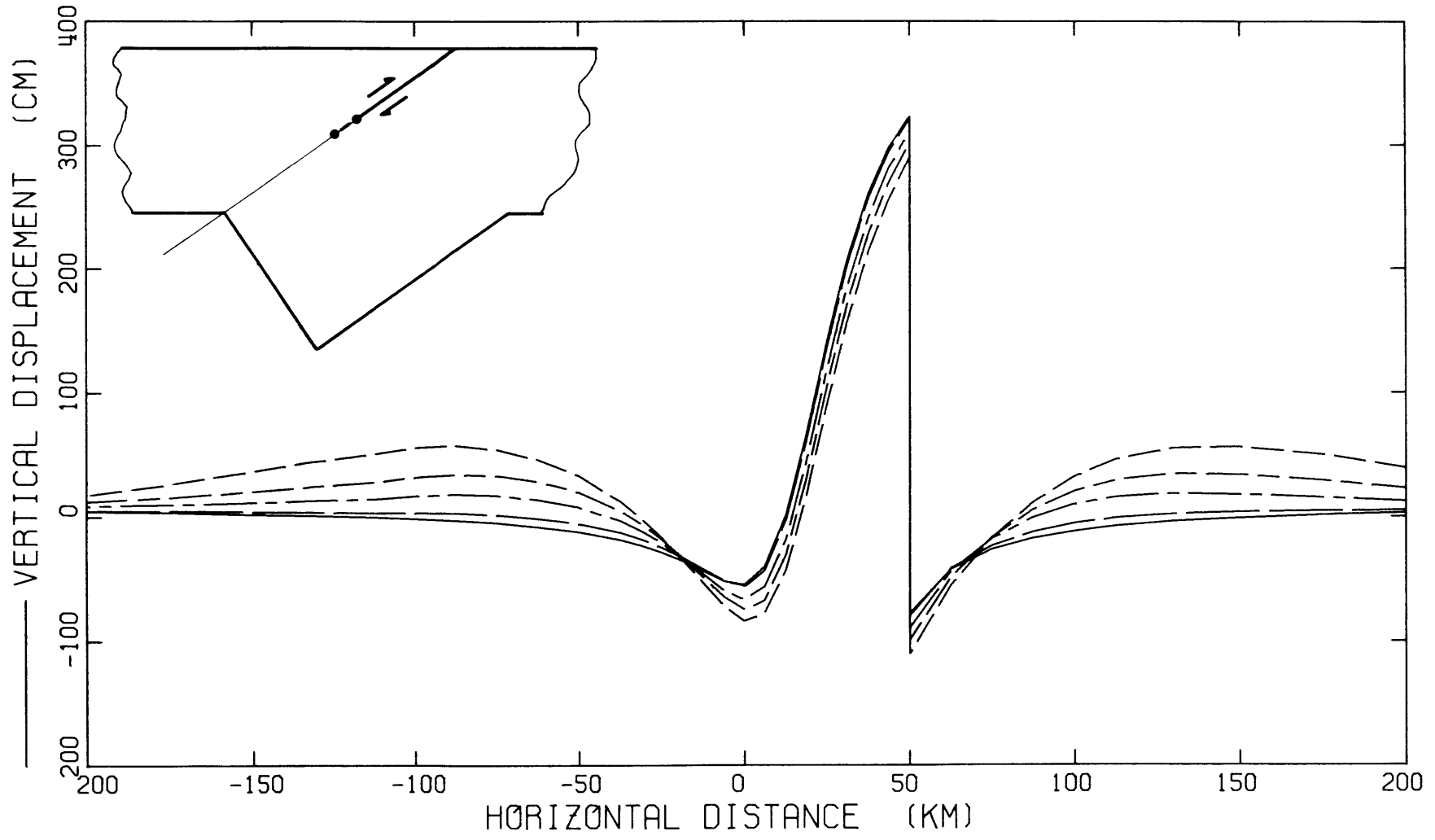


Fig. 4.8b

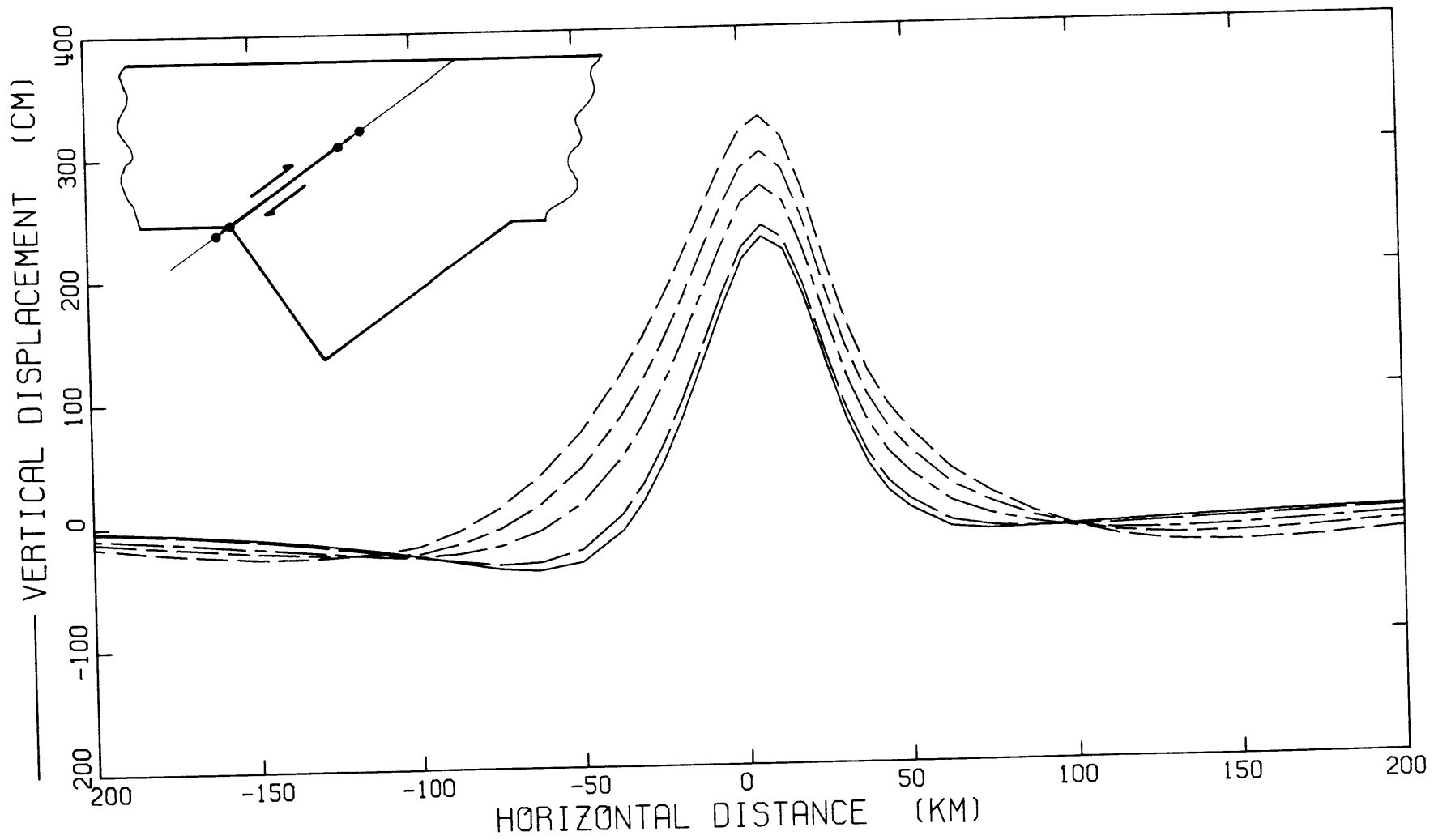


Fig. 4.8c

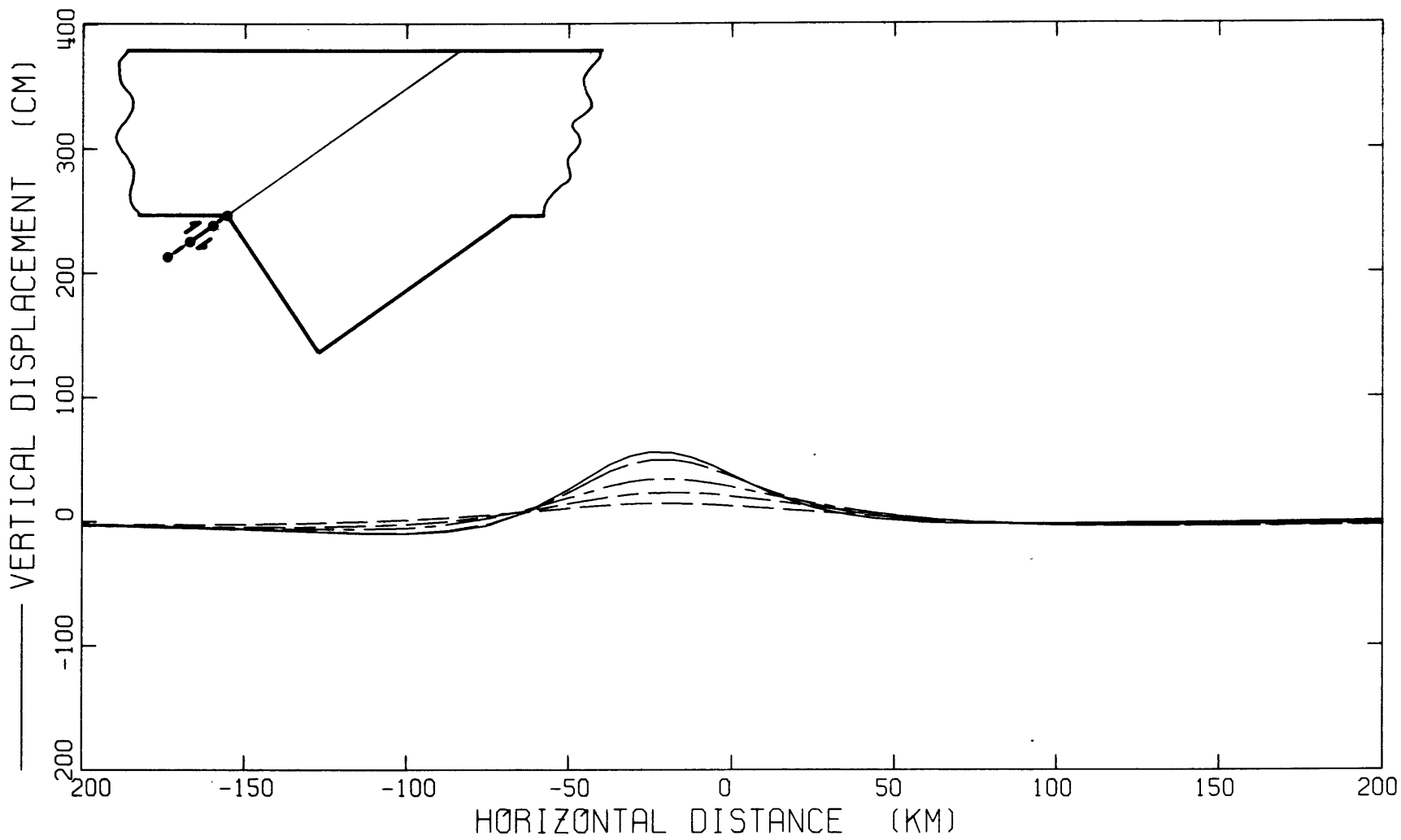


Fig. 4.8d

wavelength. If the fault depth is varied as between Figures 4.8a,b, the dominant wavelength for relaxation remains near 200 to 300 km. Instead, the fault depth and geometry drastically alters the profile. The fault dip influences the horizontal scaling as Figure 4.8a illustrates for a 35 degree dipping slab if we compare it to our previous model in Figure 4.6a for a 50 degree dip. Within a range of dips, the shape remains similar from one dip to the next, rather than the distinctive changes occurring for the geometric ratio D/H . The dip, of course, produces subtler variations analogous to the elastic solution. These include amplitudes of uplift and subsidence. Yet the models confirm their relative insensitivity to dip. Consequently, scaling the dimensions by D/H approximates a variety of circumstances.

In addition to the ratio of fault depth to lithospheric thickness, the fault can be considered as a sum of individual fault segments. Each component contributes to the total deformation. Figures 4.8b-c depict three such fault segments: the previous fault extending only half the thickness of the lithosphere and breaking the surface; a buried fault within the lithosphere; and a fault segment contained within the asthenosphere. For the first two, relaxation of the asthenosphere causes further surface deformations as its elastic restoring force decays. The displacements for the last segment contained within the

asthenosphere completely relax since the media deforms around the dislocation until complete stress relaxation occurs. This is an important distinction. Any extension of the fault within the asthenosphere will relax together with the corresponding surface displacements for a constant dislocation. All the surface displacements eventually result from the fault interface between the two 'elastic' lithospheres. Creep along the fault would continually stress the asthenosphere and introduce an equilibrium between the dislocation extending into the asthenosphere and its relaxation. If the creep is sufficiently slow, however, the displacements are still primarily given by the dislocation between the elastic lithospheres. The extremes of these conditions are discussed in the following section.

In this section we investigated the effects of the fault and its geometry upon the surface displacements. These effects reduce to the relative dimensions of the fault to the lithosphere, both maximum and minimum depth, and to fault segments exterior to the lithosphere. Other parameters such as dip and asthenospheric thickness are relatively unimportant. In the next sections we will explore other conditions imposed near the fault, that is, the descending lithosphere and the physical process occurring along the fault.

4.5 Descending Lithosphere as a Boundary Condition

The analytic models represent a layered media rather than the complex structure of an island arc. The previous numerical models generally simulate a short descending lithosphere; thus, they are similar to the layered case. A deep descending lithosphere, on the other hand, characterizes many island arc systems such as Honshu and Tonga. This introduces a significant, new aspect to the problem: a long slab acting as a vertical stress guide within the mantle. In effect we are altering the boundary conditions along the fault. The oceanic interface is now partially tied to the higher viscosity mesosphere through the slab, thereby restricting the modes of relaxation.

To illustrate this point, Figure 4.9 compares two models dipping at 45 degrees. The maximum depth for the slab's penetration now represents the only change between the models. The long slab functions as a stress guide in the viscous mantle. It inhibits any motion of the lithosphere near the fault and emphasizes other modes of relaxation. The asymmetry which is noticeable during relaxation of the short slab does not occur for the long slab; instead, the stress guided by the descending lithosphere equalizes the deformations on either side of the fault plane and allows greater vertical uplift on the oceanic lithosphere.

Figure 4.9

Comparison of two different penetration depths for the descending lithosphere. The coarse element grid in Figure 4.1 simulates both cases. The inset shows the fault geometry for the two models; the dashed line represents the short slab. At time 0. the solution for both geometries is equivalent. For post-seismic deformations the vertical displacements progressively diverge. At time 6.3 the short slab is dashed; the solid line denotes the long, 600 km descending lithosphere. Notice the asymmetric, post-seismic deformations for the short slab as opposed to the more symmetric displacements of the long slab.

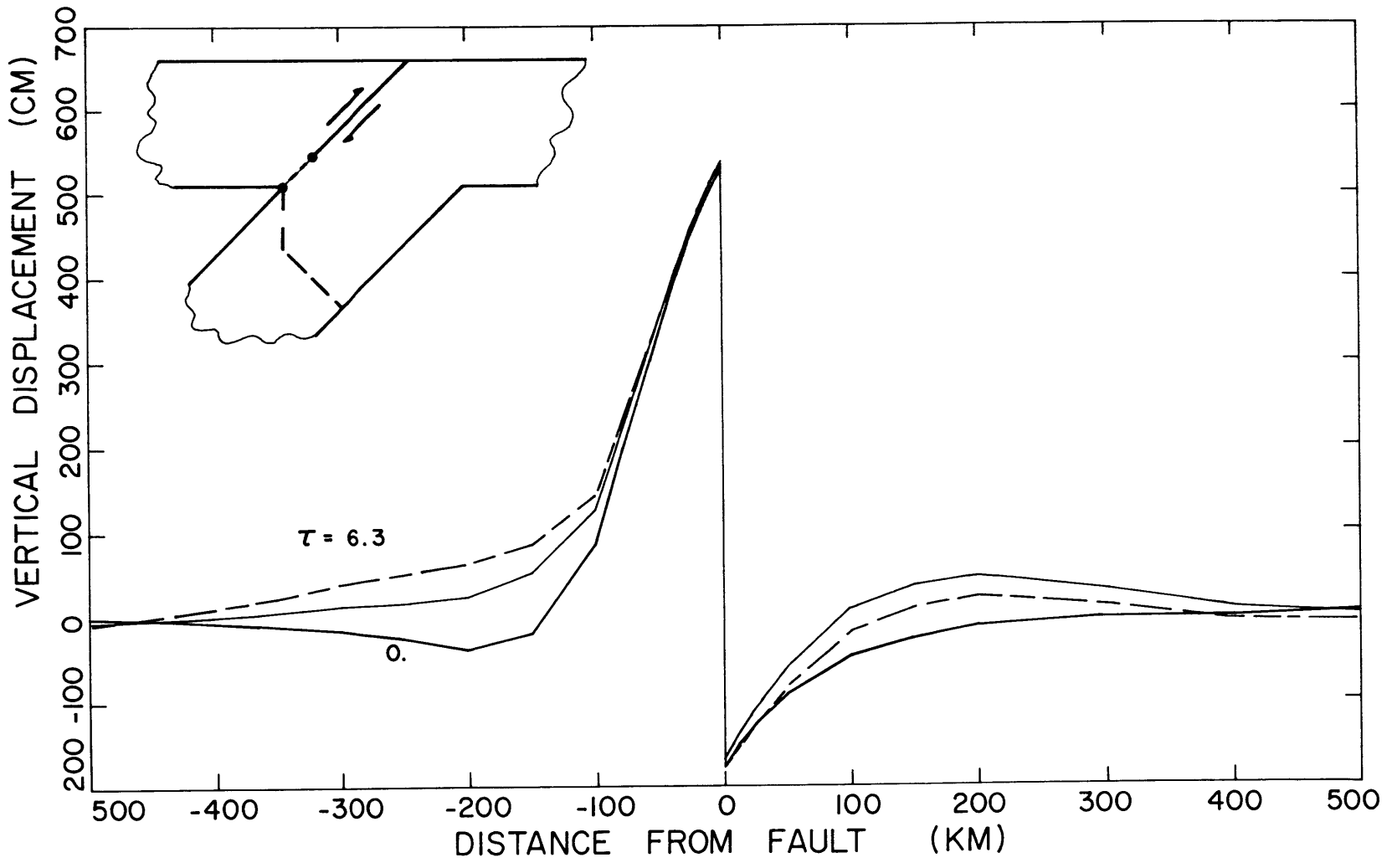


Fig. 4.9

This example emphasizes the importance given the proper geometry for an island arc regime. While the perturbations are less than altering the ratio of fault depth to lithospheric thickness, the maximum depth of the slab is important for inverting the data to a best fitting model. Consequently, every possible constraint on the problem must be introduced to define the dip and slab configuration.

4.6 Fault Interface: Stress drop or Dislocation Boundary Conditions

Our previous models have all imposed a displacement condition along the fault plane, thus creating a generalized Somigliana dislocation (Bilby and Eshelby, 1968). In the time domain this implies an initial step-function displacement profile and subsequent locking of the fault. Any further displacements along the interface such as creep are impossible; however, the stress released along the interface is free to vary with time. This introduces an implicit assumption for the faulting process: once the rupture occurs, the static friction retains its value prior to the earthquake. This does not exclude aftershocks at stress concentrations, rather it prevents any creep along a weakened fault zone.

At this point it is instructive to consider alternative representations for the boundary condition imposed

on the fault. Suppose we examine a likely physical process for faulting. The episodic behavior of earthquakes suggests a net decrease in the stress and potential energy along the fault interface. The stress reaccumulates again at some later time until it attains the yield or rupture strength of the fault zone. The fault is analogous to a crack, except the shear stress along the interface is not necessarily zero. Rather we can associate a stress drop with the faulting process (Berg, 1968). There exists no a priori reason that the fault plane corresponds to the plane of maximum shear for the initial stress, only that the shear stress along the plane decrease during the rupture. Assuming a process of failure occurs along the fault plane, the earthquake may be visualized as an initial value problem involving the propagation of the rupture along the plane. The criteria for rupture, from one point of view, rests upon the stress near the fault tip exceeding a critical value (i.e. Griffith, 1921; Barenblatt, 1959). Here we encounter a highly complex phenomena depending on the stress and material inhomogeneities within the media.

Our concern is the boundary value problem that results after the rupture. Both a displacement discontinuity and a stress drop occur along the fault zone. For the quasi-static problem either of these provides a representation for the fault (Bilby and Eshelby, 1968), but each implies

different behavior in time. The dislocation, as we have seen, specifies the displacement and allows the stress release to vary in time. Alternatively, the fault zone may be weakened and only slowly recover its former strength. This extreme specifies the stress release as an imposed condition after the earthquake and allows creep along the fault to compensate for relaxation within the asthenosphere.

To model an imposed stress release or stress drop along the fault, a couple is applied to the adjacent nodes at the fault interface. On one face the stress could be $+C$ and directed along the plane of the fault; for the node located on the opposing face the stress becomes $-C$ (see section 2.5). Since the two opposing nodes are constrained to the same plane, this introduces a couple analogous to the stress release or stress drop of an earthquake. The reaction of the medium gives a net double couple without any mathematical tricks.

The vertical displacement for the two alternate models, constant stress release or constant displacement with time, is illustrated in Figure 4.10a,b. Unlike the previous models, the fault extends fully through the lithosphere and terminates within the asthenosphere. The stress condition or dislocation linearly decays over the last 25 km of the fault. These boundary conditions now give

Figure 4.10a,b

Vertical displacements for two models, one with a constant dislocation extending into the asthenosphere, the other having a constant stress release. The finite element grid in Figure 4.1 uses a long, 600 km descending lithosphere. The five dimensionless times are 0. (solid line), .63, 3.2, 6.3, and 12.6. The fault geometry conforms to the diagram in the upper left corner where the slip initially has linear decay over the dashed segment. For later times this dashed segment is free to slip as it responds to mantle relaxation.

(a) A constant 10 m dislocation along the arrows. As the asthenosphere relaxes, further forward slip along the lower fault segments (dashed) now allows continued uplift over the fault zone.

(b) A constant stress release denoted by the arrows. The stress at the fault interface normalizes the vertical displacements. Since the continental lithosphere is free to slip in response to the constant stress release, the deformations continue increasing as the restoring force decreases during mantle relaxation.

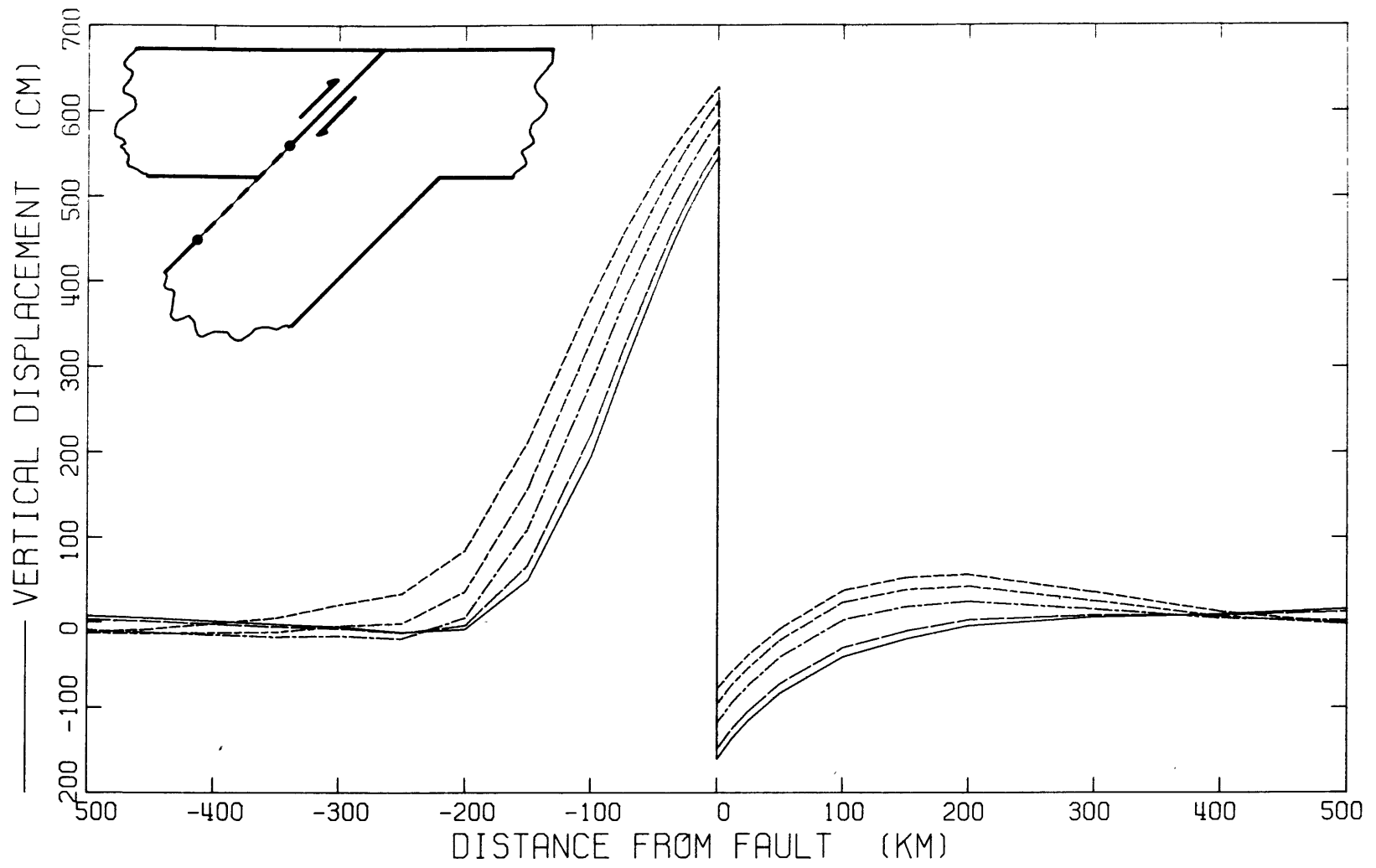


Fig. 4.10a

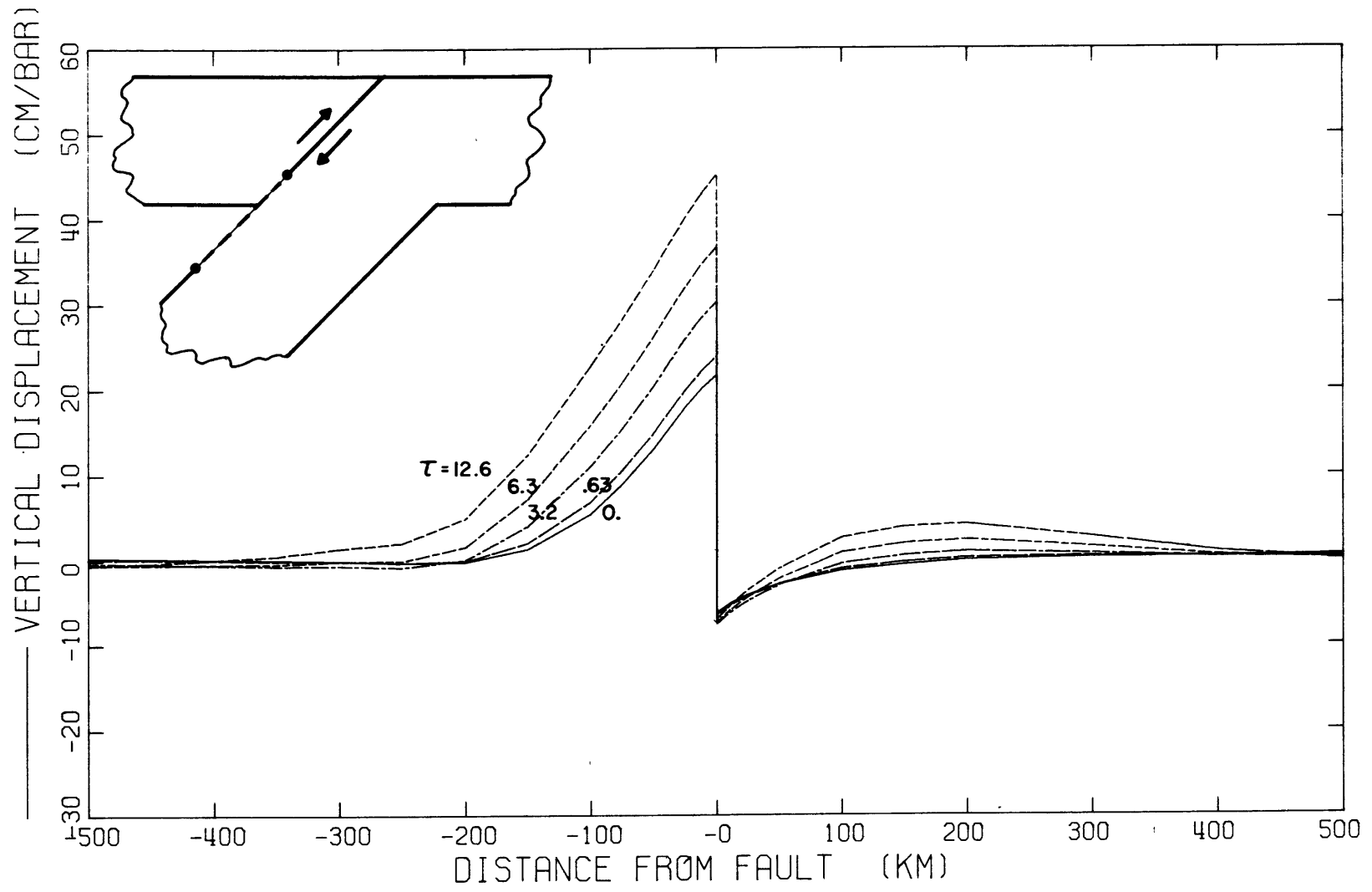


Fig. 4.10b

dramatically different results.

A constant dislocation allows stress relaxation within the asthenosphere: the vertical displacements tend to approach a limiting value. The wavelength of the spacial harmonics also increases as the relaxation proceeds within the mantle. On the other hand, a constant stress drop prevents any stress relaxation within the mantle. Since the fault interface along the elastic lithosphere is free to slip, only the viscoelastic asthenosphere resists the stress drop. Consequently, the fault creeps with the asthenosphere until the flexure rigidity of the lithosphere and the gravitational restoring force balances the stress drop. These deformations continue growing long after specifying the stress drop. The results are then analogous to the first order theory in section 3.2.

The vertical surface deformations are not the only indication for time-dependent variations nor the only diagnostic to the physical process occurring along the fault. Both the horizontal surface deformations and the stress within the media vary for each problem. The comparison of these two fault conditions presents an opportunity to introduce these other indicators. Neither the stress nor the horizontal displacements are as sensitive to the fault, yet the effects of each may exist in the observations: aftershocks and other earthquakes may show the state of

stress, while the geodetic measurements give the relative horizontal displacements. To evaluate their significance, the same finite element models give these displacements and stresses.

The horizontal displacements for the two specified boundary conditions, stress drop or dislocation, are reproduced in Figures 4.11a,b. Although some deviations occur between the two models, they are not as large as the vertical displacements. It is the horizontal gradient that provides the usable information. Unlike the vertical deformation, the constant dislocation model now gives similar variations with time for this measure. Even these deformations when referred to a baseline far from the fault are not much greater than one meter. Moreover, the corresponding geodetic triangulations are more difficult and inaccurate than elevation. They only give the horizontal displacements referred to a baseline, an important point for strike-slip faults where the largest components are horizontal strains. Throughout the bulk of this paper, then, we will ignore the relative horizontal displacements and concentrate instead on the vertical deformations.

The stress state within the media shows small but distinctive variations with time between the models. Figures 4.12a,b compare our previous models, one with its stress drop specified and the other with a constant dislocation. Each line corresponds to an individual time. Here

Figure 4.11a,b

Horizontal displacements using the two different boundary conditions on the fault, constant dislocation or constant stress release. The problem is identical to Figure 4.10.

(a) A constant 10 m dislocation. The gradient of the horizontal displacements contains the important geophysical measurement.

(b) A constant stress release on the fault. The small change in the gradient between the models and difficult geophysical measurements suggest horizontal displacements are not as suitable an indicator unless measured across the fault.

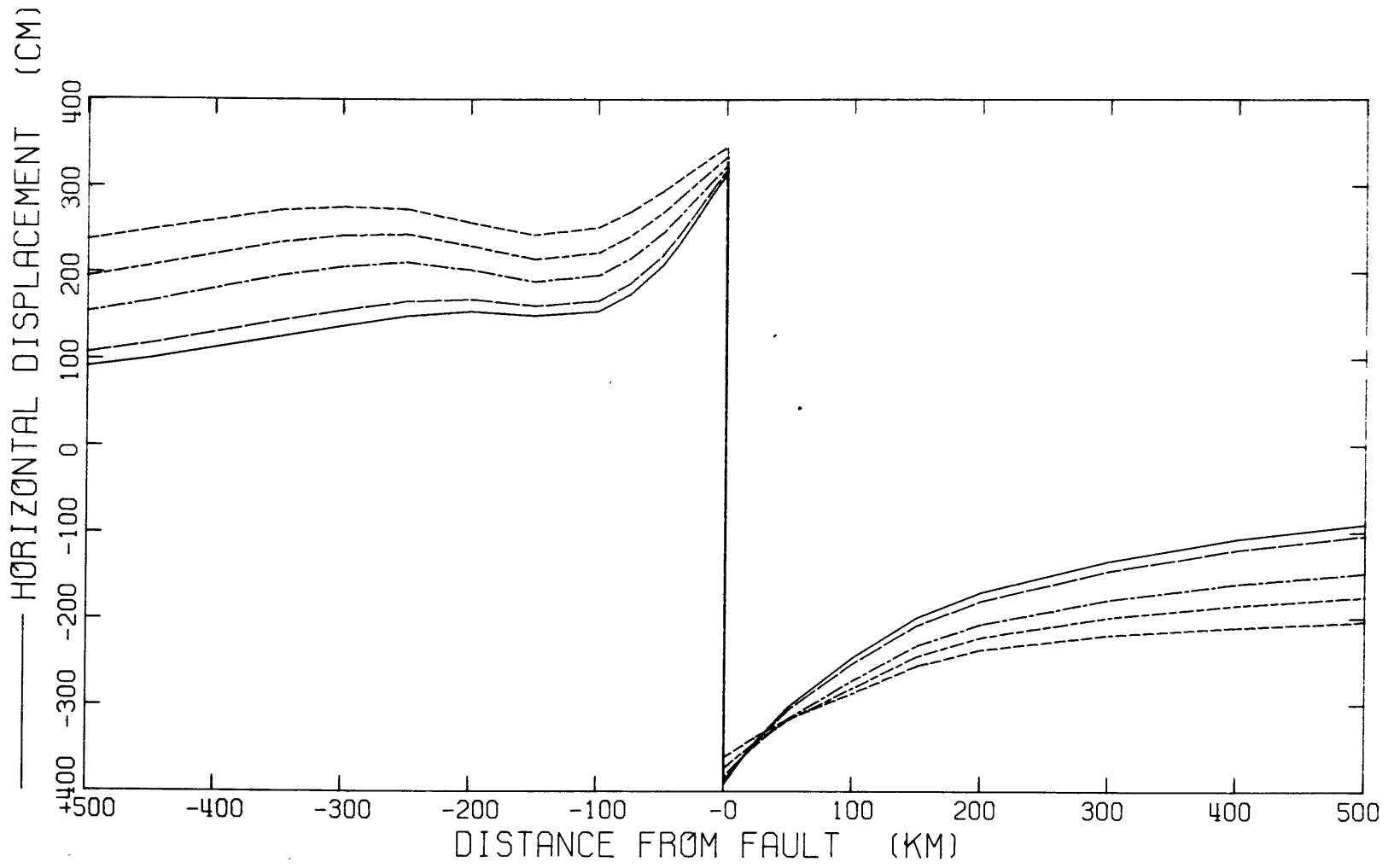


Fig. 4.11a

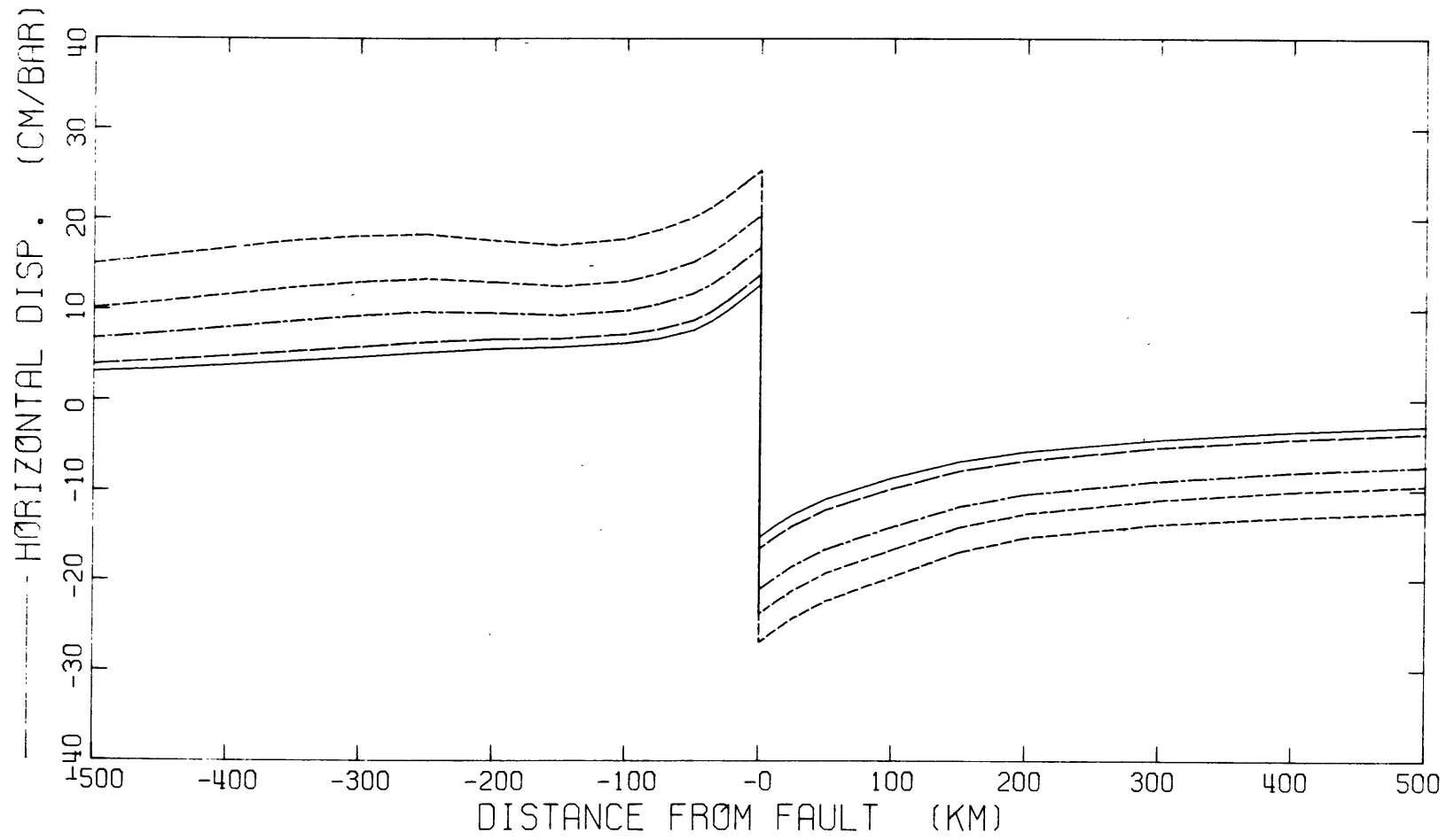


Fig. 4.11b

Figure 4.12a,b

Maximum shear stress and direction of the principle compressive stress for the two fault boundary conditions, a constant dislocation or a constant stress release. The parameters are those of Figure 4.10. Each line segment represents a separate time at a specific element. Unfortunately, the dashing for the lines is often obscure. The length of each line denotes the magnitude of the maximum shear stress in bars on a logarithmic scale in the lower right. The direction indicates the orientation of the maximum compressive stress at each time. As before the dimensionless times are 0. (solid line), .63, 3.2, 6.3, and 12.6.

(a) Constant 10 m dislocation. Stress relaxation in the asthenosphere allows relaxation of the shear stress and rotations of the principle axes. The maximum shear stress generally decreases near the fault: it tends towards the prior initial stress

(b) Constant stress release on the fault normalized to one bar. This condition prevents complete stress relaxation in the asthenosphere; thus, the shear stress remains relatively constant throughout the region.

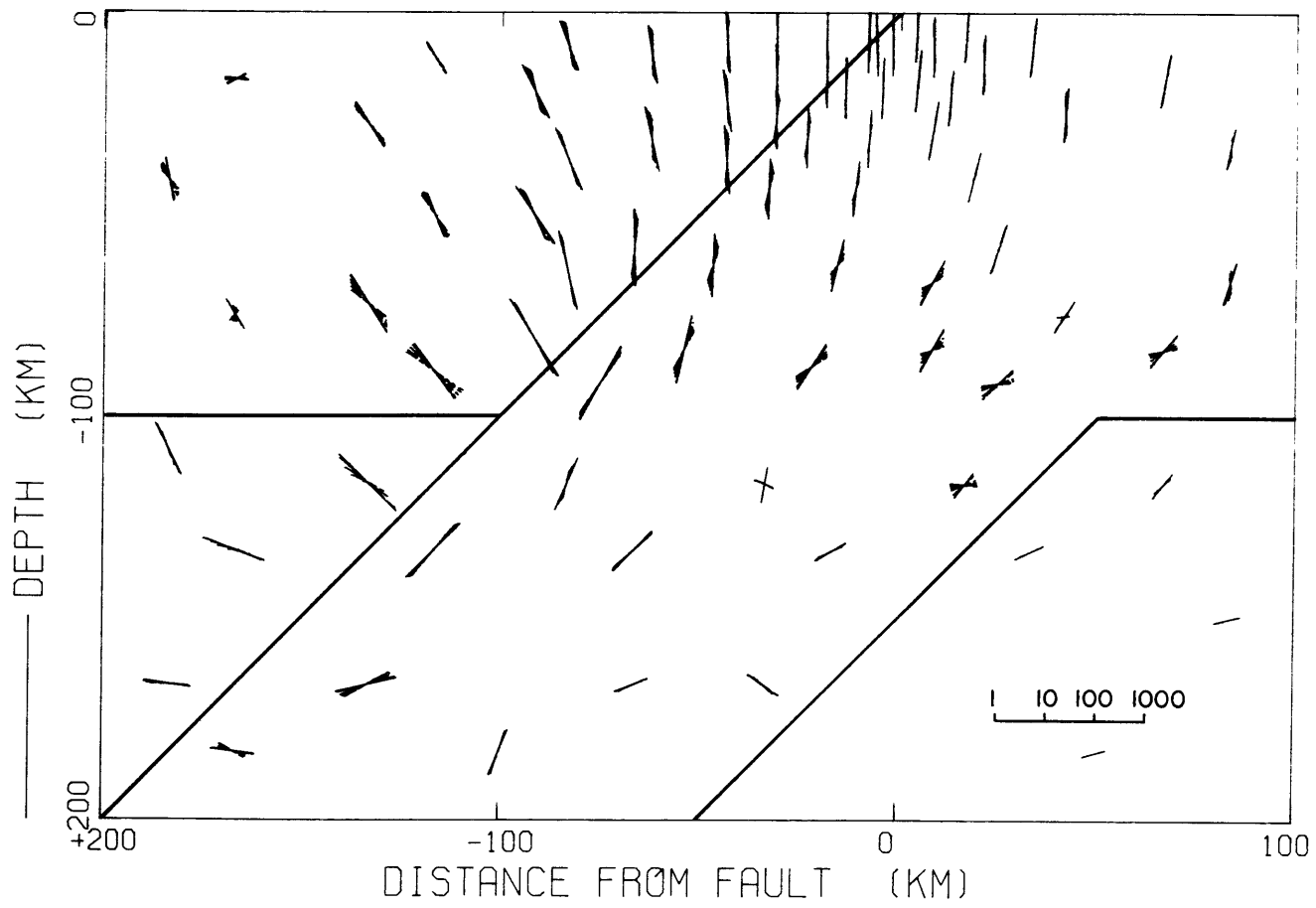


Fig. 4.12a

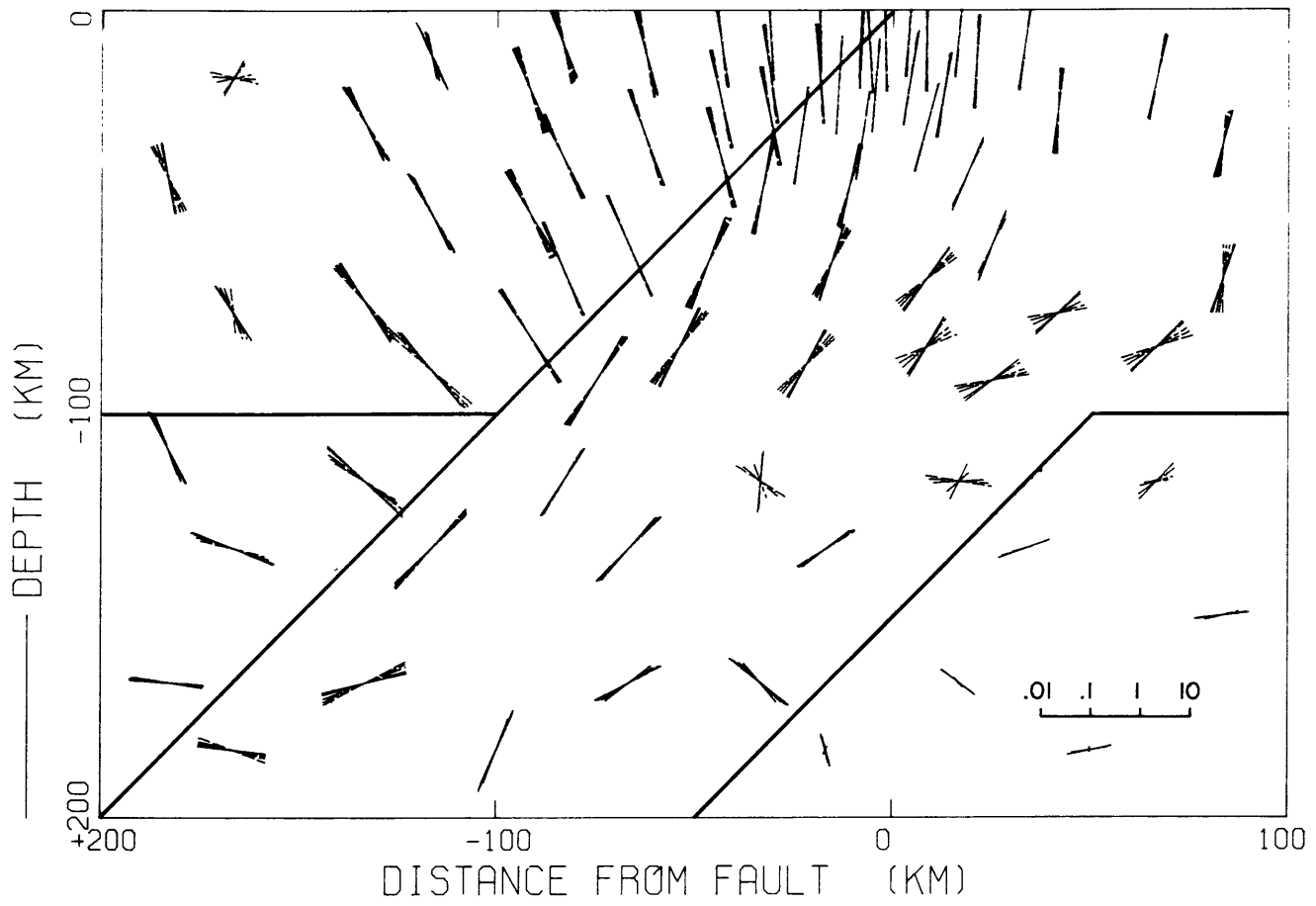


Fig. 4.12b

the directions of the lines correspond to the direction of the maximum compressive stress, while the length denotes the logarithm of the maximum shear stress in bars. The diagram only displays a segment of the problem enclosing the fault. Constant strain triangles or isoparametric quadrilaterals are used for the elements; consequently, the individual elements represent an average stress over the region. Comparison of the two boundary conditions shown in the models now yields some obvious distinctions.

As we first conjectured, a constant stress drop produces relatively constant stress near the fault and for adjacent regions within the asthenosphere. Remembering that we are observing the change in stress caused by the 'earthquake', the stress perturbations near the surface manifest the stress release along the fault: the plane of maximum shear stress corresponds to the fault plane. Thus tension or minimum principal stress is approximately horizontal, opposite the prestressing according to our initial assumption. Near the fault the stress varies little in time. But within the subducting lithosphere and the island arc lithosphere, the directions rotate and small magnitude changes occur far from the fault. Within the asthenosphere only partial relaxation is possible. Overall the behavior for a constant stress drop is as expected: large variations in the vertical displacements and small changes in the stress field.

The dislocation specified on the fault also agrees with our previous expectations. We observe significant rotations and stress relaxation within both the lithosphere and asthenosphere. In some cases the stress increases rather than decreases. Within the asthenosphere the relaxation is virtually complete; in the lithosphere the stress pattern easily varies by a factor of two.

In Figure 4.13 the magnitude of the maximum shear stress for a few representative regions is superimposed on the previous diagram for the shear stress resulting from a constant dislocation. Throughout the subducting lithosphere, the stress exponentially decays towards a new non-zero value corresponding to a new equilibrium for a relaxed asthenosphere. The asthenosphere, of course, decays towards zero. In other regions such as in the island arc lithosphere, relatively constant or even slightly increasing shear stress spans large portions of the domain. These variations of the released shear stress are significant; their possible influence on strain accumulation and earthquakes may be important. In addition, if we examine regions far from the fault, evidence of stress propagation should be apparent in these variations.

When all the possible modes of relaxation are considered, stress propagation per se does not manifest any distinct behavior near the fault. As we have seen, the

Figure 4.13

Profiles of maximum shear stress σ in bars versus non-dimensional time τ within the lithosphere for a 10 m fault dislocation. The stresses are those from Figure 4.12a and correspond to the problem in Figure 4.10a. The inserts plot the maximum shear stress at representative elements. Unlike the previous logarithmic scale, these plots emphasize the significant change in magnitude that accompanies mantle stress relaxation. Recalling that this represents the stress release following the earthquake, the stress returns to its initial prestress prior to the earthquake.

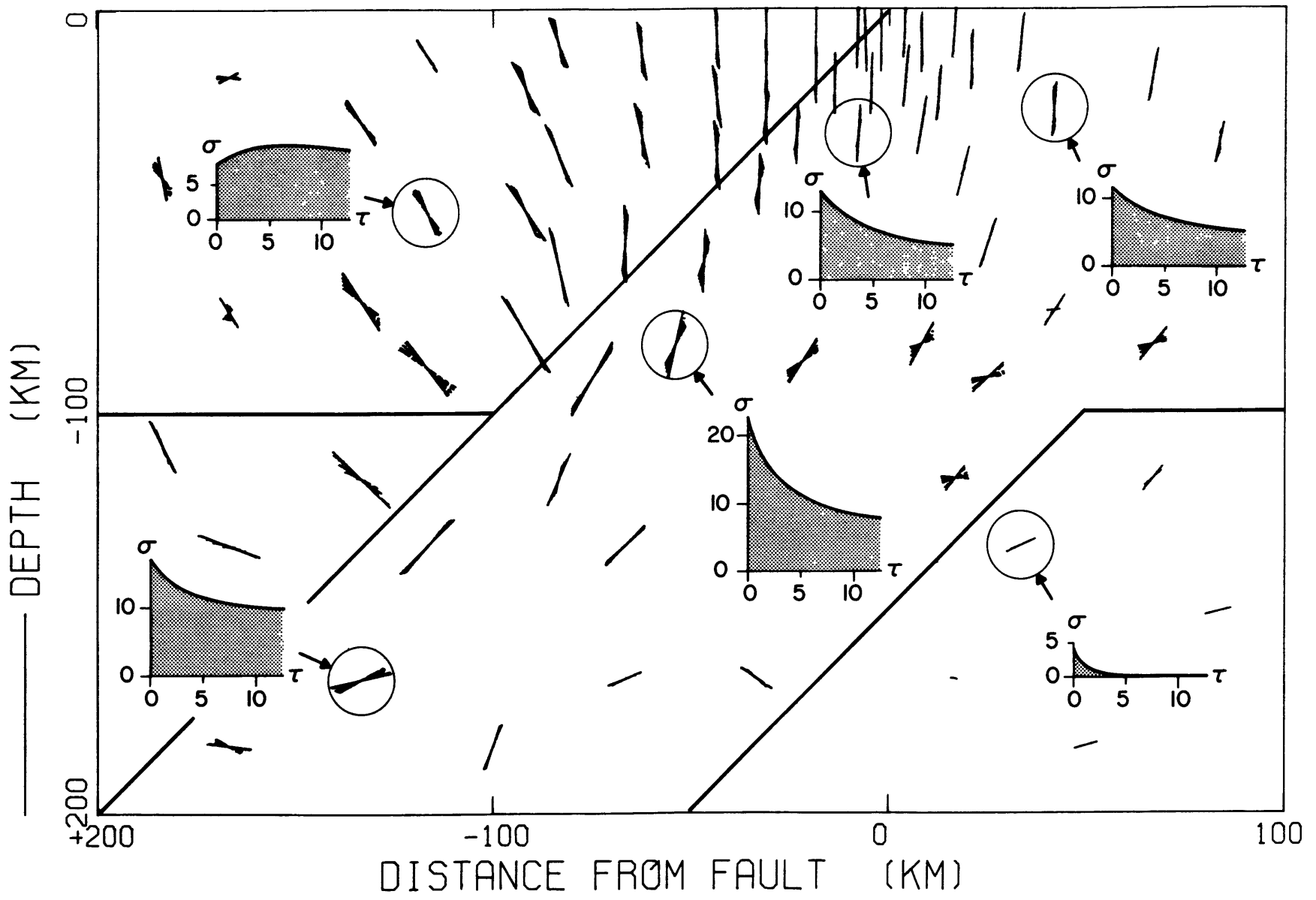


Fig. 4.13

stress release only gradually decays. Farther away, however, the complexities of the dislocation are not as significant. Figure 4.14 presents examples from the previous model that satisfy this criterion. As we proceed from the fault, clear indications of stress propagation become evident: the curves show a break or change in slope characteristics. If we plot the arrival of the front versus the distance from the fault, the arrivals fall within the band predicted by the simple first order model for stress propagation (see section 3.4). Figure 4.15 illustrates this plot. Since both our simple first-order analysis and the finite element model depend on linear viscoelasticity, this result should hold true. We see then that stress propagation does occur, albeit insignificantly for most circumstances. It is overwhelmed near the fault by more complex relaxation modes.

The two models that have been discussed here, constant stress drop and constant dislocation, constitute the best approximation to the first order theory: they allow slip along the whole fault boundary separating the island arc and the subducting oceanic lithospheres. Perhaps a more realistic representation limits the constant stress drop and the dislocation to the lithospheric interface. Figures 4.16a,b depict two models, one with a constant dislocation and the other with a constant stress drop when the fault does not fully extend through the

Figure 4.14

Profiles of maximum shear stress σ in bars versus nondimensional time τ which suggest stress propagation far from the slab. The problem uses the same model as Figures 4.13, 4.12a, and 4.10a: (a 10 m dislocation on the fault). The notation conforms to the previous Figure, 4.13. The distinct change in the shear stress with time suggests stress propagation; the stress first decays then increases or vice versa. Near the fault complex relaxation modes overwhelm simple stress propagation.

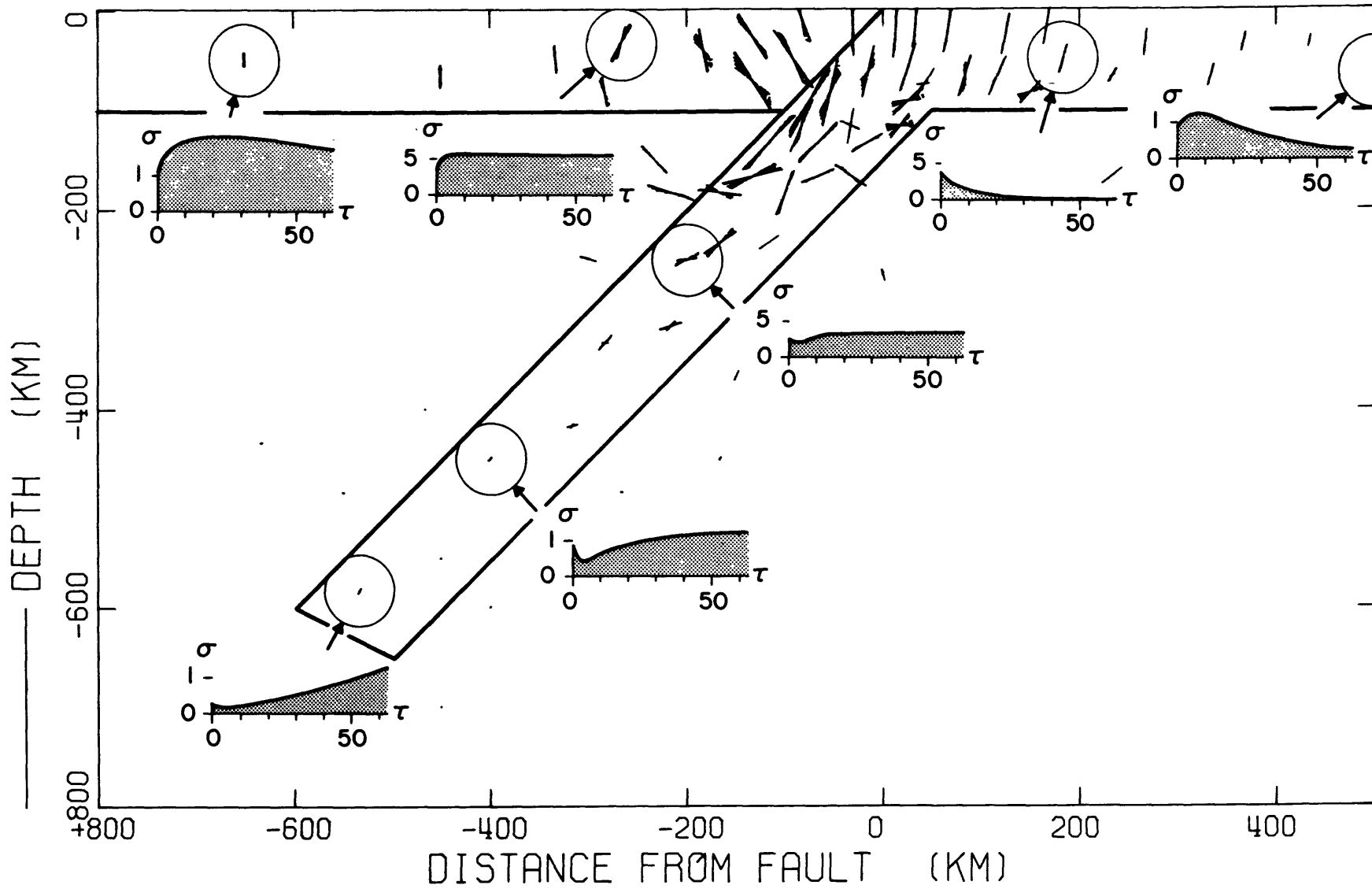


Fig. 4.14

Figure 4.15

Arrival times of the diffusive stress front plotted on the first-order model of stress propagation, Figure 3.9. Sketched on the graph of distance versus time are the first order bounds using the theory in section 3.5. The arrival times estimated from Figure 4.14 fall within the bounds.

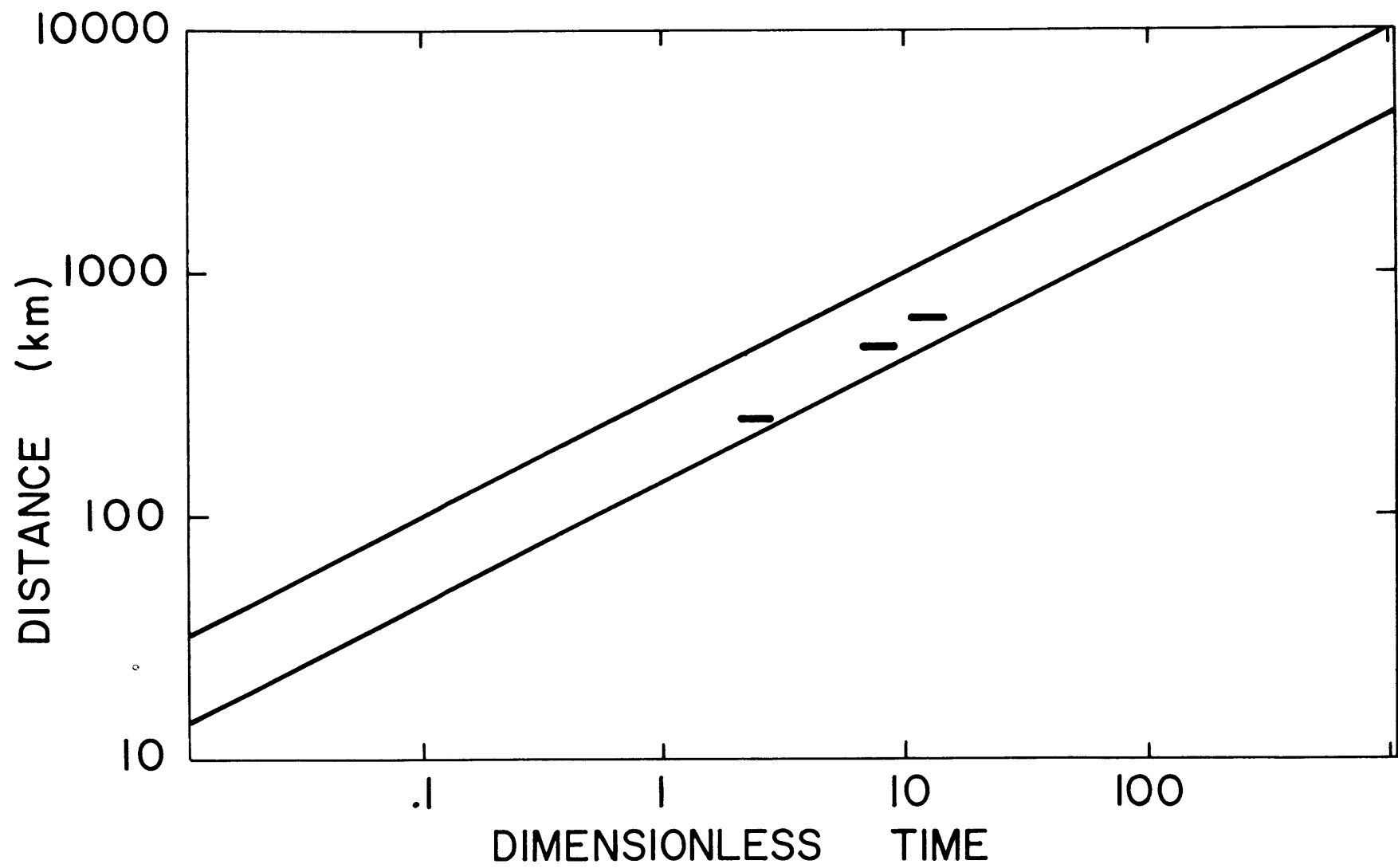


Fig. 4.15

Figure 4.16a,b

Comparison of two models with different boundary conditions, a constant dislocation or a constant stress release, when the fault terminates within the lithosphere. The models are identical to the previous comparison in Figure 4.10 except for this different fault geometry. But the results are quite different when the fault is partially constrained in the lithosphere.

(a) A constant 10 m dislocation when the slip decays linearly to the base of the lithosphere. This model is similar to 4.8a, 4.6a, or 4.4, except the descending lithosphere now extends to 600 km depth.

(b) A constant stress release normalized to one bar on the fault. The vertical offset and displacements continue near the fault. Uplift occurs as before in Figure 4.10b, except not as extreme. The deformations are not symmetric any longer about the fault; post-seismic subsidence occurs on the oceanic plate in response to the fault creep.

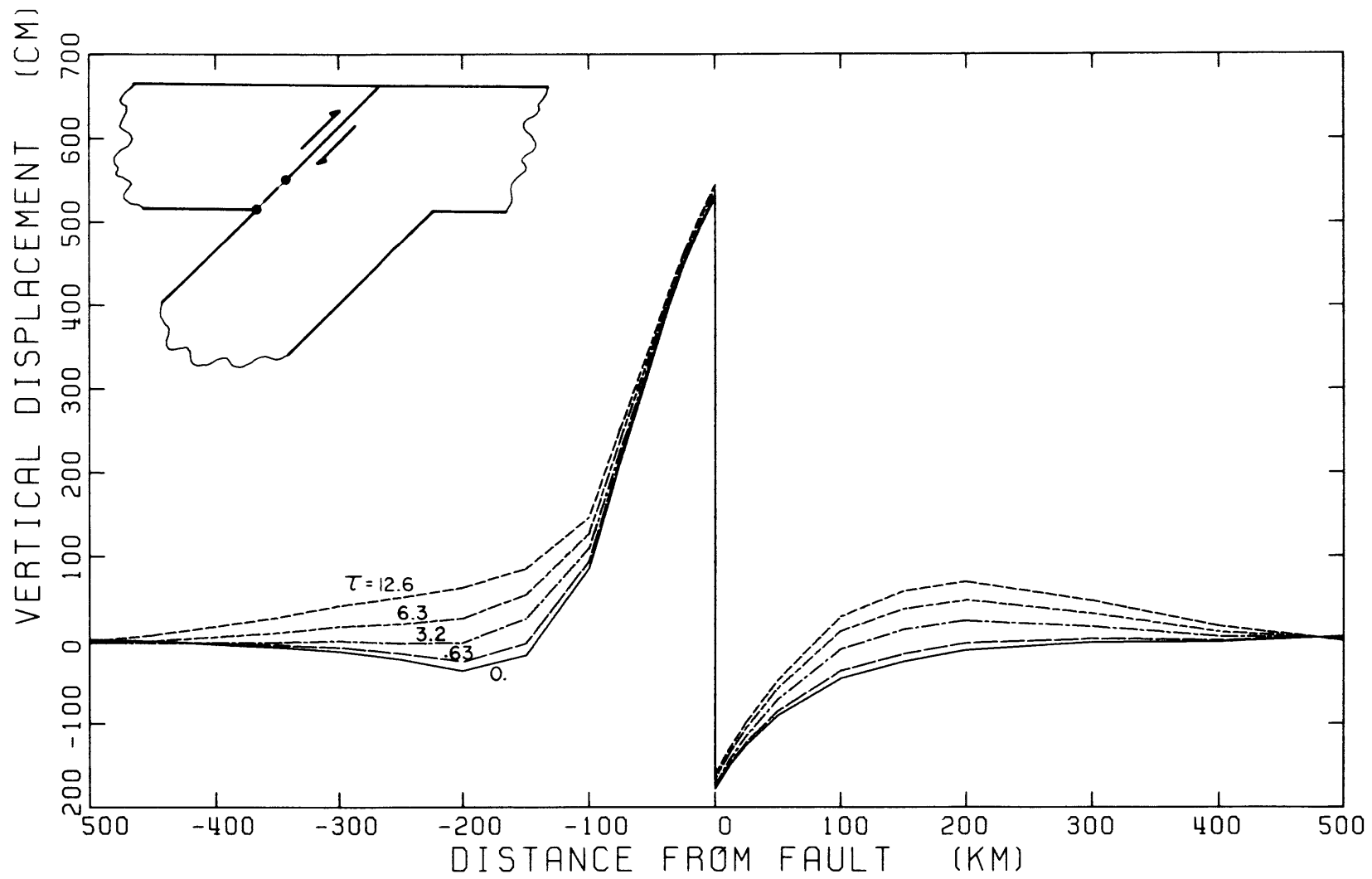


Fig. 4.16a

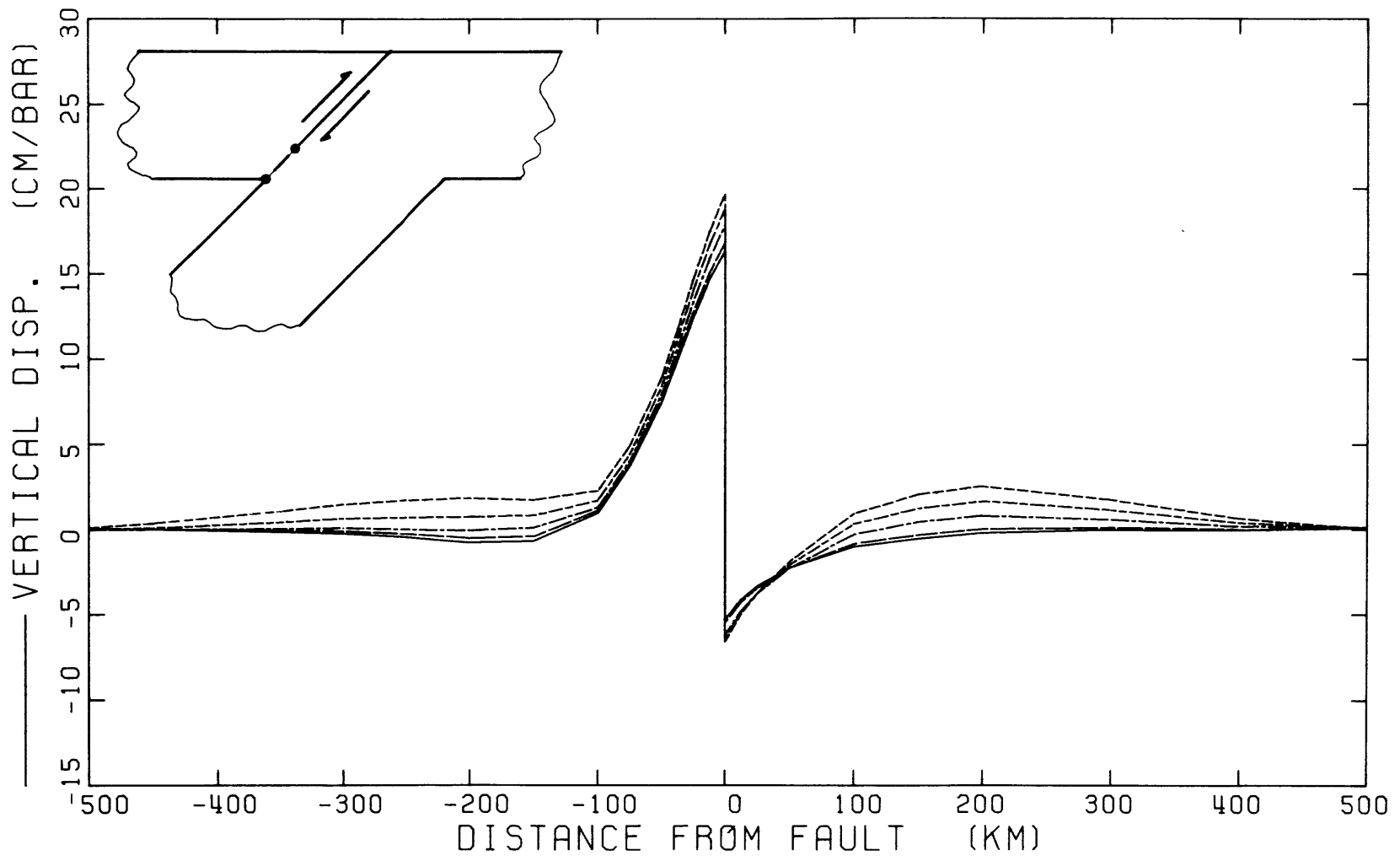


Fig. 4.16b

lithosphere. This partially locked condition conforms to the models in section 4.4. The distinction between the results is now more obscure, although present.

The constant stress drop generates forward creep along the fault, thus increasing the total slip as the asthenosphere relaxes. The major contribution to the vertical deformation occurs at the island arc since the subducting slab acts as a stress guide and restricts the modes of deformation for the oceanic lithosphere. At greater distances from the fault, say 200 km, the relaxation occurs over a wider area for the specified stress drop. Similar behavior is possible, however, by increasing the constant dislocation with depth for a specified slip model. The horizontal displacements give similar variations as Figures 4.17a,b demonstrate. The differences are also less distinct; the largest change is found near the fault zone. The same pattern holds for the stress distribution given by Figures 4.18a,b; the differences between the two specified boundary conditions on the fault are relatively insignificant. Locking the fault at its tip allows only limited creep along the fault. The geodetic data, then, holds the greatest promise as an indicator of the fault process. Still, to distinguish between these alternative representations, it is essential to constrain the models with geodetic data near the fault zone.

Figure 4.17a,b

Horizontal displacements for the previous model in Figure 4.16 using the two boundary conditions, a constant 10 m dislocation or a constant stress release following the earthquake. The fault only extends to the base of the lithosphere. The same five dimensionless times are shown: 0. (solid line), .63, 3.2, 6.3, and 12.6. When referred to a baseline far from the fault, the horizontal displacements differ only slightly between the two cases and their post-seismic deformations.

(a) A constant 10 m dislocation.

(b) A constant stress release normalized to one bar.

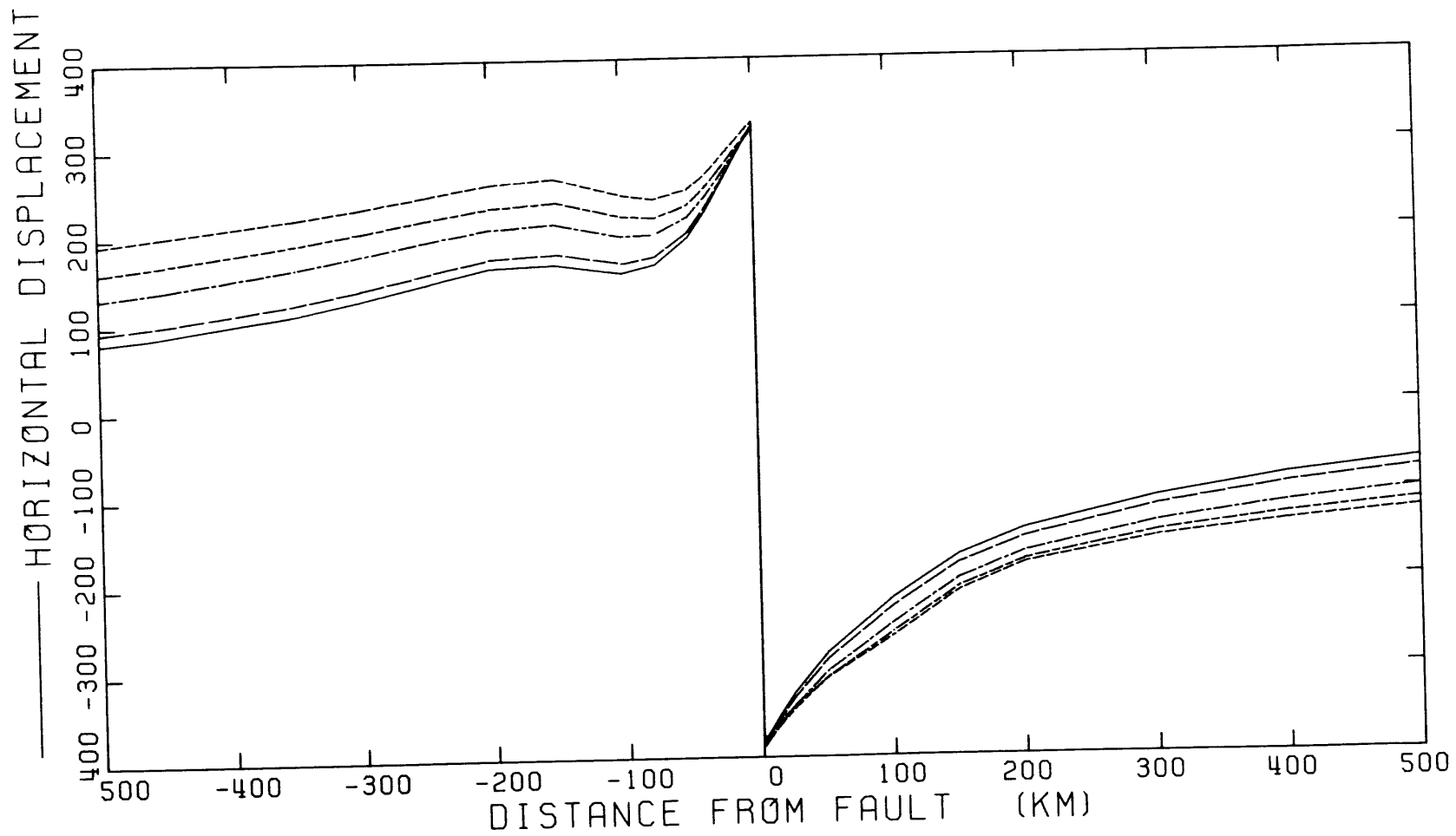


Fig. 4.17a

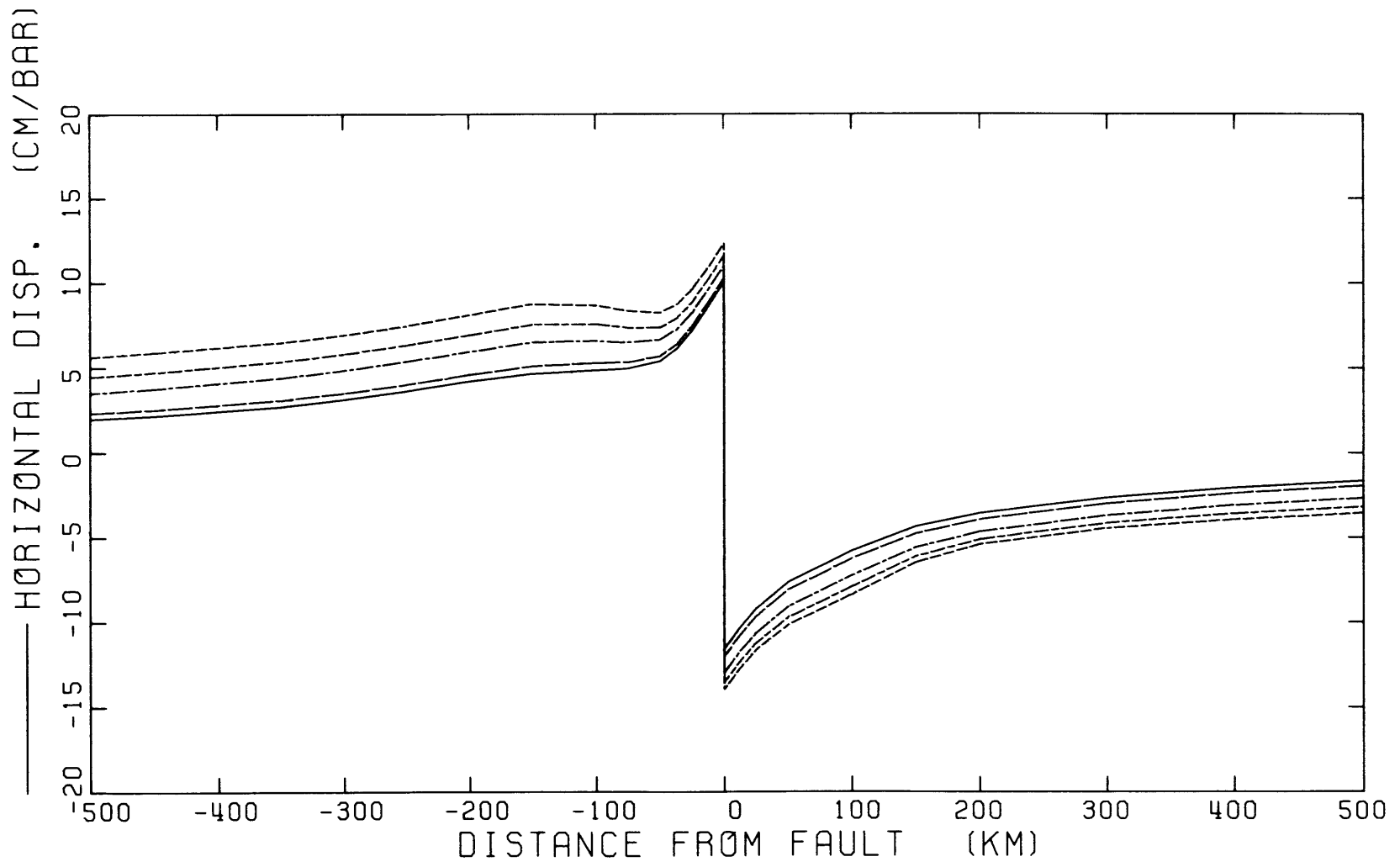


Fig. 4.17b

Figure 4.18a,b

Maximum shear stress and the direction of the maximum compressive stress for the two boundary conditions, a constant 10 m dislocation or a constant stress release. The notation duplicates Figure 4.12.

(a) A constant 10 m dislocation. Both stress relaxation and rotations occur in the lithosphere. The changes are smaller with time than if the fault extends into the asthenosphere; however, they still approach 50%.

(b) A constant stress release normalized to one bar. Locking the fault at the base of the lithosphere now allows stress relaxation in the asthenosphere unlike Figure 4.12b. Thus, both rotations and magnitude variations occur in the lithosphere.

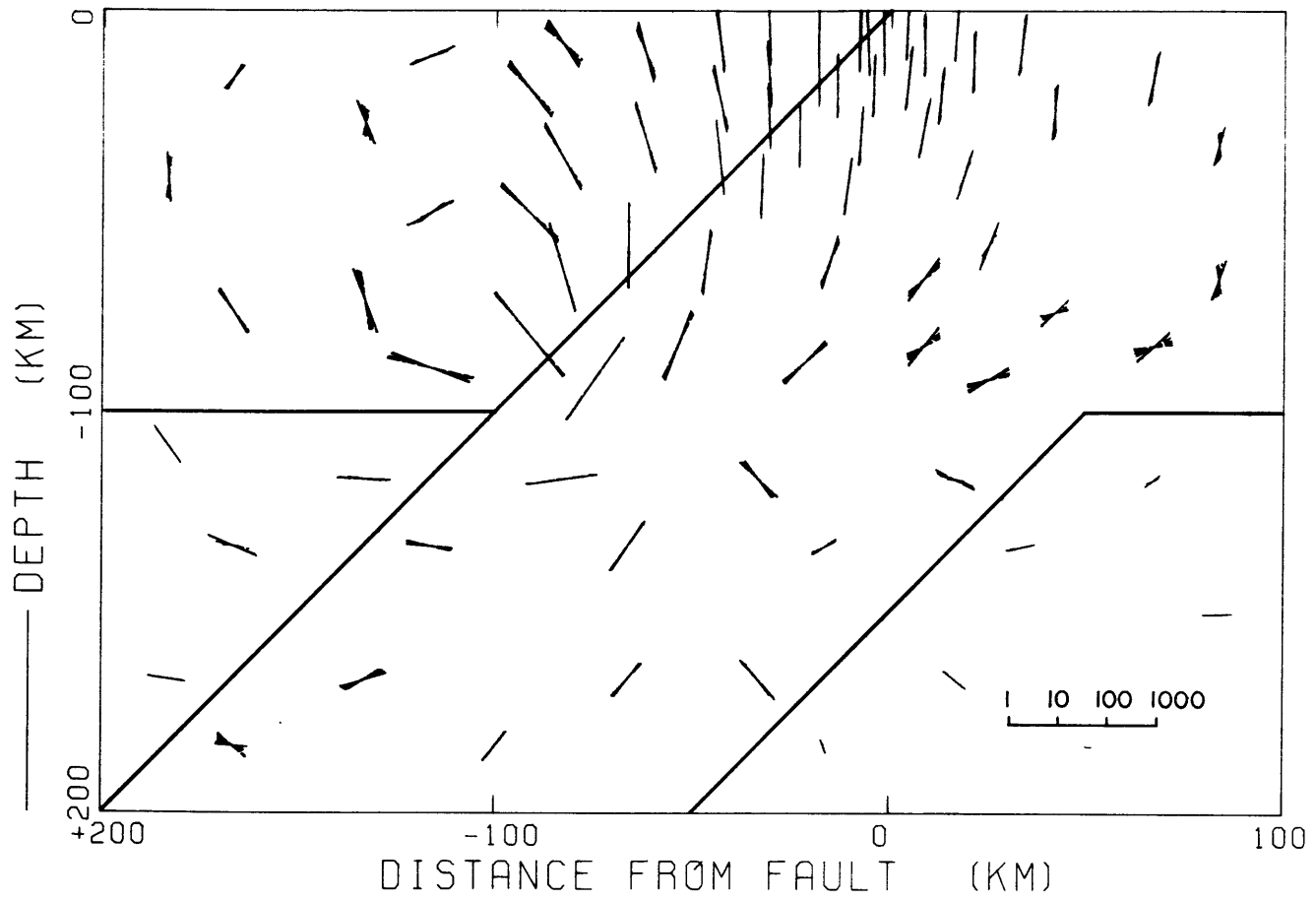


Fig. 4.18a

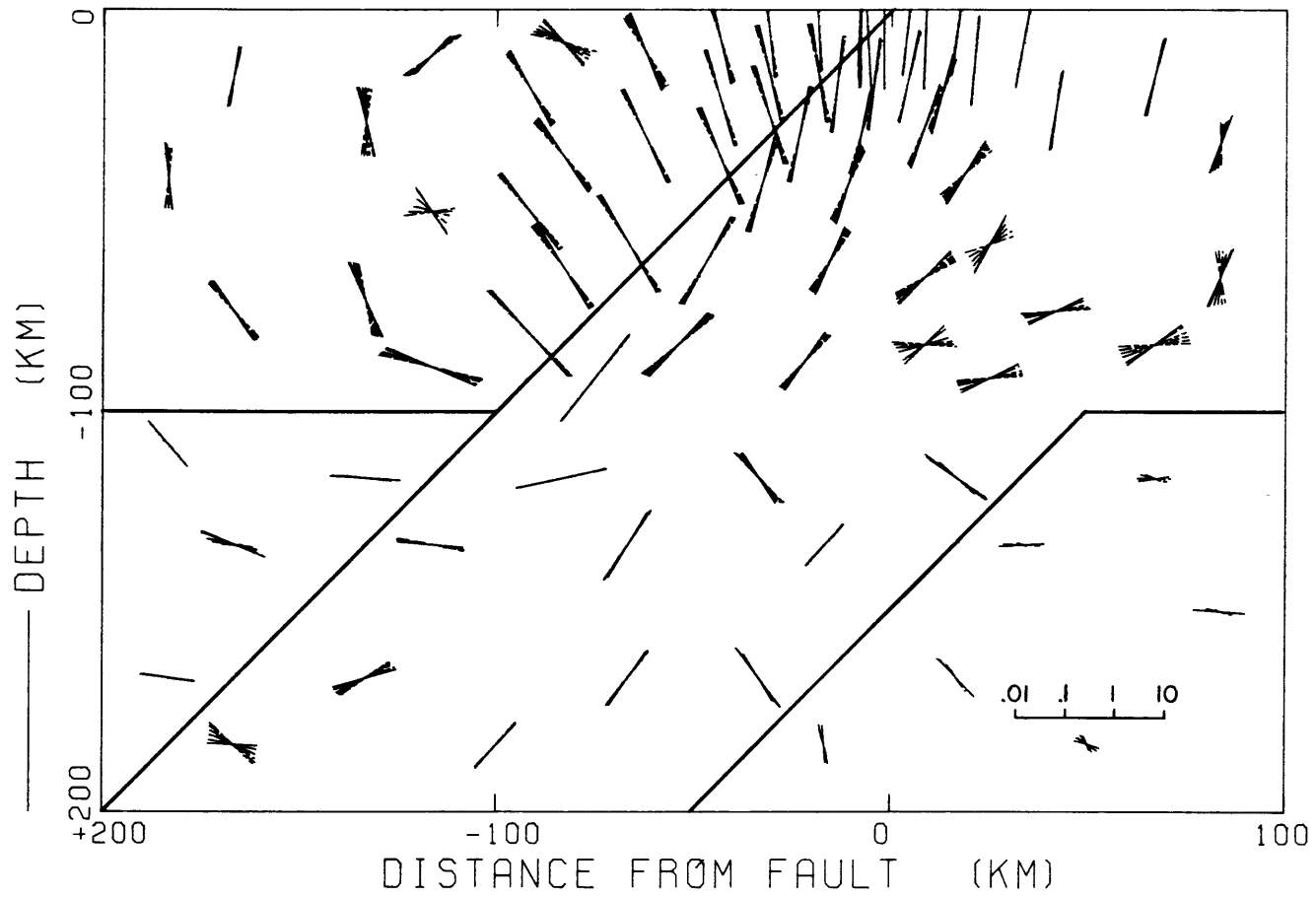


Fig. 4.18b

The boundary condition specified on the fault interface has then a substantial influence on the surface deformations and the interior stress patterns when the fault extends through to the asthenosphere. Our simple models for viscoelastic behavior did suggest the correct response: a constant stress drop produces rapidly changing displacements and constant interior stress; a constant dislocation implies limited displacements and stress changes, both decaying to asymptotic values.

4.7 Initial Stress State Within the Lithosphere

An earthquake introduces a perturbation into the existing stress field, where the faulting represents a partial release of the preexisting strain field. So far nothing has been said of this initial strain field. To treat this problem, we must examine the probable mechanisms behind plate tectonics and the stresses they introduce. In a previous work this problem has been extensively treated from the perspective of the descending lithosphere (Smith, 1971; Smith and Toksöz, 1972). In this section the problem will only be summarized: we will confirm the previous models suggesting both that the rheology of the mantle and lithosphere and that the density anomalies due to the colder descending lithosphere and phase changes control the stress distribution. The

shallow regime will be examined in order to compare the stresses introduced by the earthquake and the initial pre-stress from the density anomalies.

The density anomalies within the descending lithosphere and the rheology of the system exert a profound influence on the overall stress pattern within the lithosphere. It was Elsasser (1969) who first proposed that the descending lithosphere acts as a 'stress guide': the viscous mantle prevents the accumulation of strain within itself; instead, the stress concentrates within the lithosphere. Isacks and Molnar (1969, 1971) found ample evidence in the focal mechanisms to support this belief. The denser lithosphere introduces a relatively constant stress which is guided within the slab. Smith (1971) examines the effects of potential density anomalies: thermal density anomalies due to the colder lithosphere (Toksöz et al., 1971; McKenzie, 1969), and density anomalies caused by the elevation of the phase boundaries (Toksöz et al., 1971; Smith, 1971). Each contribution, thermal and phase transformation, produces a distinct density and stress pattern within the lithosphere. Together they yield a viable explanation for the direction of the principle stresses observed from focal mechanism solutions (Smith, 1971; Smith and Toksöz, 1972). In addition, the detailed stress models verify that a one-dimensional model along the slab gives reasonable behavior for the intermediate and deep stress patterns.

These models, however, introduce approximations for both the boundary conditions and the solution strategy. The fault was taken as locked; thus, all the stress is transmitted directly through the region and no relaxation occurs along the thrust fault. The solution technique also involves significant approximations. The problem is taken as quasi-static, steady-state viscoelasticity. To calculate a solution using a modified integral form of the finite difference method, the material constants are estimated assuming a load time applied to the medium (Smith, 1971). This is an approximation to the flow behavior. Using the finite element scheme outlined in this thesis, the stresses are exact for a specific time within the numerical accuracy of the element approximation (see section 2.6). In addition, a slip boundary along the fault interface may represent the long term behavior for the fault. The effect of these boundary conditions is now resolvable. It is appropriate, then, to calculate a new model using a viscoelastic medium and finite elements. Later we can compare the stresses to the focal mechanisms for the Kuril islands.

The finite element model chosen is identical to the previous models originating from Figure 4.1: a 100 km lithosphere together with a 650 km deep slab. The fault imposes a free slip condition along the interface; other

boundary conditions such as a locked fault do not materially effect the result. To properly model the stresses generated by the internal body forces, we examine the stress after a long time interval has elapsed since loading. The stress then approaches an asymptotic value and direction. In this case the time interval is 3×10^5 when nondimensionalized by the viscosity of the asthenosphere. At the boundary for the oceanic lithosphere, one kilobar compression represents the ridge driving force. The models also include the effect of gravity. The resulting stresses are insensitive to both the boundary conditions and the fault interface; instead, our previous conclusions hold true: the stress distribution depends on the relative viscosity contrasts within the mantle and the distribution of density anomalies within the slab (Smith, 1971; Smith and Toksöz, 1972).

Figure 4.19 depicts a representative model. The density anomalies within the slab correspond to approximately $.1 \text{ gm/cm}^3$ and conform to the thermal anomaly for a slab descending at 8 cm/yr. (Figure 12, Toksöz, et al., 1973). For depths greater than 400 km, the maximum compressive stress remains down-dip and the magnitude of the maximum shear stress increases to 1800 bars at 600 km depth. Within the region depicted in the diagram, the maximum shear stress averages 500 bars in the

Figure 4.19

Magnitude of the maximum shear stresses and direction of principle compressive stresses caused by thermal density anomalies. The density anomalies duplicate Figure 12 in Toksöz, et al. (1973): approximately $.1 \text{ gm/cm}^3$ in the descending lithosphere. The model uses the coarse element mesh in Figure 4.1 when free slip is allowed on the fault. In addition, at the exterior boundary to the oceanic lithosphere, 1 kbar of compressive stress simulates a spreading ridge. These two conditions, the fault boundary and the spreading ridge, do not materially effect the results. The model calculations assume the body forces within the descending lithosphere are introduced at time zero, the stresses then relax to equilibrium assuming linearity holds. By nondimensional time 3×10^5 the equilibrium has been effectively attained; these stresses are shown here. As before in Figure 4.12, the lengths of the line segments indicate the logarithmic magnitude of the maximum shear stress; the direction represents the final orientation of the maximum compressive stress. The model indicates an equilibrium shear stress of 10 bars in the asthenosphere and higher stresses in the order of 500 bars within the lithosphere. For depths greater than 400 km, the stress is downdip compression and increases to 1800 bars.

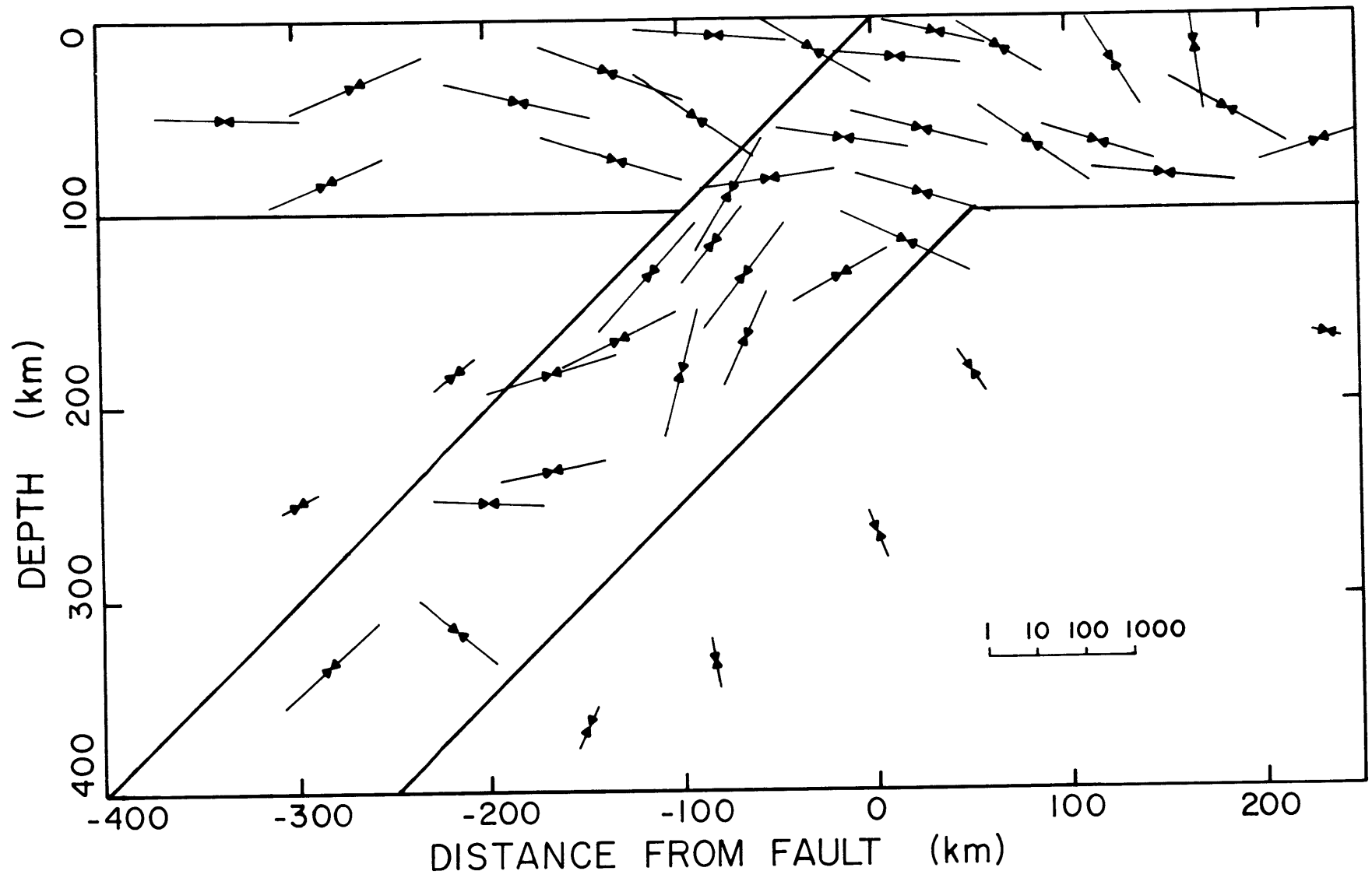


Fig. 4.19

slab and near 10 bars within the asthenosphere. The lithosphere predominately exhibits horizontal compression, except where it bends into the mantle. Here horizontal 'tension' or minimum compressive stress is evident, even with one kilobar compression applied at the oceanic lithosphere where an active spreading ridge would be located. The results are only slightly different without this boundary stress.

Comparing these stresses to those generated by the 10 meter dislocation in Figure 4.18a, it is apparent that the dislocation only introduces a small perturbation. Near the fault the dislocation reduces the maximum shear stress, a feature consistent with our requirement that the earthquake must reduce the strain energy. Deeper within the descending lithosphere the earthquake reinforces the existing stress field. This may indicate a predisposition for later earthquakes: a series of shocks propagating down the descending lithosphere. Continuing this line of speculation, the oceanic plate near the trench also conforms to this pattern. Larger stress concentrations occur near the fault tip that are not resolvable in these models. It is here, at the ends of the slip plane, that after-shocks are most likely to occur in response to the stress concentrations. Only at the tip are stresses opposite to the pre-stressing conceivable. This is necessary to

explain aftershocks whose focal mechanisms have the opposite polarity to the main shock (e.g. Aver'yanova, 1973).

The stress pattern that the density anomalies introduce has analogous features to those at island arcs based upon shallow and intermediate depth earthquakes. Figure 4.20 gives a representative pattern of stress orientations determined from earthquake focal mechanism for the Hokkaido-Kuril-Kamchatka region overlain on the previous model for the initial stress (Aver'yanova, 1973, Fig. 96f). Near the trench and within the oceanic lithosphere normal faulting prevails within both the idealized model and the observations. This identical behavior occurs at other island arcs (Stauder, 1968b). These mechanisms have been correctly attributed to bending of the lithospheric plate as this model demonstrates. In other regions horizontal compression predominates in the observations. Even with free slip along the fault interface, the model also gives this orientation. At 250 km depth the horizontal orientation of the compressive stress originates from the sharp increase in mantle viscosity. Perhaps the correspondence with the observations justifies a similar interpretation within the earth. These similarities may not extend to all island arcs; thus, further observations and analysis are warranted for the future.

In conclusion, the initial prestress introduced by

Figure 4.20

Comparison of the previous model (Fig. 4.19) for the initial stress to principle stresses deduced from focal mechanisms near Hokkaido. Aver'yanova (1973, fig. 96f) compiles the focal mechanism solutions for this section. Here the horizontal hatching denotes horizontal, maximum compressive stress; the more vertical hatching represents horizontal minimum compressive stress, or in a two dimensional model, vertical maximum compressive stress. The arrows denoting the theoretical model and the focal mechanisms compare quite favorably. Notice similar domains of tension where the slab bends during subduction. This pattern also holds for a locked fault with or without the compressive stress applied at the 'spreading ridge'.

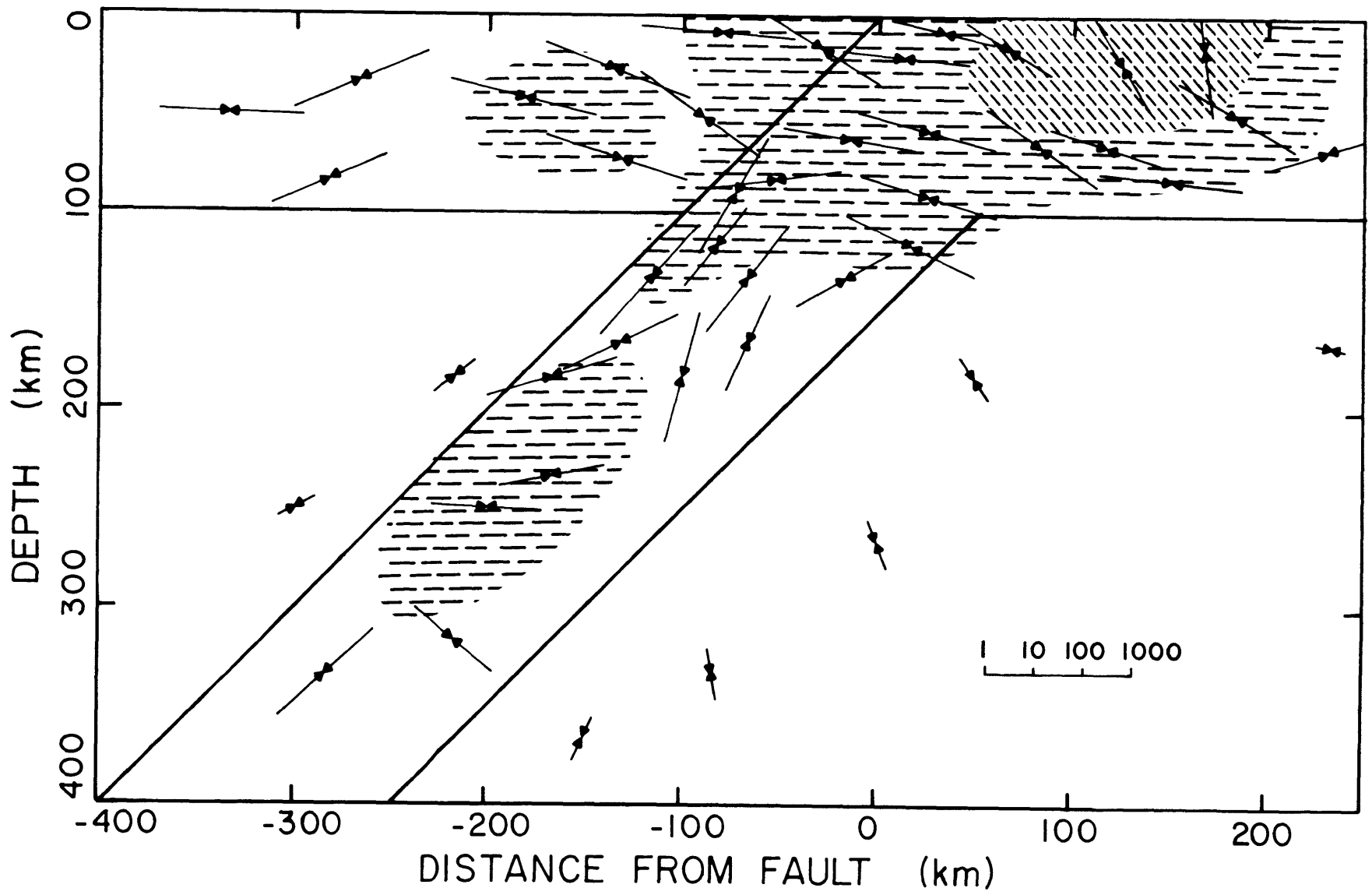


Fig. 4.20

the gravitational body forces within the descending lithosphere is consistent with the stress release. Except at stress concentrations near the fault tip, the stress perturbations caused by the earthquake are small, less than 10 percent, compared to the initial stress. This in turn suggests that the earthquake represents only a partial release of strain energy. The stress orientations also agree with earthquake focal mechanisms near Hokkaido.

4.8 Predictions and Conclusions

The numerical experiments verify the major factors effecting the behavior of mantle relaxation. To recapitulate the significant points, they are given below:

- (1) Scaling by the lithospheric thickness and by the fault depth primarily controls the relaxation characteristics.
- (2) The asthenospheric relaxation time directly scales the time.
- (3) Inclusion of gravity significantly perturbs the time-dependent deformations.
- (4) The boundary conditions imposed on the fault interface, whether prescribed offset or stress release, give different time-dependent deformations.
- (5) Stress relaxation within the asthenosphere rotates the orientations and changes the magnitude of the stress released within the lithosphere.

(6) Following the earthquake, stress propagation occurs far from the fault, albeit small.

(7) The geometry of the descending lithosphere, whether a long or short slab, emphasizes different relaxation modes for the post-seismic deformations.

(8) Changing the dip shifts and perturbs the deformation pattern.

The vertical deformations following the earthquake prove to be the strongest constraint on the parameters. The horizontal measurements are not as sensitive since the baseline for the measure also deforms. In addition, the models demonstrate the versatility of the time-dependent finite element strategy. The computations are relatively inexpensive while retaining good resolution near the fault zone.

Starting with the linearity assumption contained in this analysis, a partial stress release is consistent with prestressing produced by gravitational density anomalies. Comparison of the models with focal mechanisms at island arcs again suggests the importance of mantle rheology. This, then, sustains our previous conclusions for the stress orientations in the descending lithosphere, and extends them to shallow earthquakes.

5. AN ISLAND ARC-MODEL: THE 1946 NANKAIDO EARTHQUAKE AND SOUTHWEST JAPAN

5.1 Introduction

In the previous chapters relaxation in the asthenosphere has been approached primarily as an idealized problem, except in Chapter 4 when geodetic data and seismicity motivate the extension to two-dimensional models. From these models the primary factors that influence the deformation and stress field have emerged from a series of numerical experiments. The capability now extends to specific regional models.

Geophysical observations can introduce constraints on the possible modes of deformation associated with an earthquake. Geodetic measurements are perhaps the best diagnostic. Other constraints include gravity, the stress field deduced from focal mechanisms, and the seismicity. In this chapter the geodetic data constrains time-dependent models for the 1946 Nankaido earthquake and provides bounds on the relevant parameters when possible. Effects such as dilatancy and fault creep are also germane and the measurements again may define their role. Yet before these problems are approached, relevant geophysical measurements and the factors that determine their usefulness must be closely examined to expedite the selection process. Following this review and using the preferred discriminants it suggests, only Japan and Alaska are acceptable regions. Finally, the 1946

Nankaido earthquake represents the best data, and also the most remarkable region. Starting with the assumption of mantle relaxation, the tectonic structure of this region is further defined and gives a consistent picture of the subduction process.

5.2 Interpretation of Constraining Data

The vertical movements following an earthquake impose severe constraints on the model for the time-dependent variations. This is evident from the previous discussions in Chapter 4. Our concern lies with the post-earthquake deformations; thus, we must address ourselves to possible sources of error contained in the data. Fitch and Scholz (1971) have outlined the problem in the context of the 1946 Nankaido earthquake; it would be appropriate here to summarize the salient points. We will concentrate on how these influence the inversion to a fault model.

Geodetic measurements are the key to discriminate between various potential processes. It was such data that first suggested the elastic rebound mechanism for earthquakes (Reid, 1910). Similarly, the most direct evidence for underthrusting at the continental margins also relies upon vertical and horizontal movements following great earthquakes (Savage and Hastie, 1966; Plafker, 1972). For the majority of island arcs, however, the geodetic data is totally lacking or fragmentary. Even for the 1964 Alaskan

earthquake few surveys are available and these give little constraint on the time variations immediately following the earthquake. Tidal stations improve the situation, yet here meteorological and oceanographic errors may creep into the analysis. These will be discussed later.

Japan has the most complete network of geodetic stations. These have been periodically surveyed since the late 1800's, particularly following major earthquakes. The data includes both leveling and triangulation. For the former an extensive network of first order level lines has been resurveyed three times in the last 100 years, excluding regional surveys in the vicinity of major earthquakes or for the earthquake prediction program (Rikitake, 1974). The triangulation surveys have been completed twice, the last in 1950. An extensive network of tidal stations has also been in operation since before 1950 (Hayashi, 1970). The offset in these records gives a measure of the vertical displacement during the earthquake, and they provide an absolute datum for gradual pre- and post-earthquake changes. The displacements measured at the shorelines using terraces and lines of marine growth provide an additional measure for the vertical displacements. Each of these indicators, however, contains errors.

The leveling surveys include more than just the earthquake displacements; they involve an interval prior to the earthquake when the strain was accumulating. Post-earthquake

deformations immediately following the earthquake also contaminate the surveys. For each earthquake, then, we must estimate these stages by subtracting the secular or pre-earthquake and post-earthquake displacements. In addition, each survey must be referenced to a specific datum which in turn may deform. One solution uses a bench mark far from the seismic zone and assumes that it remains constant. Yet this may still obscure changes unless some verification of its constant elevation is possible. Fitch and Scholz (1971) use tidal records to provide this verification and, alternately, an absolute datum for the geodetic surveys.

Records from tidal stations afford a convenient measure if the absolute datum is taken as sea level; however, it is not free from errors. Before these stations are usable as a datum, corrections are introduced for the following perturbations: annual variation of sea level, atmospheric pressure, wind gradient, precipitation and land runoff, cyclones, sea water density, and ocean currents (Tsumura, 1964).

An absolute datum is possible if the mean sea level can be corrected for these effects. Yamaguti (1968) has concluded that the monthly mean sea level corrected for the effects of mean annual variations, barometric pressure, and sea water temperature one meter below the water surface reveals the crustal movements. Unfortunately, these corrections do not include oceanic currents, such as the Kuroshio. The meandering of the Kuroshio alone produces a 10 cm gradient over

15 km between Uragami and Kushimoto tidal stations on Kii Peninsula (Tsumura, 1964). Although this represents an extreme, it emphasizes the care necessary to distinguish absolute crustal movements occurring over short-time intervals from the meteorological or oceanic influences.

Coastal Japan, however, reduces to similar oceanographic regions where the irregular variations are similar (Tsumura, 1964, 1970). Thus Uragami and Kushimoto represent two separate oceanographic provinces: Kushimoto and Shikoku island to Kochi define one region, while Uragami to Uchura are similar (Tsumura, 1970). Taking the difference between any two stations within a region dramatically reduces the irregular oceanic variations. Over distances greater than 100 km the standard deviation of the monthly mean values is reduced to approximately 10-20 mm from the original deviation ranging from 35 to 55 mm. This is comparable to precise leveling (Tsumura, 1964).

An alternate approach determines the regional mean fluctuation by computing the mean for all the stations within an oceanographic province. Each station is then referenced to this mean. Both these reduced sea-levels are almost free from seasonal variations and irregular variations characteristic of each region (Tsumura, 1970). But both of these methods give relative variations: one with respect to a particular station, the other an average over a region. Consequently, potential fluctuations may be masked, or

particularly abnormal oceanographic variations may not be equivalent throughout the averaging region. Unless precise leveling data also exists, extreme caution must be used during interpretation.

The implications for any inversion process are clear: the relative elevations are known much more precisely than the absolute datum. Using the geodetic data for the 1946 Nankaido earthquake, Fitch and Scholz (1971) estimate their errors for the absolute datum as 10 cm. This error also contains unavoidable pre- and post-seismic movements in the survey data for the earthquakes; the surveys are the sum of secular, seismic and post-seismic deformations. In addition, each survey requires an interval of time for completion. This is particularly important during rapid post-seismic deformations (Fitch and Scholz, 1971). These examples suggest that the relative elevations or tilts place the strongest constraint on the model, and less emphasis is indicated for the absolute datum. In the inversion these hypotheses can be checked against the fit to the proposed model.

Gravity offers another important constraint. The process of mantle relaxation involves a net transport of material; thus, a strong deviation from constant free-air anomaly results for time-dependent relaxation. Indeed, the correction to the free air must be larger than the normal Bouguer since the density of the asthenosphere exceeds 2.67 gm/cm^2 . If fault creep or aftershocks are responsible

for the deformations, the correction would be closer to the Bouguer. Primarily crustal lithosphere is underthrust rather than the motion of the denser asthenosphere. Dilatancy gives a change even closer to the free-air correction. Here mass transport is insignificant (Biehler, 1974). We have then a diagnostic that can distinguish between alternate models for post-seismic deformations.

For the 1964 Alaskan earthquake, Rice (1969) reports a $+0.15$ milligal change with subsidence of $.4$ feet. Unfortunately these observations are within the probably error of the gravity survey. As it is the gravity changes are four or five times larger than the free air corrections. Further evaluation of this discriminant must await accurate post-seismic gravity observations.

Fujita, et al. (1974) report both post-seismic subsidence and a large, net mass decrease following the 1973 Hokkaido earthquake. This is consistent with mantle relaxation where outward flow occurs below the subsiding region.

5.3 Discussion of Earthquake Selection

As the last section has emphasized, few island arcs are endowed with extensive geodetic nets. This essentially limits the choice of regions to Japan and Alaska. In this section the available data for large earthquakes within these regions further reduced our choice. The criteria for the selection process follows from the types of errors

contained in the data. Thus short period tidal fluctuations are suspect. A series of both tidal and leveling data spanning the years following the earthquake represent the ideal combination. In the first chapter we note earthquakes having unusual pre- and post-earthquake deformations as a motivation for this investigation. Limiting the examples to large thrusting or reverse mechanisms, a number of outstanding cases are available. These include the 1946 Nankaido earthquake, 1964 Niigata earthquake, and to a lesser degree, the 1964 Alaskan earthquake. Of these the 1946 Nankaido earthquake will prove to have the most suitable data.

The 1964 Alaskan earthquake conforms to a megathrust between the continental and oceanic lithosphere (i.e. Plafker, 1972; Alewine and Jungels, 1974). Geodetic observations indicate uplift near the fault on Middleton and Montague islands, while a broad area of subsidence extends through Kenai peninsula (Small and Wharton, 1969; Plafker, 1972). Unfortunately, the leveling data after the earthquake are fragmentary. Near Anchorage subsidence and tilts continue during the years following the earthquake (Small and Wharton, 1969). Gravity observations are also consistent with this interpretation (Rice, 1969). On Middleton island, however, gravity suggests further uplift after the earthquake. But by 1968 any further variations in gravity are unresolvable when comparing Middleton island station to the Anchorage reference (Rice, 1969). Although the sign of the vertical

displacements is consistent with stress relaxation within the asthenosphere following a low-angle thrust earthquake, shown in Figure 5.1, the data are too fragmentary and offer little constraint on possible mechanisms.

The 1964 Niigata earthquake in the Sea of Japan between Awashima island and mainland Honshu represents a classic and often quoted case of both premonitory and post-seismic deformations (Tsubokawa, et al., 1964; Okada and Kasahara, 1966). In this instance one meter uplift occurs during the earthquake on Awashima island, while on the mainland corresponding to the opposite side of the fault, subsidence results. The mechanism is a reverse fault with a preferred dip of 60 degrees and maximum depth of 30 km (Abe, personal communication, 1974).

Prior to the Niigata earthquake various authors claim premonitory changes related to the earthquake (Tsubokawa, et al., 1964). This assertion stems from both tidal records and leveling data. Yet it is far from conclusive. Tsubokawa, et al. (1964) base the variations on the difference between the tidal records at Nezugaseki and Kashiwazaki, in this case a 2 cm fluctuation occurring one year prior to the earthquake. Similar fluctuations, however, occur periodically through the records for these stations and similar stations in Japan without any association with earthquakes (Tsumura, 1970). This is a short term fluctuation easily within the realm of meteorological and oceanographic variations. The

Figure 5.1

Vertical displacements for a shallow, 15° dipping fault. The schematic in the upper left corner illustrates the geometry using the scale for the horizontal distance. Thus the lithosphere is 50 km thick. The arrows on either side of the fault denote the direction of slip while the length represents the magnitude of slip at each node. Here the scale conforms to the 5 m. segment. At the surface the slip is 2 meters and increases to 6 meters at 30 km. depth. Increasing slip with depth on a shallow dipping fault also fits the displacements for the 1964 Alaskan earthquake (Alewine, 1974). The model illustrates post-seismic uplift near the fault and subsidence near the region of maximum uplift. The dimensionless times are 0. (solid), 3.16, 15.8, 31.6, and 63.1.

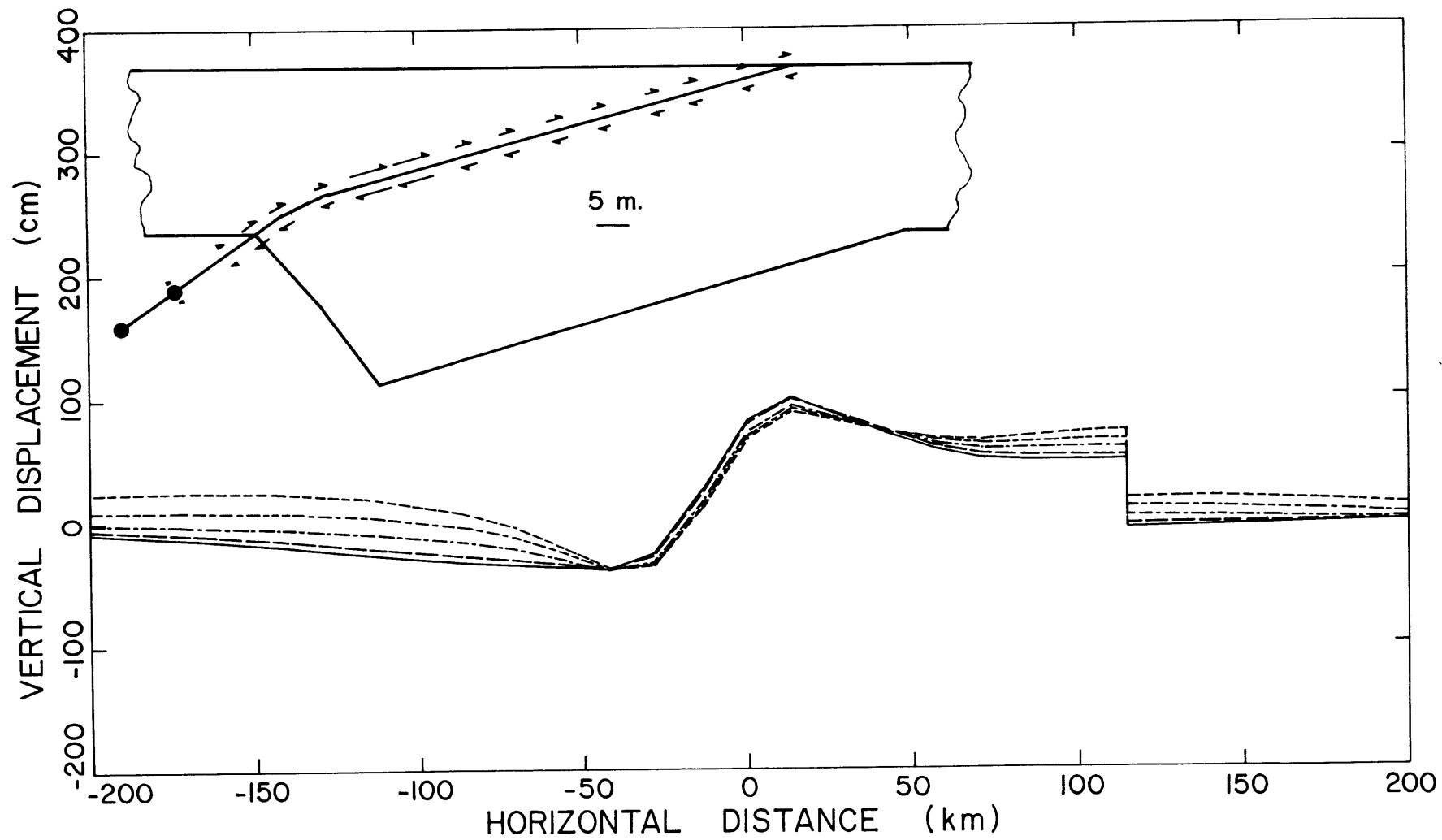


Fig. 5.1

leveling data taken between Kashiwazaki and Nezugaseki prior to the earthquake also suggest a premonitory change (Tsubokawa, et al., 1964). But the change is small and inconclusive when the external influences such as gas mining and industrial development are included along the route. While this is the strongest case for premonitory displacements, any proof awaits a finer net of tidal stations and leveling.

The post-seismic deformations depend solely on tidal records (Tsubokawa, et al., 1964; Okada and Kasahara, 1966). The mainland stations, Kashiwazaki and Nezugaseki, are spaced relatively far apart. Few stations occupy this oceanographic province of the Japan sea which limits, in turn, the accuracy of the tidal corrections. On Awashima island only temporary stations employed after the earthquake give data for the months immediately following the earthquake. Consequently, inadequate controls exist for the meteorological and oceanographic influences, which implies that the rapid subsidence claimed after the earthquake deserves skepticism (Tsumura, 1970). The evidence favors, then, no measurable post-seismic deformations and probably no premonitory variations (Nakamura, et al., 1964; Tsumura, 1970).

These arguments do not imply that asthenospheric relaxation could not satisfy subsidence on both sides of the fault; a steeply dipping fault as in Figure 4.6b which

partially extends through the lithosphere generates just this behavior. Rather the problem lies with the reliability of the data and its time scale. We cannot resolve variations that are buried in the random fluctuations or extend in time beyond the data set. Thus, the 1964 Niigata earthquake is not a good case.

The 1946 Nankaido earthquake represents the best geodetic data set and, coincidentally, the most remarkable deformations. Tidal and geodetic observations confirm a broad region of uplift during the years following the earthquake (Kawasumi, 1956; Matuzawa, 1964; Fujita, 1969; Tsumura, 1970; Fitch and Scholz, 1971). Post-seismic uplift occurs for regions of both seismic uplift and subsidence and for both Kii peninsula and Muroto promontory. This contradicts the expected recovery that should be similar to the pre-seismic down-warping. Moreover, the post-seismic deformations occur for years and far exceed the meteorological and oceanographic influences (Tsumura, 1970). Other unusual circumstances are evident for the earthquake and the region as a whole: seismicity and aftershock distribution, electrical conductivity, and tectonic setting (Kanamori, 1972). These motivate a series of numerical models that will attempt to clarify the processes occurring in Southwest Japan with the assumption of stress relaxation within the asthenosphere. The next section will treat these problems and the geodetic data in the context of the regional tectonics.

5.4 1946 Nankaido Earthquake

The 1946 Nankaido earthquake (M 8.2) is one of two major earthquakes occurring in southwest Japan and north of the Philippine Sea. The other is the 1944 Tonankai earthquake (M 8.1). The combined influence of these two adjacent earthquakes has been the focal point of considerable investigations (i.e. Matuzawa, 1964; Fitch and Scholz, 1971; Kanamori, 1972). Because of the close spacial and temporal proximity of these two earthquakes, they are generally considered as one in the following analysis. Further justification will follow for this assumption. But first let us consider the tectonic setting.

In the following review and analysis, strong evidence exists that southwest Japan represents juvenile underthrusting of the oceanic plate (Fitch and Scholz, 1971; Kanamori, 1972). A pattern emerges from the present geophysical and structural data and from the late Cenozoic and recent history that reinforces this conclusion and adds to its description. Following a long episode of lithospheric underthrusting, these patterns suggest the recent proximity of the active ridge system in the Philippine Sea until the Pleistocene. During this period strike-slip motion predominates along the Median Tectonic Line. The termination of spreading along the active ridge system initiates subduction in southwest Japan (Uyeda, 1974). Yet the remnants of this history are evident in the abnormally high heat flow and the proposed

mantle relaxation. The geodetic data for the Nankaido earthquake will prove to offer additional constraints over and above those imposed by the region's seismicity and focal mechanisms when we include the assumption of stress relaxation within the asthenosphere.

Figure 5.2 gives a map of southwest Japan which delineates the important structures. One should first notice its location between two major arc systems: Izu-Bonin ridge and Honshu to the east, and Kyushu-Ryukyu arc on the Philippine Sea. Both these arc systems show characteristic features of island arcs. These include a well defined volcanic front, distinct trench with low heat flow, and a progression from shallow to deep earthquakes. On the other hand, the Median zone including Shikoku and Kii peninsula violate these properties to a substantial degree. The region straddles the Izu-Bonin-Honshu triple arc junction and the Kyushu-Ryukyu arc. A shallow trough lies offshore containing little sediment and gives the appearance of a juvenile trench (Hilde, et al., 1969; Ludwig, et al., 1973). A deformed ridge of sediments separates this trough from flat-lying, sediment-filled basins occurring to the east of each promontory (Ludwig, et al., 1973). The Median Tectonic Line separating the inner and outer zones defines a right-lateral strike-slip fault having Quaternary movements (Okada, 1968; Sugimura and Uyeda, 1973, p. 136). In addition, Quaternary deformations show north-south trending folds following the axis

Figure 5.2

Map of major structural divisions of southwest Japan taken from Ludwig, et al. (1973). Stippled areas represent zones of Neocene volcanism; solid triangles correspond to active volcanoes. Hatching designates sediment-filled depressions (H, Hyuganada basin; T, Tosa basin; KS, Kii Suido basin; K, Kumanonada basin; E, Enshunada depression; N, Nankai trough). The broad dotted line corresponds to thick sediments in a crustal trough underlying the continental slope south of Kyushu. A represents Ashizurizaki; M, Murotosaki; S, Shionomisaki; SP, Shima peninsula; O, Omaezaki. The median tectonic line passes from Honshu-Izu-Bonin ridge to Kyushu (reproduced from Ludwig, et al., 1973).

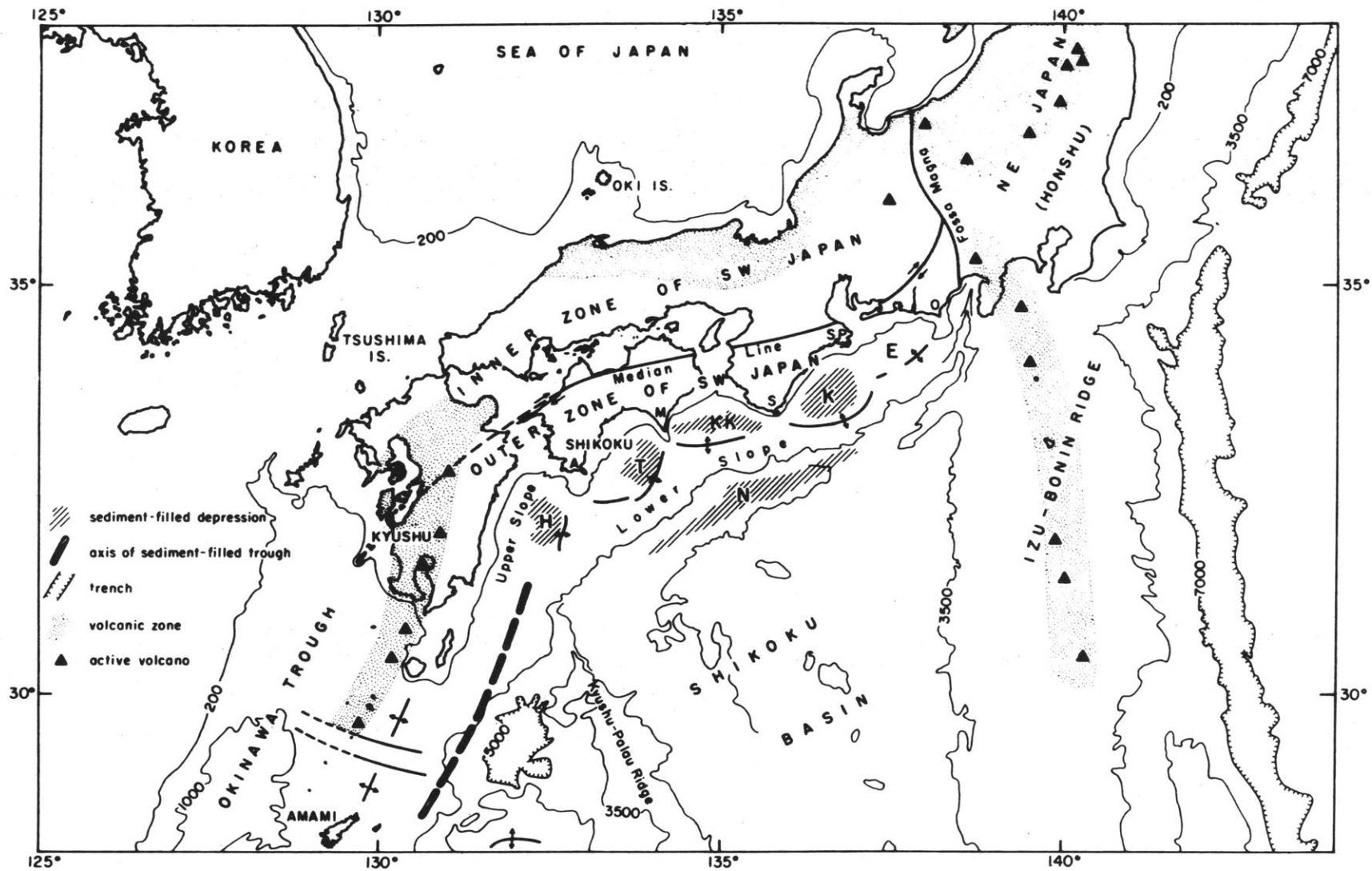


Fig. 5.2

of the promontories, rather than the azimuth of the trough. Finally, the region is devoid of active volcanoes; the most recent date from the early Pleistocene (Sugimura and Uyeda, 1973, p. 111). These structural features combine to suggest a most unusual tectonic region.

Geophysical indicators are also anomalous. Contrary to other island arc systems, the heat flow from the adjacent basins and the trough are high (Watanabe, et al., 1970). The distribution of hot springs retains this unusual behavior (Sugimura and Uyeda, 1973, p. 62). These two do not necessarily reflect current conditions, rather they are strongly related to the previous history of southwest Japan. The electrical conductivity, however, also suggests an anomalous region of high conductivity compared to the adjacent arcs (Rikitake, 1966). This may be related to the absence of a pronounced subducting lithosphere (Kanamori, 1972).

Before we continue, it is appropriate here to review the previous history of this region and possible conjectures in view of the previous observations. Huzita (1962) and Sugimura and Uyeda (1973) summarize the recent structural history of southwest Japan. The following characteristics are evident for the Median zone:

- (1) Southwest Japan shows generally more cratonic character than northeast Japan during the Neogene.
- (2) The province subsided in Miocene and Plio-Pleistocene times allowing formation of thin shallow-sea and terrestrial

deposits, and lacustrine.

(3) Volcanic activity peaked in the Late Miocene, a second maximum in the Middle Miocene, and ending in the Early Pleistocene. Further, the primary magma evolves from tholeiite in Early Miocene to subalkaline in the Middle and Late Miocene for the Median zone. According to Sugimura and Uyeda (1973), this reflects a decrease of underthrusting from Early Miocene to Middle Miocene.

(4) The apparent decrease in underthrusting corresponds to cessation of intense deformation. During this period the extensive volcanics are deposited on Honshu and some on Shikoku. Subduction now ceases while the ridge system in the Philippine Sea becomes active. Subsidence occurs along southwestern Japan; the anomalous heat flow begins and reflects the absence of subduction and the proximity of the spreading center; and the deformations cease. Again a change in direction of plate motion accompanies the cessation of spreading at the ridge during the Plio-Pleistocene. Subduction once again initiates but with a new orientation (Uyeda, 1974). Some small anomalies such as a bend in the Hawaiian chain offer support to this assertion (Uyeda, 1974). It is this new episode of subduction that currently dominates our observations. The seismicity now adds another dimension to the problem.

Kanamori (1971, 1972) has summarized the seismicity and focal mechanisms for southwest Japan. Figure 5.3 shows the

Figure 5.3

A schematic of the tectonic features and the epicenters for historic, great (M 8.0) earthquakes in southwest Japan since 1400. Adjacent to the approximate epicenter lies the year of occurrence. (Reproduced from Kanamori, 1972).

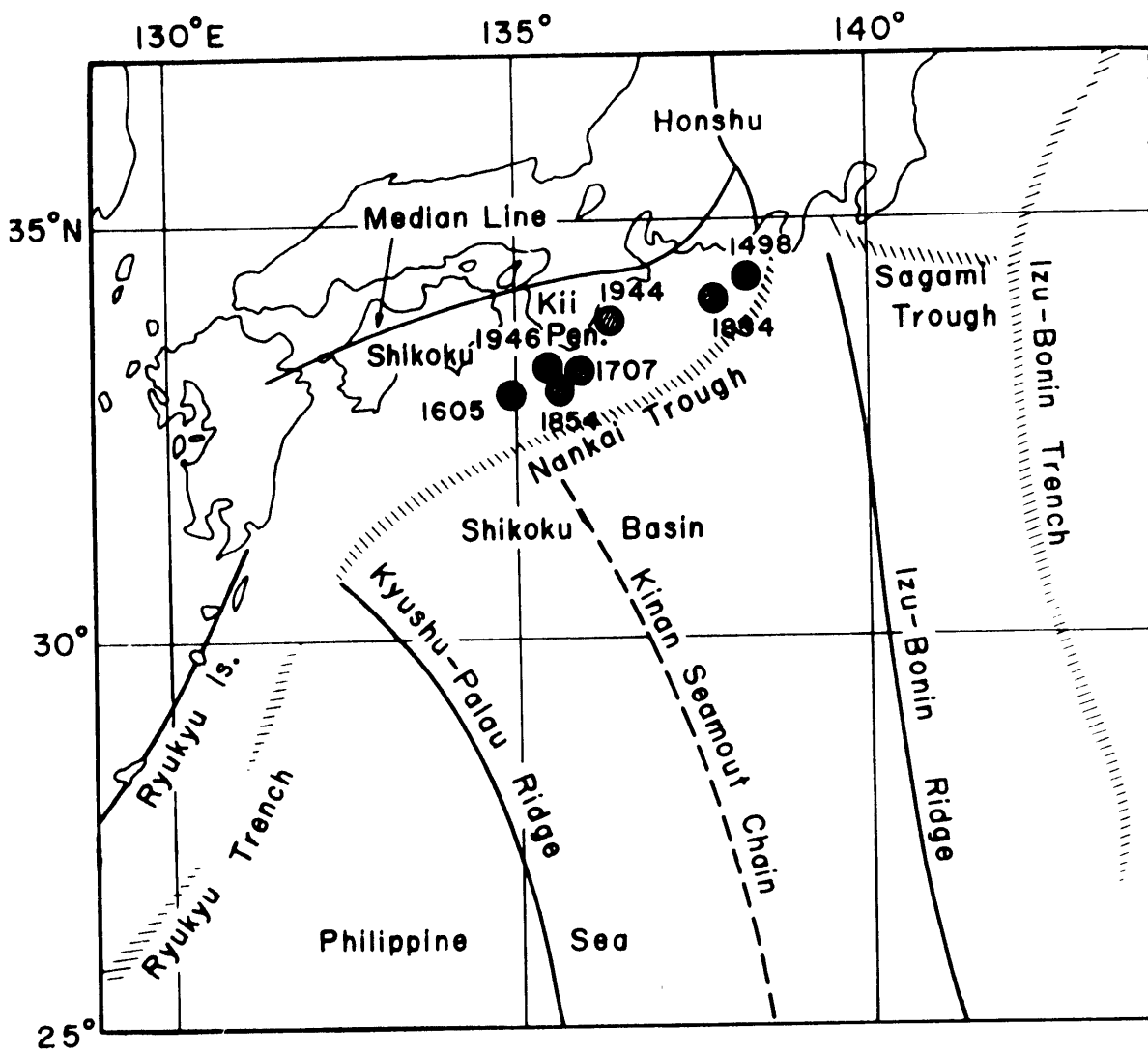


Fig. 5.3

epicenters of large historical earthquakes with the year of their occurrence together with an outline of the tectonic structure. A regular pattern emerges of temporal seismicity: the 1944 and 1946, two in 1854, and perhaps a twin set in 1707 reflect a remarkable pattern of paired earthquakes. Kanamori (1972, 1973) notes that this may signify a different mode of interaction or evolutionary stage for the arc as opposed to other more developed regions including Honshu. Throughout the Median zone the seismicity is predominately shallow, with only a few intermediate earthquakes and no deep ones. In addition, Western Shikoku is devoid of both historical and current seismicity. This may reflect the location of the extinct ridge.

The seismicity and focal mechanisms suggest a shallow dipping plane for underthrusting near the hypocenters of the 1944 Tonankai and 1946 Nankaido earthquakes (Kanamori, 1972). The micro-seismicity distribution in Figure 5.4 for the Kii peninsula shows a wedge-like feature extending towards the trough (Kanamori and Tsumura, 1971). The focal mechanism for the 1944 and 1946 earthquakes conform to this wedge; Figure 5.4 also illustrates the faults dipping at approximately 10° towards the mainland (Kanamori, 1972). The locations for the earthquakes cannot exceed 40 km depth and could easily be 20 km (Kanamori, 1972). Farther inland diffuse seismicity occurs with anomalous clustering at 50 km depth (Shiono, 1970a; Kanamori and Tsumura, 1971). While the

Figure 5.4

The hypocenters for microseismicity from January 1969 to July 1969, using the projection in the left-hand figure. The hatched region on the left shows the seismicity trend from 50 to 70 km depth. The mechanism diagrams and slip vectors of the 1944 Tonankai and 1946 Nankaido earthquake are also shown on the left. Distinct clustering occurs at 50 km depth beneath the Kii peninsula (reproduced from Kanamori, 1972).

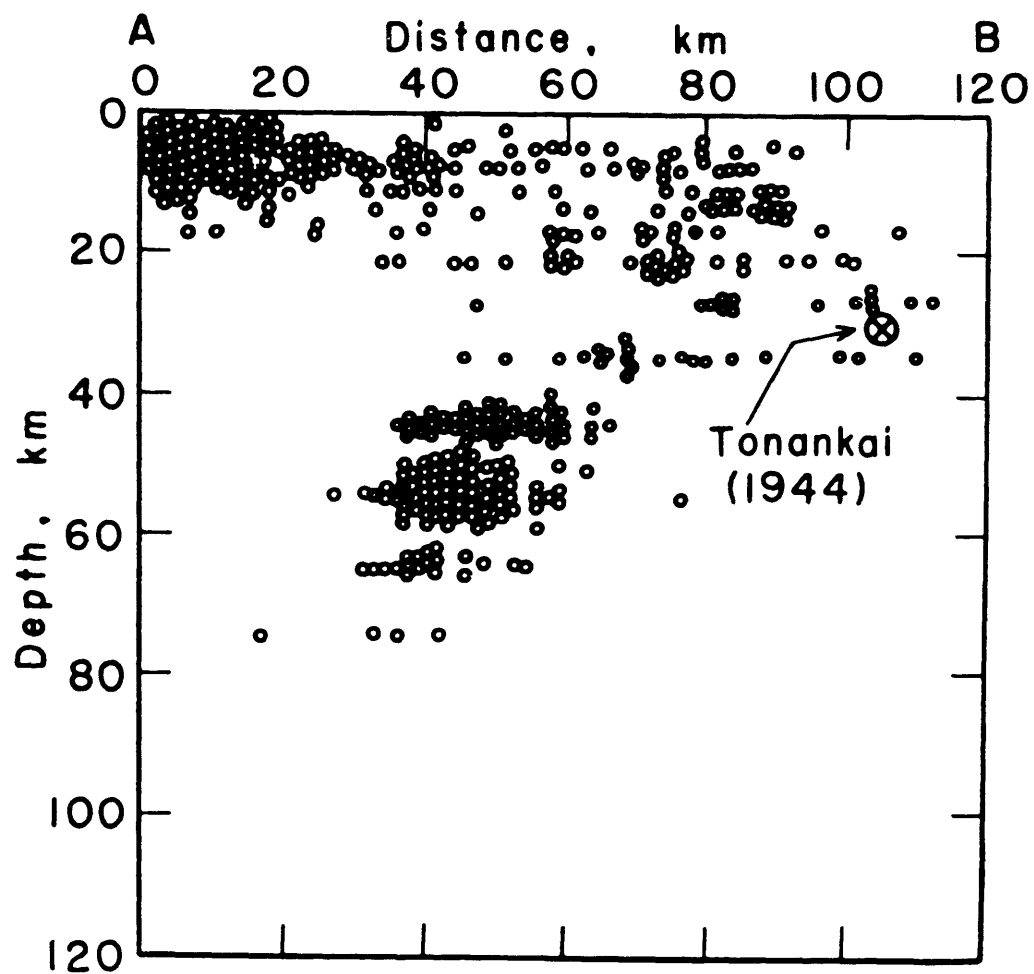
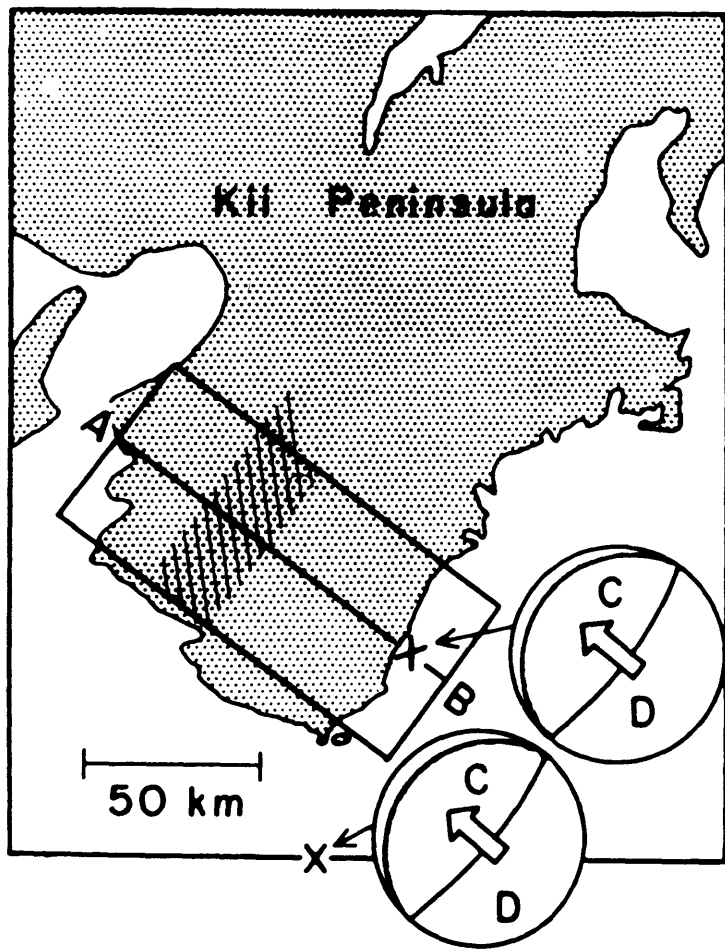


Fig. 5.4

station grid only samples Kii peninsula, Kanamori (1972) argues that the seismicity for moderate size earthquakes justifies extending this pattern toward the south and offshore from Shikoku.

The focal mechanisms deduced by Shiono (1970a,b) for the microseismicity near Kii peninsula present a new aspect to the problem. Concentrating on only the deeper earthquakes, two major groupings are evident: extending from 40 to 60 km depth within the Kii peninsula, the predominant solutions have their P axis following the trend of the proposed slab. Thus the dominant force is compression in the direction of motion (Kanamori, 1972). The nodal planes show no systematic orientation. In addition, a preponderance of strike-slip solutions occur in the Kii channel between Shikoku and the Kii peninsula. This (together with the distinct embayed shoreline and basins) would suggest a segmented lithosphere as it descends or a distorted continental crust. These also conform to the slip direction deduced from the earthquakes or the relative plate motions, but are skewed 10 to 15 degrees to the trend of the Nankai trough.

Two alternate models are possible that account for the seismicity. The first places the seismicity at 50 km within the descending lithosphere. The orientations then reflect the state of stress within the slab, either generated by the gravitational body forces or by collision with the continental lithosphere. The strike-slip motion would indicate

tearing within the lithosphere as Stauder (1968a) proposed for the Aleutians. The structural history could be satisfied if the slab terminated soon after the seismicity cluster. This creates a short slab. The alternate model places the seismicity within the deformed continental lithosphere (Kanamori, 1972). Now the descending lithosphere terminates sooner or bends abruptly downward if the shallow dip for the 1944 and 1946 earthquakes is to be maintained at the megathrust. The geodetic data can provide the distinguishing factor between these hypotheses.

Using a fault model which invokes constant slip and dip with depth, Fitch and Scholz (1971) found that the geodetic data constrains the fault plane to roughly 35° dip. This configuration, however, contradicts both the structural observations and the focal mechanism. The surface fault trace would occur approximately 45 km inland from the trench margin. There is no evidence from bathymetry and submarine morphology to indicate such a major thrust fault (Ludwig, et al., 1973). Furthermore, Kanamori's (1972) fault plane solutions will not admit a mechanism having this dip. These argue for an alternative solution if we eliminate the restriction of constant slip.

Requiring a shallow dip near the hypocenter of the 1944 and 1946 earthquakes and constraining the surface fault trace to the inner margin of the Nankai trough still allow alternate fault geometries along the deeper fault segments. We

must discriminate between these alternate hypotheses using the geodetic data. The time-dependent deformations now offer additional constraints if one initially assumes mantle stress relaxation occurs and is significant following the earthquake. As the preceding discussion has emphasized, southwest Japan gives every indication of an anomalous asthenosphere. If stress relaxation occurs, here represents relatively ideal conditions: a large earthquake exciting the deformations, and the proximity of a ridge in the recent past. In the next section alternate hypotheses are eliminated until the geodetic data limits us to one preferred fault orientation.

5.5 Models for the 1946 Nankaido Earthquake

The observations, both geophysical and structural, limit any initial model for southwest Japan. The source parameters for the 1944 Tonankai and 1946 Nankaido earthquakes confine us to a shallow dipping fault near the hypocenter (Kanamori, 1972). Combining this with the restriction that the fault trace intersects the Nankai trough places the depth at 20 to 25 km for a fault initially dipping at 15° . Figure 5.5 delineates the alternate models now available using a dislocation boundary condition on the fault interface:

(1) The fault plane may continue at this shallow dip and extend beneath Shikoku. The cluster of deep seismicity would then lie within the subducting lithosphere.

Figure 5.5a, b

Fault planes for five different models of southwest Japan projected on the hypocenters of the microseismicity in Figure 5.4. The models are given in Table 5.1.

a) Diagram for model A-1 using a fault plane dipping at 35° . The model is similar to the preferred model of Fitch and Scholz (1971), except the dislocation varies along the fault to yield the best fit to the Nankaido data and the plane is displaced 12 km towards the arc. The dotted line outlines the continental and descending lithospheres.

b) Fault planes A-2 through A-5 superimposed on the microseismicity. The thick line segments indicate the position of the lithospheres. The models span possible locations for the microseismicity: either within the descending lithosphere or in the continental plate. The lithosphere varies between 50 and 60 km thickness.

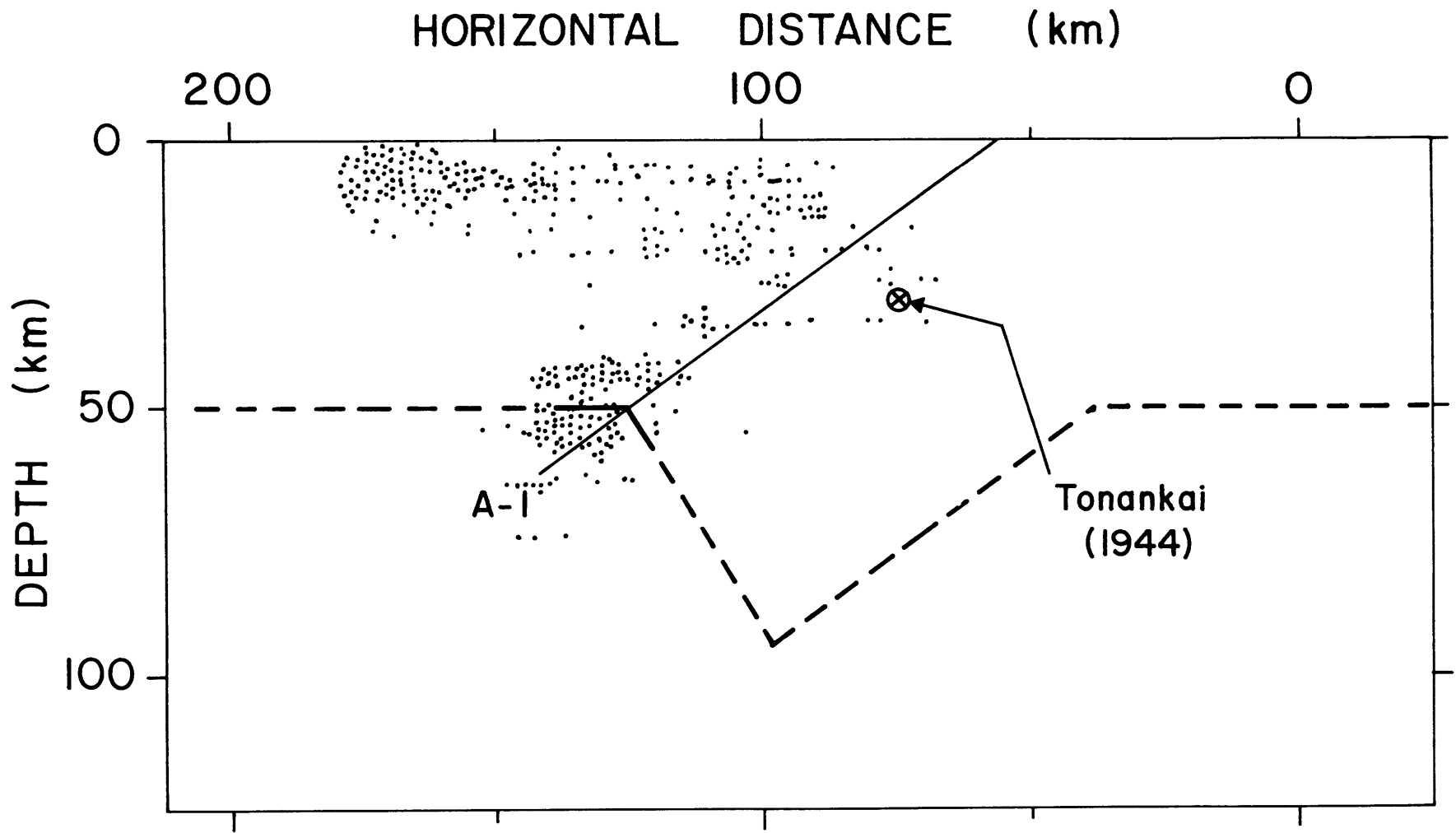


Fig. 5.5a

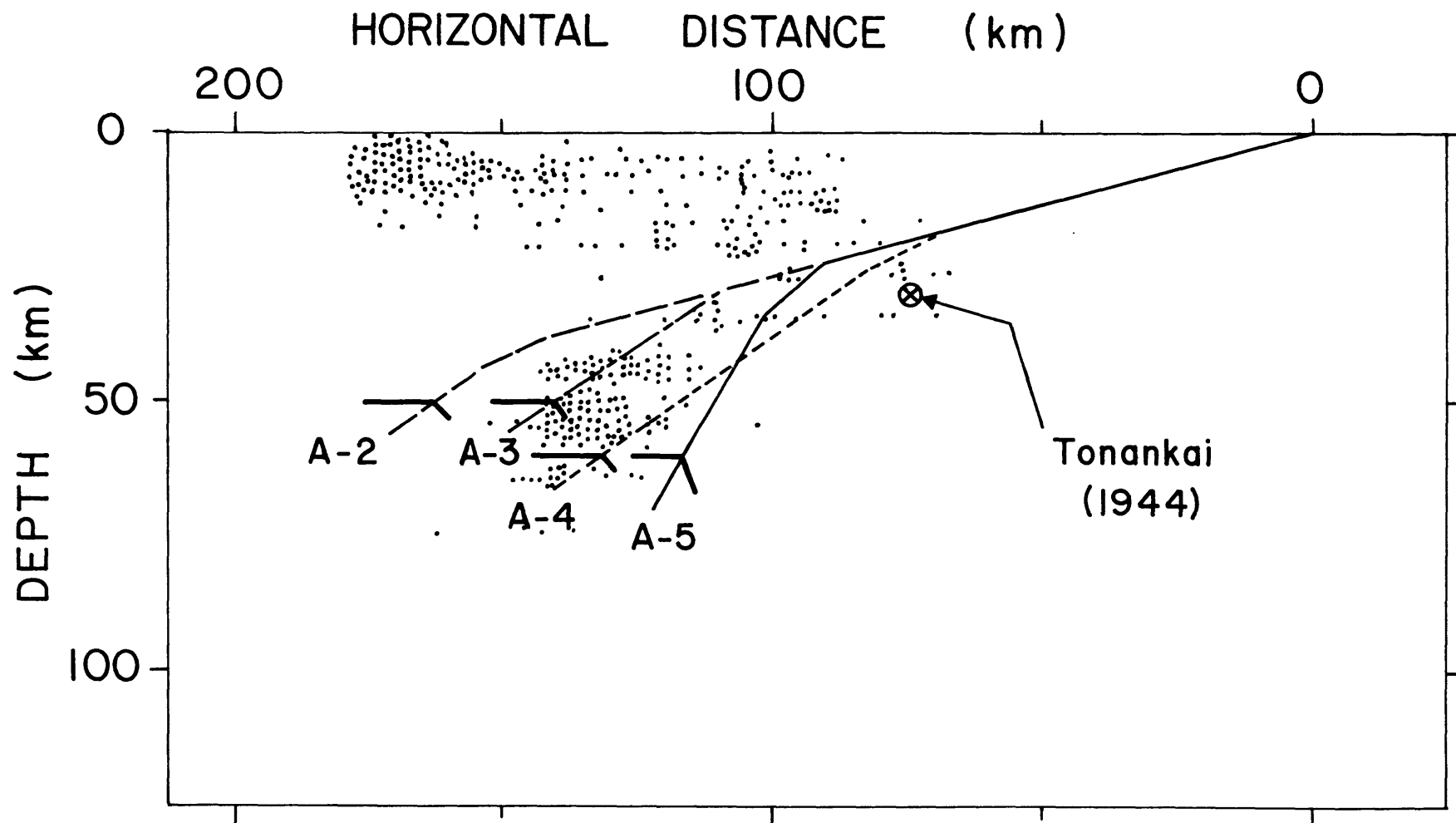


Fig. 5.5b

(2) The lithosphere gradually bends under the continental lithosphere towards a steeper dip. Depending on the dip and depth of the bend, the seismicity remains within the slab or on the fault interface that separates the two lithospheres. There exists no a priori justification for this latter case; the nodal planes have no preferred direction (Shiono, 1970a).

(3) The seismicity exists in the continental lithosphere. Here the deeper fault segment must dip at least 35° in order to satisfy the focal mechanism and hypocenter for the 1944 or 1946 earthquakes. For each category and the additional model using constant 35° dip, the inversion of time-dependent geodetic data compiled by Fitch and Scholz (1971) gives a maximum likelihood model (section 2.8; Searle, 1971; Wiggins, 1972).

Fitch and Scholz (1971) examine the geodetic and tidal data for the pre-earthquake or secular, seismic, and post-seismic deformations; these profiles are outlined in Figure 5.6. For profiles A and C post-seismic deformations are available where tidal records impose an absolute datum. Section 5.2 discusses some of the errors associated with this absolute datum; they primarily originate from meteorological and oceanographic influences. To compensate for these errors, the inversion weights the level of the absolute datum less than the geodetic surveys and their tilts. These weights depend on the errors associated with the individual observations: larger errors imply less weight. In addition,

Figure 5.6

Outline of displacement profiles, A through C and Kii, in southwest Japan determined by Fitch and Scholz (1971). The dashed and dot-dashed lines denote the leveling lines used in the profile. The filled circles indicate principle bench marks. The stripped regions are examples of uplifted marine terraces (reproduced from Fitch and Scholz, 1971).

a two-dimensional simulation defines the model. The error introduced by this assumption progressively increases as we move from the fault. Yet compared to the inaccuracies of the geodetic data, this error is probably relatively small (e.g. Jungels and Frazier, 1973).

Another consideration also tied to the real three-dimensional character of southwest Japan is the divergence between the axis of subduction defined by the Nankai trough and the slip vectors determined by earthquake or relative plate velocities. It is this divergence that may account for the peculiar segmented basins and embayed shoreline that characterize southwest Japan (see section 5.4). The difference is not small; it is on the order of 15° (Kanamori, 1972; Ludwig, et al., 1973). The focal mechanisms for the 1944 and 1946 earthquakes show no strike-slip components within this range (Kanamori, 1972); thus, one can conjecture that the segmentation of the slab and crust follows the breaks defined by the promontories. The strong strike-slip component of the large aftershock near the Kii peninsula (15 June 1948, M 7.0; see Ichikawa, 1971) may reflect motion between these adjacent segments. Unfortunately, the solution may be unreliable. The structure may also account for the tendency towards paired earthquakes; they occur in adjacent segments. To model this complex behavior necessitates a three-dimensional problem; instead, one must assume the simpler two-dimensional profile through the trench. The

model, then, conforms to an average behavior across the arc. The assumption should not materially effect asthenospheric relaxation for any given profile. For the same reasons, the 1944 Tonankai and 1946 Nankaido earthquakes reduce to one earthquake. We must assume their spatial and temporal proximity conforms to a continuous break.

Aftershocks pose the final source of contamination to the geodetic data and the model. Figure 5.7 illustrates the aftershock epicenters following the 1946 Nankaido earthquake. The aftershocks which pose the greatest problem are those located on Shikoku near our profiles and two large aftershocks on the Kii peninsula. For the latter the distance separating the profile and the aftershocks should minimize their influence on the time-dependent geodetic data. The swarm of shallow aftershocks following the main shock on Shikoku, however, lies close to the center of our profiles. Although these earthquakes do not exceed magnitude 5.5, their cumulative effect could distort the profile (e.g. Tsubokawa, et al., 1968). Evidence of this perturbation actually exists in profile A; the anomalous bulge at 110 km in the post-seismic deformations has strong gradients suggesting a shallow, buried fault (see Figure 5.8). To compensate for these anomalies during the inversion, the observations near the bulge are given little weight.

Profile A of Fitch and Scholz (1971) for the vertical displacements represents the best compromise for the

Figures 5.7

Aftershocks of the 1944 Tonankai (circles) and the 1946 Nankaido (triangles) earthquakes. Filled circles and triangles are those within one month after the main shock. The size suggests the magnitude of the shock. The filled square represents the epicenter for a large ($M \sim 6.9$) aftershock during June 15, 1948. The hatched zone shows the fault surfaces deduced from seismicity (reproduced from Kanamori, 1972).

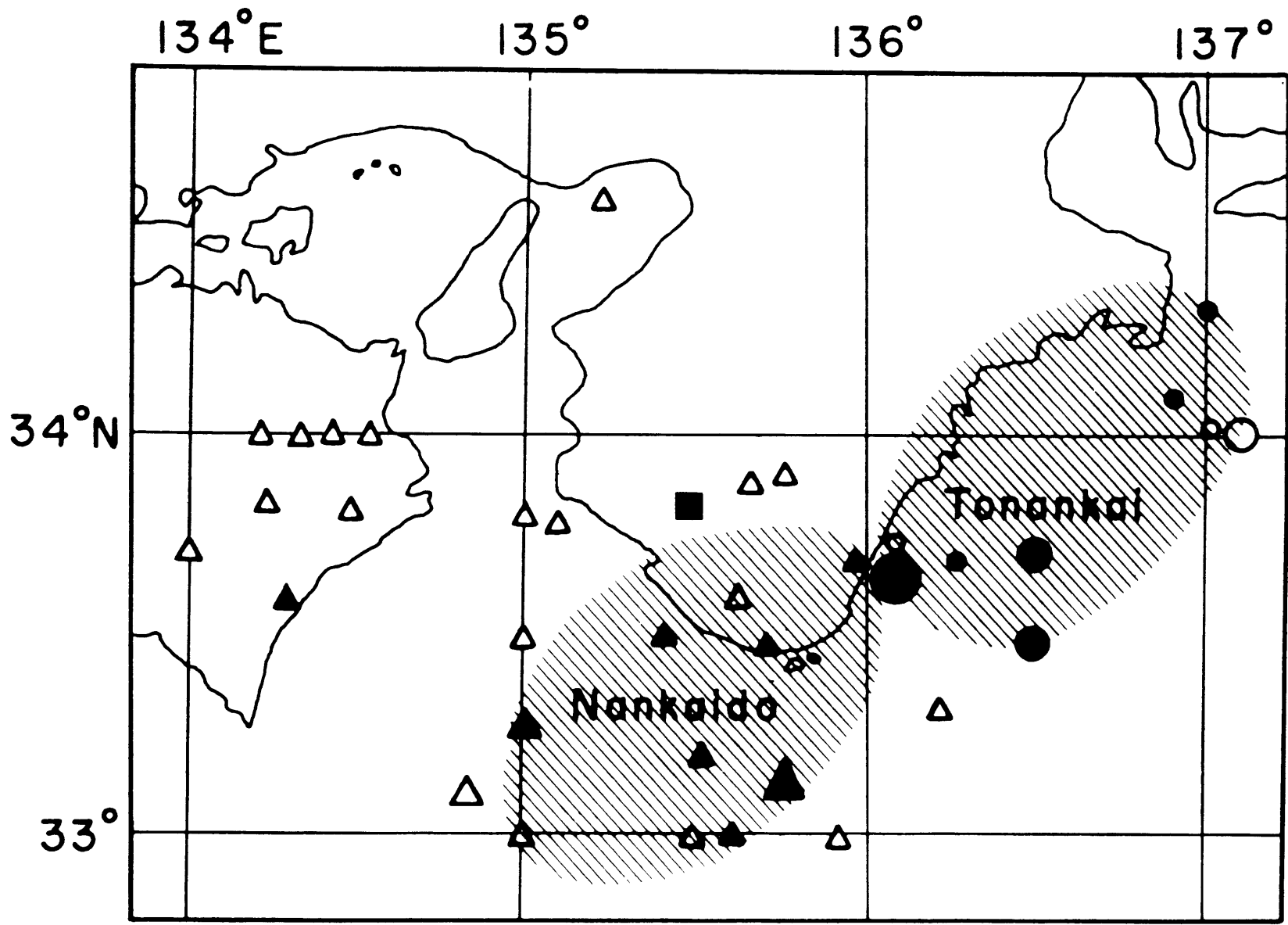


Fig. 5.7

Figure 5.8

Profile A showing vertical displacements for the Nankaido earthquake determined by Fitch and Scholz (1971). From top to bottom, pre-seismic, seismic, post-seismic, and sum of seismic and post-seismic vertical displacements for eastern Shikoku (see Figure 5.6) projected onto vertical planes perpendicular to the Nankai trough. The abscissa gives the distance from the Fitch and Scholz (1971) model for the trace of the megathrust. The inner margin of the Nankai trough is an additional 45 km to this distance (reproduced from Fitch and Scholz, 1971).

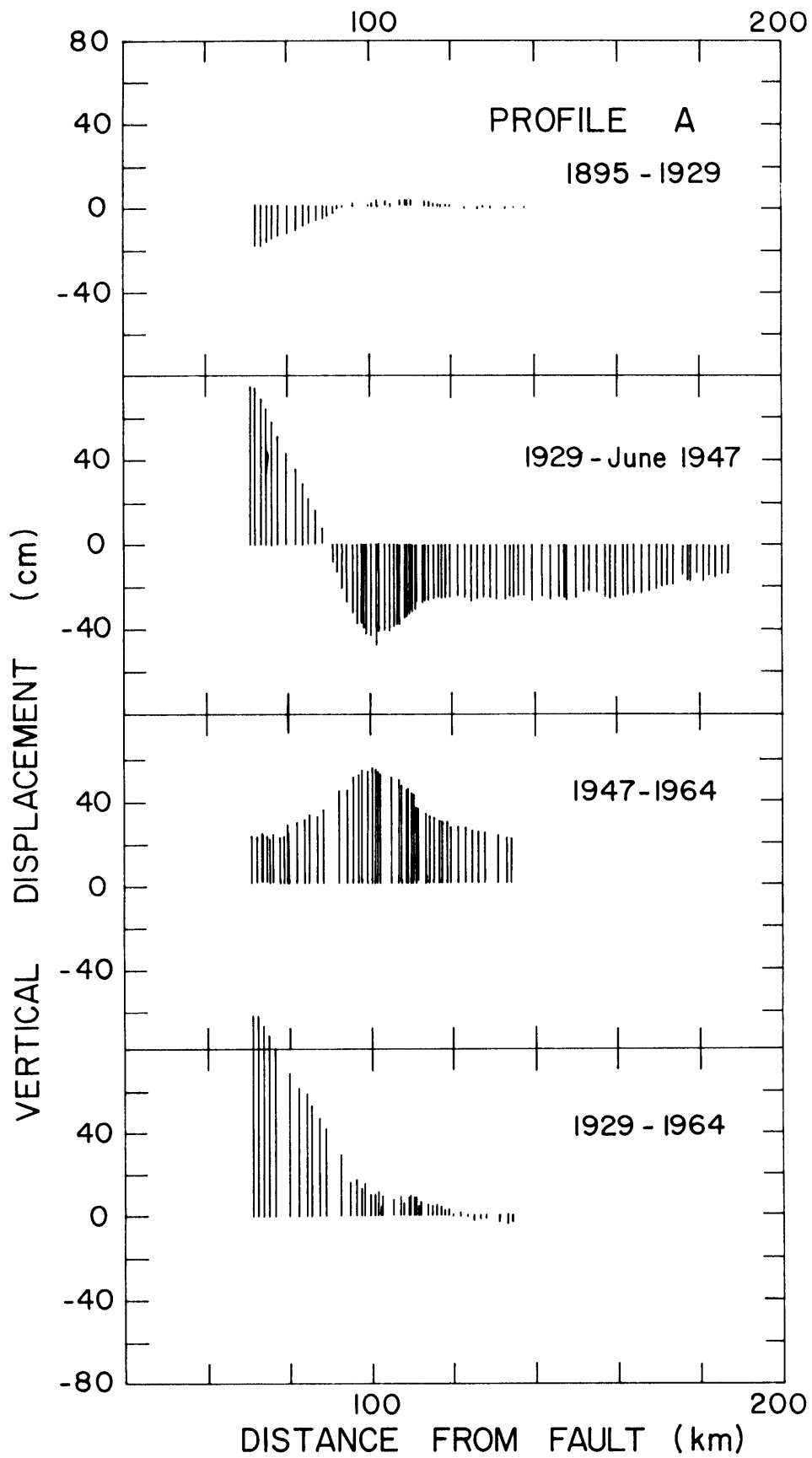


Fig. 5.8

inversion. Figure 5.6 illustrates its location and the profile itself is shown in Figure 5.8. The profile is nearest the central axis of the fault for the 1946 Nankaido earthquake. This minimizes edge effects at the ends of the fault (e.g. Fitch and Scholz, 1971; Jungels and Frazier, 1973). Profile C, which lies at one extreme of the fault, also verifies similar post-seismic deformations.

To generate the data set for the seismic and post-seismic deformations, the contribution of the pre-seismic movements contained in the profile is estimated and subtracted from the geodetic displacements. Here we assume linear accumulation prior to the earthquake (Okada and Nagata, 1953). Thus for profile A we estimate rates of downwarping for the interval from 1895 to 1929. These rates are used to estimate the net pre-seismic or secular movement occurring between 1929 and 1946 or 1964; with this correction the 1929 to June 1947 or the 1929 to 1964 profiles give the net seismic or post-seismic deformations. Figure 5.9 shows the resulting data set for profile A. The net vertical displacements are now generally greater than those contained in the original profile. This data set provides the starting point for the forthcoming models. Matching the data set to the surface nodes for the finite element model discretizes the data giving a fixed number of observations. This is not a deterrent; the number of observations and parameters are both greater than the resolvable and

Figure 5.9

Reduced profile A after removing the pre-seismic strain accumulation. The abscissa has two scales for the horizontal distance: the inner corresponds to the original scale of Fitch and Scholz (1971) in Figure 5.8 for profile A; the outer scale represents the perpendicular distance from the inner margin of the Nankai trough. The latter scale defines the distance from the fault trace for models A-1 to A-5 in Figure 5.5. The two curves show the seismic displacement from June 1947 and the seismic plus post-seismic by 1964 after removing the pre-seismic deformation between 1929 and 1947. The rate of pre-seismic deformation is extrapolated from the deformation observed between 1895 and 1929 in Figure 5.8.

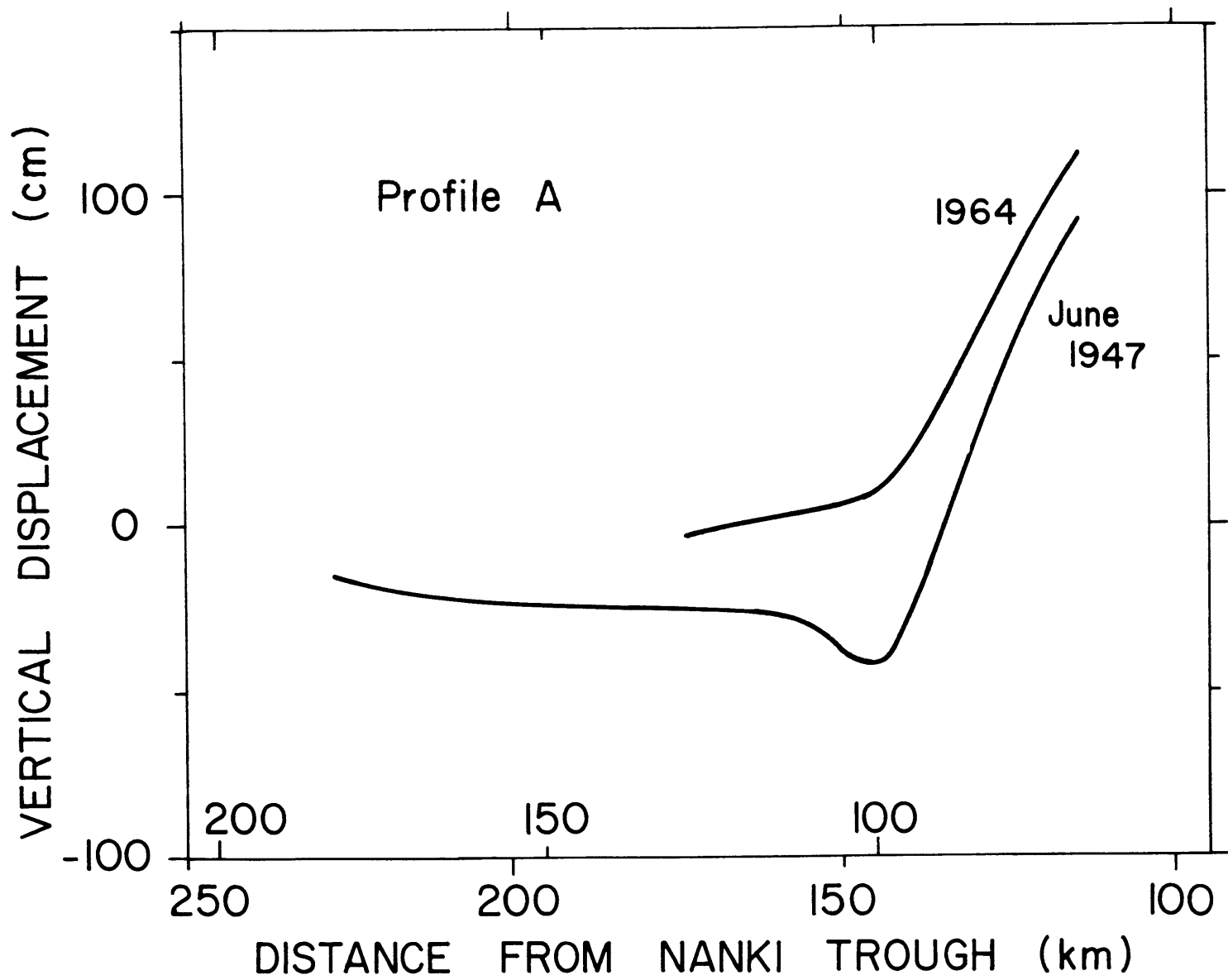


Fig. 5.9

independent parameters (Wiggins, 1972).

The tsunami generated by the 1946 Nankaido earthquake provides one additional constraint. Hatori (1966) estimates vertical displacements of a few meters in the source area. Any model, then, must have surface displacements in this range. Although not included as an explicit constraint except during selection of the initial model for the inversion, the source parameters do introduce one criterion for the final model.

Adopting five geometries for the region spans the domain of probable fault configurations. The previous Figure 5.5 shows these models overlain on the microseismicity of the Kii peninsula. Thus, models exist that place the seismicity both within the descending lithosphere and within the continental lithosphere. For each geometry a variety of initial fault displacements provide the starting point for the inversion (see section 2.8). Even without the nonlinear viscosity, minimizing the perturbations from the initial model requires careful selection of the starting point. Iterating from different initial models will usually produce similar final models if the final fit is good. A poor geometry for the problem, however, generally has unstable convergence and will never give a good fit to the data. This goodness of fit indicates how adequately the models simulate the actual process if the errors chosen for the data are correct (Wiggins, 1972); unstable convergence and a poor fit suggest improper geometry

for the fault or incorrect initial assumptions. In addition, we assume a priori reasonably smooth models. Large swings for the slip from node to node along the fault are ignored; consequently, this limits the independent degrees of freedom within the data (Wiggins, 1972). Yet some fault geometries still give actual reversals in slip along the fault or reversals at the surface. These slip reversals often violate the tsunami data or the inferred slip direction from the focal mechanism. These criteria will guide our evaluation of the final models.

Table 5.1 lists the best and most reasonable final models derived from the inversion of each fault geometry. Included within the table are the number of independent degrees of freedom selected for a smooth model, the standard deviation of the model's fit to the data, and any pertinent comments. The two best models use the original dip of 35° proposed by Fitch and Scholz (1971) and a shallow dip of 15° followed by a steep 60° dip. These models are compared later. The other models violated one or more of our restrictions: large errors in the absolute level giving rise to subsidence over the region, small vertical offset in the tsunami source area, large reversals in slip on the fault, or a poor fit combined with unstable convergence. The models giving the best fit have a common property: the fault plane intersects the asthenosphere between the region of maximum seismic subsidence and the surface fault trace. This is not

TABLE 5.1

<u>MODEL</u>	<u>DESIGNATION</u>	<u>DIP</u>	<u>DEPTH OF BEND (KM)</u>	<u>LITHOSPHERIC THICKNESS (KM)</u>	<u>DEGREES OF FREEDOM</u>	<u>STD</u>	<u>COMMENTS</u>
A-1	N9-23.1	35°	none	50.	4	2.35	Good tsunami displacements,
A-2	N19-35.3	15°, 35°	40.	50.	4	2.70	Absolute datum poor. Small vertical disp. in tsunami zone,
A-3	N17-29.4 -29.5	15°, 35°	30.	50.	4	3.74	Reversals of slip. Large and increasing slip with depth, or subsidence instead of uplift over region if correct slip (large error in absolute datum).
A-4	N18-32.4	15°, 35°	20.	60.	4	3.97	Sections of normal slip along fault. Large error in absolute level datum.
A-5	N21-37.4	15°, 60°	26.	60.	5	1.60	Preferred model. 3-15 meters displacement.

surprising. Chapter 4 demonstrates this relationship as a direct result of relaxation. Altering the dip affects it slightly, but the basic phenomenon remains. Thus with a fault dipping at 15° under Shikoku, one expects post-seismic subsidence and not uplift after the earthquake. A sharp change in dip must then occur to create the zone of uplift if the focal mechanism requires the shallow dip.

The first model, A-1, intersects the asthenosphere near the proper location to obtain uplift for post-seismic deformations; however the model intersects the surface 45 km from the Nankai trough. The geometry corresponds to Fitch and Scholz's (1971) best fitting model. Although violating the focal mechanism and structural features, allowing arbitrary slip along the fault yields a good fit to the seismic and post-seismic deformations. As a reference point, the results are given for this model. It may then suggest possible improvements.

Figure 5.10 delineates the fault geometry and displacements for this model, a fault dipping at a constant 35° . The geodetic data set uses the discretized version of Figure 5.9 and includes both seismic and post-seismic deformations (Appendix C). The geodetic surveys are tied to an arbitrary level; consequently, only the tilts constrain the fault displacements. In spite of this restriction, the results agree with the absolute datum determined from tidal records. The resulting fault displacements show increasing

Figure 5.10

Vertical displacements for model A-1 in Figure 5.5a compared to seismic and seismic plus post-seismic deformations using profile A. The inset in the upper-left indicates the fault offset when the length denotes the magnitude. The 5 meter line gives the scale. Near the surface the offset equals 5 meters and increases to 8 meters at 40 km depth. The dislocation then remains constant with time. The vertical bars extending from the baseline give the observed seismic vertical displacements. The dotted region indicates the seismic plus post seismic displacements after 18 years. The dotted region extends from either the observed baseline or the seismic deformation. For a viscosity of 3.2×10^{19} poise the dotted lines correspond to 0. (solid), 1., 5., 10., and 20. years after the earthquake. The fit suggests only a small baseline correction from the zero line of the model. The same baseline applies to both sets of observations, the seismic and seismic plus post-seismic. Model A-1 constrains a priori the fault offset near the surface to satisfy the tsunami source region.

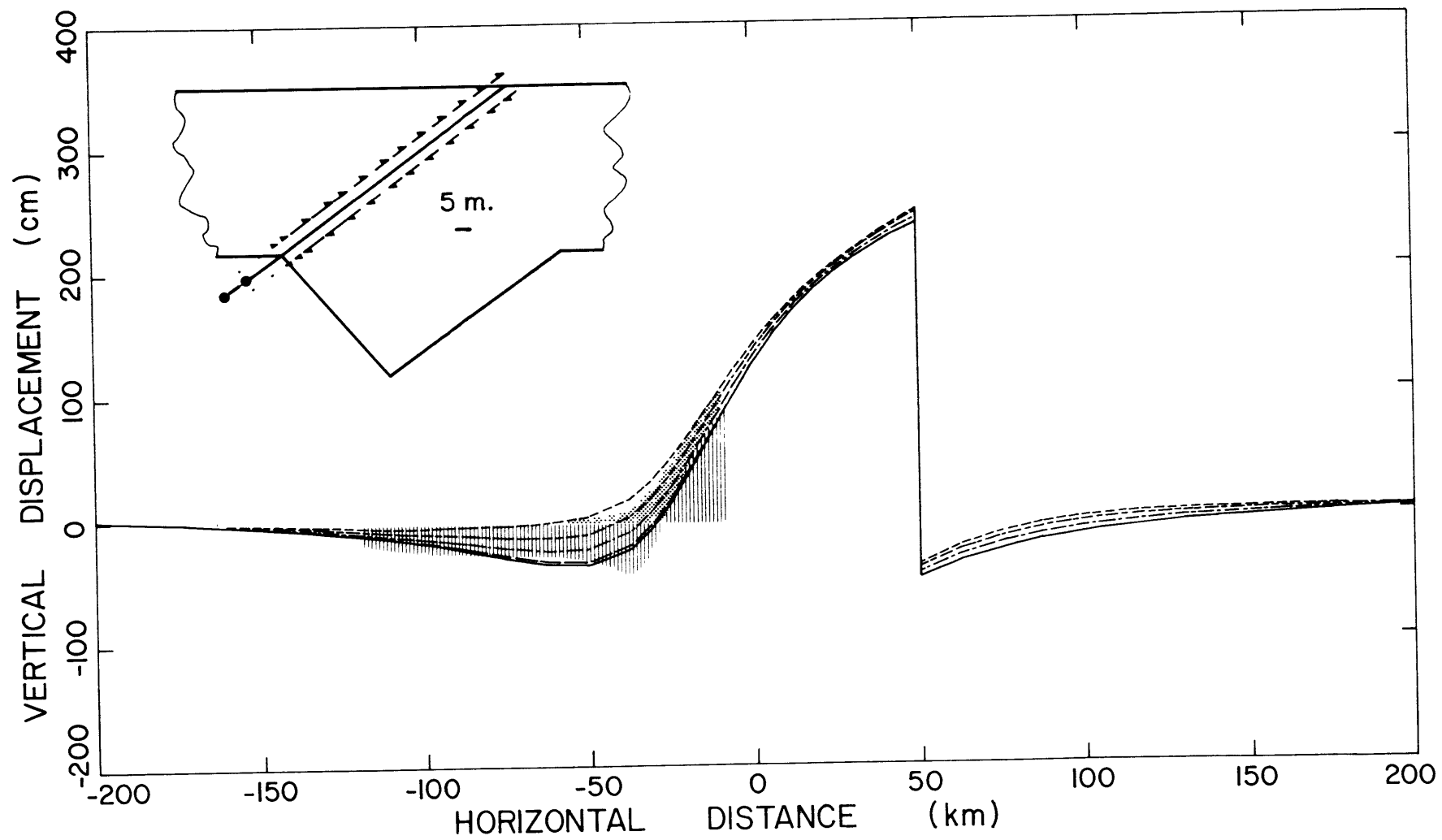


Fig. 5.10

slip to 40 km depth, then decreasing until the asthenosphere. Within the asthenosphere the slip is virtually zero. The diagram also indicates the standard deviations and resolution for these displacements. The surface displacements only slightly constrain the fault near the surface. To satisfy the tsunami data, these segments are restricted to 500 cm displacement; arbitrary displacements do not significantly change the slip at greater depths.

Using this geometry and fault slip inverted from profile A, the model reproduces the time-dependent behavior in the geodetic profile. Figure 5.10 compares the reduced profile A to the resulting vertical displacements. Except near the anomalous bulge, the fit is good; it yields a broad zone of uplift throughout the profile. Decreasing the slip on the deepest segments tends to decrease the uplift. This is important if an error in the absolute datum occurs in the data set. Unfortunately, the constant 35° dip violates the focal mechanism solution and structural features.

The simplicity of the previous model does argue for a variation that fulfills all the constraints. First, the dip near the hypocenter must be shallow to satisfy the focal mechanism and to intersect the Nankai trough. Second, the fault must meet the asthenosphere between the zone of seismic subsidence and the trough. An obvious model follows the inner margin of the microseismicity in Figure 5.5. Indeed, this model, A-5, does give the preferred behavior.

Profile A again represents the discretized data set

after correcting for the secular deformations (Appendix C). The absolute datum is now retained during the inversion, although the weighting is halved. The resulting fault slip and surface displacements, although at first peculiar, faithfully produce the major features of the time-dependent deformations. Figure 5.11 gives the fault parameters determined for the preferred inversion. In this case the parameters are free to vary from the surface to the asthenosphere. Again the resolution improves with increasing depth along the fault. This reflects the surface distribution of geodetic data. The model shows one unusual feature: the slip has a minimum near the hypocenter. Unfortunately, the resolution lengths indicate incomplete discrimination for adjacent nodes. Again the fault slip decays near the asthenosphere. With decreasing depth the resolution rapidly deteriorates; the geodetic data controls the surface displacements only slightly. In this case the starting model for the inversion had near-surface fault displacements that satisfy the tsunami data.

The vertical displacements are given in Figure 5.12 overlain by the geodetic data. The model incorporates a slight change in the absolute datum: the net post-seismic uplift decreases over the whole survey. This is insignificant relative to the errors found in tidal records. Again the deformations show a large deviation from the bulge tentatively attributed to the swarm of aftershocks. The tsunami source region shows vertical offsets within the proper

Figure 5.11

Fault parameters and resolution for model A-5. The schematic at the bottom gives the fault configuration using the horizontal scale; the arrows indicate positive fault slip. Projected above each node on the fault are the displacements for the fault slip (filled circles) based on the inversion. The vertical bars extending from each displacement denote the standard deviation for the slip, while the horizontal bars give the resolution length at each fault node. Both the resolution and errors are smallest along the deeper segments of the fault. Near the surface both are poor using the geodetic data; however, the tsunami source region constrains the initial model. The hatching suggests the inferred limits on the fault displacement introduced by the resolution and error analysis. The inversion gives a 3 m offset near the fault bend, but the analysis indicates only partial resolution. The shading reflects smoothing over the resolution length.

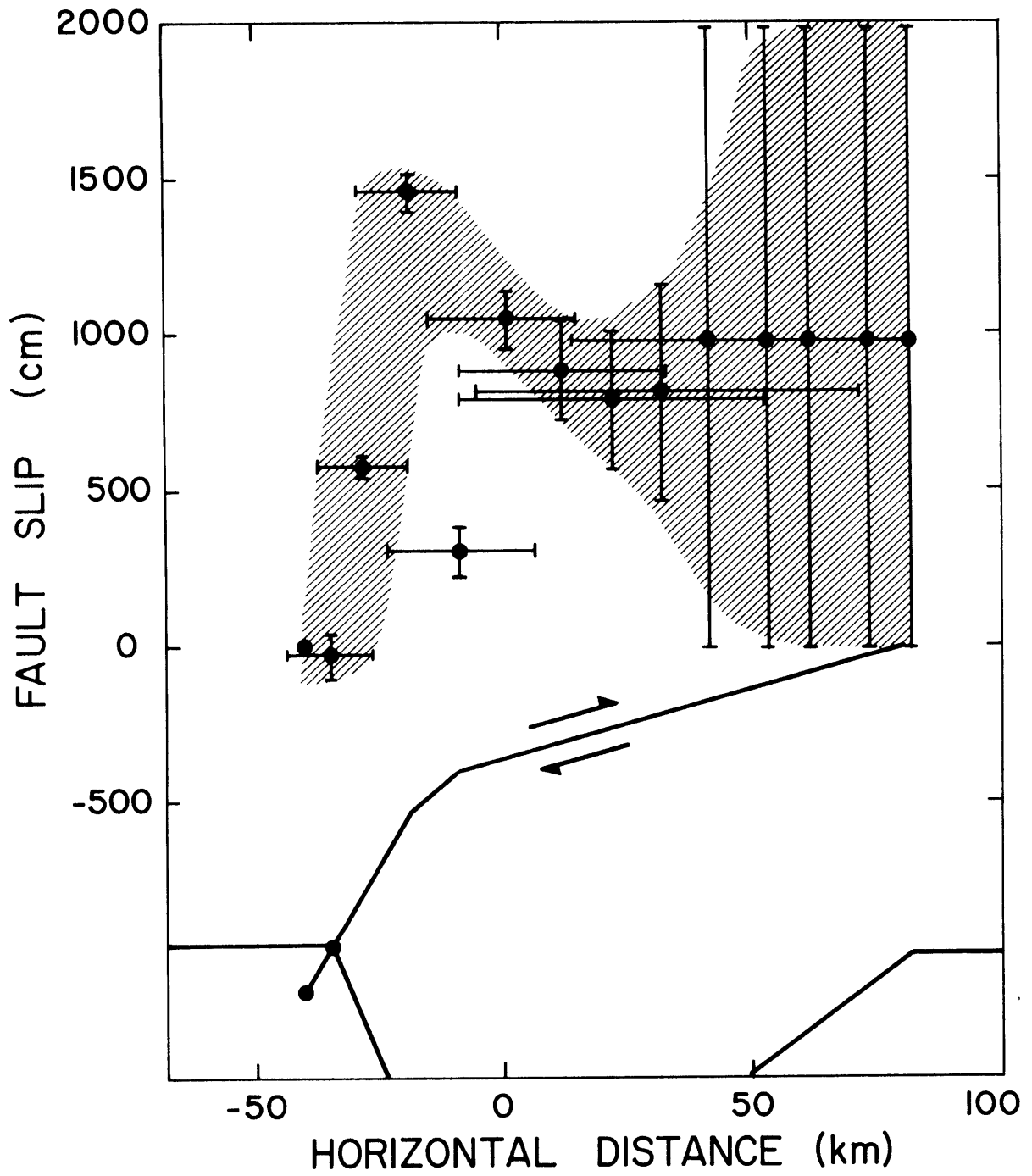


Fig. 5.11

Figure 5.12

Vertical surface displacements for model A-5 in Figure 5.5b constrained by profile A. The inset depicts the geometry and fault displacements when the 10 meter line gives the scale for the fault offset. The offset reaches a maximum of 14.5 meters at approximately 30 km depth, while near the surface it averages 9.7 meters. Again we assume constant displacements with time. The vertical bars extending from the baseline denote the seismic displacements following the earthquake from the reduced profile A. This seismic baseline is offset 4 cm from the zero line for the best fitting model. The seismic plus post-seismic deformations are indicated by the dotted region extending from its baseline. The post-seismic baseline is offset 7 cm relative to the seismic baseline which lies within the error margin for the absolute datum (Fitch and Scholz, 1971). For a viscosity of 1.4×10^{20} poise the curves denote the seismic displacement at 0. (solid), and post-seismic plus seismic at 2., 10., 20., and 40. years following the earthquake.

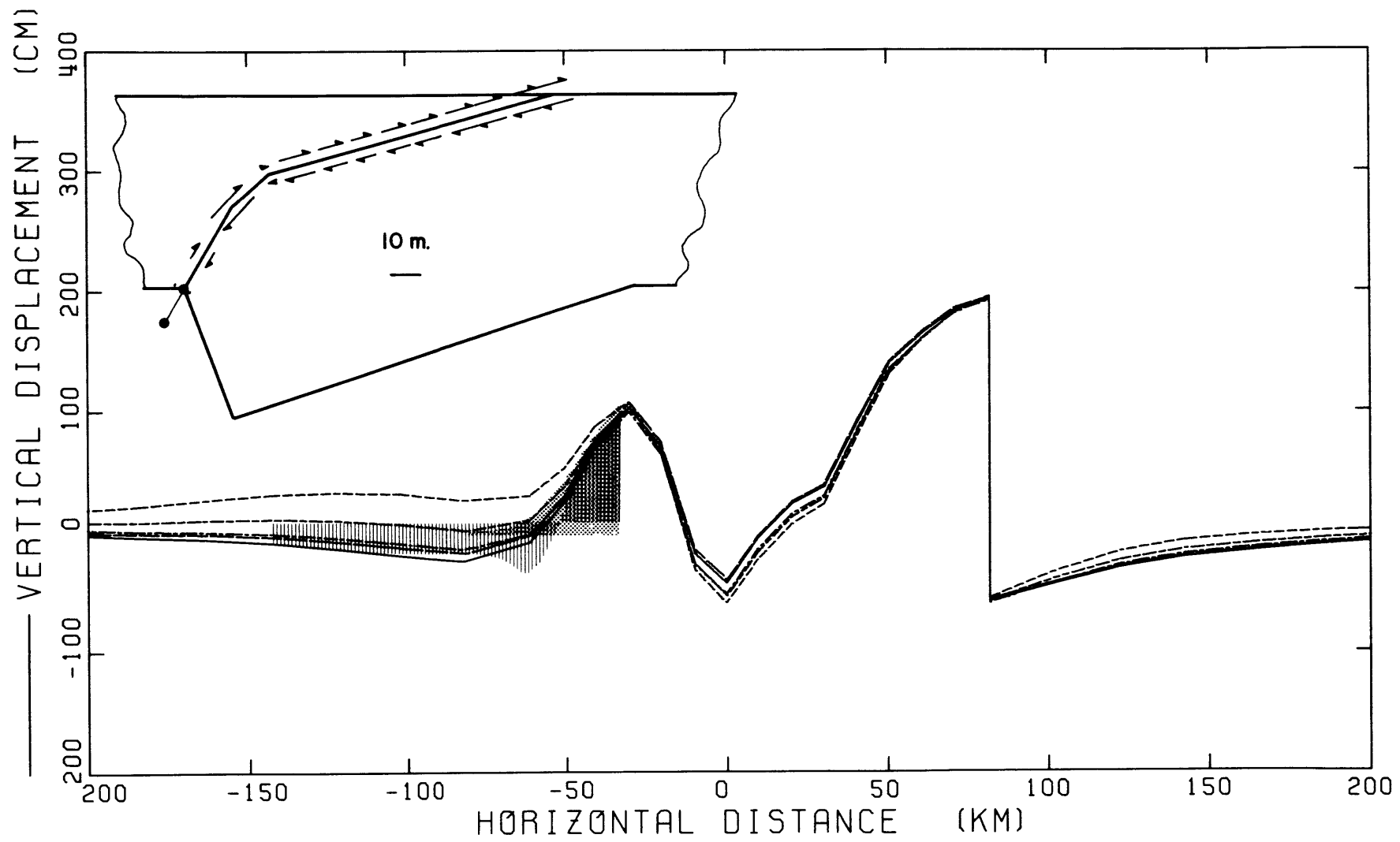


Fig. 5.12

range, a few meters. The model, however, gives an anomalous region of subsidence between the geodetic and tsunami controls. Yet a corresponding structure exists offshore in the form of sedimentary basins (Ludwig, et al., 1973). Although the model does not simulate finite deformations, this predisposition does suggest the origin of the basins: they form near an abrupt bend in the descending oceanic lithosphere. A distinct gravity minimum comparable to the Nankai trough occurs within the basins (Ludwig, et al., 1973). The morphology of the basins further supports this assertion. It suggests flat-lying sediments with an outer ridge thrust upwards from the Nankai trough. Thus the surface deformations may reflect the bending slab beneath the island arc.

Independent tilt data is also available for the 1946 Nankaido earthquake at Muroto promontory. Figure 5.13 gives this data (Okada and Nagata, 1953). Assuming a linear trend for the secular deformations, the seismic offset becomes 6.2 seconds. This corresponds well with tilts estimated from model A-5 in Figure 5.14. The decay following the earthquake, however, differs from the post-seismic model. The observations suggest a relaxation time of 1/2 year, but the model indicates a decay time closer to 5 years. Before any conclusions are drawn, a number of factors need further consideration. If the tilt observations are correct, significant tilts occur before and during the geodetic survey in 1947. Thus, the effects of the short term tilts are obscured

Figure 5.13

Recent history of tilting at Muroto promontory when leveling lines are projected on a line perpendicular to the fault trace. The ordinate gives the tilt in seconds of arc, while the abscissa extends from 1830 to 1970 in increments of 10 years. Positive tilt corresponds to uplift of the promontory relative to inland Shikoku. The tilt data, denoted by dots, are taken from leveling lines; the dotted or dashed curves are extrapolations. The double arrows estimate the permanent tilt (from Okada and Nagata, 1953; Fitch and Scholz, 1971).

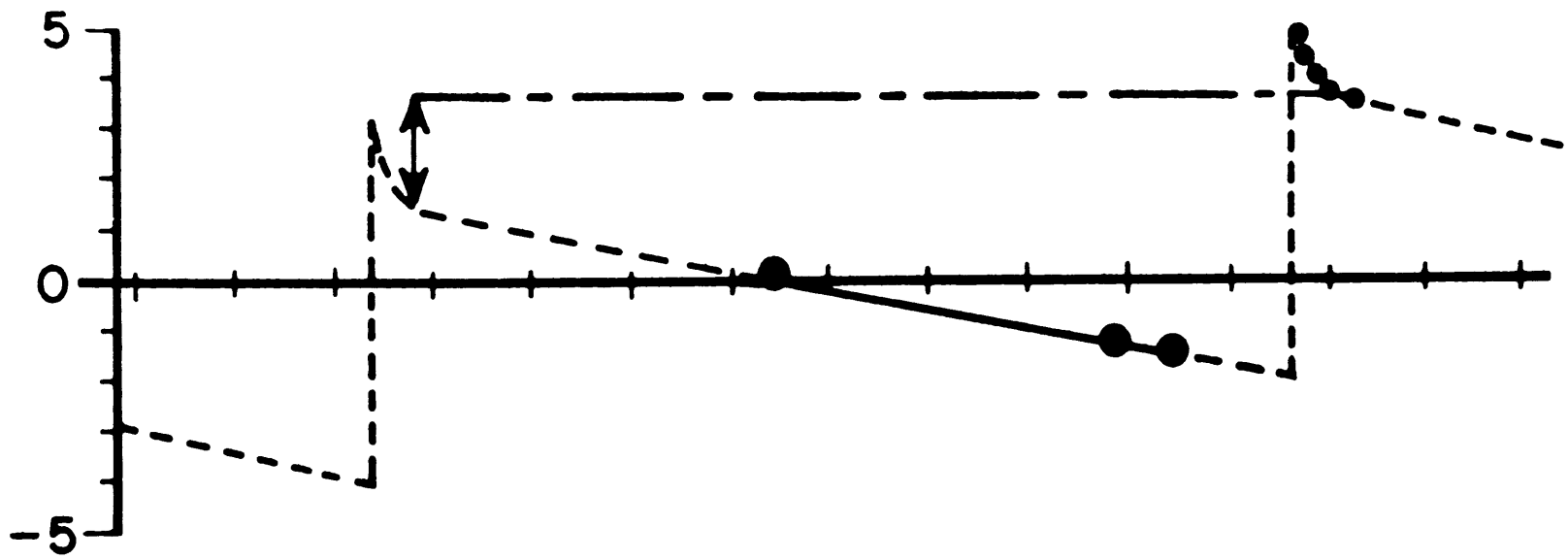


Fig. 5.13

Figure 5.14

Tilts from model A-5 using the horizontal scale of Figure 5.12. For a viscosity of 1.4×10^{20} poise, six times after the earthquake are shown: 0. (solid), 2., 10., 20., 40., and 200. years. The tilt is estimated using a central difference approximation. Muroto point corresponds approximately to -40 km on the horizontal distance scale.

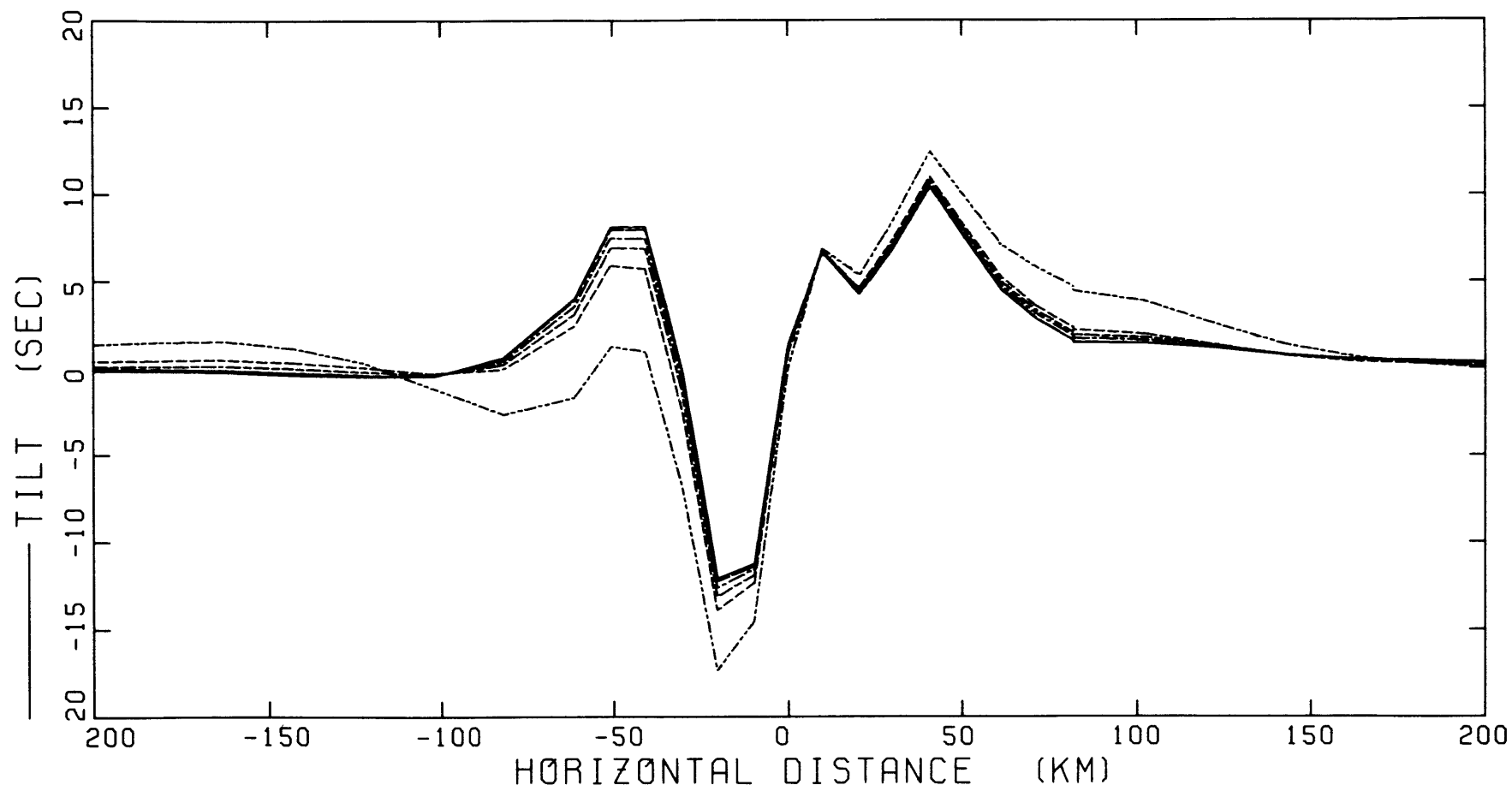


Fig. 5.14

in the original profiles for the seismic displacements; the tilts are partially contained in the seismic deformations. In this analysis, then, they are not considered too significant. Yet they could reflect different processes occurring on a shorter time scale, such as fault creep (Kanamori, 1973) or dilatancy (Scholz, 1974). This time-scale cannot be resolved using the present analysis.

No post-seismic data exists for the horizontal displacements; however, horizontal displacements are available for the seismic deformations when referred to a baseline approximately 300 km from the fault (Fitch and Scholz, 1971). Unfortunately, the displacements are seriously contaminated by pre-seismic deformations. Moreover, the baseline's distance from the fault makes a two-dimensional model only a rough approximation. Only a cursory comparison is then appropriate.

Figure 5.15 gives the horizontal deformations using the model A-5 in Figure 5.5 for southwest Japan. The baseline follows the axis of the plot; consequently, extending the slope from the baseline at approximately -200 to -150 km in Figure 5.15 gives a corrected zero line. Using this as a guide, the maximum horizontal displacements from the theoretical model become 1.5 to 2.0 m; within 50 km they decay to less than 1.0 m. Fitch and Scholz (1971) report similar behavior on Shikoku after correcting for secular deformations. Under these circumstances, the results appear quite good.

Figure 5.15

Horizontal displacements resulting from model A-5 in Figures 5.5b and 5.12. Again the curves show six times using a viscosity of 1.4×10^{20} poise for the asthenosphere: 0. (solid), 2., 10., 20., 40., and 200. years following the earthquake. The thick, dotted lines represents the baseline extrapolated from the horizontal displacements far from the fault. The maximum displacement on Shikoku then approaches 2 meters.

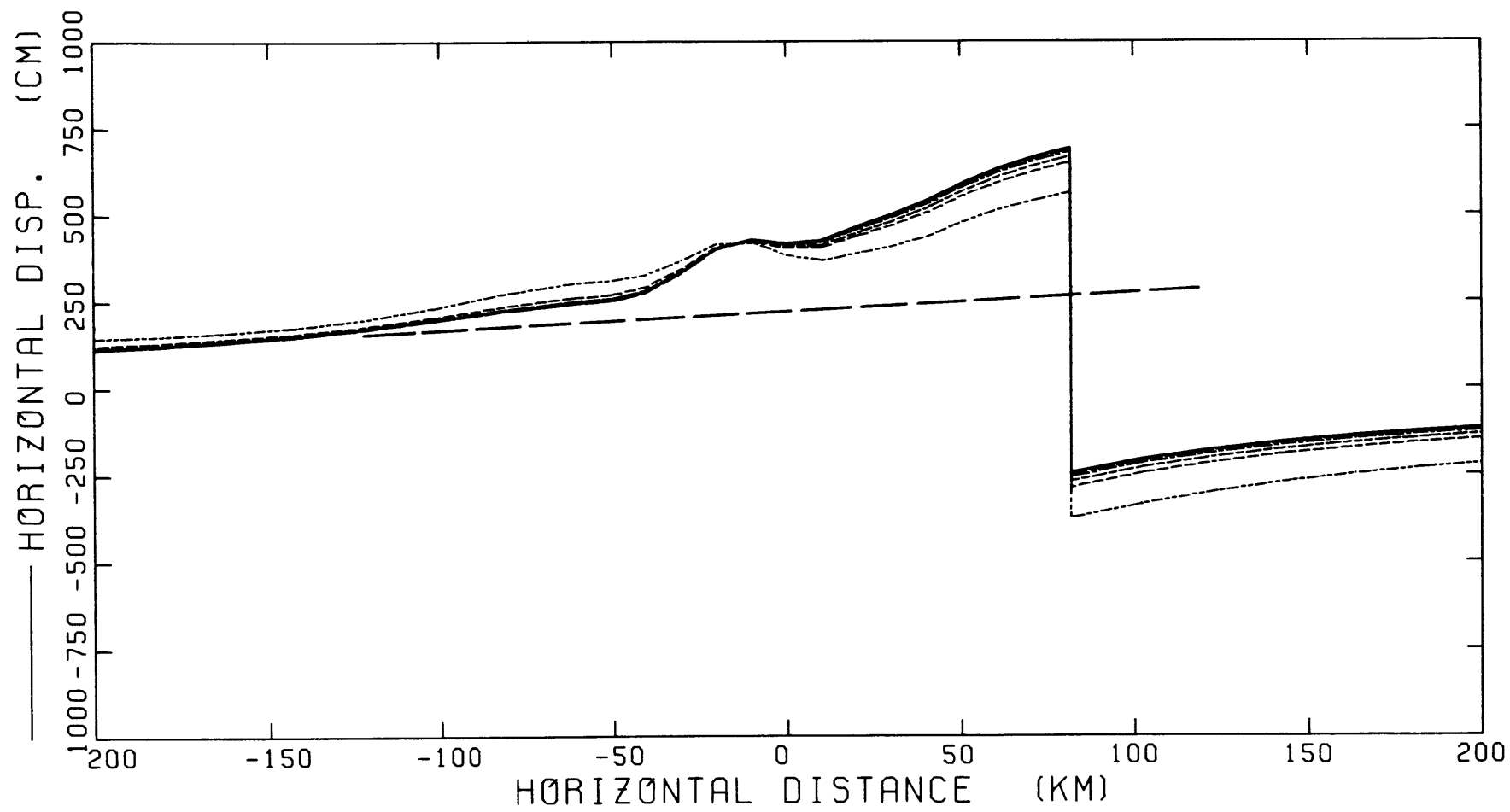


Fig. 5.15

The maximum shear stress resulting from this model now suggests the origin of the crustal seismicity: within the continental lithosphere the shear stress released by the earthquake attains a maximum near the bend. Figure 5.16 illustrates this phenomenon for the preferred model. Near the bend the stress release reaches 500 bars. Comparing the zone of deep microseismicity in Figure 5.5 to this model, the earthquakes occur precisely in the regions of highest stress change. Here the stress change increases the initial stress after assuming a model similar to Figure 4.19. Although this does not represent a causal proof, it does pose the possibility.

Unlike the vertical deformations, the maximum shear stress varies only 10% during the first 20 years. It is doubtful that these variations are responsible for the after-shock sequences. The evidence, instead, supports the concept based on stress concentrations and inhomogeneities near the fault tip (Rybicki, 1973). Only this hypothesis allows short decay times together with mechanisms having their polarity opposite to the main shock as observed in the Kurils (Aver'yanova, 1973).

To summarize, this model of southwest Japan represents a consistent explanation for the regional structure, geodetic data, seismicity, and focal mechanisms. It suggests mantle stress relaxation as a result. With this assumption the geodetic data constrains the mantle viscosity to

Figure 5.16

Maximum shear stress and direction of the maximum compressive stress for model A-5. The heavy line outlines the configuration of the lithosphere and the fault plane. The direction of each line segment represents the orientation of the maximum compressive stress, while the length denotes the magnitude of the maximum shear stress. The scale in bars is given in the lower-right. Each line segment represents the stress within a particular element at a separate time; these times are 0. (solid), 2., 10., 20., 40., and 200. years after the fault dislocation. Only small magnitude variations occur during the first 20 years. The earthquake, however, introduces large (500 bars) stress changes near the bend in the fault.

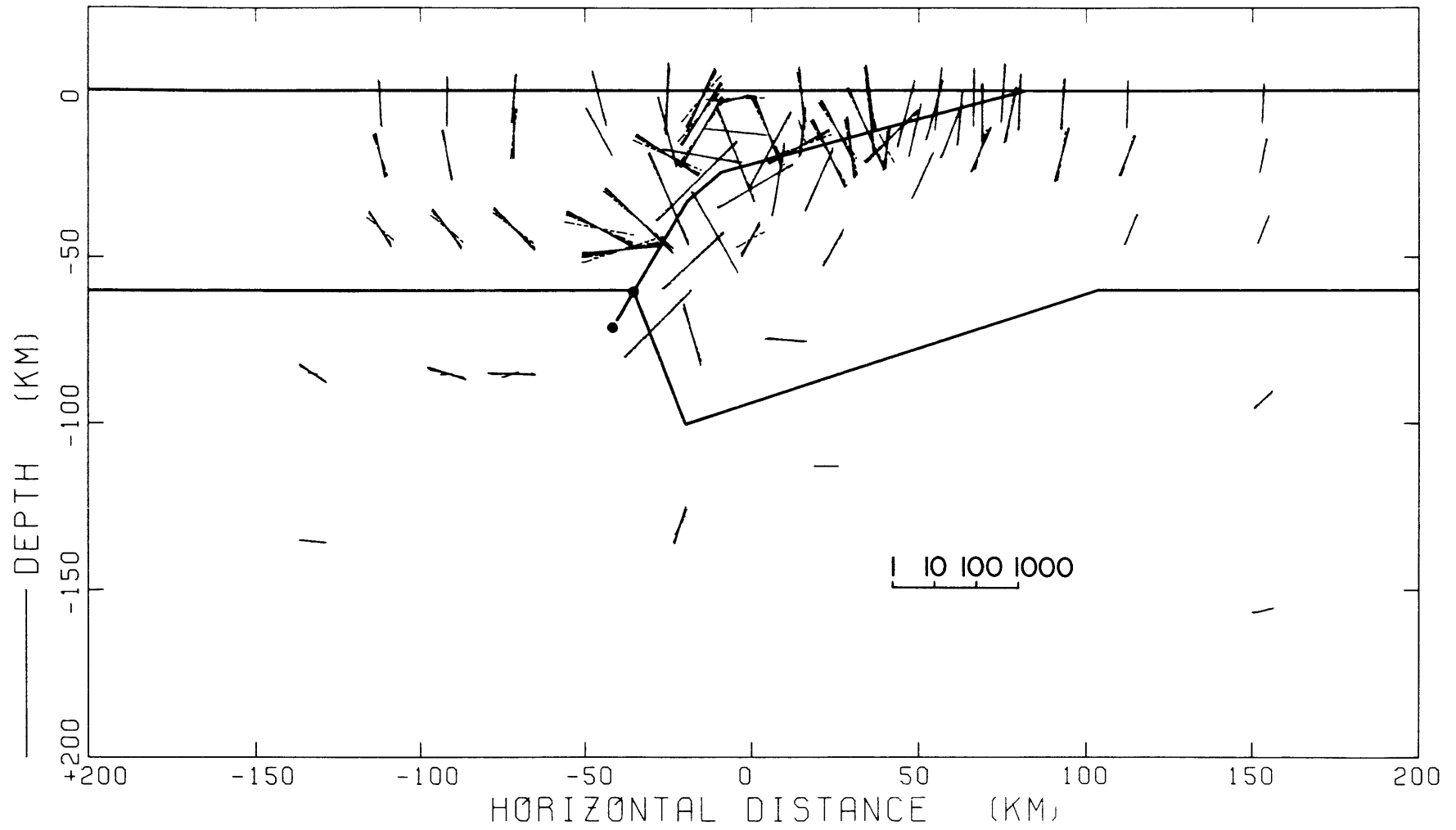


Fig. 5.16

10^{20} poise and the lithosphere to 60 km thickness. These are reasonably consistent with other independent estimates considering the unusual region. In addition, the data requires a sharp bend in the fault. This is similar to Kanamori's (1972) proposal for the region, except the bend does not necessarily imply that the descending slab abruptly terminates.

6. CONCLUSIONS AND DIRECTIONS

6.1 Conclusions

This thesis suggests an approach to resolve time-dependent strains in an earthquake zone. Concentrating upon only one aspect of the problem, the consequences of stress relaxation within the asthenosphere on post-seismic deformations, a tractable model first requires development. Here a numerical strategy using the finite element method proves to be optimum.

The model first reduces the material behavior to linear viscoelasticity, initial elastic deformation followed by stress relaxation. This retains the essential features of the asthenosphere. Using an approximate Laplace transform and discretizing the continuum yields a relatively inexpensive solution to deformations in the medium. Introducing the fault interface with arbitrary boundary conditions between the faces, determining the effects of gravity, and inverting the data to a model directly follow using finite elements. Thus, simple fault creep is possible. The technique gives an extremely versatile solution method for linear viscoelasticity or any other problem having a similar mathematical structure. The models here are two-dimensional, but only minor changes are necessary for three dimensional computations given the additional computer time. Using convolutions, the approach is directly extendable to

other time-dependent problems involving loading (ie. sedimentation, glacial, or strain accumulation prior to an earthquake), and fault creep.

Beginning with the assumption of mantle stress relaxation occurring on the time scale of the strain accumulation for earthquakes, the method yields solutions that conclusively demonstrate its effects and defines its relative significance. Thus, for thrust faults the vertical surface displacements provide the most sensitive and practical indicator of mantle relaxation. But these displacements alone may be insufficient to distinguish between alternate mechanisms: fault creep and dilatancy. Measurements on opposite sides of the fault and gravity hold the greatest promise as a tool to constrain the mechanism and modes of post-seismic deformation. Comparing the stress release and the initial pre-stress to the aftershocks gives an additional constraint.

The results for idealized numerical experiments prove that stress relaxation in the asthenosphere can play an important role. For viscosities near 10^{19} to 10^{20} poise alterations in the post-seismic deformations and stresses are evident. The lithospheric thickness and the relative fault depth dominate the shape of the post-seismic deformations. The boundary conditions imposed on the fault interface, whether prescribed offset or stress release give different time-dependent deformations and stress

states within the lithosphere. This is analogous, respectively, to no fault creep as opposed to fault creep along a weakened zone. The models favor either fault creep or a constant dislocation within the lithosphere. Extending the fault through the lithosphere gives large and continuing surface deformations, particularly for a constant stress release applied at the fault interface. These models and relationships suggest, then, regions where asthenospheric stress relaxation manifests itself.

Furthermore, the models contradict Scholz's (1974) assertion that stress relaxation in the asthenosphere cannot account for post-seismic subsidence on both sides of the fault. According to his analysis, post-seismic deformations for the 1964 Niigata earthquake originate from dilatancy recovery. Yet a definitive result is still not forthcoming; dilatancy, stress relaxation or both may occur. Only the data is insufficient to uniquely resolve the contributions. This emphasizes the clear need for extensive pre- and post-earthquake monitoring: the role of dilatancy as opposed to mantle stress relaxation or fault creep is germane to earthquake prediction.

Reviewing evidence of post-seismic surface deformations, the 1946 Nankaido earthquake presents the most complete and convincing evidence. Other geophysical evidence and the conjectured history of southwest Japan are also consistent with a low viscosity for the asthenosphere,

an essential property for stress relaxation. Using only mantle stress relaxation as the mechanism producing the anomalous surface deformations, inversion theory gives the preferred model satisfying the geodetic data and auxiliary constraints. These additional constraints include a smooth initial model, a low-angle thrust fault near the hypocenter, and a tsunami source region that remains consistent with the observations. The results suggest a general interpretation for the tectonics of southwest Japan: the structure and seismicity originates from a recently subducted lithosphere that abruptly bends beneath the continental margin. Moreover, the model indicates the following properties:

1. The constraints impose a shallow, 15° dipping fault plane from the inner trench margin to 26 km depth, then plunging at 60° dip. A short, 150 km descending lithosphere satisfies the data; thus, the model is consistent with recent dates for the initiation of subduction (3 my according to Moore, 1974).
2. The slip along the reverse fault varies from 9 meters near the surface to a maximum of 14 meters at 35 km depth, then decays towards the base of the lithosphere at 60 km depth. The error for the lithospheric thickness becomes approximately 10 km.
3. The viscosity for the asthenosphere is 10^{20} poise for the preferred model. This is an order of magnitude lower

than most results from post-glacial rebound (Artyushkov, 1967; McConnell, 1968; O'Connell, 1971).

4. The deformation pattern suggests the origin of the sedimentary basins off each promontory in Figure 6.1: they originate from the abrupt bend during the lithospheric descent.

5. The preferred model, A-5, both suggests and supports a segmented descending lithosphere depicted in Figure 6.1. These segments are partially decoupled allowing the unique pattern of major earthquakes (i.e. Kanamori, 1972; Ando, 1974), an embayed shoreline characterized by submarine basins off each promontory (i.e. Ludwig, et al., 1973), and a slip direction for the 1946 Nankaido earthquake that neither lies perpendicular to the trench axis nor shows any evidence of strike-slip components (Kanamori, 1972). In addition, focal mechanisms for the microseismicity suggest strike-slip solutions within the Kii sound (Shiono, 1970b). These are consistent with slip between adjacent lithospheric segments, and thus, are similar to tearing that occurs beneath the Aleutians or Honshu (Stauder, 1968a; Abe, 1972; Carr, et al., 1973).

6. The maximum shear stress released by the earthquake approaches 500 bars near the bend. Although the stress approximation has first-order errors, the magnitude and orientation of the stress tensor places the greatest change in shear stress near the fault bend. Moreover, the stress

Figure 6.1

Inferred tectonic structure for southwest Japan based on model A-5. Hatching denotes the sedimentary basins off each promontory, and the stippled area corresponds to the Nankai trough (Ludwig, et al., 1973). The preferred model and constraints suggest a sequence of major lithospheric tears that separates and partially decouples each segment; the dotted lines indicate these subdivisions or tears. The structural divisions of the embayed shoreline, microseismicity, historical earthquakes (Kanamori, 1972; Ando, 1974), relative plate velocities (McKenzie and Parker, 1967), slip vectors for the 1944 and 1946 earthquakes (Kanamori, 1972), and implications of the preferred model A-5 are consistent with this interpretation.

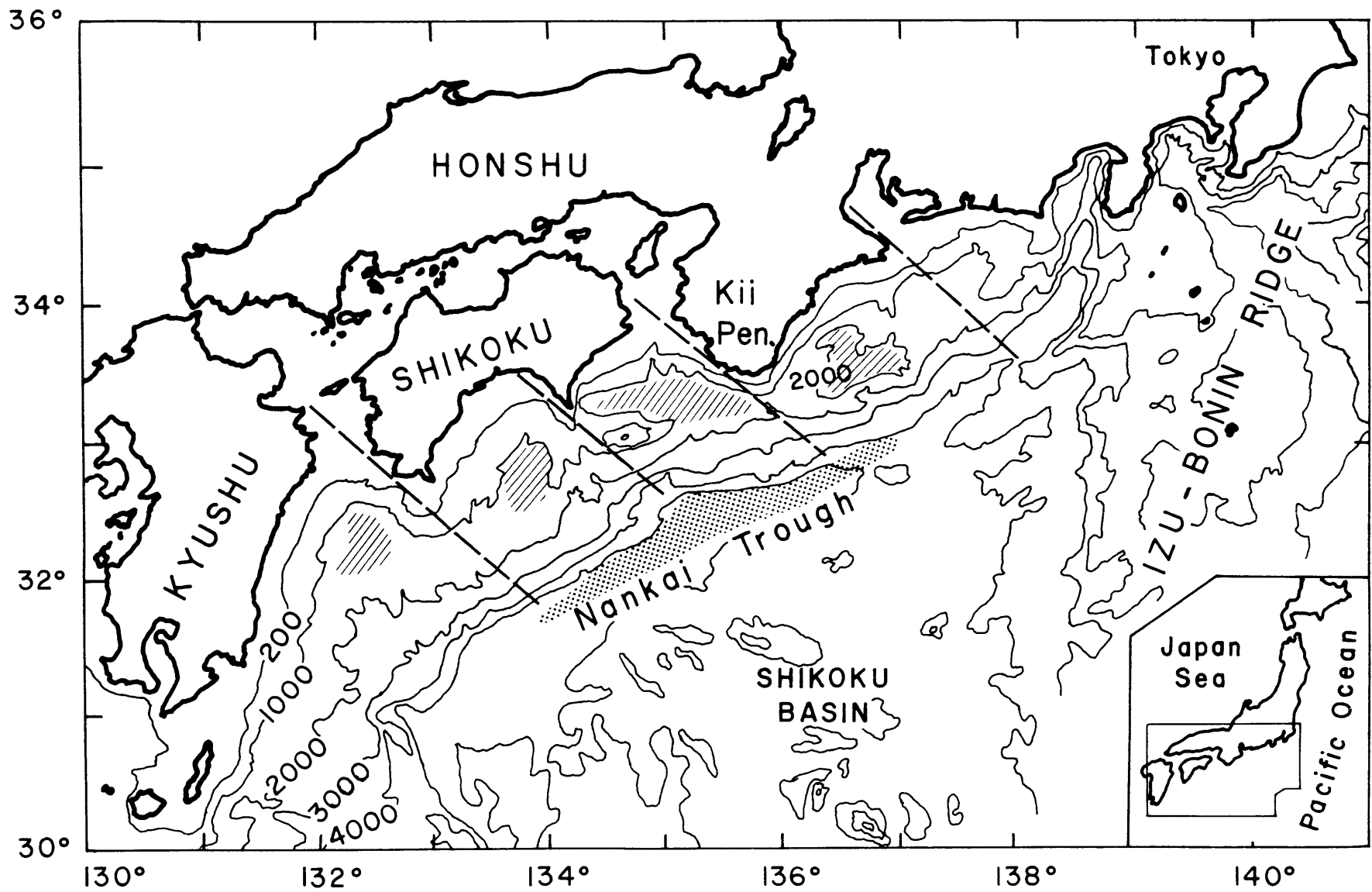


Fig. 6.1

microseismicity. The predicted effects would be essentially similar.

6.2 Implications and Future Directions

Using the preferred model containing a bending lithosphere and assuming only mantle stress relaxation, the structure, seismicity, and subduction history for southwest Japan reduce to a consistent scenario. Yet the potential contributions of other mechanisms, fault creep and dilatancy recovery, on the post-seismic deformations remain obscure. Additional data may resolve the relative contributions of the two mechanisms. Gravity, in particular, could discriminate between these alternate explanations. Still, further sophistication using computer models may realize insights into fault creep processes and dilatancy recovery if they are included, first separately then jointly, in the analysis and inversion. Combined with extensive geodetic and gravity surveys, tidal stations, continuous tilt records, and seismic velocities, both questions of post-seismic anomalies and predictive methods would reap immense benefits.

Seismic gaps and strain accumulation do pose further questions for lithospheric and asthenospheric interactions. Coupled with pattern recognition and a statistical analysis, these questions represent an extension of the theoretical analysis contained in this thesis: how does the mantle control the short-term accumulation of strain energy at an

reinforces the initial stress originating from thermal density anomalies. The region of maximum stress then corresponds to the one of deep microseismicity on the Kii peninsula. Compared to the idealized models where the stress release hovers near 10% of the initial stress, the 1946 Nankaido earthquake may relax a larger fraction of the prestress over localized regions.

The preferred model, A-5, based on the geodetic data and on the assumption of asthenospheric stress relaxation both satisfies and explains these additional features of southwest Japan. Significantly, a model satisfying the focal mechanism and tsunami source and excluding any sections of normal faulting, but placing the microseismicity within the descending lithosphere, could not be established if only mantle relaxation occurs following the earthquake. Eliminating the shallow dip on the fault plane allows a model that is similar to Fitch and Scholz's (1971). Yet no evidence exists for a major fault trace between Shikoku and the Nankai trough. The preferred, A-5, model, however, resembles Kanamori's (1972) proposal for the structure of southwest Japan using only inferences from the seismicity. Both cases place the microseismicity within the continental crust and each requires a short slab. The difference is partially one of semantics: model A-5 shown here requires a sharp bend with slip also occurring deeper; Kanamori (1972) terminates the descending slab at the zone of

island arc? Here a three-dimensional analysis becomes crucial which further precludes any nonlinear phenomenon in the method.

Problems within the realm of long-term surface deformations during the evolution of a tectonic zone will not yield to this approach. Nonlinear creep probably controls crustal deformations, formation of the trench margin, and similar quasi-fluid dynamic processes. Thus, these require a different approach for a clear resolution. At this point, whether finite elements or finite differences are optimum, must await further developments.

REFERENCES

- Abe, K., Seismological evidence for a lithospheric tearing beneath the Aleutian Arc, Earth and Planet. Sci. Letters, 14, 428-432, 1972.
- Adey, R. A. and C. A. Brebbia, Efficient method for solution of viscoelastic problems, ASCE, EM6, 1119-1127, Dec. 1973.
- Alewine, R. W., Application of linear inversion theory toward the estimation of seismic source parameters, Ph.D. thesis, Calif. Inst. of Tech., 1974.
- Alewine, R. W. and P. H. Jungels, Applications of stochastic inversion theory and the finite-element method to zero-frequency seismology: the 1964 Alaskan earthquake, submitted to Geophys. J. R. Astr. Soc., 1974.
- Allen, C. R. and D. V. Helmberger, Search for temporal changes in seismic velocities using large explosions in southern California, in Proceedings of the conference on tectonic problems of the San Andreas fault system, ed. R. L. Kovach and A. Nur, Stanford U., 1973.
- Anderson, D. and J. Whitcomb, The dilatancy-diffusion model of earthquake prediction, in Proc. conf. on tectonic prob. San Andreas fault system, Stanford Univ. Publ. Geol. Sci., XIII, 417-426, 1973.
- Ando, M., Source mechanisms and tectonic significance of historical earthquakes along the Nankai trough, Japan, preprint, Disaster Prevention Research Inst., Kyoto Univ. Japan, 1974.
- Argyris, J. H., Energy theorems and structural analysis, Aircraft Eng., 26, 347-356 (Oct.), 383-387, 394 (Nov.), 1954.
- Artyushkov, E., On the isostatic equilibrium of the earth's crust, Geophys. J. R. Astr. Soc., 14, 251, 1967.
- Aver'yanova, V. N., Seismic foci in the far east, Israel Program for Scientific Translations, Jerusalem, 207 pp., 1973.
- Backus, G. E. and J. F. Gilbert, Numerical applications of a formalism for geophysical inverse problems, Geophys. J. R. Astr. Soc., 13, 247-276, 1967.

- Barcilon, Victor, On the uniqueness of inverse eigenvalue problems, Geophys. J. R. Astr. Soc., 38, 287-298, 1974.
- Barenblatt, G. I., The formation of equilibrium cracks during brittle fracture. General ideas and hypotheses. Axially-symmetric cracks, Appl. Math. Mech., 23, 623-636, 1959.
- Barker, T., Static strain in a nonuniform solid; with applications to California. Ph.D. thesis, Univ. Calif., San Diego, 1974.
- Benioff, H., Earthquakes and rock creep, 1., Bull. Seismol. Soc. Am., 41, 31-62, 1951.
- Berg, C. A., Relation between stress drop, fault friction, and crustal strength in shallow focus strike slip faulting, J. Geophys. Res., 73, 2217-2223, 1968.
- Biehler, S., A possible gravimetric method for the prediction of earthquakes, Trans. Am. Geophys. Union, 55, 355, 1974.
- Bilby, B. A. and J. D. Eshelby, Dislocations and the theory of fracture, in Fracture, ed. by H. Liebowitz, Academic Press, N.Y., Vol. I. pp. 99-182, 1968.
- Biot, M. A., Theory of stress-strain relations in anisotropic viscoelasticity and relaxation phenomena, Jour. Applied Phys., 25, 1385-1391, 1954.
- Biot, M. A., Linear thermodynamics and the mechanics of solids, Third U.S. Nat. Cong. of Appl. Mech., pp. 1-18, 1958.
- Biot, M. A., Mechanics of incremental deformations, Wiley, 504 pp., 1965.
- Biot, M. A., Variational principles in heat transfer, Clarendon, 185 pp., 1970.
- Braslau, D. and P. Lieber, Three dimensional fields due to a Volterra dislocation imbedded in a layered half-space: analytic representation of a seismic mechanism, Bull. Seism. Soc. Am., 58, 613-628, 1968.
- Burridge, R. and L. Knopoff, Body force equivalents for seismic dislocations, Bull. Seismol. Soc. Am., 54, 1875-1888, 1964.

- Carr, J. M., R. E. Stoiber, and C. L. Drake, Discontinuities in the deep seismic zones under the Japanese arcs, Bull. Geol. Soc. Am., 84, 2917-2930, 1973.
- Carslaw, H. S. and J. C. Jaeger, Conduction of heat in solids, Clarendon, 510 pp., 1959.
- Christensen, R. M., Theory of viscoelasticity: An introduction, Academic Press, 245 pp., 1971.
- Courant, R., Variational methods for the solution of problems of equilibrium and vibrations, Bull. Amer. Math. Soc., 49, 1-23, 1943.
- Desai, C. S. and J. F. Abel, Introduction to the finite element method, Van Nostrand, 462 pp., 1972.
- Dubner, H. and J. Abate, Numerical inversion of Laplace transform by relating them to the finite Fourier Cosine transform, Journ. Assoc. Comp. Mach., 15, 115-123, 1968.
- Elsasser, W. M., Convection and stress propagation in the upper mantle in The application of modern physics to the earth and planetary interiors, ed. S. K. Runcorn, pp. 223-246, Wiley - Interscience, 1969.
- Fitch, T. J. and C. H. Scholz, Mechanism of Underthrusting in southwest Japan: A model of convergent plate interactions, J. Geophys. Res., 76, 7260-7292, 1971.
- Fujita, N., Recent vertical displacements in coast of Japan, Journ. Geol. Soc. Japan, 14, 159-161, 1969.
- Fujita, N., Y. Fujii, and T. Tada, Crustal activities in the eastern part of Hokkaido, Japan, International Symposium on Recent Crustal Movements, 1974 in Switzerland, 1974.
- Fung, Y. C., Foundations of solid mechanics, Prentice-Hall, 525 pp., 1965.
- Gelfand, I. M. and S. V. Fomin, Calculus of variations, Prentice-Hall, 232 pp., 1963.
- Griffith, A. A., The phenomenon of rupture and flow in solids, Phil. Trans. Roy. Soc. London, A, 221, 163-198, 1921.
- Gurtin, M. E., Variational principles in the linear theory of viscoelasticity, Arch. Rational Mech. Anal., 13, 179-191, 1963.

- Hai-Chang, Hu, On some variational principles in the theory of elasticity and the theory of plasticity, Sc. Sinica, 4, 33, 1955.
- Haskell, N., Motion of a viscous fluid under a surface load, Physics, 6, 265, 1935.
- Hatori, T., Vertical displacement in a tsunami source area and the topography of the sea bottom, Bull. Earthquake Res. Inst., Tokyo Univ., 44, 1449-1464, 1966.
- Hayashi, T., A study of the vertical movements of the earth's crust by means of the precise leveling, J. Geol. Soc. Japan, 15, 1-69, 1970.
- Head, A. K., The interaction of dislocations and boundaries, Phil. Mag., 44, 92-94, 1953.
- Hetyenyi, M., Beams on elastic foundations, U. of Michigan Press, 255 pp., 1946.
- Hilde, T. W. C., J. M. Wageman, and W. T. Hammond, The structure of Tosa Terrace and Nankai trough of south-eastern Japan, Deep Sea Res., 16, 67-75, 1969.
- Hoskin, B. C. and E. H. Lee, Flexible surfaces on visco-elastic subgrades, Journ. Eng. Mech. Div., ASCE, 85, EM4, 2195; 11-30, 1959.
- Huzita, K., Tectonic development of the Median Zone (Setouti) of southwest Japan since the Miocene, with special reference to the characteristic structure of the central Kinki area, J. Geosci., Osaka City Univ., 6, 103-144, 1962.
- Ichikawa, M., Reanalyses of mechanism of earthquakes which occurred in and near Japan, and statistical studies on the nodal plane solutions obtained, 1926-1968, Geophysical Mag., 35, 207-274, 1971.
- Isacks, B. and P. Molnar, Mantle earthquake mechanisms and the sinking of the lithosphere, Nature, 223, 1121-1124, 1969.
- Isacks, B. and P. Molnar, Distribution of stresses in the descending lithosphere from a global survey of focal-mechanism solutions of mantle earthquakes, Rev. Geophys. Space Phys., 9, 103-174, 1971.

- Isacks, B., J. Oliver, and L. Sykes, Seismology and the new global tectonics, J. Geophys. Res., 73, 5855-5899, 1968.
- JMA (Japan Meteorological Agency), Catalogue of major earthquakes which occurred in and around Japan (1926-1958), Seismol. Bull. Japan Meteorol. Agency, Suppl. Vol. 1, 1-91, 1958.
- Jordan, T. H. and J. N. Franklin, Optimal solutions to a linear inverse problem in geophysics, Proc. Nat. Acad. Sci., 68, 291-293, 1971.
- Jungels, P. H. and G. A. Frazier, Finite element analysis of the residual displacements for an earthquake rupture: Source parameters for the San Fernando earthquake, J. Geophys. Res., 78, 5062-5083, 1973.
- Kanamori, H., Tectonic implications of the 1944 Tonankai and the 1946 Nankaido earthquakes, Phys. Earth Planet Interiors, 5, 129-139, 1972.
- Kanamori, H., Mode of strain release associated with major earthquakes in Japan, in: Annual Review of Earth and Planetary Sciences, F. A. Donath (ed.), Vol. I, 1973.
- Kanamori, H. and K. Tsumura, Spatial distribution of earthquakes in the Kii peninsula, Japan, South of the Median Tectonic Line, Tectonophysics, 12, 327-342, 1971.
- Kawasumi, H., Real state of crustal deformations in the Sikoku District, which occurred at the time of and after the Great Nankaido earthquake of Dec. 21, 1946, Publication of Sikoku-Tiho Sogo-Kaihatu Singi-Kai (Committee for the Synoptic Development of the Sikoku District), 1956.
- Kelleher, J. A., Space-time seismicity of the Alaska-Aleutian seismic zone, J. Geophys. Res., 75, 5745-5756, 1970.
- Lanczos, C., Linear differential operators, Van Nostrand, 554 pp., 1961.
- Lee, E. H., Stress analysis in viscoelastic bodies, Quart. Appl. Math., 13, 183, 1955.
- Lee, E. H., J. R. M. Radok, and W. B. Woodward, Stress analysis for linear viscoelastic materials, Trans. Soc. Rheology, 3, 41-59, 1959.

- Lieber, P. and D. Braslau, On an earthquake and aftershock mechanism relating to a model of the crust and mantle, Nonr - 222 (87), Rept. No. AM-65-8, U. C. Berkeley, 1965.
- Love, A.E.H., Mathematical theory of elasticity, 4th ed., Dover, 643 pp., 1944.
- Ludwig, W. J., N. Den, S. Murauchi, Seismic reflection measurements of southwest Japan margin, J. Geophys. Res. 78, 2508-2516, 1973.
- Maruyama, T., On the force equivalents of dynamic elastic dislocations with reference to the earthquake source mechanism, Bull. Earthquake Res. Inst., Tokyo Univ., 41, 467-486, 1963.
- Maruyama, T., Statical elastic dislocations in an infinite and semi-infinite medium, Bull. Earthquake Res. Inst., Tokyo Univ., 42, 289-368, 1964.
- Maruyama, T., On two-dimensional elastic dislocations in an infinite and semi-infinite medium, Bull. Earthquake Res. Inst., Tokyo Univ., 44, 811-871, 1966.
- Matuzawa, T., Study of earthquakes, Uno Shoten, Tokyo, Japan, 213 pp., 1964.
- McConnell, R. K., Isostatic adjustment in a layered earth, J. Geophys. Res., 70, 5171-5188, 1965.
- McConnell, R. K., Viscosity of the mantle from relaxation time spectra of isostatic adjustment, J. Geophys. Res., 73, 7089, 1968.
- McCowan, D. W., P. Glover, and S. S. Alexander, An inversion technique for the static finite element method (FEM), Trans. Am. Geophys. Union, 55, 353, 1974.
- McKenzie, D. P., Speculation on the consequences and causes of plate motion, Geophys. J. R. Astr. Soc., 18, 1-32, 1969.
- McKenzie, D. P. and R. L. Parker, The North Pacific: An example of tectonics on a sphere, Nature, 216, 1276-1280, 1967.
- Mogi, K., Relationship between shallow and deep seismicity in the western Pacific region, Tectonophysics, 17, 1-22, 1973.

- Moore, C., personal communication, 1974.
- Mura, T., The Continuum Theory of dislocations in Advances in Materials Research, ed. H. Herman, Vol. 3, pp. 1-108, Wiley, 1968.
- Nakamura, K., K. Kasahara, and T. Matsuda, Tilting and uplift of an island, Awashima, near the epicentre of the Niigata earthquake of 1964, J. Geol. Soc. Japan, 10, 172-179, 1964.
- Nur, A. and Mavko, G., Post-seismic viscoelastic rebound, Science, 183, 204-206, 1974.
- O'Connell, R. J., Pleistocene glaciation and the viscosity of the lower mantle, Geophys. J. R. Astr. Soc., 23, 299-327, 1971.
- Okada, A., Strike-slip faulting of Late Quaternary along the Median Dislocation Line in the surroundings of Awa-Ikeda, northeastern Shikoku, Quaternary Res., 7, 15-26, 1968.
- Okada, A. and T. Nagata, Land deformation of the neighborhood of Muroto point after the Nankaido great earthquake in 1946, Bull. Earthquake Res. Inst., Tokyo Univ., 31, 169-178, 1953.
- Okada, A. and K. Kasahara, Postseismic subsidence of Awashima island, Bull. Earthquake Res. Inst., Tokyo Univ., 44, 247-259, 1966.
- Orringer, O. and S. E. French, FEABL, AFOSR TR72-2228, Dept. Aeron. and Astro., Mass. Inst. of Tech., 1972.
- Plafker, G., Alaskan earthquake of 1964 and Chilean earthquake of 1960: Implications for arc tectonics, J. Geophys. Res., 77, 901-925, 1972.
- Post, R. L. and D. T. Griggs, The earth's mantle: evidence of non-newtonian flow, Science, 181, 1242-1244, 1973.
- Reid, H. F., The mechanics of the earthquake. In The California Earthquake of April 18, 1906. Rept. State Earthquake Invest. Comm., Carnegie Inst., Washington, D.C., 192 pp., 1910. (original rebound theory)
- Rice, D. A., Gravity observations in Alaska, U.S. Coast Geodetic Survey, Vol. III: The Prince William Sound, Alaska, earthquake of 1964 and aftershocks, pp. 5-20, 1969.

- Richtmyer, R. D. and K. W. Morton, Difference methods for initial-value problems, Interscience, 2nd ed., 1967.
- Rikitake, T., Electromagnetism and the Earth's interior, Elsevier, Amsterdam, 308 pp., 1966.
- Rikitake, T., Japanese national program on earthquake prediction, in T. Rikitake (ed.), Focal processes and the prediction of earthquakes, Tectonophysics, 23, 225-236, 1974.
- Rosenman, M. and S. J. Singh, Quasi-static strains and tilts due to faulting in a viscoelastic half-space, Bull. Seism. Soc. Am., 63, 1737-1752, 1973a.
- Rosenman, M. and S. J. Singh, Stress relaxation in a semi-infinite viscoelastic earth model, Bull. Seismol. Soc. Am., 63, 2145-2154, 1973b.
- Rybicki, K., The elastic residual field of a very long strike-slip fault in the presence of a discontinuity, Bull. Seismol. Soc. Am., 61, 79-92, 1971.
- Rybicki, K., Analysis of aftershocks on the basis of dislocation theory, Phys. Earth Planet. Int., 7, 409-422, 1973.
- Savage, J. C. and L. M. Hastie, Surface deformations associated with dip-slip faulting, J. Geophys. Res., 71, 4897-4904, 1966.
- Schapery, R. A., Approximate methods of transform inversion for viscoelastic stress analysis, Proceedings of the Fourth U.S. Nat. Cong. of Appl. Mech., 1075-1085, 1961.
- Schapery, R. A., Irreversible thermodynamics and variational principles with applications to viscoelasticity, Ph.D. thesis, California Institute of Technology, 1962.
- Schapery, R. A., On the time dependence of viscoelastic variational solutions, Quart. Appl. Math., 22, 207-215, 1964.
- Scholz, C., Crustal movements in tectonic areas, in: E. F. Savarensky and T. Rikitake (ed.), Forerunners of Strong Earthquakes, Tectonophysics, 14, 201-217, 1972.
- Scholz, C., Post earthquake dilatancy recovery, Lamont-Doherty Geological Observatory Contribution No. 2112, 1974.

- Scholz, C. H., M. Wyss, and S. W. Smith, Seismic and aseismic slip on the San Andreas fault, J. Geophys. Res., 74, 2049-2069, 1969.
- Scholz, C. H., L. R. Sykes, and Y. P. Aggarwal, Earthquake prediction: a physical basis, Science, 181, 803-810, 1973.
- Searle, S. R., Linear Models, Wiley, 532 pp., 1971.
- Shimazaki, K., Pre-seismic crustal deformation caused by an underthrusting oceanic plate, in eastern Hokkaido, Japan, Phys. Earth Planet. Int., 8, 148-157, 1974.
- Shiono, K., Focal mechanism of local earthquakes in Wakayama region (Part 1), J. Seismol. Soc. Japan, 23, 226-236, 1970a.
- Shiono, K., Focal mechanism of local earthquakes in Wakayama region (Part 2), J. Seismol. Soc. Japan, 23, 253-263, 1970b.
- Small, J. B. and L. C. Wharton, Vertical displacements determined by surveys after the Alaskan earthquake of March 1964, U.S. Coast Geodetic Survey, Vol. III: Geodesy and Photogrammetry, The Prince William Sound, Alaska earthquake - 1964 and aftershocks, pp. 21-33, 1969.
- Smith, A. T., Stress-distribution beneath island arcs, M.S. thesis, Mass. Inst. of Tech., 1971.
- Smith, A. T. and M. N. Toksöz, Stress distribution beneath island arcs, Geophys. J. R. Astr. Soc., 29, 289-318, 1972.
- Stauder, W., Mechanisms of the Rat Island earthquake sequence of February 4, 1965, with relation to island arcs and sea-floor spreading, J. Geophys. Res., 73, 3847-3858, 1968a.
- Stauder, W., Tensional character of earthquake foci beneath the Aleutian trench with relation to sea-floor spreading, J. Geophys. Res., 73, 7693-7701, 1968b.
- Strang, G. and G. J. Fix, An analysis of the finite element method, Prentice-Hall, 306 pp., 1973.
- Sugimura, A. and S. Uyeda, Island arcs: Japan and its environs, Elsevier, 247 pp, 1973.

- Thatcher, W., Re-analysis of geodetic data for the 1906 San Francisco earthquake, Trans. Am. Geophys. Union, 55, 426, 1974.
- Toksöz, M. N., J. W. Minner, and B. R. Julian, Temperature field and geophysical effects of a downgoing slab, J. Geophys. Res., 76, 1113-1138, 1971.
- Toksöz, M. N., N. H. Sleep, and A. T. Smith, Evolution of the downgoing lithosphere and the mechanisms of deep focus earthquakes, Geophys. J. R. Astr. Soc., 35, 285-310, 1973.
- Tsubokawa, I., Y. Ogawa and T. Hayashi, Crustal movements before and after the Niigata earthquake, Jour. Geod. Soc. Japan, 10, 165-171, 1964.
- Tsubokawa, I., A. Okada, S. Izutuya, Levelling resurvey associated with the area of Matsushiro earthquake swarms (2), Bull. Earthquake Res. Inst., 46, 417-429, 1968.
- Tsumura, K., Japanese contributions to the study of mean sea level (a review), J. Geod. Soc. Japan, 10, 192-202, 1964.
- Tsumura, K., Investigation of mean sea level and its variation along the coast of Japan (Part 2), Jour. Geod. Soc. Japan, 16, 239-275, 1970.
- Turner, M. J., R. W. Clough, H. C. Martin, and L. P. Topp, Stiffness and deflection analysis of complex structures, J. Aeron. Sci., 23, 805-823, 1956.
- Utsu, T., Anomalies in seismic wave velocities and attenuation associated with a deep earthquake zone (I), J. of Faculty of Science, Hok. Univ., Japan, Ser. VII, 3, 1-25, 1967.
- Uyeda, S., personal communication, 1974.
- Washizu, K., On the variational principles of elasticity and plasticity, Rept. 25-18, Cent. N5ORI-07833, Mass. Inst. of Tech., March 1955.
- Watanabe, T., D. Epp, S. Uyeda, M. Langseth, and M. Yasui, Heat flow in the Philippine Sea, Tectonophysics, 10, 205-224, 1970.
- Wiggins, R. A., The general linear inverse problem: Implications of surface waves and free oscillations for earth structure, Reviews Geophys. Space Phys., 10, 251-285, 1972.

Wilkinson, J. H. and C. Reinsch, Linear Algebra, Springer-Verlag, Berlin, 438 pp., 1971.

Yamaguti, S., On the changes in the heights of yearly mean sea-levels in recent years, Bull. Earthquake Res. Inst., Tokyo Univ., 46, 901-906, 1968.

Zienkiewicz, O. C., M. Watson, and I. P. King, A numerical method of visco-elastic stress analysis, Int. J. Mech. Sci., 10, 807-827, 1968.

APPENDIX A

Implementation of time-dependent, finite element method

Chapter 2 outlines a finite element method for linear time-dependent problems; now the implementation of this scheme introduces new problems. Flexibility is needed for the method: elastic solutions, gravity, faults, and inversions should be available. Each finite element solution must yield both displacement and stress solutions in the time-domain. These requirements place tremendous demands upon input-output control within the programming. All these require careful implementation to give an efficient and useful computational strategy.

These requirements are obvious in the solution method. Each finite element solution in the Laplace domain demands a separate factoring of the stiffness matrix; each element's contribution involves an integral of the transformed relaxation function \bar{G}

$$\tilde{K} = \sum_n \frac{1}{2} \int_V \phi^T \tilde{E}^T \tilde{G} \tilde{E} \phi dv \quad (\text{A.1})$$

where the notation conforms to Chapter 2. For each Laplace time the transformed displacement \bar{q} are the solution to

$$\tilde{K} \bar{q} = \bar{Q} \quad (\text{A.2})$$

where the boundary conditions and loads \bar{Q} start at time zero (section 2.3). The inversion to the time-domain using collocation or least-squares requires the transformed displacements \bar{q} for each reduced time. If stresses are necessary, we also save the stress-strain matrix for each reduced Laplace time and element. This involves enormous data retention. Once the finite element solutions are available in the Laplace domain, least-squares fits the displacements \bar{q} or element stresses to the transformed exponential series:

$$[\bar{q}]_{P=1/\gamma_j} = \left[\sum_{i=1}^n \frac{S_i}{1+\gamma_i P} \right]_{P=1/\gamma_j} \quad j = 1, n \quad (\text{A.3})$$

where

$$q = \sum_{i=1}^n S_i (1 - e^{-t/\gamma_i}) \quad (\text{A.4})$$

in the time domain (section 2.6). Notice that all initial displacements or stresses correspond to a step function at time zero. The fitting implies access to many solutions in the Laplace domain. Inversions multiply this requirement: each fault segment needs its own time-dependent solution. Fortunately, multiple factoring is unnecessary for the stiffness matrix K ; rather, forward-backward substitution yields each solution when intermediate results are available. Again efficient data management is paramount.

Figure A.1

Outline of system structure for finite element computations and inversion. Three systems are represented:

- i) The finite element computations (FEM) include SETUP, SOLUTION, and INVERSION stages. Three direct-access files on disk represent intermediate storage modes. For the solution program, gravity, the Laplace times for the solutions, and the problem type (elastic or viscoelastic) must be specified. The subsequent inversion to the time domain involves either the stress or displacement when the series times and, if necessary, a constant flow term are selected.
- ii) The second system plots the displacements and stresses for models derived from either inversions or specific FEM problems. The program accesses the mesh configuration stored on disk and plots at desired times using the series approximation (equation 2.6.9).
- iii) Given an initial model and the constraining data, the inversion stage generates new models together with the resolution and errors for each. The first program formulates the problem into an eigenvalue problem and the resulting work files are stored on direct-access disk. The second solves the problem, while the last generates new models and determines the resolution and errors for a specific number of eigenvalues. These models may now serve as a new initial model.

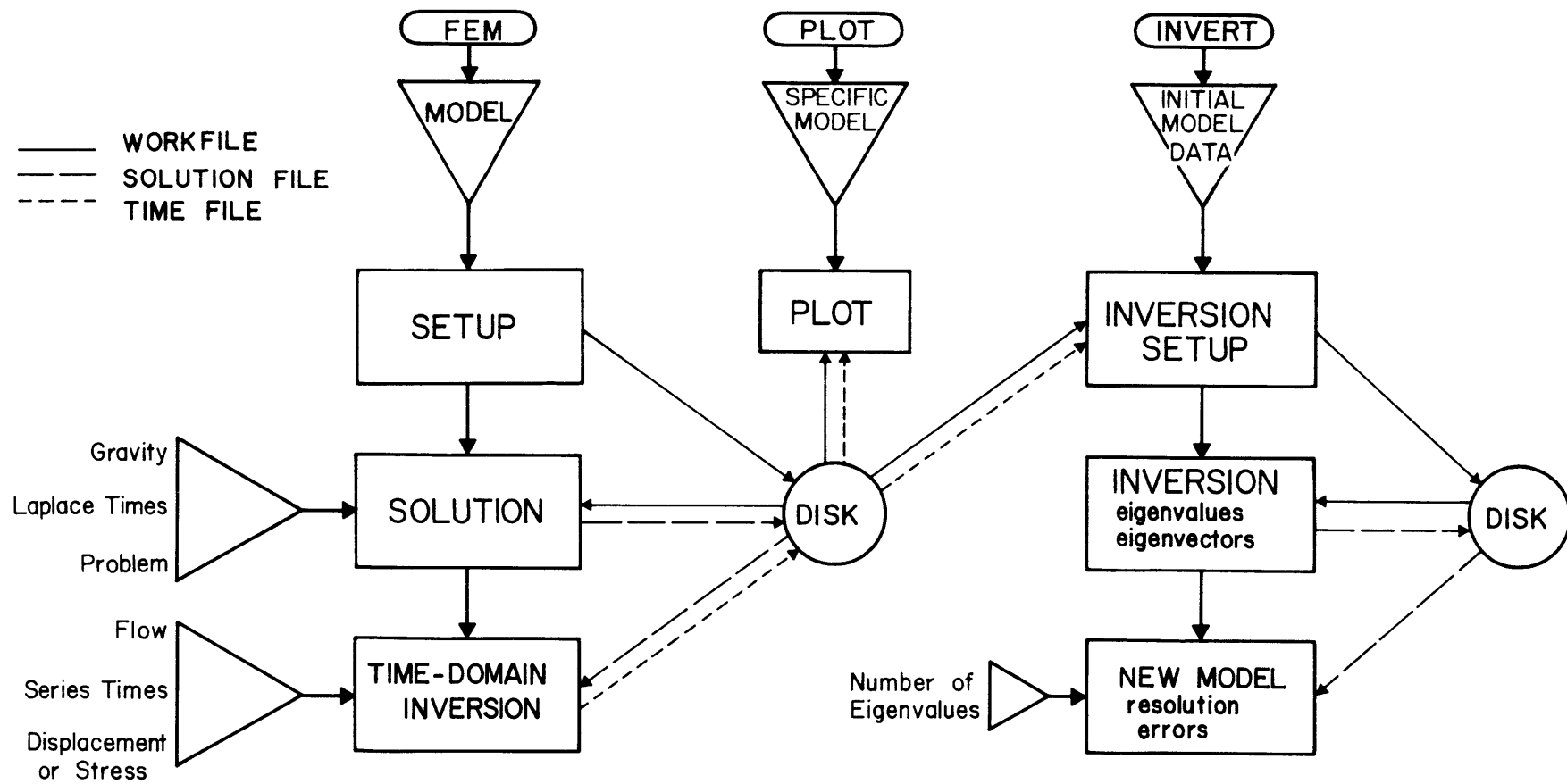


Fig. A.1

On-line core storage is crucial. Adopting a scheme used by Orringer and French (1972), we store each band of the stiffness matrix beginning with the first non-zero entry. A significant savings in space results compared to the maximum bandwidth mode. Subroutines from the FEABLE system (Orringer and French, 1972) have been incorporated with modifications for setting up the problem, factoring the matrix using Cholesky's algorithm, and subsequent solution using forward-backward substitution. These provide an efficient solution scheme when we retain the whole stiffness matrix in core.

Figure A.1 shows the system structure adopted for the viscoelastic solution. A crucial element is sufficient versatility to allow solution of various problems: elastic, viscoelastic, and inversion for both displacements and stresses. Information must be accumulated for each. For example, the stress-strain matrix for each Laplace time and element must be saved for computing time-dependent stresses. To accomplish these tasks, we subdivide the problem into the following operations:

- I. SETUP assigns locations to the storage areas (i.e. stiffness matrix, solution-force vector, bookkeeping variables, etc.) based upon the dimensions of the problem, and reads and stores the element information. This is independent of the type of solution, whether elastic or viscoelastic; it

only depends on the grid structure. All this is stored on a disk work-file together with the element information, material constants, node locations, densities, boundary conditions, and other assorted information. Access to the disk file occurs one track at a time to reduce input-output operations.

II. SOLUTION constructs the stiffness matrices and solves them for the specified problem. For an elastic solution just one factoring is necessary while a visco-elastic solution requires half a dozen or more separate assembling and factoring operations. Each factoring may involve more than one solution if a generalized matrix inversion is necessary. All the input is accessed from the disk work-file, while all output is stored on a disk solution-file. This dramatically decreases input-output expense when combined with an additional buffer variable located in a read-write subroutine. Large blocks of input or output may be transferred thereby reducing the input-output operations to the computer.

III. TIME DOMAIN INVERSION reads the displacement solutions for each Laplace time and inverts using the series approximation for either displacement or stress. The resulting coefficients are stored on disk file. Once

these solutions are available, various modes of processing can be executed including plotting and constructing the variational parameters for the inversion solutions.

IV. DATA INVERSION

The generalized matrix inverse allows a simple inversion scheme for the fault displacements. We access a file containing the time inverted coefficients for the displacements and introduce a starting model. SETUP fixes the viscosity ratios for the asthenosphere and mantle; however, scaling allows us to vary the initial viscosity in the asthenosphere. In the starting model we constrain this initial viscosity and define the fault segments for the inversion. The resulting coupling and variational coefficients together with appropriate weighting and errors define the coefficient matrix for the inversion.

Now the first of two routines multiplies the coefficient matrix by its transpose and factors into a tridiagonal matrix using Householder's method, solves for the p largest eigenvalues using bisection, and finds the eigenvectors. With the results stored on disk, the second routine selects the number of eigenvalues and generates the solution, variances, resolution matrix, and weighting matrices for the next iteration. The structure facilitates alterations and new models without solving a new finite element model.

APPENDIX B

TEST PROBLEM: Pressurization of a viscoelastic cylinder with an elastic case.

We desire a problem with an analytic solution for comparison to the numerical method. A problem often encountered in engineering literature is the pressurization of an infinite viscoelastic cylinder enclosed by an elastic case. Using the correspondence principle of viscoelasticity and the elastic solution, we can compute an analytic solution. The strategy is similar to the operational form of the variational principle, except the Laplace transform of the Euler equations reduce to equations analogous to the elastic problem (Christensen, 1971). Thus elastic solutions are applicable when the elastic moduli are replaced by the corresponding transformed viscoelastic moduli. We then transform the operational solution in the Laplace domain to the time domain. Using this approach, Lee et al. (1959) have calculated the stresses for an externally reinforced viscoelastic cylinder. These results allow direct comparison with our finite element solution.

The numerical solution uses the method previously outlined: finite element solutions in the Laplace domain and a series inversion using collocation to the time domain. In addition, a finite element solution using

stepping in the time domain is available (Zienkiewicz, et al., 1968). Assuming a Maxwellian viscoelastic behavior in shear and elastic behavior for the bulk modulus, the constituent relations are:

$$G_{ijkl}(t) = [k(t) - \frac{2}{3}\mu(t)] \delta_{ij}\delta_{kl} + \mu(t) [\delta_{ik}\delta_{jl} + \delta_{il}\delta_{jk}] \quad (B.1)$$

where $k(t)$ is the bulk modulus relaxation function and $\mu(t)$ is the shear modulus relaxation function. Therefore one has

$$\begin{aligned} \sigma_{ij} = \delta_{ij} \int_0^t [k(t-\tau) - \frac{2}{3}\mu(t-\tau)] \frac{\delta \epsilon_{kk}(\tau)}{\delta \tau} d\tau \\ + 2 \int_0^t \mu(t-\tau) \frac{\delta \epsilon_{ij}(\tau)}{\delta \tau} d\tau \end{aligned} \quad (B.2)$$

where the relaxation functions for our case are

$$k(t) = K \quad (B.3)$$

and

$$\mu(t) = \mu_0 e^{-t/\tau} \quad (B.4)$$

For the thin elastic case, these moduli are set to

$$K = 3.778 \times 10^7 \text{ lb/in}^2; \mu_0 = 1.1525 \times 10^7 \text{ lb/in}^2; \tau = 1. \quad (B.5)$$

The relaxation time τ is in arbitrary units. For the internal viscoelastic cylinder these take the values

$$K = 1 \times 10^5 \text{ lb/in}^2; \mu_0 = .375 \times 10^5 \text{ lb/in}^2; \tau = 10^4 \quad (B.6)$$

Thus the case is essentially elastic.

The element configuration adopted for the problem is given in Figure B.1. The elements are all constant strain triangles. The boundaries simulate a full cylinder; free slip is specified along the edge of each quadrant. The interior is then given an outward, arbitrary pressure of one unit. Finally, the inversion of stresses to the time domain uses five reduced times.

Figure B.2 illustrates the principle stresses for two times, zero and ten, plotted on the element array. The zero time is obscured by time ten except where a tensional hoop stress occurs along the inner boundary. The ends of the tensional stress are denoted by small asterisks superimposed on the isotropic stress at time ten. The stiffer elastic case receives the brunt of the tensional hoop stresses as the shear modulus relaxes within the viscoelastic cylinder. These results correspond precisely to both our intuition and the analytic solution.

The results for the radial stress, σ_{rr} , are given in Figure B.3 with a comparison to the analytic solution of Lee, et al. (1959). The results correspond very favorably when the individual elements are properly averaged for each radial distance. The elements, constant strain triangles, do not give exceptionally accurate results since stress is constant throughout the element. Better results occur when adjacent elements are averaged to obtain an approximation

Figure B.1

Finite element net for viscoelastic cylinder with elastic case. Using plane strain, one quadrant simulates the full cylinder when slip boundary conditions are applied to the faces. The origin then represents the center of revolution. Shaded elements correspond to the viscoelastic medium; the surrounding, thin elastic case conforms to the outer, unshaded elements. The inner arrows represent the pressurization of the interior at time zero.

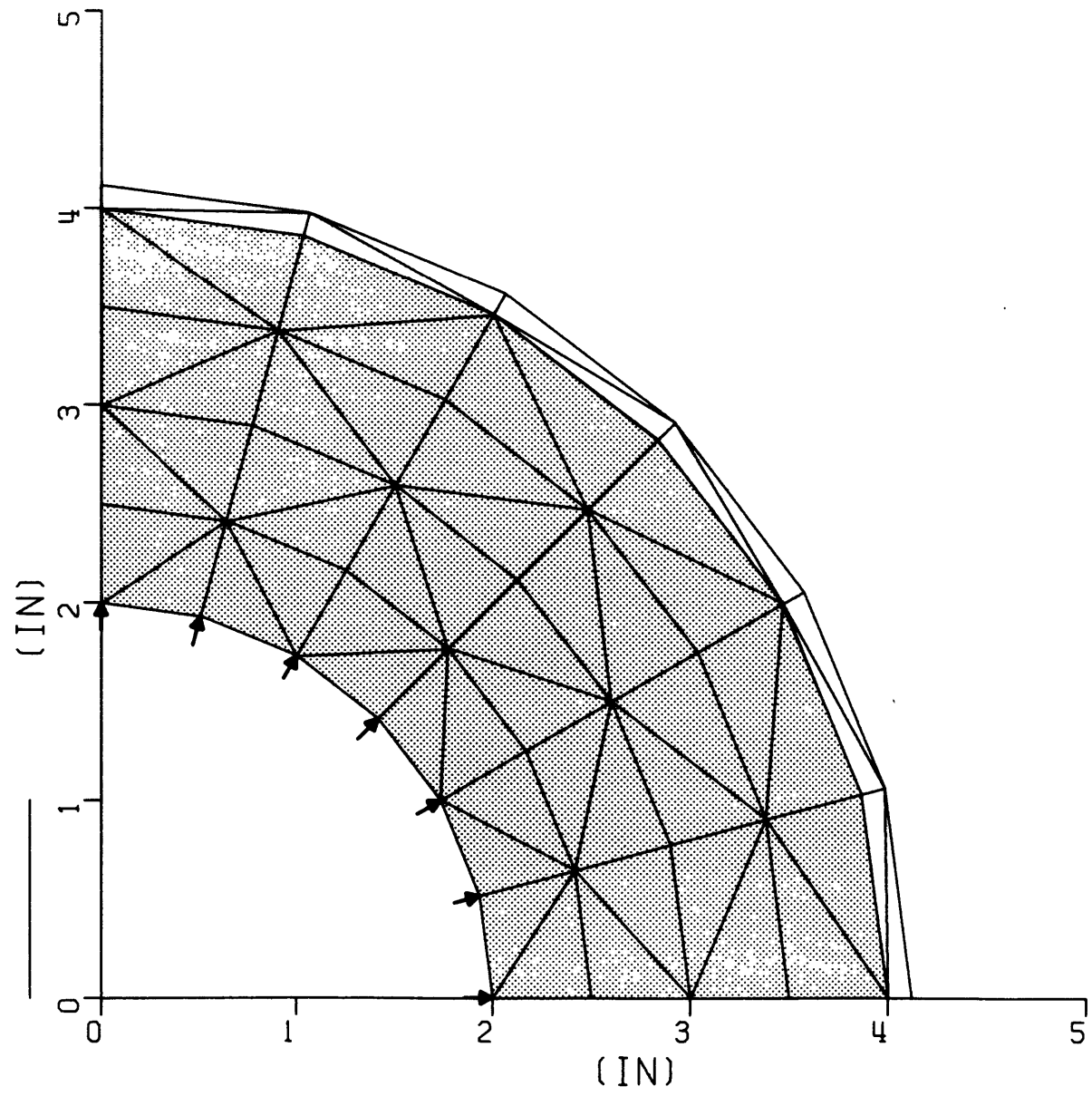


Fig. B.1

Figure B.2

Principle stresses plotted on the element array. Two dimensionless times, 0. and 10., are shown in the diagram. The length of the line segment denotes the magnitude normalized by the pressure; the orientations correspond to the minimum and maximum stress. The scale is in the upper right. Asterisks mark the ends of the tensional stress. Note that time 10. generally obscures time 0. except when the asterisks are visible. By time 10. the stress within the viscoelastic cylinder is virtually isotropic; the elastic case absorbs the tensional hoop stress.

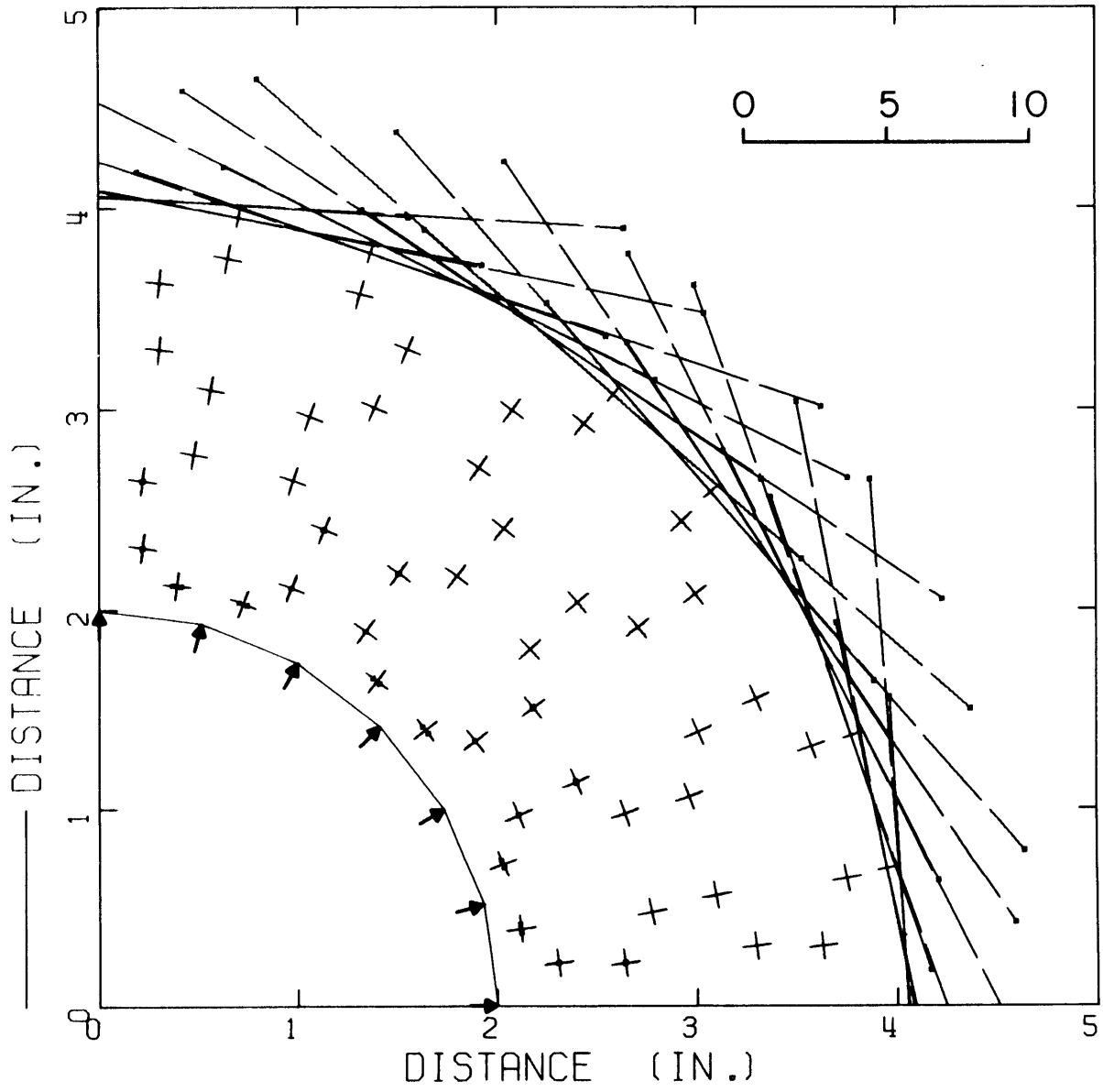
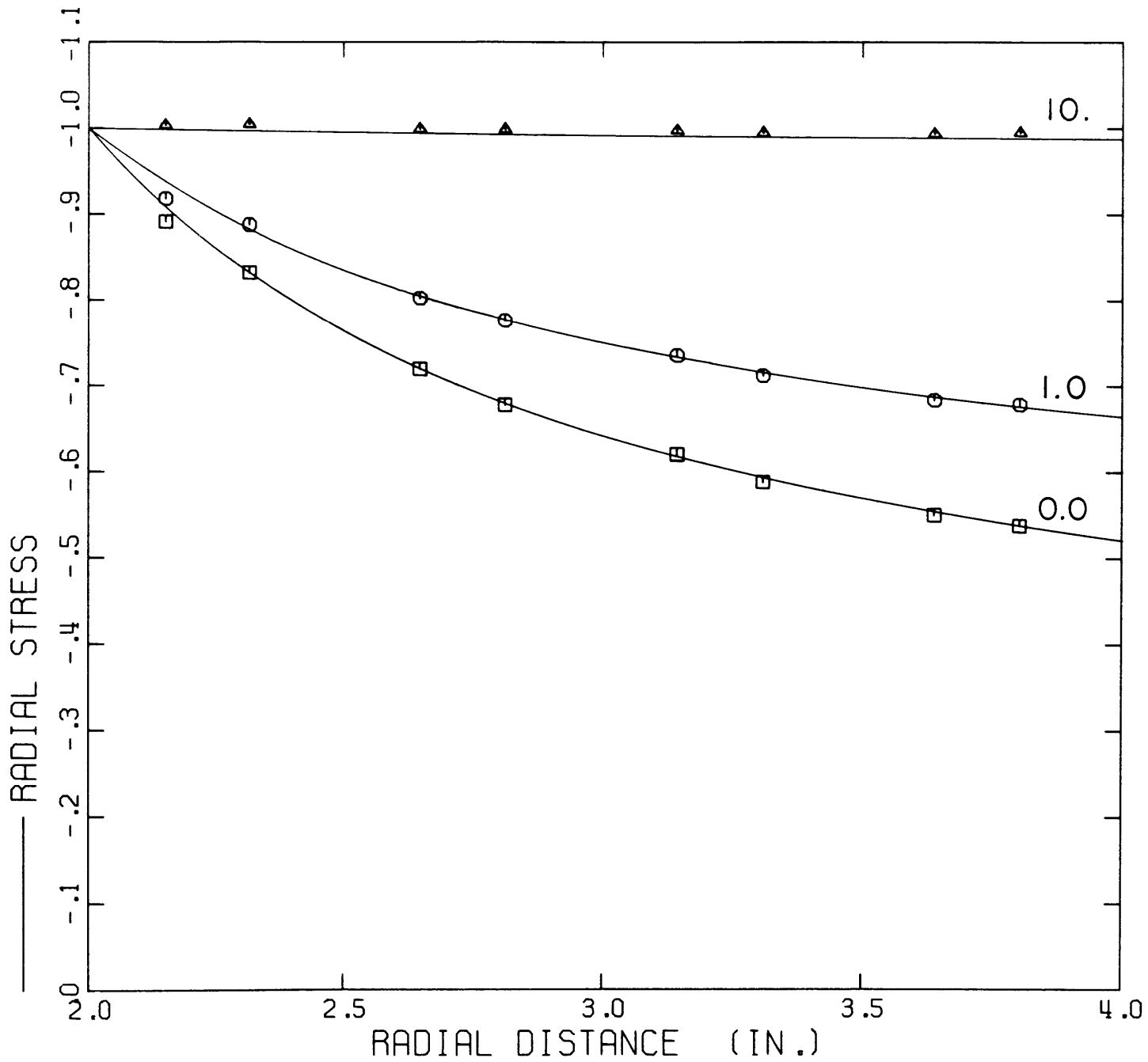


Fig. B.2

Figure B.3

Normalized radial stress from the finite element solution compared to an analytic solution by Lee, et al. (1959) for pressurization of a viscoelastic cylinder with an elastic case. Three times are shown after pressurization: 0., 1., 10. The symbols indicate the finite element solution at specific elements; the lines are the analytic solution. Averaging two adjacent elements yields the best approximation since CST (constant strain triangles) give constant stress. The comparison is then quite good.

Fig. B.3



midway between the two (Desai and Abel, 1972). One effectively obtains then a second order approximation similar to a six node triangle.

The solution given by Zienkiewicz, et al. (1968) requires many more individual solutions than the operational strategy. His solutions use time increments of .1; thus, 100 solution steps span the time domain. This is 20 times more than the transformed solution. An iterative solution technique can successfully be applied to save time for both methods. It was not used for the transformed principle since many unique solutions are required for the fault plane inversion at each reduced time. The inversion solutions are also impossible with the time-stepping strategy. The operational strategy requires then only one twentieth the solutions as an efficient stepping method, not to mention the versatility gained for inversion problems and the avoidance of error propagation.

APPENDIX C

Results for Models A-1 and A-5.

Table C.1 represents the original output for model A-1 from the inversion. The first part gives the parameters for the model, standard deviations and resolution. The initial model constrains the fault displacements from 26 km depth to the surface at 500 cm. This is held constant during the inversion. From 57 to 35 km depth the initial model is zero. The table includes the following notations and comments:

PARAMETERS

TYPE: Depth of node (km) on fault where displacement occurs, or VIS represents the viscosity parameter.

DEPTH: Depth of node (km) on fault, or -1. if viscosity parameter.

PARAM OLD: Old or initial value of parameter if used in inversion. In model A-1, it is set to zero if constrained during the inversion.

PDELP: Change in parameter during inversion.

STD: Standard deviation for fit. To obtain true estimate, this value is multiplied by model fit in std (i.e. 2.35).

RLEN: Resolution length of parameter in km. The distance represents the depth extent.

DATA

TYPE: Horizontal distance (km) from fault trace. The first group of eight are for .5 year since the earthquake; the

second represents 18 years.

OBVAL: Observed value (cm) for geodetic observations. In model A-1 the displacements are relative to 63 km, and the absolute datum is not constrained.

STD: Standard deviation (cm) assigned each observation.

DELCN: Calculated value (cm) from the new model for each observation.

FIT STD: Fit of new model to observations in the standard deviations assigned each data point.

RLEN: Number of adjacent data that represents an independent observation.

Table C.2 gives the corresponding results for model A-5. The first part gives an additional display of the new model with the sum of the old parameters plus the change. Thus, the new model is designated PARM NEW. In the DATA section, the type also includes tilt observations from Muroto promontory (T122) at times 0., 1., 2., and 5. years after the earthquake. V designates vertical displacements, again in time groups of .5 and 18. years. In each case the number represents the distance from the fault trace in figure 5.5. The observed value (OBVAL) are relative to T122 or V112 (for both times); however, the inversion now retains the absolute datum as a constraint.

TABLE C.1 - Model A-1

PARAMETER RESOLUTION - DEVIATION/RES. LEN.
EIGENVALUE

TYPE	57.	50.	43.	35.	20.	17.	VIS
DEPTH	57.00	50.00	43.00	35.00	20.00	17.00	-1.000
PARM OLD	.0	.0	.0	.0	.0 -500.	.0 -500.	.0 -500.
PDELPH# 4	-16.14	-151.9	-781.0	-491.9	-.1402E-10	-.1072E-10	-.3141E-01
STD# 4	39.64	38.75	16.03	33.54	.4134E-11	.2732E-11	.0800E-01
RLEN	7.138	11.50	10.15	9.564	.4138E+27	.7734E+27	1.011

DATA DENSITY - NUMBER OF ADJACENT DATA REQUIRED
EIGENVALUE 4 MODEL FIT IN STD= 2.35E+00

Viscosity = $3.2 \pm 0.8 \times 10^{19}$ poise

TYPE	63	69	75	100	112	125	137	150	63	69
OBVAL	.0	-29.40	-69.77	-127.5	-128.2	-130.6	-132.4	-133.1	30.59	-.8428
STD	2.000	2.000	2.000	2.000	2.000	2.000	2.000	2.000	3.000	3.000
DELGN	-.2461E-12	-31.58	-64.84	-131.5	-135.5	-133.9	-129.7	-125.8	22.42	-7.062
FIT STD# 4	-.1230E-12	-1.089	2.464	-1.075	-3.602	-1.654	1.382	3.674	-2.723	-2.073
RLEN# 4	.9677E+27	5.197	2.121	3.138	5.208	4.411	3.340	2.896	3.903	3.129
TYPE	75	87	100	112						
OBVAL	-40.40	-91.70	-108.1	-110.3						
STD	3.000	3.000	3.000	3.000						
DELGN	-38.50	-84.38	-108.1	-118.3						
FIT STD# 4	.6635	2.440	.9567E-02	.3159						
RLEN# 4	3.096	4.098	2.722	2.255						

TABLE C.2 - Model A-5

TYPE	60	50	34	24	22	19	16	13	11	VIS
DEPTH	-60.00	-50.00	-34.00	-24.00	-22.00	-19.00	-16.00	-13.00	-11.00	.0
PARM OLD	94.50	-577.8	-1501.	-287.0	-1105.	-1001.	-978.0	-689.0	-829.0	.0
PDELP	-58.16	1.658	45.88	-6.899	60.83	115.5	186.2	-121.8	-142.0	-1.310
PARM NEW	36.34	-576.1	-1455.	-293.9	-1744.	-885.5	-791.8	-810.8	-971.0	-1.310
STD# 5	44.26	18.94	41.63	44.95	55.17	96.77	135.7	215.3	623.1	.9846E-01
RLEN	17.84	18.13	20.74	29.20	31.70	41.63	61.11	77.48	57.46	1.007
W	60.00	65.00	73.00	122.0	143.0	316.0	745.0	1006.	1013.	.5000
WSTD	132.9	220.1	166.7	268.2	283.7	473.4	942.3	1010.	598.0	23.48
WRES	39.07	42.67	51.25	101.6	124.1	314.3	897.8	1365.	1184.	.7735E-01

PARAMETER RESOLUTION - DEVIATION/RES.LEN.
EIGENVALUE 5

Viscosity = $1.4 \pm 0.6 \times 10^{20}$ poise

TYPE	60	50	34	24	22	19	16	13	11	VIS
DEPTH	-60.00	-50.00	-34.00	-24.00	-22.00	-19.00	-16.00	-13.00	-11.00	.0
PARM OLD	94.50	-577.8	-1501.	-287.0	-1105.	-1001.	-978.0	-689.0	-829.0	.0
PDELP# 5	-58.16	1.658	45.88	-6.899	60.83	115.5	186.2	-121.8	-142.0	-1.310
STD# 5	44.26	18.94	41.63	44.95	55.17	96.77	135.7	215.3	623.1	.9846E-01
RLEN	17.84	18.13	20.74	29.20	31.70	41.63	61.11	77.48	57.46	1.007

DATA DENSITY - NUMBER OF ADJACENT DATA REQUIRED
EIGENVALUE 5 MODEL FIT IN STD= 1.60E+00

TYPE	T122	T122	T122	T122	V112	V126	V132	V143	V163	V184
OBVAL	-2.009	-3.325	-3.350	-2.980	-5.696	.8961	-.6376	-25.70	1.648	-2.750
STD	3.000	3.000	3.000	3.000	4.000	2.000	2.000	10.00	2.000	2.000
DELGN	-.7797E-01	.1023	.2661	.7537	1.738	-.8054	-.2451	-.2306	-2.036	-3.341
FIT STD# 5	.6436	1.142	1.205	1.245	1.859	-.8508	.1963	2.547	1.842	-.2959
RLEN# 5	505.0	537.6	580.2	707.8	8.956	2.308	2.378	33.67	2.294	4.618

TYPE	V205	V225	V112	V126	V132	V143	V163
OBVAL	-7.764	-4.309	27.43	-13.07	-19.04	-35.93	-44.59
STD	2.000	2.000	4.000	2.000	2.000	2.000	2.000
DELGN	-3.752	-3.650	23.60	-11.45	-20.85	-31.24	-47.77
FIT STD# 5	2.006	.3294	-.9556	.8117	-.9055	2.343	-1.588
RLEN# 5	3.498	2.276	1.220	2.376	3.694	2.294	1.486

APPENDIX D

Glossary of Symbols

A and A'	Matrix giving variational parameters for inversion.
B_u	Boundary surface having prescribed displacements.
B_σ	Boundary surface having prescribed stress.
Δc	Difference between observations and values calculated from initial model for inversion.
D	Flexural rigidity = $Eh^3/12(1-\nu^2)$.
D_j	Differential operator of order j.
da	Integral over surface.
dv	Integral over volume.
$\underline{\underline{E}}$	Strain operator.
e	Dilatation.
F_i	Component of body force.
$G_{ijkl}(t)$	Relaxation function. Represents kernel for stress strain relation with viscoelastic medium.
g	Gravitational acceleration at earth's surface.
h	Thickness of beam or plate. Characteristic dimension of element.
\tilde{K}	Stiffness matrix for sum of elements.
\tilde{k}	Stiffness matrix for one element.
k	Foundation modulus.
N	Axial load on plate or beam.
n_j	Normal vector to surface.
Δp	Parameter change during inversion.

\underline{Q}	Force vector for sum of elements.
\underline{Q}^e	Force vector for one element.
Q_v	Shear stress on beam.
q_j	Nodal parameters (i.e. displacement).
S	Prescribed stresses on boundary of solid.
\underline{S}	Covariance matrix proportional to dimensions of observations or errors for inversion.
U	Eigenvectors in data space.
u_i	Displacements in continuum.
V	Eigenvectors in parameter space.
v^h	Trial function for finite element method.
X_j	j th component of body force.
x	Horizontal distance on beam.
y	Vertical displacement perpendicular to beam.
z_j	Node j in finite element mesh.
α	$=(\lambda^2+N/4D)$ Dimensionless number for beam solution.
β	$=(\lambda^2-N/4D)$ Dimensionless number for beam solution.
Δ	Prescribed displacements on boundary of solid.
ϵ_{ij}	Infinitesimal strain tensor.
η	Viscosity.
Λ	Eigenvalue vector arranged in descending order.
λ_j	Eigenvalue j .
λ	$=(k/4D)$ Dimensionless number for beam solution.
ν	Poisson's ratio.

π	Variational functional for extremum (also constant π).
π_d	Simplified variational functional for displacements.
ρ	Density.
ρ_f	Fluid density of medium producing hydrostatic stress.
σ_{ij}	Stress tensor.
τ	Variable in time (often dimensionless)
ϕ_j	Trial function for each model parameter q_j
ψ	Representation for displacements or stress using approximate Laplace transform.

BIOGRAPHICAL NOTE

I first saw the light of day December 13, 1946, in San Diego, California, the result of a post-war boom. My parents, Dr. Albert T. and Vera T. Smith, quickly moved on to other sections of the country, yet we were always inexorably drawn back to California. My star-struck youth, from elementary school through Grossmont High School in San Diego, found me gazing into a telescope. Beginning at U.C. San Diego in 1965 as a Regent's Scholar, physics seemed an appropriate means to continue these heavenly pursuits. But Freeman Gilbert and the Scripps crew brought me down to earth during my senior year. After many years in San Diego I considered a change in climate for my health; MIT appeared as the ideal solution. Since that moment I have eagerly followed the moving plates with the propitious encouragement of Professors M. Nafi Toksöz, Keiiti Aki, Frank Press, and the MIT environment. Support during these years includes an MIT fellowship, research assistantship, and a Fannie and John Hertz Foundation Fellowship, the latter encouraging diversions in research. The intangible joys have been many; the material results include:

Smith, A.T. and M.N. Toksöz, Stress distribution within a downgoing slab (abs), Trans. Am. Geophys. Union, 51, 823, 1970.

- Toksöz, M.N., A.T. Smith, N.H. Sleep, and J.W. Minear, Temperature and stress distributions in descending lithospheric plates, Symposium on Ocean Floor Spreading, International Association of Seismology and Physics of the Earth's Interior, IUGG, Moscow, August 2-14, 1971.
- Smith, A.T., Stress distribution beneath island arcs (abs), Trans. Am. Geophys. Union, 52, 924, 1971.
- Toksöz, M.N., N.H. Sleep, and A.T. Smith, Evolution and properties of the downgoing lithosphere, Geophys. J. R. Astr. Soc., 35, 285-310, 1973.
- Smith, A.T., Deep earthquakes: An internal instability? (abs), Trans. Am. Geophys. Union, 54, 365, 1973.
- Smith, A.T., M.N. Toksöz, and N.H. Sleep, Stresses in downgoing lithosphere and the mechanism of deep focus earthquakes, Symposium on Geodynamic Processes, International Association of Seismology and Physics of the Earth's Interior, IUGG, Lima, Peru, August 22-31, 1973.
- Smith, A.T., Time-dependent strain accumulation and release at island arcs (abs), Trans. Am. Geophys. Union, 55, 427, 1974.
- Smith, A.T., M.N. Toksöz, Stress distribution beneath island arcs, Geophys. J. R. Astr. Soc., 29, 289-318, 1972.